# PREPARATION AND EVALUATION OF METAL SURFACES FOR USE AS PHOTOCATHODES

Thesis submitted in accordance with the requirements of
Loughborough University for the degree of Doctor in Philosophy by

**Sonal Mistry**

June 2018

.

ॐ श्री परमात्मने नमः इति

# Contents

# List of Figures

# List of Tables

# Abstract

In linear accelerator driven 4th generation Free Electron Lasers (FELs), the final beam quality is set by the linac and ultimately by its photoinjector and photocathode. Therefore, to deliver cutting-edge beam characteristics, there are stringent requirements for the photocathode used in the photoinjector. Understanding how surface properties of materials influence photocathode properties such as quantum efficiency (QE) and intrinsic emittance is critical for such sources.

Metal photocathode research at Daresbury Laboratory (DL) is driven by our on-site accelerators VELA (Versatile Electron Linear Accelerator) and CLARA (Compact Linear Accelerator for Research and Applications), a free electron laser test facility. Metals offer the advantage of a fast response time which enable the generation of short electron pulses. Additionally, they are robust to conditions within the gun cavity. The main challenge with metal photocathodes is to maximise their (relatively) low electron yield.

In this PhD thesis, the goal has been to carry out an experimental investigation on alternative metals to copper, correlating surface properties with photoemissive properties. A range of surface analysis techniques have been employed: surface composition was investigated using X-ray Photoelectron Spectroscopy and Medium Energy Ion Scattering, Kelvin Probe apparatus and Ultra-violet Photoelectron Spectroscopy were used to measure work function, and Atomic Force Microscopy and Interferometric microscope provided images characterising surface morphology. The photocathode properties studied include: QE measured using a 265 nm UV LED source that was later upgraded to a 266 nm UV LASER, and Mean Transverse Energy measured using the Transverse Energy Spread Spectrometer.

As a result of this work, Mg, Nb, Pb, Ti and Zr have all been identified as photocathode candidate materials, each exhibiting a QE greater than Cu. Additionally, surface preparation procedures for optimising QE from a selection of metals has been explored; the findings of these experiments would suggest that *ex-situ* Ar plasma treatment followed by *in-situ* heat treatment is well suited to remove surface contaminants without altering the surface morphology of the cathode. As part of this work, metallic thin films produced by magnetron sputtering have been produced; ultimately the chosen cathode metal will be deposited onto a cathode plug which will be inserted into the electron gun that will drive CLARA. Thus the preparation of metal thin films has been investigated and the effect of different substrate materials on the film properties

has been explored. Preliminary experiments studying the effects of surface roughness on photoelectron energy distribution have been conducted; the findings have not been conclusive, thus further systematic studies are required.

# Acknowledgements

I would like to express thanks to my supervisor, Michael Cropper, for his support, balanced perspective and good humour. I am grateful to my ASTeC industrial supervisors, Reza Valizadeh and Boris Militsyn for their mentorship and patient guidance day to day. I have been very fortunate to have been taught and guided by them both.
Working within the Photocathode Group has provided me with excellent opportunities to work with and learn from a fantastic group of individuals: Tim Noakes, Lee Jones and Elaine Seddon. Thank you for your kind support and (unofficial) mentor ship.
I have been fortunate to be part of the eclectic, and somewhat eccentric, Vacuum Group (a.k.a Vacfam). I am very grateful to Adrian Hannah and Neil Pashley for their patience and technical support; I have learnt so much from you both and enjoyed working with you. Thanks to James Conlon, Joe Herbert, Keith Middleman and Oleg Malyshev.
To the students of the Vacuum Group, past and present, only you know the drama and madness that comes with working in the VacLab. In order of appearance...Sihui Wang, Stuart Wilde, Paolo Pizzol, Lewis Gurran, Taaj Sian, Nathan Lewis, Ruta Sirvinskaite. You are all brilliant and I am grateful to have spent the past 4 years working, laughing and crying with you! I also want to thank the lovely people at Daresbury who have made this experience for me: Alexandra Alexandrova, Bruno Camino, Kareem El-Abiary, Ryan Cash and Thomas Beaver.
I especially want to thank Sam Jones for his continual support and belief in me.
Lastly I am so very grateful for my dear family and the love and blessings I have received from them during this time and always.

# Chapter 1

# Introduction

The advances in Free Electron Laser (FEL) technology have made it possible to produce short-wavelength X-Rays with high pulse energies and short durations [2], thus facilitating experiments that would be impossible with third generation light sources. In order to deliver cutting-edge pulse characteristics, linear accelerator (linac) based sources have stringent requirements particularly with respect to the photocathode used in the photoinjector [3]. For example, the ideal photocathode should have a high quantum efficiency (QE), small intrinsic emittance, fast temporal response and a long lifetime. This combination of properties does not exist for a single cathode material, forcing a trade-off between these requirements. For example, the world's first hard X-Ray FEL, the Linac Coherent Light Source (LCLS), uses a copper photocathode [4] which, though a notoriously poor photo-emitter, exhibits a fast response time enabling the production of short electron pulses.
The Compact Linear Accelerator for Research and Applications (CLARA) is the new X-Ray FEL test accelerator currently under commission at Daresbury Laboratory. The CLARA photoinjector is a normal conducting radio frequency (RF) gun with an interchangeable photocathode plug, which will deliver average charge and low emittance beams [5]. Therefore, the choice of photocathode material and its surface preparation will be critical to delivering the required beam. The motivation for this research is to optimise the preparation procedure for metallic photocathodes for eventual implementation in the CLARA electron gun.

## 1.1 Electron sources

There are two principal means of generating electrons for accelerator applications: thermionic emission and photoemission. Both processes and examples of injectors that utilise each will be briefly discussed in the sections below. Whilst field emission is not used in accelerator applications, it is another technique that can be used for electron emission.

### 1.1.1 Thermionic emission

In thermionic emission, a cathode material is heated to generate electrons. The potential charge that can be extracted for a given material is dependent on the kinetic energy of the electrons in the conduction band. According to the Fermi-Dirac equation the kinetic energy of these electrons depends on the temperature. The probability that a particle will have energy $E$ is:

$$f(E) = (1 + \exp((E - E_F)/kT))^{-1} \tag{1.1}$$

where $E_F$ is the Fermi energy, T is the temperature and k is the boltzmann constant.

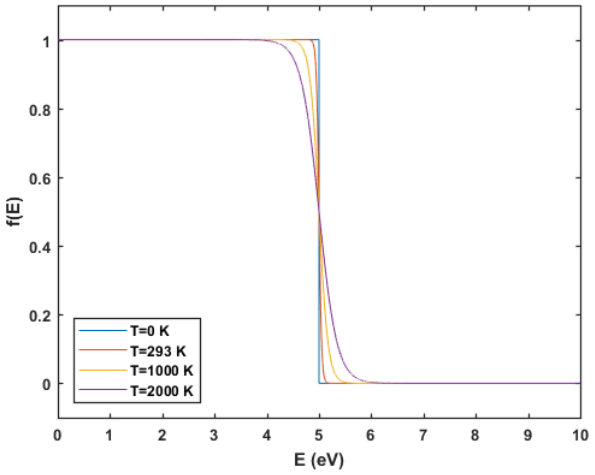


FIGURE 1.1: Fermi-Dirac distribution at 0 K, 293 K, 1000 K and 2000 K.

Thus as evidenced in Figure 1.1, as the temperature of the metal increases the electrons can move up to higher unoccupied states, or even overcome the work function. As an approximation, integrating the density of electrons at energies above the work function gives the following equation [6]:

$$J(T) = A_{RD}T^2 \exp(\frac{-e\phi}{kT})\,. \tag{1.2}$$

The Richardson-Dushmann equation (see equation 1.2) expresses the emission current density, $J$, from a metal with a work function, $\phi$, and at a temperature $T$. From this relation it becomes clear that a good thermionic emitter should have a low work function and also be stable at high temperatures [6].

This requirement for low work function and stability at high temperatures is met by few materials. Lanthanum hexaboride ($LaB_6$) is one such solid with a low work function and can be operated up to 1700 K [6]. Other thermionic cathodes are formed by taking materials that can operate at high temperatures, e.g. tungsten, and then cesiating the surface so as to lower the work function suitably.

There are several drawbacks to using a thermionic cathode as an electron source for an injector. Firstly, there is the issue of the cathode lifetime. In an RF gun during deceleration phase, the continuous stream of photoemitted electrons will return back to the cathode in a phenomena termed back-bombardment [7] [8]. Typically these cathodes have sensitive surface coatings which deteriorate with back-bombardment, thus reducing the operational lifetime. Secondly, the heated cathode must be kept thermally isolated from the rest of the gun and therefore choke joints must be employed [7]. Due to the cw stream of low energy electrons, the beam will have a large spread in energy and time [8] thus limiting applications. Additionally, for RF acceleration, the continuous stream must be chopped up into small packets; it is difficult to achieve ultra short pulses in this way. The advantage of a thermionic injector over a photoinjector is the comparatively low cost; the laser systems required to drive a photoelectron gun are costly and complex. Thermionic guns on the other hand are relatively robust and simple.

### 1.1.2 Photoemission

In photoemission, electrons are generated by a photocathode as a result of the absorption of photons, i.e. the photoelectric effect (see Chapter 2). Experimentally the photoelectric effect had been observed by Heinrich Hertz and his assistant Philipp Lenard in 1887 [9]. They showed that below a threshold energy, no electrons are emitted; but above that threshold the energy of the emitted electron is the same, independent of the intensity. It was Einstein that postulated that the reason for this phenomena was due to the particle nature of light, and in 1921 he was awarded the Nobel prize for the discovery of the photoelectric effect. The photoelectric effect is defined by Equation 1.3:

$$E_k = h\nu - \phi \tag{1.3}$$

where $E_k$ is the kinetic energy of the emitted electron, $h$ is planck's constant ($6.626 \times 10^{-34} J.s$), $\nu$ is the frequency of incident light and $\phi$ is the work function.

In a photocathode electron gun, the same principles are used. The main constituents of a photoinjector are the RF gun with integrated photocathode, an RF source and a laser system which generates pulsed light that is synchronised with the RF source [10] (see Figure 1.2). The cathode is illuminated by the pulsed laser light generating a specific electron pulse shape as defined by the laser [8].

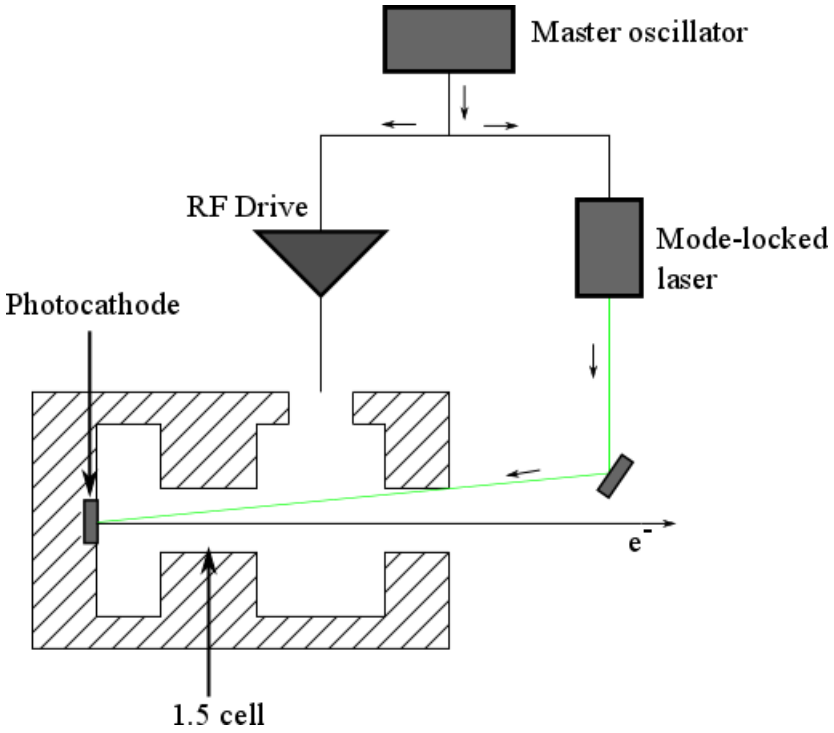


FIGURE 1.2: Components of a typical RF photoinjector.

With the advent of the photoinjector came a massive improvement in the beam quality; the emittance (see section 1.2.2) reduced by an order of magnitude compared with the traditional thermionic guns [11]. However there remains room for improvement, particularly with respect to the photocathode. Of course photocathodes are a critical part of the electron source, and so improving electron emission from the source would greatly impact the gun performance.

## 1.2 Photocathode properties

The photocathode properties that are pertinent to the performance of the photoinjector are quantum efficiency, intrinsic emittance, response time and life time [12]. Depending on the specific application a particular property may be of more or less importance, and as such an appropriate photocathode material will be chosen to meet the requirements of the electron beam.

### 1.2.1 Quantum efficiency

The quantum efficiency (QE) of a photocathode is the ratio of the number of electrons emitted, $N_e$, to the number of incident photons, $N_\gamma$, as defined in equation 1.4:

$$QE = \frac{N_e}{N_\gamma}\,. \tag{1.4}$$

In practice, the QE is calculated using equation 1.5 which is shown to be derivable from equation 1.4 when $N_e = I/e$ and $N_\gamma = (P\lambda)/(hc)$

$$QE = \frac{Ihc}{\lambda eP} \tag{1.5}$$

where $I$ is the photocurrent (A), $c$ is the speed of light ($2.998 \times 10^8 \text{m.s}^{-1}$), $\lambda$ is the wavelength of incident light (m), $e$ is the electron charge ($1.6 \times 10^{-19}$ C) and $P$ is the power of the incident light (W).

The QE is an important property for characterising a photocathode as it gives an idea of the amount of current that can be extracted. For a material with a high QE, less laser power is required to produce the same current from a material with a low QE [12]. Certain applications require high average currents and therefore photocathodes with a high QE are required. For example the ALICE ERL at DL requires a high average current from a photocathode; this is provided for by a GaAs photocathode with QE in the range 0.12-0.16 with light in the visible range (635 nm) [13].

### 1.2.2 Intrinsic emittance

The emittance of a particle beam defines its size; it is the area or volume in the phase space of the particles [14]. If the value of emittance can be reduced, the overall beam quality will improve due to the relation between the brightness of the beam and the emittance, as shown in equation 1.6 [15]:

$$B = \frac{N_e}{\epsilon_{nx}\epsilon_{ny}\epsilon_{nz}} \tag{1.6}$$

where $B$ is the brightness, $N_e$ is the number of electrons per bunch, $\epsilon_{nx}$ and $\epsilon_{ny}$ is the normalised emittance in the x, y and z planes.

With respect to the electron source, the contributing factor to the normalised emittance is the intrinsic emittance. This is essentially the lowest value of the the normalised emittance at any point in the accelerator system [16].

Electrons are emitted from the photocathode at a range of energies and directions producing a solid angle from the surface of the cathode that in combination with the beam diameter defines the intrinsic emittance (see Chapter 2). Lowering the intrinsic emittance will lower the total emittance and hence improve the overall quality of the beam.

### 1.2.3 Response time

This is the the time taken between absorption of the light pulse and photoemission. Whether a material has a long or short response time is influenced by the photon absorption length and the mean free path of the excited electrons [12]. Thus for a particular

material, the response time may also vary with photon energy. Typically, the mean free path of excited electrons within metals is relatively short; for an electron that has undergone a scattering event it is assumed that it will not have sufficient energy to escape [17]. Thus the response time of metals is very fast, of the order of femtoseconds. However for semiconductors it is electron-phonon scattering that dominates during transport of excited electrons to the surface, therefore the time between photon absorption and electron emission is significantly slower (order of picoseconds), resulting in longer tails.

The longitudinal shape of the electron bunch is characterised by the temporal shape of the laser pulse incident on the cathode [18]. If the response time is too long, the laser pulse has no effect in shaping [18]. A large longitudinal spread in the electron bunch leads to an increase in emittance and a reduction in the beam quality. For those accelerator applications that require the production of short electron pulses, a material with a fast response time must be used.

### 1.2.4 Lifetime

This is a measure of how robust a photocathode is to the environment within an injector. The lifetime can be defined as the time taken for the QE of a cathode to reduce to $1/e$ of the original value [19].

There are two main factors which will contribute to the degradation of the electron source: the vacuum conditions and the influence of the emission current [20]. If the vacuum in the electron gun is not sufficient, then surface contamination may occur as a result of the residual gasses, thus reducing the emissivity from the cathode surface. Additionally, during operation, ionised residual gas from the electron beam is accelerated back to the negatively charged cathode causing surface damage, non-uniformities and increased surface contamination. The result of this degradation is that the photocathodes need to be replaced periodically, and therefore the longer the lifetime of the photocathode the less frequent the interruptions need be.

## 1.3 Overview of photocathode materials

### 1.3.1 Metals

Copper is an attractive choice of photocathode material as it opens up the possibility of a simple all-copper electron gun [21]. One of the earliest examples of an all-copper electron gun was constructed at the Brookhaven National Laboratory Accelerator Test Facility (BNL ATF) [22]. X.J Wang *et al.* describe how without a choke joint installed to incorporate a non-copper material into the cavity, much higher accelerating fields were achieved; this was a significant advantage of an all copper gun.

Though the cavity material and the cathode may be the same, the copper cathode may require different preparation to the rest of the cavity; for example, the surface preparation employed to maximise the QE may not be suited to achieving good RF performance [17]. Consequently several means of inserting copper cathodes into the

cavity were developed. The plug design was employed in the all copper electron gun at BNL mentioned above [22], and has subsequently been adapted and used in other photo-injectors. However, even with an all copper plug, at high surface fields, RF break down problems surfaced [17]. The flange cathode circumvented these issues by installing a copper flange in place of the cavity back wall. This solution is employed in the photoinjector that drives the Versatile Electron Linear Accelerator (VELA) at Daresbury Laboratory. The choke joint mentioned earlier is another means of installing the cathode which is particularly useful in super conducting RF (SCRF) guns where a normal conducting cathode needs to be kept isolated from the cavity [17][23].

The advantages and disadvantages of using a copper cathode are summarised in Table 1.1.

Table 1.1: A summary of the advantages and disadvantages of using a copper photocathode in a normal conducting RF gun

| **Advantages** | **Disadvantages** |
|---|---|
| Simple and convenient | High $\phi$, requires UV light |
| Achieve high accelerating fields | Low QE |
| Long lifetime | |
| Fast response time | |
| Can be transferred in air | |

The beam extracted from copper photocathodes is sufficient for certain applications where a low to intermediate average current is required or when very short electron bunches are required. Many high gradient S-band RF guns utilise copper cathodes for the reasons mentioned above. For example, the LCLS (Linear Coherent Light Source) at SLAC is driven by an all copper RF gun, which proves sufficient for the requirements of the LCLS [4] [24]. The low intrinsic emittance of metal cathodes is just one of the factors that enables the production of the high brightness beam for the LCLS [3]. Additionally, VELA at Daresbury Laboratory used a copper photocathode flange which enables the production of short electron bunches and generates up to 250 pC of bunch charge [25]. The SPARC RF gun also uses a copper flange as the back wall of the cavity; a peak field of 120 MV/m on the cathode is achieved [26]. The low emittance of the copper cathode is a contributing factor to the high brightness electron beam generated [27].

Though copper is a strong and reliable cathode material, it is not an efficient emitter. Therefore, over the years several groups have investigated different preparation procedures to optimise the emissivity of copper. These techniques will be discussed later on in this section. Despite some small improvements with copper, future fourth generation light sources place more stringent requirements on the photocathode which demand new photocathode technology to meet these challenges.

Looking back, for 1st, 2nd, 3rd generation accelerators, the electron beam from the electron gun goes through the linac and is then accelerated and stored in the booster

for a time long enough that the 6D beam phase-space distribution is fully defined by the characteristics of the booster and not of the electron source [15]. The 6D beam phase space distribution describes the shape and size of the beam, as well as its momentum distribution. In linac based 4th generation light sources, such as free electron lasers (FELs) and energy recovery linacs (ERLs), the situation can be quite different. Indeed, in these cases, the final beam quality is determined by the linac, its injector and the photocathode [15]. Consequently the need to incorporate alternative and appropriate photocathode materials to meet specific requirements has become increasingly important. This poses two questions:

1. How will an alternative material be incorporated in a copper/niobium cavity?

2. Which materials exhibit better photocathode properties than copper?

Several techniques have been investigated for incorporating different materials; each brings with it a plethora of challenges!

Press-fitting is a technique where two materials are simply pushed together to form a join. This technique was used to incorporate a bulk magnesium disc cathode into the removable back plate of the 1.6 cell RF gun at BNL in 1997 [28]. The magnesium disk was press-fitted into an indent made in the centre of the copper plate. Later on in this section the merits of magnesium as a cathode material will be discussed; for now the means of incorporation of a non-copper metal into a copper cavity will be explored. The issue of using this technique is touched upon by T. Nakajyo *et al* in [29]. In an RF gun, a gap is formed between the magnesium cathode and the copper cavity due to different thermal expansion coefficients. Such defects or non-uniformities in the cavity limit the maximum RF field that can be generated in the cavity (RF breakdown). Electroplating is another alternative but again due to issues of RF break down it is not ideal. Thin film deposition could circumvent issues of RF breakdown. Indeed the majority of cases in which a non-cavity material photocathode is used is achieved by thin film deposition. There are several ways of depositing alternative materials, each of which are assessed in Table 1.2.

Table 1.2: Summary of thin film deposition techniques

| *Deposition technique* | *Advantages and Disadvantages* |
|---|---|
| Ion Sputtering | ✗ Rough surface finish |
| | ✗ Adherence varies with target material |
| | ✓Full substrate coverage |
| Laser Deposition | ✗ Issues of droplet formation |
| | ✓Good adherence |
| | ✓Clean vacuum |
| | ✓Better nucleation process |
| | ✓Dual target used to form multiple layers |
| Arc Deposition | ✓Smooth surface |
| | ✓Clean vacuum |
| Evaporation | ✗ Rough surface finish |

(Magnetron) ion sputtering is a popular method for producing thin films [30]. For more information on the technique see Chapter 3. Good surface coverage can be achieved and given the right deposition parameters, good substrate adhesion too [30]. In a paper comparing different preparation techniques of lead cathodes, including several methods of deposition, J. Smedley *et al* concluded that the surface finish from a sputtered lead cathode may be too rough for an injector [31]. However, an earlier investigation at BNL showed that perhaps the surface roughness of a sputtered film could be reduced by polishing. T. Srinivasan Rao *et al.* were investigating the use of ion sputtering magnesium onto a copper substrate to circumvent the issues of RF breakdown experienced with bulk magnesium. After sputtering, the magnesium films were polished with 1 $\mu$m diamond compound [32]. Thus, although "as-received" the surface finish may have been too rough, it would perhaps be possible to rectify this.

Several groups have been investigating laser deposition techniques in the past decade, and so it is becoming an increasingly viable option for integrating alternative metals to copper in an electron gun. For pulsed laser deposition (PLD), the laser-evaporated materials have a high kinetic energy upon reaching the substrate which leads to good adhesion [33]. An additional advantage of laser deposition techniques is illustrated by A. Perrone *et al.* With the use of a dual material target (magnesium target with graphite core), a magnesium film was deposited and immediately after a graphite protective layer was deposited on top [34]. A major drawback of this technique is the formation of droplets during deposition which produces a non-uniformity with respect to surface morphology.

Now to address the question, "Which materials exhibit better photocathode properties than copper?"

As discussed earlier, magnesium has been used at BNL as an alternative to copper because it has a lower work function (3.66 eV [35]) and a higher QE ($10^{-4} - 10^{-3}$)

[36] [32] . Magnesium is a particularly interesting photocathode material and over the years several groups (BNL, HZDR, SLAC and INFN) have investigated the preparation and installation of magnesium photocathodes for NCRF guns and even SCRF guns! Since the first friction welded magnesium disc was implemented in an RF gun [28], new advances have been made.

At INFN-Lecce, PLAD (pulsed laser ablation deposition technique) has been employed to produce magnesium films with an ultra-thin protective layer to protect the film. Magnesium is quick to oxidise in atmosphere and so to prevent surface contamination during installation, a protective MgO/graphite layer has been investigated [34][37]. Once installed, the protective layer can then be removed with the laser. However, studies have shown that removing the MgO layer is difficult due to deep penetration of oxygen [37], and that graphite would be a more suitable protective film [34].

The ELBE SRF Gun II currently uses a bulk magnesium plug that via a choke joint is kept thermally and electrically isolated from the super conducting cavity [17]. The use of a choke joint allows for the integration of normal conducting photocathodes in a SCRF gun, and this is successfully realised at HZDR. For initial commissioning, a copper cathode was used, but ultimately a higher QE cathode such as $Cs_2Te$ or Mg would be used in the gun [38]. Magnesium as a rugged metal was chosen to prevent cavity contamination. Studies at HZDR show QE values of 0.3% were achieved with a 258 nm wavelength UV laser after *in-situ* laser treatment [39].

Lead is another material to consider as an alternative photocathode material to copper. It offers all the advantages of magnesium; it has a low work function (4.25 eV [35]) and a high QE ($10^{-4}$) (compared with copper), and additionally it can be used directly in SCRF guns. Using a superconductor such as lead as a photocathode circumvents many of the challenges that arise when trying to incorporate a normal conducting cathode in a SCRF gun, and additionally it simplifies the gun arrangement [31]. The incorporation of lead films into a SCRF gun has been the subject of study for several groups at BNL, DESY, HZB and INFN. In 2008, a group at BNL investigated the QE and morphology of a variety of lead cathodes, all prepared in different ways [31]. At 213 nm wavelength laser light, the maximum QE value was measured for arc deposited lead, with sputtered and evaporated also yielding similarly high values. The arc deposited lead sample also produced the smoothest surface, which would be critical in minimising the intrinsic emittance. J.Smedley *et al.* conclude that lead is a candidate material for average current sources [31].

Tests of a lead cathode in a SCRF gun were carried out by R. Barday *et al.* in 2013. In this study, two means of implementing lead cathodes were explored: a) by directly depositing lead on the back wall of the niobium cavity, and b) by depositing lead onto a niobium plug which was then inserted into a hole in the cavity [40]. The main findings from these studies highlighted the necessity to remove surface contaminants and produce uniformly emitting cathode surfaces. The QE values obtained were a factor of 5 lower than the values achieved at BNL; this was attributed to the lack of a homogeneous

cleaning procedure [40]. The requirement for uniform, smooth and homogeneous lead films for applications in SCRF injectors has motivated research to improve the films produced by PLAD at INFN. In earlier studies, the morphology of the PLAD lead films were too high in droplet density and not sufficiently uniform [41]. By changing laser deposition parameters, an improvement in the homogeneity and the structure of the films is observed [42].

Niobium would also be an attractive cathode material, particularly for SCRF guns. The earliest work on niobium photocathodes concluded that it would be a viable option if operated with a 200 nm wavlength laser; QE values of the order of $10^{-6}$ at 248 nm were reported [43]. However later studies carried out at BNL showed that perhaps the QE from niobium could be improved upon [44] [45]. Preliminary work at ambient temperatures showed that the maximum QE for a mechanically polished, laser cleaned niobium sample with a 266 nm UV laser light was $6.5\times10^{-5}$ [44], which is still better than copper. An all niobium SCRF injector was developed by BNL, AES and JLAB in 2005, from which data for the performance of a niobium photocathode in a superconducting injector were reported for the first time [45]. QE values of $2 \times 10^{-6}$ for the laser treated niobium photocathode were obtained [45]; the reason given for the low QE value was that the cleaning process of the cathode was not effective.

Yttrium is an interesting candidate material for a photocathode. It has a work function value of approximately 3 eV [35] which is sufficiently low that photoemission may occur even with visible light. Both yttrium bulk and thin films (by PLAD) have been studied with the aim of providing a short response time photocathode for the SPARC photoinjector [46]. After *in-situ* laser cleaning, which allegedly reduced the $Y_2O_3$, the QE increases from $10^{-6}$ to $4.5 \times 10^{-4}$. However, these studies found that despite UHV conditions, the yttrium was so sensitive that residual gases caused sufficient surface contamination to significantly reduce the performance of the cathode [46].

More recently, another means of using yttrium in a NCRF gun was investigated by A. Perrone *et al.* In this case, a small circle in the centre of the bulk yttrium cathode was masked whilst a copper film was deposited [47]. The yttrium cathode would provide a high QE, and the low work function would enable the use of longer wavelength light for photoemission. The copper film would provide electrical and thermal conductivity that matched the copper cavity. Additionally, the bulk yttrium over a thin film would better stand the effects of *in-situ* laser cleaning [47]. The study showed that sputtering produced a uniform and homogeneous film with electrical conductivity comparable to that of bulk copper, making this technique suitable for use in a copper cavity. The *in-situ* laser treatment of the photocathode however did not yield as high QE values as previously reported; in the paper however this has been attributed to the damaging of the surface morphology as a result of laser treatment which in turn has reduced the emissivity of the photocathode.

Though metals are comparatively less sensitive than semiconductor photocathodes, the exposure to atmosphere does still bring about surface contamination which may lead

to poorer emissivity. Therefore *in-situ* cleaning is sometimes necessary to activate or rejuvenate a metal cathode. The principal technique for activating photocathodes is laser cleaning; the effect of this treatment is to essentially burn off the surface contaminants leaving a clean surface [39]. This takes place *in-situ* once the cathode is installed. The laser is rastered or scanned over the photocathode surface with the laser focused down to a small spot [17]. Of course this method is popular for obvious reasons- in the the gun the only means of *in-situ* cleaning is to utilise the laser. It is a convenient method but it can induce damage and non-uniformity on the photocathode surface leading to an increase in intrinsic emittance [17].

An alternative method of metallic photocathode treatment has been suggested by D. Dowell *et al.* From the work carried out at SLAC, it was shown that an atomically clean copper surface can be achieved by hydrogen ion cleaning [48]. One advantage of this technique is that the hydrogen beam does not appear to have any influence on surface roughness. This technique has been applied to the preparation of a copper cathode for the LCLS [4]. During installation the cathode must be exposed briefly to air; this of course will lead to the formation of surface contaminants. As a means to circumvent this issue, Dowell proposes and gives details for how to install a hydrogen ion gun into the injector so that cleaning can be carried out *in-situ* [48].

Another method used for preparing a cathode is *ex-situ* oxygen plasma treatment followed by *in-situ* heating. This follows from studies by R. Valizadeh *et al.* The effect of oxygen plasma treatment is to chemically remove hydrocarbon contamination. The oxygen plasma forms a protective oxygen layer which upon heating is dissolved into the bulk leaving a clean copper surface (see Chapter 3). The advantage of this technique is that the photocathode can be prepared and installed at ambient conditions.

### 1.3.2 Semiconductors

Semiconductor photocathodes are split into two main groups: positive electron affinity (PEA) and negative electron affinity (NEA). Highlights of the most commonly used semiconductor photocathodes are presented in Table 1.3.

Table 1.3: Summary of principal semiconductor materials properties

| Class | Material | QE | Response time | Operational Lifetime |
|---|---|---|---|---|
| PEA | $Cs_3Sb$ | 5-7% with green [49] | ps | hours [49] |
| | $Cs_2Te$ | $\approx$ 10% with UV [50] | ps [51] | months [50] |
| NEA | GaAs | >15% with green [52] [53] | 1-100's ps | 1-2 weeks[53] |

Within PEA semiconductors a further distinction can be made between tellurium and antimony based. Over 20 years ago at CERN, $Cs_2Te$ was shown to be a sufficiently rugged photocathode to meet the requirements of the CLIC Test Facility [54]. Since then it has become a popular choice of photocathode particularly for FEL facilities [55].

For example the FLASH FEL at DESY uses $Cs_2Te$, fabriacted at INFN Milano [56], to generate soft X-Rays. $Cs_2Te$ has a band gap of 3.3 eV and an electron affinity of $\approx 0.2$ eV [51], consequently it must be operated with UV light. Relative to other semiconductor materials, it has a long life time and a reasonably high QE. An additional advantage is that $Cs_2Te$ photocathodes can be rejuvenated by heating even if exposed to air [57]. $Cs_3Sb$ photocathodes have a small band gap and therefore have a good response to green light. This is particularly advantageous as UV lasers and the appropriate diagnostics required are costly; additionally operation in the visible range allows for an increase in the energy delivered the the photocathode [46]. Although such photocathodes have a good QE, they are short lived, and in some cases they must be changed on a daily basis [51] [58].

GaAs is an example of a NEA semiconductor photocathode. Typically GaAs photocathodes have a higher QE than other semiconductor photocathodes [59]. As with $Cs_3Sb$, it can be used with green light. A drawback to using GaAs is that it has a longer response time, which will limit its application. Also, they are particularly sensitive to contamination and therefore require XHV conditions.

# Chapter 2

# Theory of Photocathodes

This chapter contains the relevant physics of metal photocathodes. It is organised as follows. An overview of material properties of photocathodes is highlighted in section 2.1. Next, the photoemission process in metals specifically using the Spicer Model is discussed in section 2.2. QE and factors which affect the QE are considered in sections 2.2 and 2.3. Finally the intrinsic emittance of photocathodes is explained, followed by a discussion on the factors which influence this property in sections 2.4 and 2.5.

## 2.1 Metal properties

In this section, the material properties of photocathodes is explored. Band theory is critical to understanding and explaining the differences between metals, semiconductors and insulators, and so it is briefly summarised in this section.

In a metallic crystal, the outer electrons of an atom are delocalised. One can picture the metal to be a lattice of positive ions with a cloud of conduction electrons spread over the entire crystal [60]. In the free electron model, these electrons are treated as free within a confining potential. However, in band theory the interaction of these electrons (termed "nearly free electrons") with the ionic lattice is also taken into account. Consider the dispersion relation (Equation 2.1):

$$E(k) = \frac{\hbar^2 k^2}{2m} = \frac{p^2}{2m} \tag{2.1}$$

where $\hbar$ is planck's constant divided by $2\pi$, k is the wave vector equal to $\frac{2\pi}{\lambda}$ and $m$ is the mass of an electron.

For a truly free electron, there is no restriction on $k$ and hence all energies are available; thus $E(k)$ is continuous as depicted in Figure 2.1 a) [61]. However, for electrons confined within a potential well, $k$ is constrained by the condition $k = n\pi/L$, where n is an integer and $L$ is the length of the potential well.

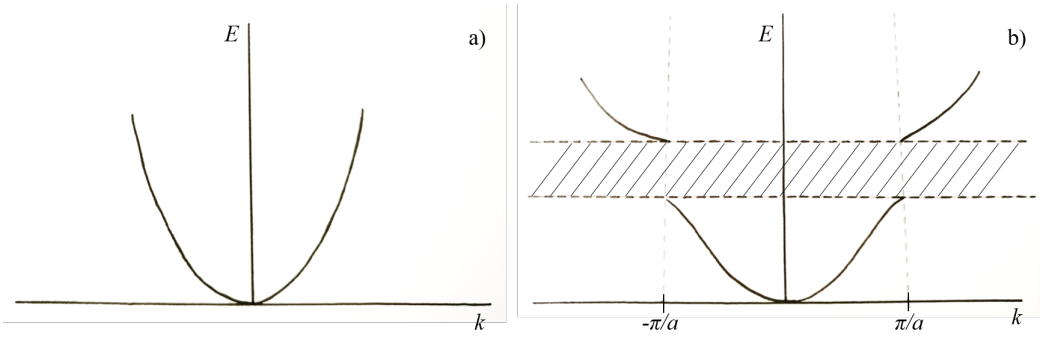


FIGURE 2.1: Electron energy as a function of wave vector, $k$, for a) a free electron and b) for a valence electron in a monatomic linear lattice with a lattice constant $a$ [61].

An illustration of the bound and nearly free electrons with respect to potential energy is shown in Figure 2.2.

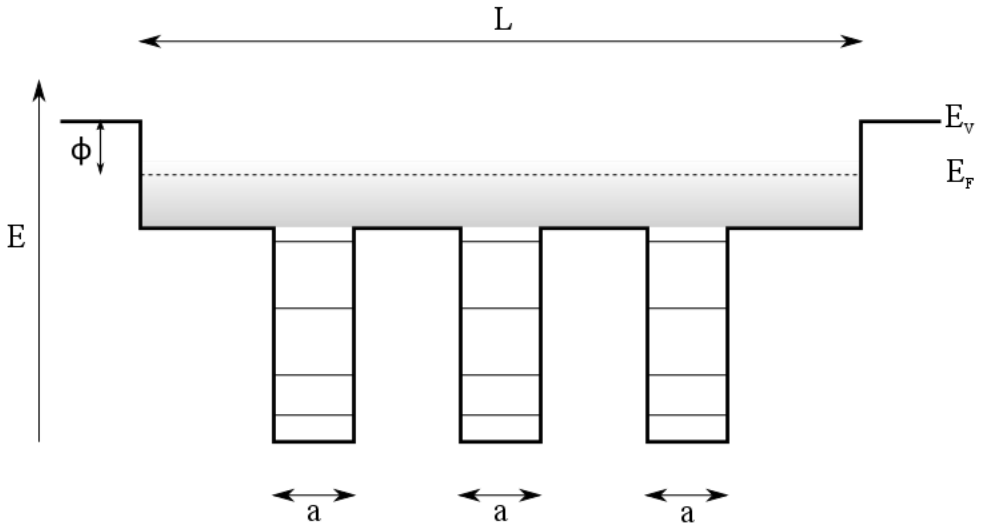


FIGURE 2.2: Potential energy, $E$, illustration for bound and nearly free electrons in a metal. Where $L$ indicates the length of the metal, $\phi$ is the work function, $E_V$ is the vacuum level, $E_F$ is the Fermi level and $a$ is the width of the potential well of the ion.

For the bound electrons, the length of the potential well $L$ is shown as $a$, (which is of the order of angstroms, and therefore the values for subsequent $k$ values are far apart. Consequently the allowed energy levels are also spread. However, for nearly free electrons in a bulk material, $L$ is large and therefore the $k$ values are almost continuous. It is important to note that the energy values are still quantised but appear to be continuous. The interaction between the allowed values of $k$, for nearly free electrons, and the periodic potential of the lattice results in energy bands and gaps in the distribution of nearly free electrons. This process is briefly described below.

Bragg planes arise from the reciprocal lattice and are representative of the periodic structure [61]. The interaction of the nearly free electron wave vectors with the Bragg

planes results in the formation of energy bands i.e. regions of allowed and forbidden energies.

The position of the Fermi level within the energy band determines whether the material is a conductor or an insulator. In the case of metals, the Fermi level lies half way through a band as indicated in Figure 2.3 a). Here the electrons near the Fermi level are able to absorb energy and move into higher unoccupied states within the band. For insulators and semi-conductors, the Fermi level lies at the top of a band (see Figure 2.3 b)). The crucial difference between the two is the difference in the size of the energy gap.

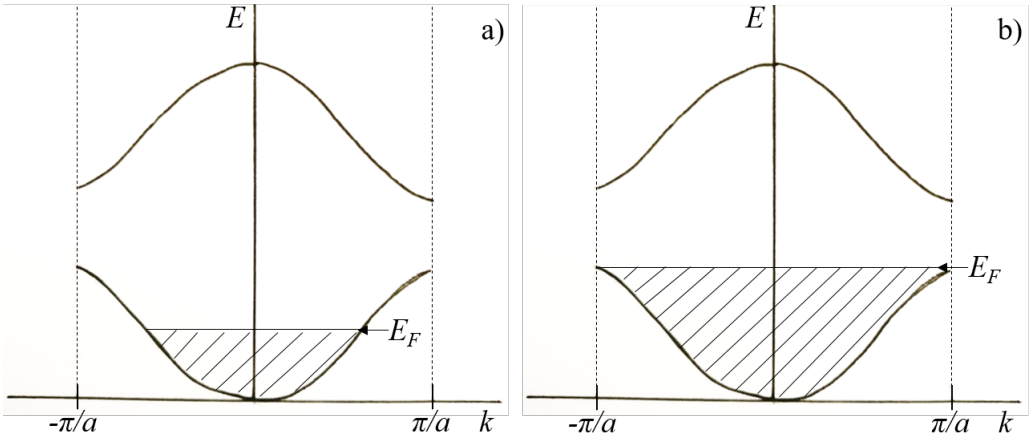


FIGURE 2.3: Reduced zone scheme for a) partially filled energy band characteristic of conductors and b) filled energy band corresponding to an insulator/semi-conductor depending on the size of the energy gap.

Figure 2.4 shows the photoemission process for a metal. In the case of a metal, if a "nearly free electron" at the Fermi level absorbs a photon of energy $h\nu$ (where $h\nu$ is greater than the work function) then the electron can pass into vacuum as a free electron. At T = 0 K the minimum energy the electron must absorb is equal to the work function. For a metal this is typically 4-5 eV; consequently light between 248-310 nm (UV light) is required to liberate such electrons.

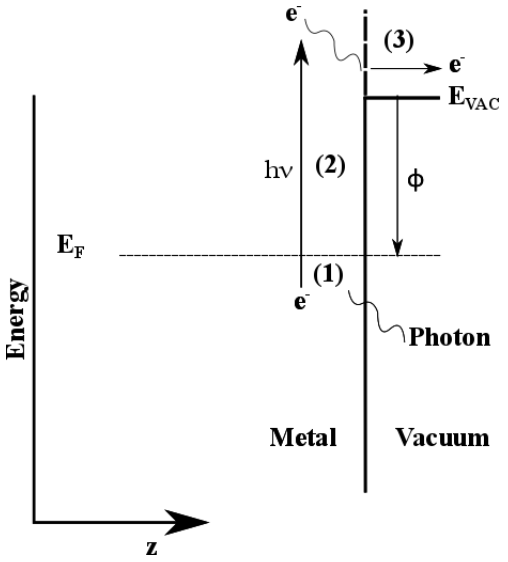


FIGURE 2.4: Energy band diagrams for metal photocathodes. A photon with energy $h\nu$ is incident on a metal surface. An electron within the conduction band absorbs the photon and the excited electron moves up over the potential barrier into vacuum, only if the energy absorbed is greater than the work function $\phi$.

## 2.2 Photoemission in metals

The Spicer model can be used to describe photoemission from both metals and semiconductors. The theory describes the process in three independent steps: (i) the excitation of an electron after photon absorption, (ii) the transport of the excited electron to the surface, and (iii) the escape of the electron from the surface to vacuum. The probability for each step is considered in the sections below as described by D.Dowell in *An Engineering Guide to photoinjectors* [17].

**Step 1: Electron excitation**

There are two processes to consider in this first step. Firstly, the probability that the incident laser light is transmitted through the material. This is dependent on the reflectivity, $R(\nu)$, of the material in question. Thus the probability of transmission, $T(\nu)$, can be calculated from the reflectivity as shown in the Equation 2.2:

$$T(\nu) = 1 - R(\nu)\,. \tag{2.2}$$

Once the photon is absorbed, the probability of exciting an electron with an initial state energy, $E_0$, to a final state energy, $E = E_0 + h\nu$, is considered. The probability of excitation will be proportional to the number of initial states, $N(E_0)$, and the number of final states, $N(E)$, available for such a transition to occur (see numerator of Equation 2.3). Dividing by the total number of transitions possible, an expression for the fraction of electrons that can be excited to an energy $E$ is obtained:

$$P(E, h\nu) = \frac{N(E)N(E - h\nu)}{\int_{E_f}^{E_f + h\nu} dE' N(E')N(E' - h\nu)} \,. \tag{2.3}$$

**Step 2: Electron transport**

In Step 2, the probability that an excited electron is transported to the surface of the material with sufficient energy to escape is calculated. This step is governed by scattering processes, and in the case of metals, it is electron-electron scattering that dominates. In this theory, it is assumed that if an excited electron undergoes scattering with another electron, then enough energy will have been lost such that neither electron is left with sufficient energy to escape. Thus the probability that an electron undergoes no scattering is considered only.

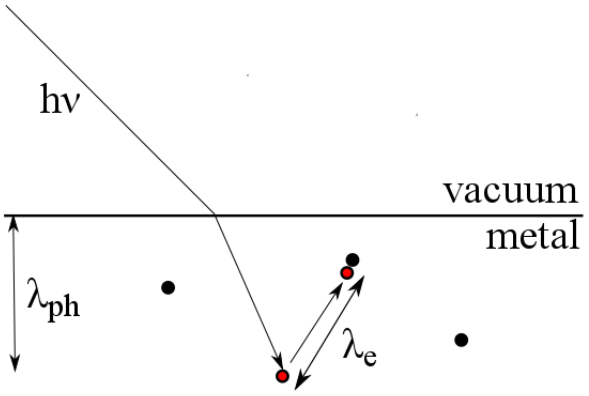


FIGURE 2.5: A photon with energy $h\nu$ is incident on a metal surface. The photon is absorbed by an electron at a distance $\lambda_{ph}$ from the surface normal. The excited electron (red) collides with a valence electron (black) after traversing a distance $\lambda_e$.

The distance that the excited electron must traverse is determined by the photon absorption length, $\lambda_{ph}$ (see Figure 2.5). It therefore follows that the probability of electron transport, $T(E, \nu)$, is dependent on the electron scattering length, $\lambda_e$, in relation to the photon absorption length, $\lambda_{ph}$ as shown in Equation 2.4:

$$T(E, \nu) = \frac{\lambda_e(E)}{\lambda_e(E) + \lambda_{ph}(\nu)} \,. \tag{2.4}$$

For example, in the case that $\lambda_{ph} << \lambda_e$, the probability $T(E, \nu)$ tends towards unity. In the case where $\lambda_{ph} >> \lambda_e$, $T(E, \nu)$ tends towards 0.

The absorption length, $\lambda_{ph}$, is a unique property of the material and it varies as a function of the incident light wavelength.

The electron scattering length, $\lambda_e$, is calculated from the product of the excited electron velocity, $v(E)$, and the lifetime, $\tau(E)$, of the excited electron state:

$$\lambda_e(E) = v(E)\tau(E) \tag{2.5}$$

where the velocity is given to be proportional to the square root of the kinetic energy of the excited electron:

$$v(E) \propto \sqrt{E - E_f} \tag{2.6}$$

and the lifetime is inversely proportional to the scattering probability, $S(E)$:

$$\tau(E) \propto \frac{1}{S(E)} \propto \frac{1}{\int_{2E_f-E}^{E_f} dE_0 \int_{E_f-E_0}^{E-E_f} d(\Delta E) N(E_0) N(E-\Delta E) N(E_0+\Delta E)}\,. \tag{2.7}$$

Here the scattering probability, $S(E)$, is shown to be proportional to the number of valence electrons $N(E_0)$ with energy $E_0 < E_f$, the number of empty states $N(E_0+\Delta E)$ with energy $E_0+\Delta E$, and the number of empty states $N(E-\Delta E)$ with energy $E-\Delta E$.

Thus the scattering length can be expressed as shown in equation 2.8:

$$\lambda_e(E) = v(E)\tau(E) = \frac{\lambda_0\sqrt{E - E_f}}{\int_{2E_f-E}^{E_f} dE_0 \int_{E_f-E_0}^{E-E_f} d(\Delta E) N(E_0) N(E-\Delta E) N(E_0+\Delta E)} \tag{2.8}$$

where $\lambda_0$ is a constant of proportionality.

**Step 3: Electron escape**

In the third step, we calculate the probability that an excited electron (having reached the surface without scattering off valence electrons) will be travelling in the correct direction for escape and have sufficient energy to overcome the potential barrier. The direction of motion for an excited electron must exist within the confines of a cone; the parameters of the cone are determined by the electron energy and the work function of the material.

$$cos\theta = \sqrt{\frac{E_T}{E - E_f}}\,. \tag{2.9}$$

Equation 2.9 describes the opening angle of the escape cone, in which $E_T$ is equivalent to the work function and $E - E_f$ is the electron energy. The greater the electron energy is in comparison to the work function, the larger the opening angle for the escape cone becomes.

The total solid angle subtended by the cone is written as follows:

$$\Omega = \int_0^{\theta} sin\theta d\theta \int_0^{2\pi} d\phi\,. \tag{2.10}$$

The fraction of electrons that can escape can therefore be described by the fraction of the total solid angle subtended by the cone:

$$D(E) = \frac{1}{4\pi}\int_0^{\theta} sin\theta d\theta \int_0^{2\pi} d\phi = \frac{1}{2}[1 - cos\theta] = \frac{1}{2}(1 - \sqrt{\frac{E_T}{E - E_f}}) \,. \tag{2.11}$$

Integrating the product of the probabilities within each step (see Equations 2.2, 2.3, 2.4, 2.11), the quantum efficiency (QE) is obtained:

$$QE(\nu) = A(\nu)\int_{E_T}^{h\nu+E_f} dEP(E)T(E,\nu)D(E) \,. \tag{2.12}$$

Though a theoretical calculation of the QE is not presented in this thesis, the factors contributing to optimising QE as discussed in the Spicer three step model have been considered and have influenced the choices in the photocathode materials investigated and the preparation techniques employed.

## 2.3 Factors influencing QE

**Work Function**

In the case of a metal, the work function is defined as the energy difference between an electron at the Fermi level and an electron at rest in vacuum just outside the metal (see Figure 2.6). In other words it is the minimum energy required to extract an electron from a metal at absolute zero [62].

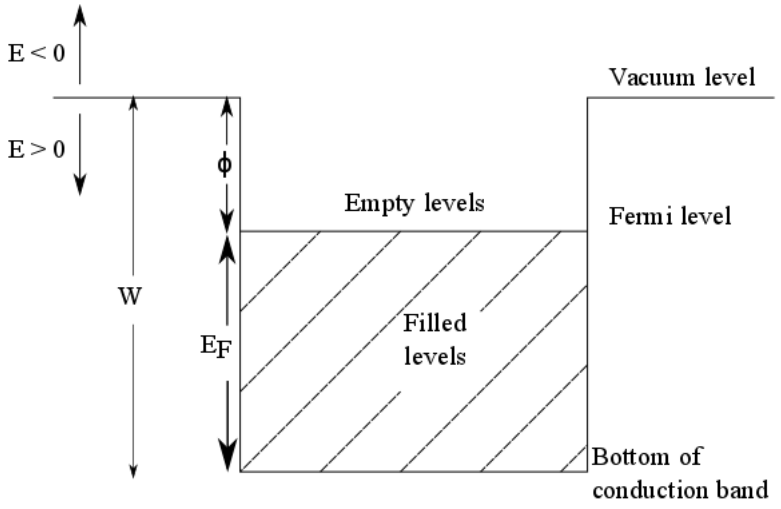


FIGURE 2.6: An illustration to show the electron energy levels in a metal. Where $W$ is the depth of the potential well, $E_F$ is the Fermi energy, and $\phi$ is the work function.

There are two main factors contributing to the work function [63].

1. The energy that is binding the electron i.e. the cohesive energy of the metal.
2. The energy necessary to transport the an electron through the surface double layer and into vacuum.

As illustrated in Figure 2.6 the depth, $W$, is the potential well that arises as a result of the bonding of the conduction band electrons to the solid. Thus the greater the bonding energy of the metal, the higher the work function. This contribution of the depth of the potential well to the work function is of the order of a few eV and therefore it is most significant. The cohesive nature of the metal is a bulk property that depends on the arrangement of the positive ions in the lattice, and therefore it is an inherent property of the metal and is not easily manipulated.

The depth of the potential well is also dependent on surface conditions. A charge double layer at the surface of a metal occurs resulting from the truncation of a three dimensional bulk metal. The absence of matter on the outer face of the surface layer produces an unsymmetrical distribution of electrons around a positive ion cores at the surface [64]; this results in a surface dipole. The magnitude of the dipole is influenced by different crystal orientations [63]. Also, any adsorbed species on the surface may modify the double layer of charge and hence the work function. If the adsorbed contaminants are polarised by the attractive interaction with the bulk surface, there are two possibilities [64] :

1. If it is polarised with the negative pole in the direction of the vacuum, the work function increases.
2. If it is polarised with the positive pole in the direction of the vacuum, the work function decreases.

Take the example of oxide layers forming on the surface of a clean metal. Oxygen atoms take electrons from the metal surface thus creating a layer of negative oxygen ions. Oxygen is an example of an electronegative species. This results in an induced positive image charge within the metal [63]. Typically this sort of arrangement of the double layer serves to increase the work function. Whereas for those surface contaminants that produce positive ions thus creating a layer of positive charge at the surface, the opposite is true; this configuration serves to decrease the work function. Cesium is an example of an electropositive species. Even in the case of neutral foreign species adsorbed on the surface of a metal, the field at the surface of the metal will still induce some polarisation in the contaminant layer.

**Schottky effect**

In an electron gun, the photocathode will be negatively biased thus producing an electric field at the photocathode surface. This of course encourages photoelectrons away

from the photocathode. Additionally the application of an external electric field induces a lowering of the potential barrier; this is known as the Schottky effect. In this section below, the change in the work function due to this effect is determined as described in *An Engineering guide to Photoinjectors* [17].

To begin with, consider the work function for a surface with no electric field applied to it. In this instance, the work function can be attributed to the attraction between the electron and its image charge inside the metal [17]. Here the potential energy between the electron and its image charge can be defined as:

$$W_{e-image}(x) = e\left(\frac{-e}{2x}\right) . \tag{2.13}$$

$$W_{surface}(x) = \frac{-e^2}{4x} \tag{2.14}$$

where $W_{e-image}(x)$ is the potential energy between the electron and its image charge, $e$ is the image charge, $-e$ is the electron charge, and $2x$ is the distance between the electron and its image charge.

The potential energy at the surface (between the electron and the surface) is therefore given by Equation 2.14 Thus the work function will be:

$$\phi_0 = W_{surface}(\infty) - W_{surface}(x_{min}) = \left(\frac{e^2}{4x_{min}}\right) \tag{2.15}$$

where $W_{surface}(\infty) - W_{surface}(x_{min})$ is the energy required to move an electron from some minimum separation to to a point at infinity.

Applying an external electric field, $E$, reduces the work function giving a combined total:

$$W_{total}(x) = \left(\frac{e^2}{4x_{min}}\right) - eEx\,. \tag{2.16}$$

The combined total has a maximum below vacuum level ($x_0$) and a minimum very close to the surface. The maximum is derived below:

$$\frac{d}{dx}W_{total}(x)_{x=x_0} = \left(\frac{e^2}{(4x_0)^2}\right) - eE = 0 \tag{2.17}$$

$$x_0 = \frac{1}{2}\sqrt{\frac{e}{E}} \tag{2.18}$$

$$W_{total}(x_0) = -e\sqrt{eE}\,. \tag{2.19}$$

For the minimum (at the surface), can assume that the potential energy from the applied field at the surface, $W_{field}(surface)$, is equal to zero. Therefore the total potential energy at the surface is:

$$W_{total}(x_{min}) = \frac{e^2}{4x_{min}}\,. \tag{2.20}$$

Subtracting maximum and minimum combined potentials, the change in the work function as a result of the Schottky effect is determined:

$$\phi = W_{total}(x_0) - W_{total}(x_{min}) = \left(\frac{e^2}{4x_{min}}\right) - e\sqrt{eE}\,. \tag{2.21}$$

**Surface preparation**

Different preparations methods can bring about changes to the metal surface properties; this in turn can alter the QE of the photocathode. As mentioned earlier, a layer of adsorbed material on a clean metal surface can either increase or decrease the surface work function. Metals readily oxidise in atmosphere and therefore often have a layer of negatively polarised oxygen ions on the surface, thus inducing a positive charge image layer in the metal. The unwanted effect of this is to increase the work function. Therefore, it is common practice to treat the metal photocathode material *in-situ* so as to remove the oxide layer and prevent further oxidation of the surface. Methods for surface contaminant removal are discussed in Chapter 3.

Coating a metal with an electro-positive species such as cesium can lower the work function of a metal photocathode and hence increase the QE. However, cesiated metals typically have short lifetimes and therefore require regular *in-situ* regeneration due to the harsh conditions in an electron gun [65].

Surface roughness can also have an effect on the work function, and by extension the QE. Sharp micro/nano-structures on rough surfaces have been shown to more readily emit electrons [66]. The attractive force keeping the electrons bonded to the solid is less at the surface of these structures due to a smaller concentration of surrounding atoms compared with a flat surface. Therefore roughening the photocathode surface can reduce the required energy to liberate electrons from the surface, i.e. it can reduce the overall work function.

To improve the QE, the photocathode surface can be engineered to minimise the reflectivity $R(\nu)$. As demonstrated in Equation 2.2, the lower the reflectivity, the higher the probability of adsorption of the incident photons. Therefore a rougher surface would serve to increase the adsorption probability. However, as will be discussed in section 2.5, a rough surface contributes to a greater angle of divergence of the emitted electrons from the photocathode surface.

## 2.4 Intrinsic Emittance

Intrinsic emittance, or thermal emittance is the angle of divergence of generated electrons at the photocathode surface. In a linear accelerator the source emittance is typically preserved, and therefore the intrinsic emittance can also be defined as the lowest achievable limit of emittance in such a system [67].

The intrinsic emittance is defined as:

$$\epsilon_n = \sigma_x \sqrt{\frac{h\nu - \phi_{eff}}{3mc^2}} \tag{2.22}$$

$$\epsilon_{i,x} = \sigma_x \sqrt{\frac{MTE}{mc^2}} \tag{2.23}$$

The excess electron energy equivalent to $h\nu - \phi_{eff}$ is equal to the kinetic energy of the photoelectron, as shown in Equation 2.23, which represents the average of the mean transverse energy (MTE) [68]. This is a value that encompasses the photocathode properties and the laser wavelength. The MTE data for copper and molybdenum samples are presented in Chapter 6.

From these equations, it is possible to lower the intrinsic emittance by [17]:

1. Reducing the laser spot size thus reducing the area over which electrons are emitted from the photocathode.

2. Closely matching the laser wavelength with the photocathode work function to reduce the $h\nu - \phi_{eff}$ term.

Matching the laser energy to the photocathode work function will reduce both the intrinsic emittance and also the QE. Therefore, in choosing a photocathode for a particular application, one must trade-off between a high QE and a low intrinsic emittance.

## 2.5 Factors influencing intrinsic emittance

As with the QE, there are a number of factors which influence the intrinsic emittance of a photocathode, and therefore it is possible to arrange a suitable set-up in which the intrinsic emittance can be predicted and manipulated by modifying either the laser spot size, the laser wavelength or the surface roughness.

#### RMS laser spot size

As mentioned in section 2.4, reducing the laser spot size will reduce the area over which the photoelectrons are emitted. This in turn will reduce the intrinsic emittance. However, one cannot simply continue to reduce the laser spot size and expect to see continual reduction in the intrinsic emittance. One must take into account the space charge effects that will become more prominent as the spot size is reduced. As soon

as the photoelectrons escape the metal, they are subject to their own image charge. This image charge serves to produce an electric field attracting the electrons back to the photocathode, countering the applied electric field [17].

$$E_{sc} = \frac{q}{A\epsilon_0} = \frac{\sigma}{\epsilon_0} = E_{applied} \tag{2.24}$$

where $E_{sc}$ is the space charge field, $A$ is the area of the laser spot size, $q$ is the charge, $\sigma$ is the beam's surface charge density, $\epsilon_0$ is the permeability of free space and $E_{applied}$ is the applied electric field.

Only when the space charge field is equal and opposite to the applied field will saturation occur. The beam's surface charge density is limited and therefore so is the laser spot size.

**Photon Energy**

Reduction of photon energy to the point that photon energy is equal to photocathode work function will reduce intrinsic emittance but simultaneously reduce the QE. Tuning the laser wavelength to reduce the emittance is a technique emplyed in several laboratories [67].

**Surface Roughness**

The theoretical calculations for intrinsic emittance (as calculated using equation 2.22) are not always in good agreement with the experimental data [69]. Several publications have suggested that the variation in surface conditions on the photocathode influences the intrinsic emittance [69] [70]. Surface roughness produces two effects which result in emittance growth, namely the slope effect and the field distortion effect [71]. Electrons emitted perpendicular to the local surface (the surface being rough) will have a transverse velocity componenet which will contribute to the transverse energy and thus the emittance growth [70]; this is known as the slope effect. Additionally the applied electric field is distorted close to the rough photocathode surface. This produces a variance in the applied electric field at different positions on the photocathode surface hence intrinsic emittance growth [71].

# Chapter 3

# Experimental Set-up and Techniques

In this chapter the experimental set-up and the techniques employed to prepare and characterise metallic samples is described. The section begins with descriptions of the systems used. An explanation and summary of the *in-situ* and *ex-situ* techniques used to prepare samples follows. Finally the specific characterisation techniques are discussed.

## 3.1 ESCALAB and Multiprobe systems

A modified VG Scientific Ltd. ESCALAB Mk II system has been used for the purpose of preparing and analysing photocathode samples for the majority of the experiments. The instrumentation consists of three chambers (see Figure 3.1 and 3.2), each of which will be described below.

The transfer of samples into and out of the UHV preparation chamber is carried out via an attached load lock chamber. The load lock is a small cylindrical steel chamber inside which is a sample transfer mechanism that has the capacity to carry one sample at a time. At atmospheric pressure the load lock can be opened and a sample inserted or taken out. The chamber is then pumped down to a pressure of approximately $10^{-7}$ mbar. This is achieved in two stages of pumping: first a rough vacuum ($10^{-2}$ mbar) is generated by means of a scroll pump, and then a turbomolecular pump is used to further pump the chamber down to $10^{-7} - 10^{-8}$ mbar. Once the sample has been outgassed and a pressure of $10^{-7} - 10^{-8}$ mbar is achieved, the gate valve between the loading chamber and the preparation chamber can be opened and the sample is transferred onto another transfer rail within the preparation chamber by means of a wobble stick.

The preparation chamber is held at a UHV pressure of approximately $10^{-10}$ mbar. The chamber is pumped by a turbomolecular pump backed by a HiCube combination pumping station (a combination of a turbo pump and a backing pump). The preparation chamber is utilised to clean the samples of surface contamination by two processes: heat

treatment and $Ar^+$ ion sputtering. A description of the instruments used and an explanation of the processes is given in section 3.2.

The analysis chamber is a spherical steel vessel, which is also held at a UHV pressure of approximately $10^{-10}$ mbar by means of a turbomolecular pump backed by a HiCube combination pumping station. A sample is transferred from the preparation chamber to the analysis chamber by opening the gate valve between the two. The transfer rail is then extended into the analysis chamber, and the sample is picked up and transferred onto the end of a (three stage) manipulator. This chamber is equipped with several instruments for surface characterisation:

- A dual anode X-Ray source and hemispherical analyser.
- A Kelvin Probe (KPTechnology UHVKPm100).
- A 265 nm LED (Roithner LaserTechnik UVTOP260-HL-TO39) and a Soitec photodiode.
- A commercial diode laser system (Crylas FQSS 266-Q4) generating light at 1064 nm which is frequency-doubled twice to generate a 266 nm UV beam.
- A VG He lamp with two stage pumping.

The functions of each and the associated characterisation techniques are described in section 3.3.

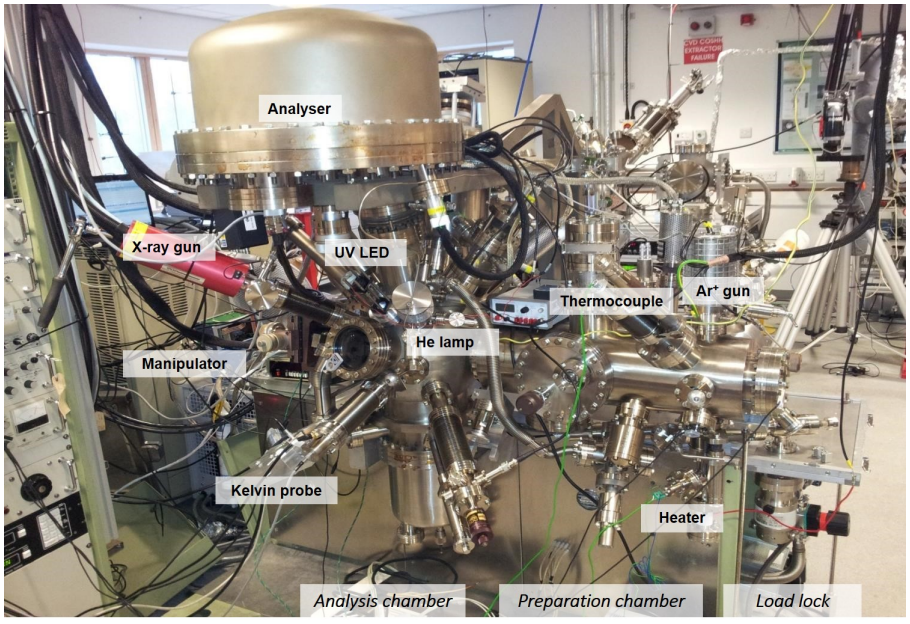


FIGURE 3.1: Photograph of the ESCALAB Mk II surface analysis system.

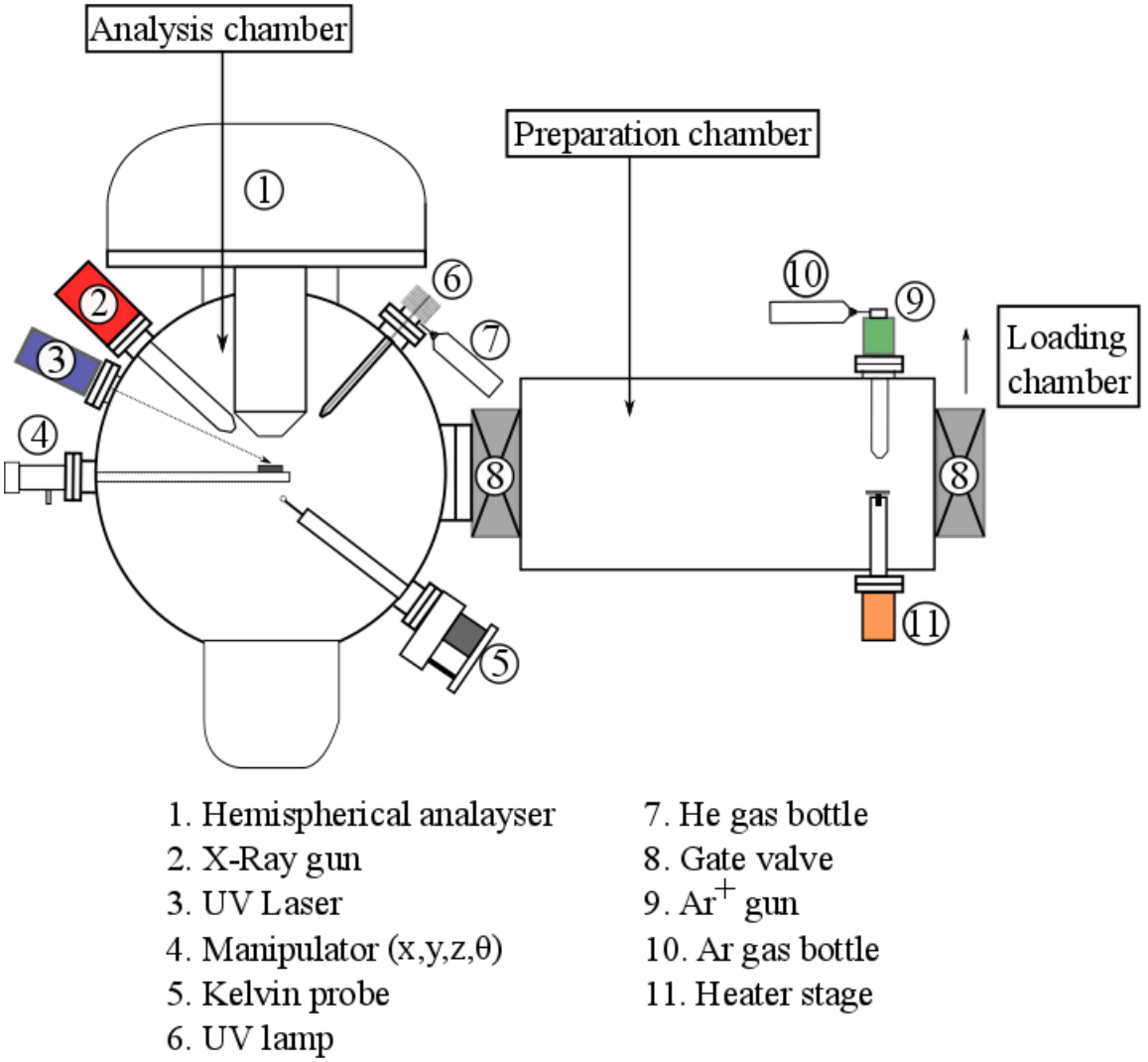


FIGURE 3.2: Schematic diagram of the ESCALAB Mk II surface analysis system.

For the latter part of experiments the Multiprobe system was used. Though it shares many similar functions to ESCALAB, it is described in the section below. The Multiprobe system consists of four chambers as shown in Figure 3.3. A schematic for part of the system is also shown in Figure 3.4. The loading chamber for Multiprobe is a six-way cross that houses a magnetic transfer arm for moving samples from the load lock through to other chambers. One port is connected to a smaller six-way cross that houses a penning and pirani gauge from which the pressure is monitored. At atmospheric pressure, the loadlock door can be opened and omicron flag-style samples are loaded onto the end of the transfer arm. The chamber is pumped down much in the same way as the ESCALAB loadlock by means of a turbo pump backed by a scroll pump. Once the chamber has reached a pressure of $10^{-7} - 10^{-8}$ mbar, the gate valve can be opened and the sample at the end of the transfer arm can be moved into the main chamber.

The main chamber in Multiprobe combines the functions of the preparation chamber and the analysis chamber of ESCALAB. Samples are cleaned by $Ar^+$ sputtering and heat

treatment in this chamber. The heater stage is integrated on the manipulator and is compatible with omicron style-flag sample holders. It is an electron-beam heater with a thermocouple attached to the manipulator side. Additionally, the samples surfaces are characterised by XPS, UPS and QE measurements. The main chamber houses:

- A dual anode X-Ray source and hemispherical analyser.
- A commercial diode laser system (Crylas FQSS 266-Q4) generating light at 1064 nm which is frequency-doubled twice to generate a 266 nm UV beam.
- A VG He lamp with two stage pumping.

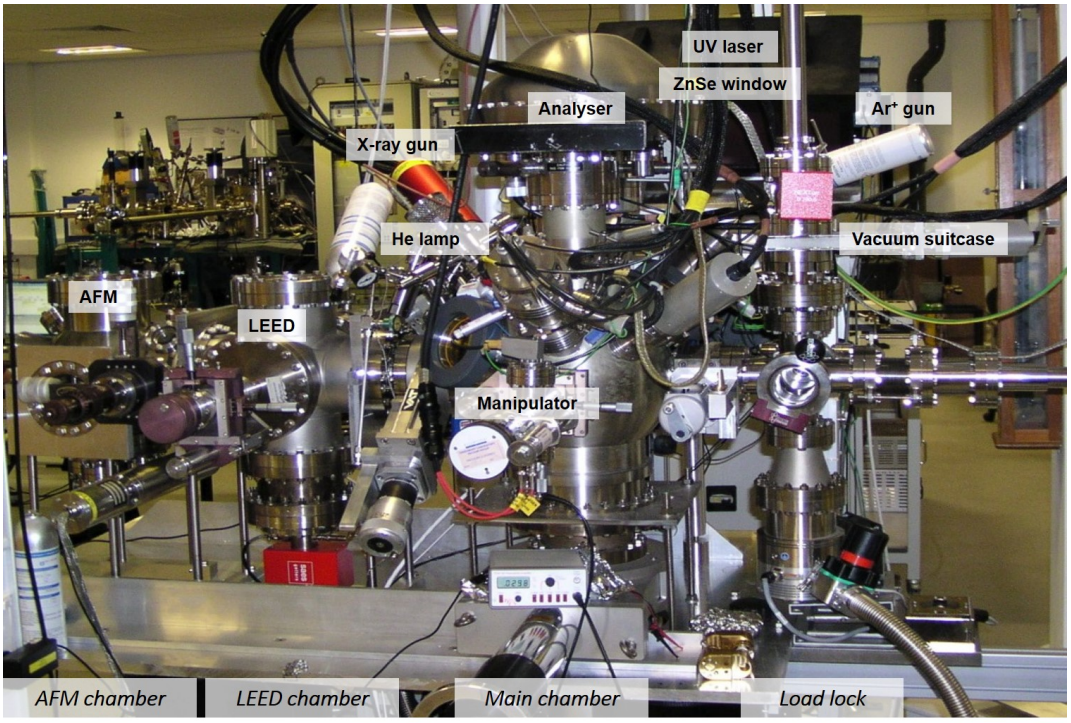


FIGURE 3.3: Photograph of the Multiprobe surface analysis system.

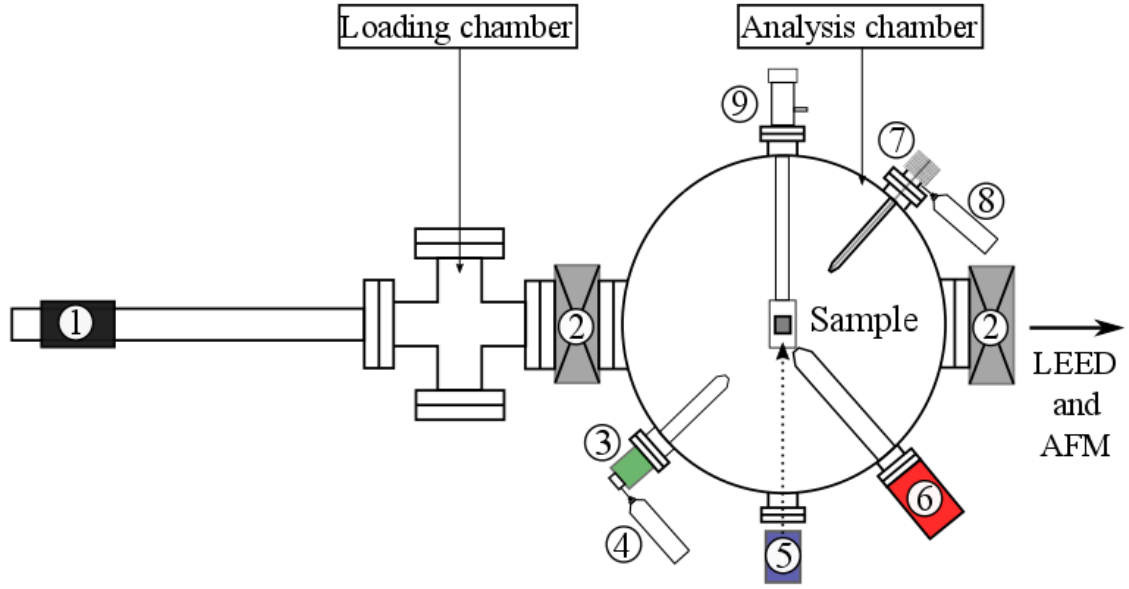


FIGURE 3.4: Schematic diagram of the Multiprobe surface analysis system.

UHV conditions are required for the preparation and characterisation of metal photocathodes. It is crucial in two aspects of these studies. The first is to allow the use of surface characterisation techniques, which rely on the detection and analysis of electrons emitted from the sample surface [72]. The second is to allow the study of atomically clean metal surfaces and ensuring that those surfaces remain contamination free for the duration of the experiment. The time, $\tau$, over which a monolayer of a particular gaseous species will form on a metallic surface is given by the following relation [73]:

$$\tau = 4 \times 10^{-8} \frac{\sqrt{TM}}{P} \tag{3.1}$$

where $T$ is the temperature (K), $M$ is the molecular weight of the gas and $P$ is the pressure in the chamber. This relation is true if we assume the sticking coefficient is unity.

It therefore follows that for a base pressure of $1 \times 10^{-8}$ and $1 \times 10^{-10}$ mbar, the time for a monolayer of the following gaseous species to form will be:

TABLE 3.1: Time for a monolayer of specific gaseous species to form on a surface in vacuum before and after baking.

| Gas | Molecular Weight (g/mol) | $\tau$ at $1 \times 10^{-8}$ mbar (s) | $\tau$ at $1 \times 10^{-10}$ mbar (s) |
|---|---|---|---|
| $O_2$ | 32 | 387 | 19400 |
| $N_2$ | 28 | 362 | 18100 |
| Ar | 40 | 433 | 21700 |
| $CO_2$ | 44 | 454 | 22700 |

At a pressure of $1 \times 10^{-10}$ mbar, Table 3.1 shows that the values for $\tau$ are of the order of $10^4$ seconds (approximately 3 hours). This is sufficient time to conduct an experiment; the investigated surface will not significantly change for the duration of the experiment. At a higher chamber pressure of $1 \times 10^{-8}$ mbar, the $\tau$ values are equivalent to a few minutes. At such pressures (and higher) there is a significant risk that the surfaces will change in the duration of the experiments.

To achieve chamber pressures better than $10^{-8}$, the system should be baked to 100-300°C. Gases adsorb on the inside of chamber walls when the system is vented and slowly desorb when the system is pumped down [74]. This of course limits the vacuum that can be achieved. Baking the system simply speeds up the rate at which this process of desorption occurs. For the ESCALAB and Multiprobe systems, both were baked to 110°C for 3-4 days. The viewports in the analysis/main chambers of both systems are made of ZnSe which can only be baked to a maximum of 120°C, hence the relatively low bake-out temperature. Custom made aluminium bake-out panels are used to encase the systems during bake-out. Ceramic heaters placed inside the enclosure were used to then heat the systems, and thermocouples used to monitor the temperature.

## 3.2 Photocathode preparation

### 3.2.1 Plasma treatment

*Ex-situ* plasma treatment of samples was carried out using a Henniker Plasma HPT-200 system. A schematic of the plasma cleaner is shown in Figure 3.5. An Edwards XDS scroll pump is used to pump down the chamber to a base pressure of approximately 0.01 mbar. Once the chamber has been evacuated, O/Ar gas is bled into the chamber to approximately 0.5 mbar. An electric voltage is then applied to the electrode plate, thus igniting the plasma.

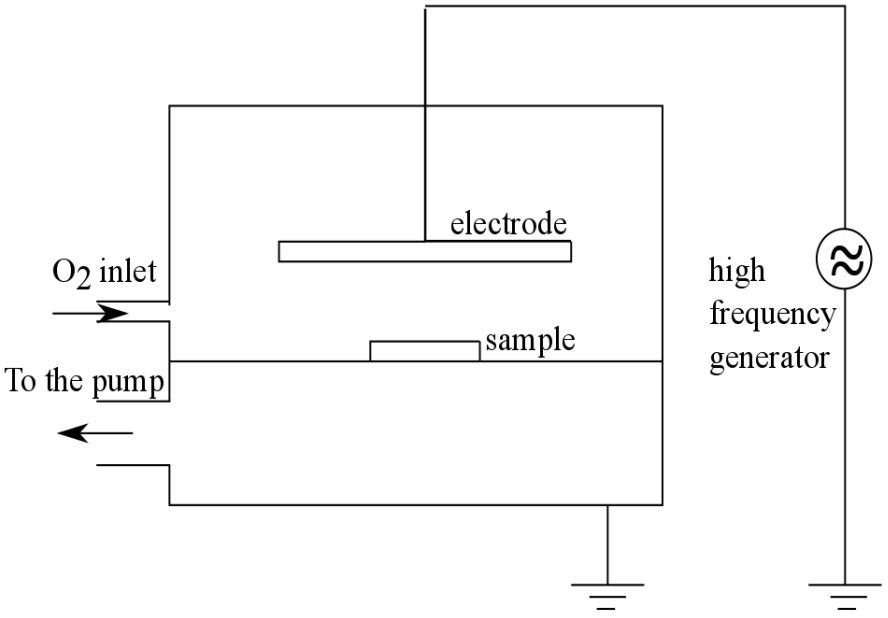


FIGURE 3.5: Schematic drawing for Henniker Plasma HPT-200 system.

### 3.2.2 $Ar^+$ sputtering

The facility to carry out sputtering is an AG21 ion source. A schematic of the source is shown in Figure 3.6. The source has the capacity to sputter etch samples with argon ions with energies up to 10 keV. Argon gas is ionised by means of electrons emitted from a cold cathode. The B-field produced by the surrounding magnet increases the rate of ionisation by increasing the electron path length. The argon ions are then accelerated and focused towards the sample surface. The energy transfer from the argon ions to the surface atoms can be sufficient for the surface atoms to escape.

A schematic of the ion current measurement is shown in Figure 3.7. Argon ions incident on the sample result in a positive charge. The net charge is a sum of the initial charges: the positive argon ions incident on the surface and the positive/ negative ions and secondary electrons leaving the surface. As the sample is earthed, a drain current is induced that is representative of the ion current. For the work presented here, each sputter cycle was for 10 minutes at 5 keV and $50\mu A$.

This technique is often used for oxidised metals to remove the surface layers, thus revelaing a surface that is similar to the bulk with respect to composition [75].

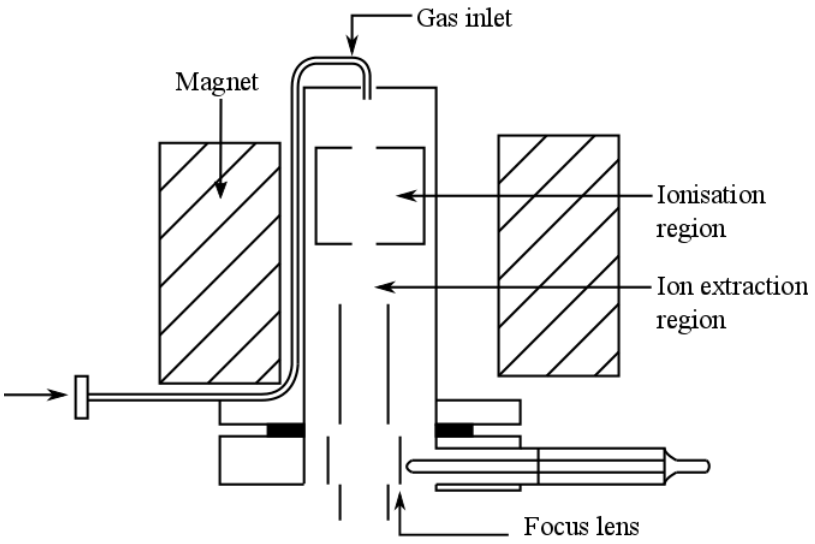


FIGURE 3.6: Schematic diagram of the VG Scientific Ltd. AG21 ion source.

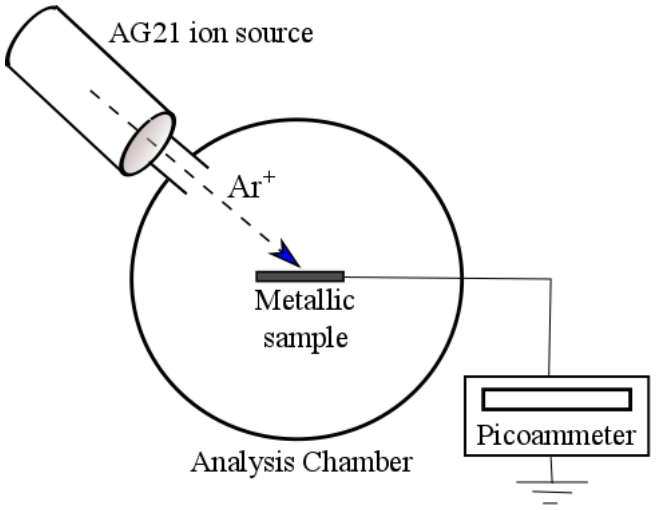


FIGURE 3.7: Schematic diagram of the ion current measurement for $Ar^+$ sputtering.

### 3.2.3 Heating

In the ESCALAB system, heating is carried out in the preparation chamber. The heater stage is an electrical resistive heater upon which the sample and holder rest. A thermocouple is wound in from another port and makes contact with the sample surface for temperature readings. In the Multiprobe system the heater stage is integrated on the manipulator within the main chamber, and is compatible with omicron style-flag sample holders. It is an electron-beam heater with a thermocouple attached to the manipulator side.

## 3.3 Photocathode characterisation

### 3.3.1 Quantum efficiency measurement

QE was calculated by measuring the photocurrent extracted from the sample, $I$, and the power of the incident light, $P$. These values were then substituted into Equation 3.2:

$$QE = \frac{Ihc}{\lambda eP} \tag{3.2}$$

where $I$ is the photocurrent (A), $h$ is planck's constant ($6.626 \times 10^{-34} J.s$), $c$ is the speed of light ($2.998 \times 10^{8}$ m.s$^{-1}$), $\lambda$ is the wavelength of incident light ($m$), $e$ is the electron charge ($1.6 \times 10^{-19}$ C) and $P$ is the power of the incident light ($W$).

The uncertainty in the QE, $\Delta QE$, is calculated by error propagation, giving the following equation:

$$\Delta QE = \sqrt{(\frac{\Delta I}{I})^2 + (\frac{\Delta P}{P})^2 + (\frac{\Delta \lambda}{\lambda})^2} \tag{3.3}$$

A schematic of the experimental arrangement for QE measurements is shown in Figure 3.8:

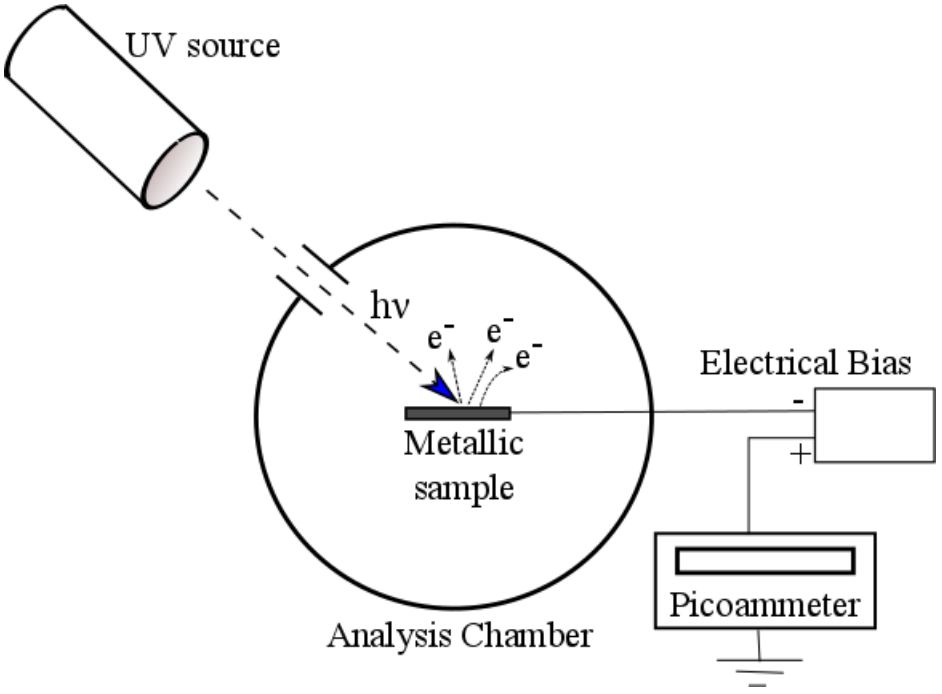


FIGURE 3.8: Schematic diagram of the total-yield QE measurement circuit.

Metal samples were biased at -18 V with a battery box that was connected between the electrical feedthrough and a Keithley type 480 picoammeter as shown in Figure 3.8. To achieve photoemission, initially a UV LED was used with 265 nm wavelength and 12

nm bandwidth. This was later replaced with a compact UV laser (Crylas FQSS 266-Q4). A diode generates light at 1064 nm, it is then frequency-doubled to generate 532 nm, and then doubled again to generate a 266 nm UV beam. This has a line width <0.1 nm, with a TEM00 spatial mode. The laser beam was pulsed using a passive Q-switch, and it delivers a 1 kHz repetition of approximately 1 ns pulses with an individual pulse energy of more than 12 mJ, focused to a spot size of *ca* 3 mm FWHM. The average UV power was measured to be around 16.3 mW using a calibrated photodiode.

It is not possible to measure the laser power directly on the samples in vacuum for each QE measurement. However, within the laser system, the laser beam can be redirected onto a calibrated photodiode (where path length from laser source to photodiode is equivalent to the path length of the laser source to the sample inside the vacuum chamber). The calibration curves for UV laser 1 and UV laser 2 (the lasers used on ESCALAB and Multiprobe respectively) are shown in Figures 3.9 and 3.10. The calibration curves were obtained using a power meter

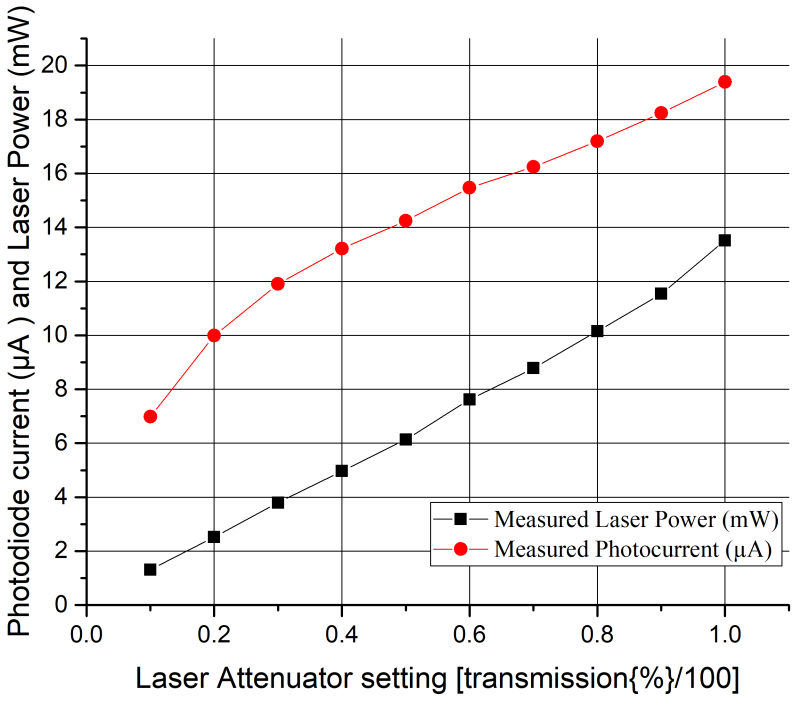


FIGURE 3.9: UV LASER 1 calibration curve.

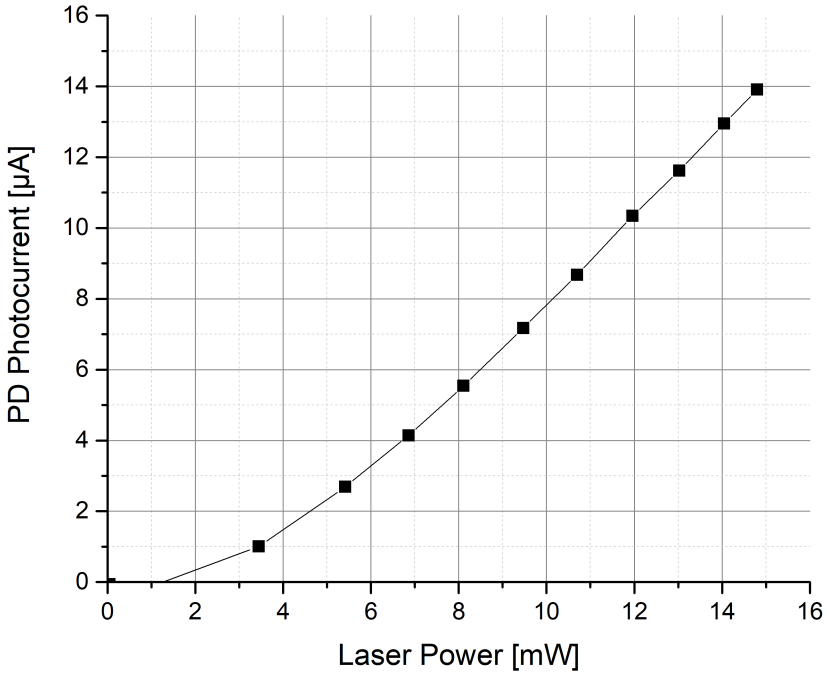


FIGURE 3.10: UV LASER 2 calibration curve.

For UV laser 2, above 40% laser attenuation, the relationship between laser power and photodiode current can be approximated by Equation 3.4:

$$LaserPower = \frac{I_{PD} + 4.685}{1.2545} \tag{3.4}$$

where $I_{PD}$ is the photodiode current in $\mu$A and laser power is in mW.

To ensure the UV light is illuminating the sample centre, a reference sample coated with phosphor is initially used to ascertain the position of the laser beam within the chamber.

For an accurate power measurement with attenuator settings above 20%:

1. Firstly measure the photodiode current in mA.
2. Use the calibration curves to determine the laser power in mW.
3. The laser is then directed to the biased sample.
4. Dark current and photocurrent measurements are taken.

### 3.3.2 X-Ray Photoelectron Spectroscopy

**Basic Principles**

XPS is a surface analysis technique used to determine the elemental composition and surface chemistry of materials. This is achieved by irradiating a sample with X-rays,

of known energy. The photo-emitted electrons are collected and their kinetic energy is measured. Using Equation 3.5 the binding energy is calculated:

$$KE = h\nu - BE - \phi_{sp} \tag{3.5}$$

where $KE$ is the kinetic energy of the emitted electrons, h$\nu$ is the X-ray energy, $BE$ is the binding energy of the bound electron and $\phi_{sp}$ is the spectrometer work function.

The binding energy is dependent on the element from which the electron was emitted; hence the XPS spectra of intensity as a function of binding energy provides information of the electronic structure of the sample material, from which the elemental composition can be ascertained [76].

In principal, the individual work function for each metal must be known to determine the binding energy. However the sample and electron spectrometer are both electrically connected to the same earth (as shown in Figure 3.11) and so their Fermi levels are aligned. Therefore, it is only necessary to know the spectrometer work function.

Finer structures within XPS spectra may yield more details with respect to chemical composition [76]. In this work, an important example of finer structures are "shake-up" satellites. Such features can appear when an excited core electron interacts with a valence electron on its way out. In the process, energy is transferred to the valence electron, thus reducing the kinetic energy of the photoelectron. This is observed as a satellite structure with a lower kinetic energy (higher binding energy). Shake up satellites are observed in the XPS spectra for copper samples (CuO) presented in chapter 4.

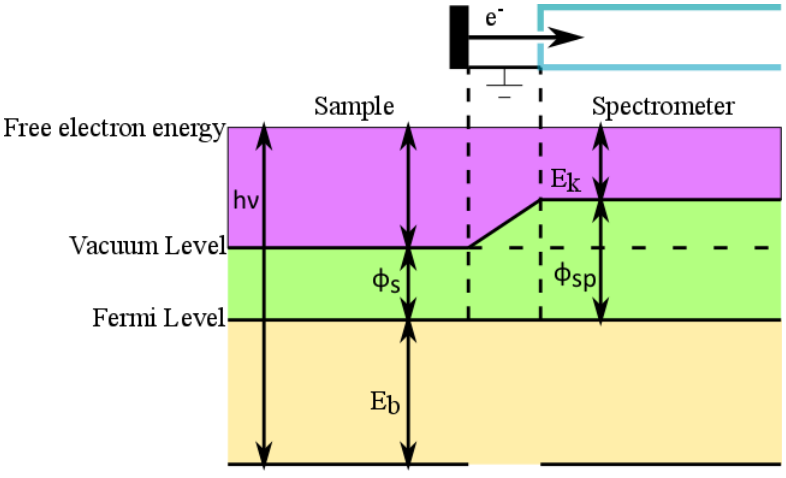


FIGURE 3.11: Energy band diagram for sample and spectrometer.

XPS technique is used for both determining the elemental composition and also chemical analysis. Chemical shifts are observed in the binding energy of core electron states when there is a change in the chemical bonding. The reason for this is briefly explained below (see [76] for more details). The binding energy of a core electron is principally due to the electrostatic force between the electrons and the nucleus. This is

altered by the removal or addition of valence electrons as a result of chemical bonding. For example, consider the oxidation of a pure metal. As oxygen is an electronegative species, valence electrons are withdrawn from the metal thus reducing the shielding of the core electron; this results in an increase in the binding energy of the core electron.

**Apparatus and Measurements**

A schematic of the VG Scientific Ltd. X-ray gun used in this work is shown in Figure 3.12. Electrically heated filaments shown at the base of the X-ray gun emit highly energetic electrons. The filaments are held at a near earth potential, but the anode is held at a positive potential of up to 15 kV. The anode of course requires cooling, and hence the gun is water-cooled with a chiller. The electrons emitted from the filaments are accelerated towards one of two anode source materials: aluminium or magnesium. When highly energetic electrons are bombarded on these surfaces, X-rays are generated with energies 1486.6 eV and 1253.6 eV respectively [72]. A thin aluminium window at the end of the gun only allows for generated X-rays, and not electrons, to transmit out of the gun. It is important to note that the X-rays are not monochromated in this set-up. This of course reduces the energy resolution of the XPS peaks and therefore the accuracy with which the chemical state can be defined.

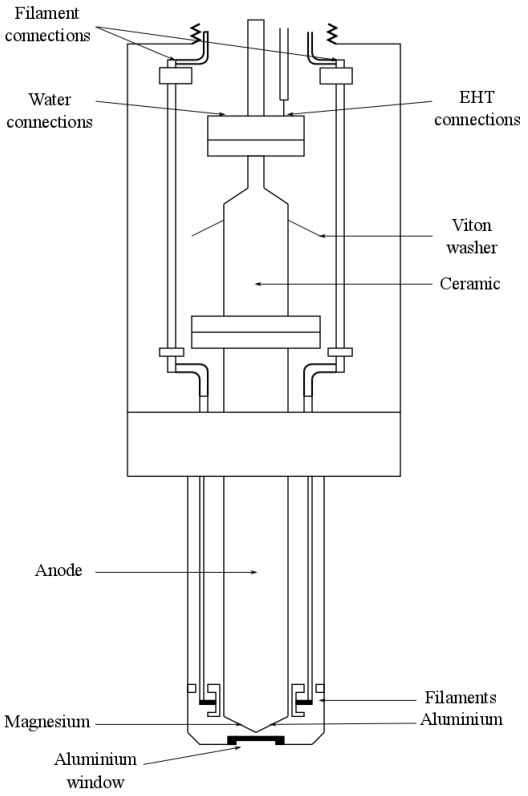


FIGURE 3.12: Schematic diagram of the VG Scientific Ltd. X-Ray source.

X-rays are directed onto an earthed sample. The emitted electrons from the sample are transmitted to the hemispherical sector analyser (HSA) also known as the spherical sector analyser (SSA); a schematic for which is shown in Figure 3.13. The electrons are directed to the analyser by the electrostatic lens and then retarded prior to entering the analyser. This is necessary because the emitted electron energies are typically too high for the analyser to produce the desired high resolution [76]. Between the inner and outer hemispheres shown in Figure 3.13, a potential difference is applied. Both hemispheres are negatively biased, but it is the outer shell that is more negatively biased. There are two factors that will determine if an electron with energy, $E$, will reach the detector: the potential difference between the hemispheres and the radii of the hemispheres.

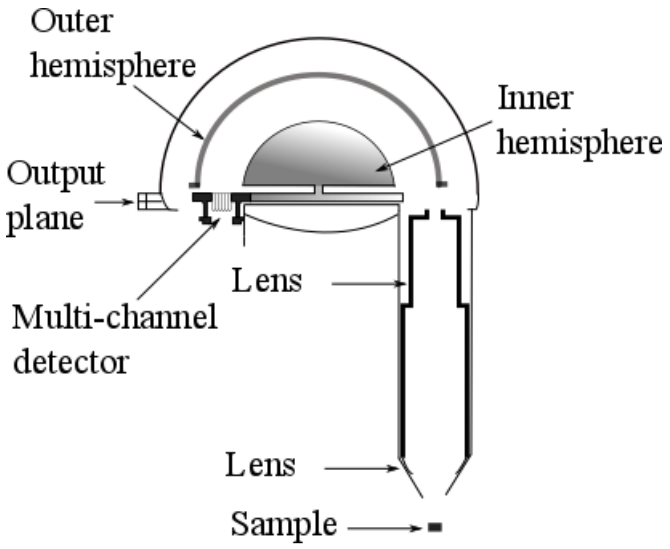


FIGURE 3.13: Schematic diagram of the VG Scientific Ltd. hemispherical sector analyser.

$$E = ke\Delta V \tag{3.6}$$

where $k$ is the spectrometer constant that depends on the size of the analyser and $\Delta V$ is the potential difference between the hemispheres.

Electrons with energies close to that given by Equation 3.6 will arrive at the output plane and will be incident on multi-channel detectors (individual channel electron multipliers) known as channeltrons [76]. Each channeltron will detect electrons of different energies and therefore the greater the number of channeltrons, the greater the sensitivity of the analyser. The ESCALAB analyser has five channeltrons, and the Multiprobe system has six. For XPS, the analyser is usually operated in constant analyser energy (CAE) mode. The energy at which the electrons pass through the analyser is fixed (between 20-100 eV), and therefore electrons are either accelerated or retarded to this fixed, user-defined energy [76]. Therefore, to generate spectra, the voltages across the

hemispheres are scanned across a range of voltages (the potential difference between the two remaining constant). Typically, the lower the pass energy, the lower the transmission, but the higher the resolution. If the pass energy is higher then there will be greater transmission but the resolution will be lower [76].

A brief summary of the parameters and conditions during XPS measurements is described below. A pass energy of CAE 20 eV was chosen and used for these experiments to ensure high resolution; a high resolution is required to determine changes in chemical states. The Al anode was used at 10 keV, generating non-monochromated X-Rays at 1486.6 eV and the source current was 20 mA.

**Data Analysis**

Raw data spectra were analysed using Casa XPS software [77] for measurements taken on ESCALAB and ThermoAdvantage for Multiprobe. Both softwares are used to qualitatively and quantitatively evaluate XPS spectra with respect to elemental and chemical composition. The atomic concentrations are determined by first subtracting an S-shaped (Shirley) background then taking the integrated area under each photoelectron peak; this defines the intensity of the photoelectron peak. This is then converted into atomic concentrations using Equation3.7.

$$Atomic\% = ((I_A/F_A/\sum(I/F)) \times 100\% \tag{3.7}$$

The intensity, $I_A$, is divided by the experimentally determined sensitivity factors [76] which takes into consideration the cross-section for photoemission, the electron attenuation length and spectrometer specific factors. Thus for each element identified, a the atomic percentage can be determined by expressing $I_A/F_A$ as a fraction of the total normalised intensities.

### 3.3.3 Ultra-Violet Photoelectron Spectroscopy

UPS is a surface analysis technique used to probe the valence states. As with XPS, light is irradiated onto a sample and the resulting photo-emitted electrons are collected and their kinetic energies measured. A typical UPS spectrum has two features that can be used to determine the work function of the metal under investigation: the Fermi edge and secondary electron cut-off. Figure 3.14 shows a UPS spectrum for a niobium sample as an example. The Fermi level is shown towards the higher energy end of the spectrum and is shown as a step distinguishing between regions of occupied and non-occupied states [78]. Of course, only regions of occupied states can contribute to photoemission, hence the drop to zero. The secondary electron cut-off is found at the lower energy end of the spectrum, and finishes with photoelectrons with only enough energy to overcome the work function (i.e. no kinetic energy). The electrons contributing to the secondary edge and cut-off are those electrons with the highest binding energies and also those electrons that have undergone scattering events during transit to the surface [78]. Knowing the

kinetic energies of the electrons at the Fermi edge and those at the secondary electron cut-off the work function of the metal can be determined using Equation 3.8

$$\phi = h\nu - W \tag{3.8}$$

where $\phi$ is the work function, $h\nu$ is the UV light energy and $W$ is the difference in energy between the electrons at the Fermi edge and the electrons at the secondary cut-off.

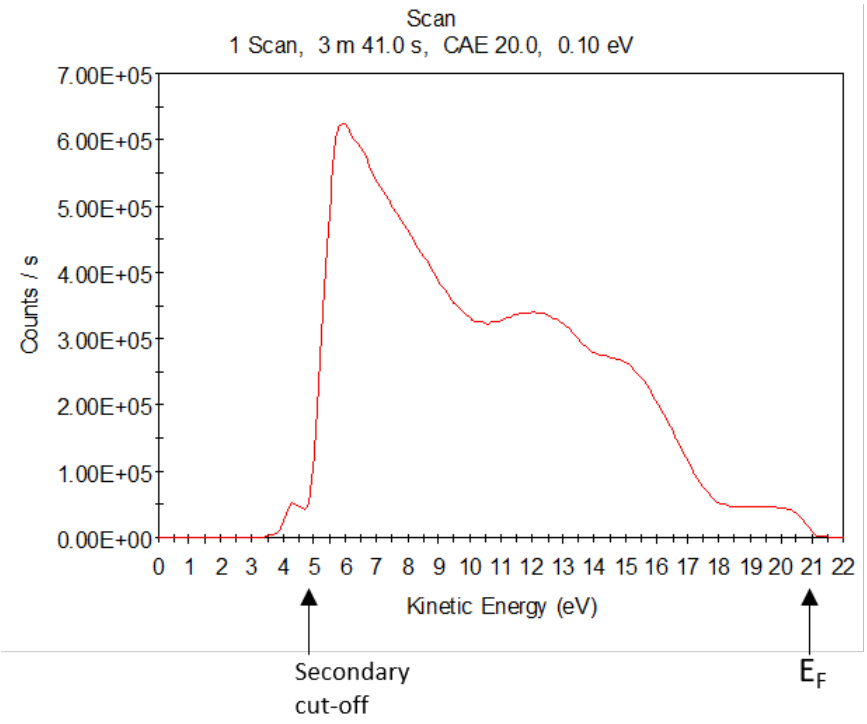


FIGURE 3.14: UPS wide spectrum for clean niobium surface.

The UV source, pictured in Figure 3.15, is a gas discharge lamp. The gas is admitted through a leak valve and the discharge is confined to a quartz capillary tube. VUV (vacuum UV light) photons are emitted by gas plasmas ignited via a power supply providing 5 kV for initiating gas discharge, and a 1 kV current stabilised supply variable from 20-50 mA to run the lamp. In order to maintain UHV during operation of the He lamp, two stage differential pumping is required: first stage pumping is a roughing pump, and second stage pumping is provided by a turbomolecular pump.

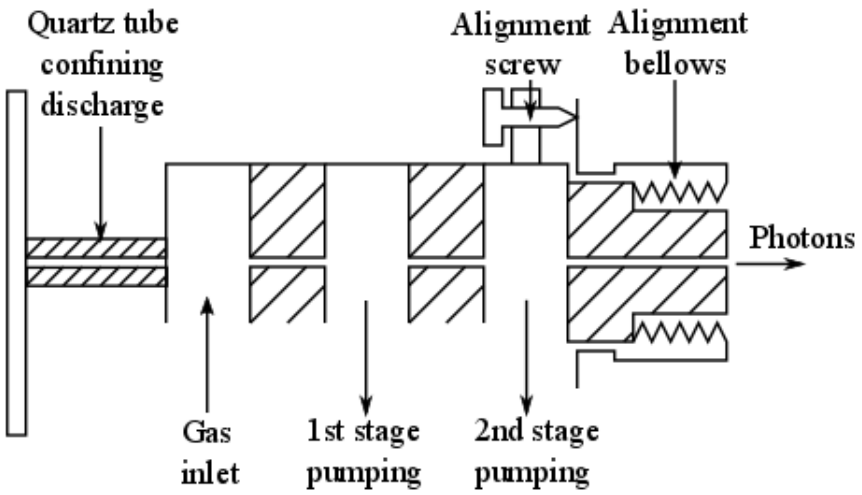


FIGURE 3.15: Schematic diagram of the VG Scientific Ltd. UV source.

### 3.3.4 Kelvin Probe

The Kelvin Probe technique is a non-contact and indirect method of measuring the work function of metals [79]. A simple explanation of the principles that govern this technique is described in this section.

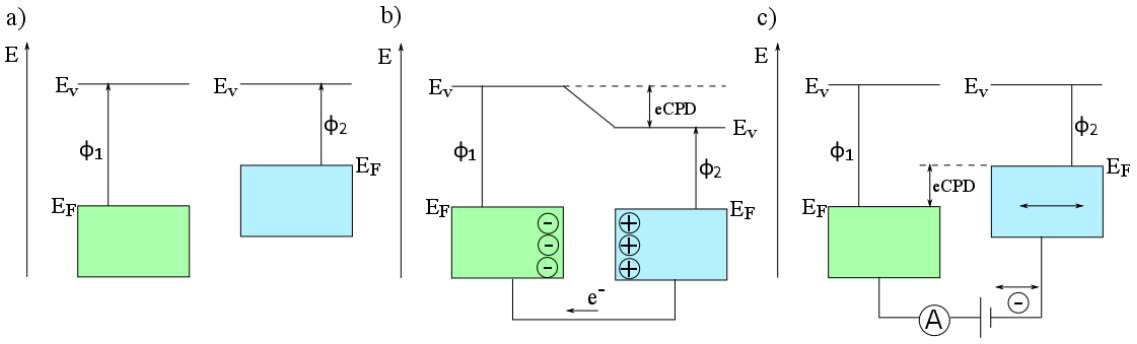


FIGURE 3.16: Energy band diagrams for two different metals a) in close contact without electrical contact, b) with electrical contact and c) with a counter potential to the CPD in the external circuit.

A diagram illustrating the electrical changes to two metals is shown in Figure 3.16. In Figure 3.16 a), two metals with different work functions are brought in close proximity (but not in electrical contact). In Figure 3.16 b) it is shown that upon electrical contact, electrons from the metal with the lower work function flow towards the metal with the higher work function until the Fermi levels align and equilibrium is achieved; the surfaces become equally and oppositely charged [80]. This induces a potential difference between the two metal surfaces that is exactly equal to the difference in work functions of the two metals (see Equation 3.9):

$$CPD = \phi_{probe} - \phi_{sample} \tag{3.9}$$

where $CPD$ is the contact potential difference between the sample and probe, $\phi_{probe}$ is the work function of the probe material and $\phi_{sample}$ is the work function of the sample.

If the contact potential difference can be measured, and if the work function of one metal is known, then the work function of the second material can be determined. The CPD can be determined by gradually applying a backing potential to oppose the CPD; the point at which there is no surface charge will be the point at which the backing potential is equal and opposite to the CPD [79] [80].

The KP Technology UHVKP100 apparatus with <3meV resolution installed on the analysis chamber of ESCALAB was used to indirectly measure the work function of samples. In this set-up, the probe (see Figure 3.16c)) is set to vibrate at a particular frequency inducing a periodic flow of charge. The "on-null method" would rely on incrementally increasing the counter potential to find the point of zero charge flow, where $CPD = -V$. However this is difficult to achieve, and so the "off-null method" is used. An $I/V$ curve is taken ($I$ is the flow of charge and $V$ is the potential between the sample and the probe) for several points and the point where $I = 0$ is extrapolated using a curve fit [80]. A calculation of the standard error from 10 repeated WF measurements gives 1 meV, which may not be representative of the accuracy of the data presented here; the systematic error associated with the instrument is likely to be bigger. The specifications for the Kelvin probe quotes that the probe has a resolution of <3 meV.

### 3.3.5 Atomic Force Microscopy

The AFM technique operates by scanning over a sample surface with a probe to image the topography [81]. A brief description of the technique is given below.

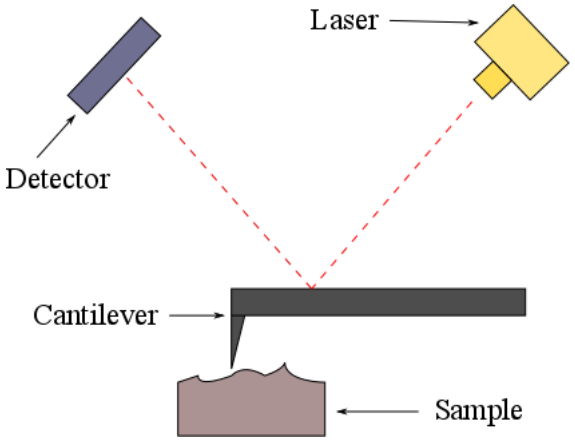


FIGURE 3.17: Illustration of AFM set-up.

The cantilever is a fine tip at the end of the thin beam illustrated in Figure 3.17. A laser beam is incident on the cantilever and the beam is reflected towards a detector; the bending of the cantilever can then be monitored. As the cantilever is only a few microns in width and approximately hundreds of microns in length, it will bend with very little

force [82]. As the cantilever moves across a sample scan area, force measurements are made that describe the topography of the area under investigation. There are two modes of operating an AFM: contact and non-contact [82]. In contact mode (or DC mode) the bending of the cantilever, or the force exerted by the cantilever on the sample is kept constant. In non-contact mode, or AC mode, the cantilever is set to oscillate at its resonant frequency. Upon close contact with the sample, there is a phase shift. This occurs even for very small forces, and hence it is a very sensitive technique.

The AFM used to image samples in the latter stages of this work is a DME HS100M (DS95-50 scanner) operated at atmosphere in AC mode. The system is used for roughness and nano-structured surface measurements. The maximum sample scan area is $50\mu m \times 50\mu m$ and the maximum height range is $5\mu m$.

### 3.3.6 Interferometric microscope

The ADE PhaseShift MicroXAM is a microscope that was used in conjunction with the AFM to measure the surface roughness and topography of samples. A schematic of the instrumentation is shown in Figure 3.18 [83].

Light is generated at a light source and is directed onto a beam splitter; half the beam is directed and then reflected off a reference surface and the other half is reflected off the sample surface [84]. At the point where the distances between the beam splitter and the sample, and the beam splitter and the reference surface is the same, the combined beam will have regions of interference which is imaged to form a 2D/3D map of the surface.

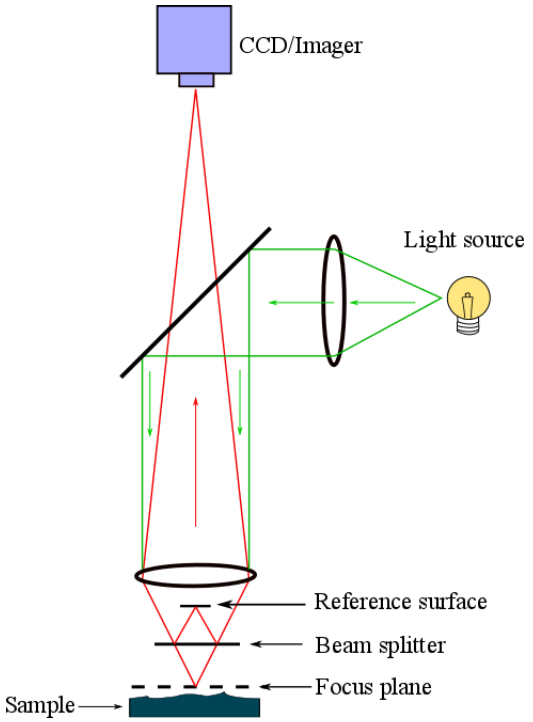


FIGURE 3.18: Schematic drawing of the ADE PhaseShift MicroXAM.

## 3.4 Thin film coatings

Ultimately photocathode materials will be deposited onto molybdenum plugs and installed into the high repetition rate gun that will drive CLARA. Therefore it is necessary to study properties of the films deposited. DC magnetron sputtering technique has been employed to produce films for this work. It is a physical vapour deposition (PVD) technique in which energetic ions bombard a target material, effectively removing atoms from the target surface which then condense on the substrate [30]. An illustration of the process is shown in Figure 3.19 and a photograph of the deposition system used is shown in Figure 3.20. Krypton gas is injected into the chamber to the required pressure to ignite a glow discharge plasma. The target is negatively biased such that the negative ions in the plasma are accelerated towards the target. Incident krypton ions bombard the target surface with sufficient energy to dislodge target atoms, which then deposit upon the substrate. Secondary electrons are also generated as a result of $Kr^+$ bombardment; the generation of additional electrons allows for the plasma to be sustained at even lower pressures. In magnetron sputtering, magnetic fields parallel to the target surface are used to trap the electrons, thus increasing the rate of ionisation [30].

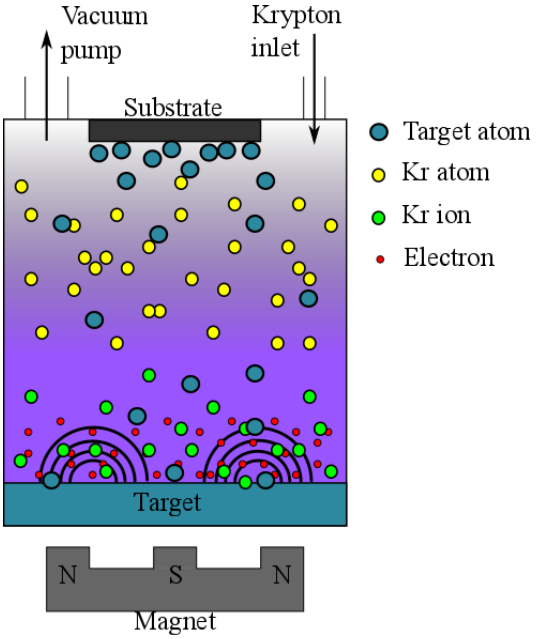


FIGURE 3.19: Illustration of magnetron sputtering system.

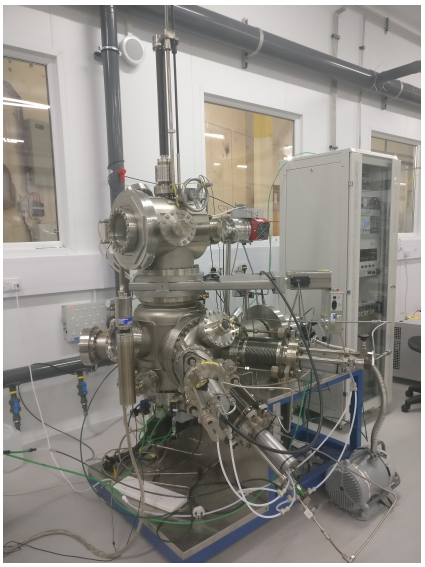

FIGURE 3.20: Photograph of magnetron sputtering system

## 3.5 Medium Energy Ion Scattering

### 3.5.1 Principles of ion scattering

In ion scattering techniques, mono energetic ions in the incident beam collide with the target, and the scattered ions are detected. The interactions between the incident ions and the target atoms is a result of Coulomb scattering from the nucleus in a central force field, and can be described in the framework of classical mechanics [85]. We will consider the elastic collisions between the incident ions and the target atoms, and the inelastic energy losses of the ions through the target as described by J.B. Craig in *Practical surface analysis, volume 2: Ion and neutral spectroscopy* [86].

#### Elastic Scattering

For scattering events that take place at the target surface, elastic scattering can be applied to describe the energy transfers. We will consider a simple binary collision model where masses $m_1$ and $m_2$ describe the mass of the incident ion and target atom respectively. In Figure 3.21, $m_1$ is shown to collide with $m_2$ and consequently is scattered through an angle $\theta$ (scattering angle). The target atom $m_2$ is deflected over an angle $\phi$.

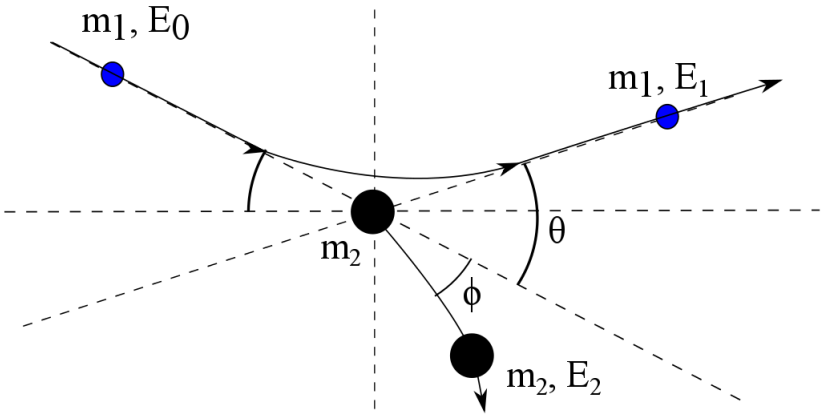


FIGURE 3.21: An incident ion, mass $m_1$ and energy $E_0$, collides with target mass $m_2$. Incident ion is deflected over scattering angle $\theta$ with energy $E_1$ and the target mass is deflected by $\phi$ and has energy $E_2$ after the collision.

In elastic scattering, the conservation principle of energy and momentum applies: the total energy/momentum before the collision equals the total energy/momentum after the collision. These principles are expressed below:

$$\frac{m_1 v_0^2}{2} = \frac{m_1 v_1^2}{2} + \frac{m_2 v_2^2}{2} \tag{3.10}$$

$$m_1 v_0 = m_1 v_1 cos\theta + m_2 v_2 cos\phi \tag{3.11}$$

$$0 = m_1 v_1 sin\theta - m_2 v_2 sin\phi \tag{3.12}$$

where $v_1$ is the velocity of $m_1$ after the collision, $v_2$ is the velocity of $m_2$ after the collision.

By first eliminating $\phi$ and then $v_2$ a ratio of the velocities of the incident ion $m_1$ can be obtained:

$$\frac{v_1}{v_0} = \frac{\sqrt{m_2^2 - m_1^2 sin^2\theta} + m_1 cos\theta}{m_1 + m_2} \tag{3.13}$$

Thus, the ratio of the incident ion energies before and after scattering, known as the kinematic factor $k^2$, can be written as follows:

$$k^2 = \frac{E_1}{E_0} = \left(\frac{\sqrt{m_2^2 - m_1^2 sin^2\theta} + m_1 cos\theta}{m_1 + m_2}\right)^2 . \tag{3.14}$$

Equation 3.14 shows that the energy of the scattered particles is dependent only on the mass of the incoming ion, the target mass and the scattering angle. Therefore, if $E_0$, $E_1$, $m_1$ and $\theta$ are known, the target mass $m_2$ can be calculated. In a target consisting of different elements (different target masses), the kinematic factor will be increasingly different with increasing scattering angles.

Therefore analysing the energy of the scattered particles allows for compositional analysis.

**Inelastic Energy Losses**

For scattering events that take place below the surface, energy loss due to inelastic scattering must be taken into consideration. This loss of energy is attributed to the inelastic interactions of the ions with the electrons in the solid. To calculate the energy of the scattered ion, Equation 3.14 is modified to include the energy lost as the ion passes through the target material (see Figure 3.22):

$$E_b(Z) = k^2(E_0 - \delta E_{\text{in}}) - \delta E_{\text{out}} \tag{3.15}$$

$$\delta E_{\text{in}} = S_1 x_1 = \frac{S_1 z}{cos\theta_1} \tag{3.16}$$

$$\delta E_{\text{out}} = S_2 x_2 = \frac{S_2 z}{cos\theta_2} \tag{3.17}$$

where $\delta E_{\text{in}}$ and $\delta E_{\text{out}}$ are the energy-loss increments before and after scattering. $S_1$ and $S_2$ are the specific energy loss components corresponding to the energy loss increments, also known as the stopping power. In MEIS the surfaces of interest are typically sufficiently thin so as to consider the stopping powers to be constant.

$E_b$ is a function of scattering depth and therefore Equation 6 can be rewritten as:

$$\delta Z = \frac{\delta E}{\dfrac{k^2 S_1}{cos\theta_1} + \dfrac{S_2}{cos\theta_2}} \,. \tag{3.18}$$

This shows that the energy scale is also a function of depth. Therefore the energy spectra from the backscattered ions in MEIS can be converted to mass and depth scales.

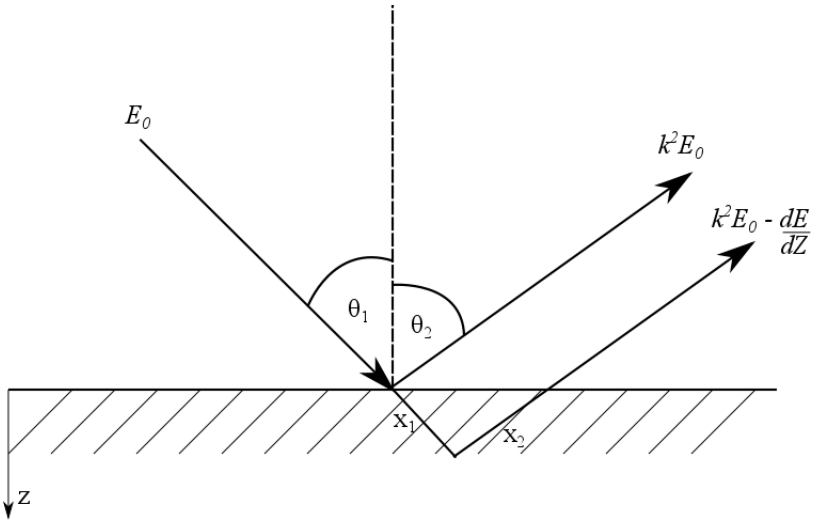


FIGURE 3.22: An incident ion with energy $E_0$, collides with a surface atom and its energy is reduced by $k^2$. For an incident ion that is scattered below the surface, additional energy, dE/dZ, is lost due to ineleastic scattering.

### 3.5.2 Experimental set-up

#### Plasma Treatment

1 $cm^2$ copper samples were cut from 99.99% purity bulk polycrystalline copper sheets, with an "as rolled" surface finish. Prior to plasma treatment/ MEIS analysis, all samples were cleaned and degreased in ultrasonic baths of acetone.

A description of the procedure for O plasma treatment is found in section 3.2.

The variable parameters for plasma treatment are plasma power and treatment time. Power levels between 10 and 100% were evaluated, along with treatment times between 5 and 20 minutes. The samples were mounted onto sample holders (see Figure 3.23) and transferred quickly in air to the fast entry vacuum loadlock on the MEIS end station.

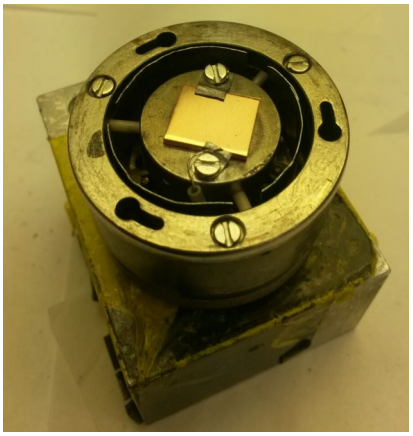

FIGURE 3.23: Image of copper samples mounted onto sample holder.

### MEIS facility at the University of Huddersfield

The analyses of the plasma treated samples were carried out on the MEIS facility in the Institute for Accelerator Applications at the University of Huddersfield [1]. The analyses were performed using 100 keV He ions. The incidence angle of the beam on the target was set at 35.3°C for all the samples analysed. The spot size of the beam on the target was 0.5 x 1.0 mm with a dose of 1.25 C per tile. In this section the components of the facility are described.

A schematic of the accelerator and end station is shown in Figure 3.24. He atoms are ionised in an experimental enclosure by electron ionisation. The ions are then accelerated through the beam line, through a quadrupole triplet lens and focused down before entering the scattering chamber [1]. Here the ion beam is directed on the sample at a known angle and the scattered particles are detected.

In the scattering chamber, the samples are loaded onto a triple axis, high precision manipulator for accurate positioning and alignment of the samples. The scattered particles are collected and analysed by a toroidal sector electrostatic energy analyser. At any given position, the angular range of the detector is 24°; however the analyser can also be rotated around the scattering centre, further extending the range of detection. The energy and scattering angle of the scattered ion can be known by position sensitive detection.

Adjacent to the scattering chamber is a sample preparation chamber. Here *in-situ* surface characterisation (Auger Electron Spectroscopy (AES) and LEED) and preparation ($Ar^+$ bombardment and heating) of the sample surface is carried out.

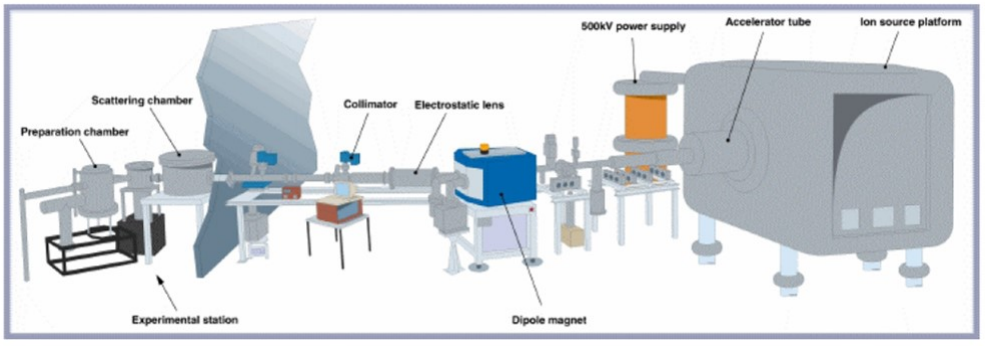


FIGURE 3.24: Schematic for MEIS facility at the University of Huddersfield [1].

### Data analysis using SIMNRA code

The raw data collected in MEIS experiments can be seen as a 2D map which describes the scattered ion intensity as a function of either the scattered ion-energy or the scattered ion-angle [87]. For analysis purposes, two specific cuts through the data maps are typically used:

- A plot of scattered ion intensity as a function of energy.
- A plot of scattered ion intensity as a function of scattering angle.

In the first case, the intensity of the scattered ions as a function of energy gives an indication of the depth dependence of the near surface composition of the sample. This is because of the relationship between the energy lost by the scattered ion and the mass of the scatterer atom (see section 3.5.1).

In the second case, the intensity of the scattered ions as a function of scattering angle provides information on the crystallographic structure of the crystal.

For the experiments carried out in this study, only the first case was used to obtain the composition depth profile of the samples. This is because the samples studied were amorphous, and therefore there was no crystallographic information that could have been extracted. The data was analysed using the SIMNRA 5.02 code [88].

A simulation of the energy spectra was used to fit the raw data of each energy spectrum systematically. The fitting procedure can be broken down into two main steps as outlined in the *SIMNRA User's Guide* [88]. Firstly the key experimental parameters must be defined and inputted into the program, such as the beam energy and scattering geometry parameters [89]. Secondly, the target must be simulated by creating each constituent layer and defining the atomic concentrations and thickness. For the plasma treated copper samples, a four layer model was employed:

1. **Surface Layer**
   This was set at a couple of monolayers thickness ($10 \times 10^{15}$ atoms/cm$^2$). The composition was allowed to vary in order to simulate a fitted value for the composition at the very surface.

2. **Oxide Layer**
   This layer typically comprised the majority of the oxide layer; both the composition and the thickness of this layer were allowed to vary to best produce a good fit.

3. **Interfacial layer**
   This layer can be considered as the inter-facial layer between the oxide film and the bulk. This layer probably has gradually varying composition, but is modelled by a single composition with some film roughness added to smear out the signal and improve the fit. As with the second layer, the third layer was allowed to have both variable thickness and composition.

4. **Copper Bulk**
   The fourth layer is essentially bulk pure copper; this allows the calibration of particles per steradian to be fitted.

Finally the spectrum can be simulated. The target parameters can then be adjusted to ensure that the fit is good.

# Chapter 4

# Preparation of Bulk Polycrystalline Metals

The preparation of a photocathode surface is critical to optimising the QE of metals and semiconductors. For that reason the effects of several preparation methods of metals have been investigated.

## 4.1 Argon ion bombardment of bulk metals in ESCALAB

The aim of the first part of this study was to investigate the effect of $Ar^+$ sputtering on polycrystalline metal photocathodes. The results from this work are published in the IPAC '14 conference proceedings [90]. Ten metals were selected for a preliminary study based on the criteria that they are vacuum compatible and have a work function equal to or lower than copper [35]. For each metal sample, measurements of surface composition, work function (WF) and photocurrent were taken "as-received". After analysis, the "as-received" samples were transported into a separate preparation chamber and surface contaminants removed using *in-situ* $Ar^+$ sputtering (10 minute cycles at 5 keV and $50\mu A$). Cycles of sputtering were repeated until surface contaminants had reduced to trace levels. Following this procedure the surfaces were re-characterised. In some cases, where the oxide was particularly tenacious, several cycles of sputtering were employed. For several metals, the effect of heat treatment post-ion bombardment was also investigated, but due to issues with equipment not all of the metals were heat treated. After ion bombardment, these samples were transported into the preparation chamber and mounted onto the heating stage, and heated to 250°C for 30 minutes (see Chapter 3 section 3.2.3).

### 4.1.1 Results

A summary of the QE (measured using UV LED) , WF (measured using Kelvin Probe) and quantified XPS measurements is presented in Table 4.1. Note that for XPS atomic

percentage quantifications, when the total percentage of metal, oxygen and carbon does not sum to 100%, the remainder can be assumed to be attributed to argon.

TABLE 4.1: A summary of WF, QE and quantified XPS data (atomic percentage) "as-received" and after $Ar^+$ Sputter treatment for a selection of metals

| | WF (eV) | QE | Metal (%) | O 1s (%) | C 1s (%) |
|---|---|---|---|---|---|
| **Ag** | | | | | |
| "As-received" | 5.09 | $8.50 \pm 0.05 \times 10^{-6}$ | 35.7 ± 1.9 | 12.1 ± 2.4 | 52.2 ± 2.6 |
| $Ar^+$ Sputter | 5.11 | $4.19 \pm 0.02 \times 10^{-5}$ | 100 | 0 | 0 |
| Heated to 250°C | 5.06 | $8.40 \pm 0.05 \times 10^{-5}$ | 94.5 ± 1.45 | 0 | 5.5 ± 1.5 |
| **Al** | | | | | |
| "As-received" | 4.02 | $9.50 \pm 0.05 \times 10^{-6}$ | 24.1 ± 1.1 | 46.2 ± 1.1 | 29.7 ± 1.2 |
| $Ar^+$ Sputter | 4.91 | $2.21 \pm 0.01 \times 10^{-5}$ | 60.3 ± 5.3 | 11.6 ± 2.7 | 15.1 ± 4.5 |
| **Cu** | | | | | |
| "As-received" | 5.35 | $5.00 \pm 0.03 \times 10^{-6}$ | 0.9 ± 0.2 | 32.9 ± 1.3 | 66.2 ± 1.3 |
| $Ar^+$ Sputter | 5.32 | $1.06 \pm 0.01 \times 10^{-5}$ | 100.0 | 0 | 0 |
| Heated to 200°C | 5.23 | $1.68 \pm 0.01 \times 10^{-5}$ | 93.9 ± 1.2 | 6.1 ± 1.2 | 0 |
| **Mg** | | | | | |
| "As-received" | 3.34 | $6.20 \pm 0.04 \times 10^{-6}$ | 12.5 ± 1.8 | 35.2 ± 1.5 | 52.3 ± 1.7 |
| $Ar^+$ Sputter | 3.37 | $1.71 \pm 0.01 \times 10^{-3}$ | 54.5 ± 1.6 | 28.6 ± 1.2 | 0 |
| **Mo** | | | | | |
| "As-received" | 5.07 | $1.47 \pm 0.01 \times 10^{-6}$ | 11.0 ± 0.5 | 24.1 ± 1.2 | 64.9 ± 1.3 |
| $Ar^+$ Sputter | 5.18 | $2.48 \pm 0.01 \times 10^{-6}$ | 74.4 ± 4.5 | 7.8 ± 1.8 | 17.8 ± 4.7 |
| **Nb** | | | | | |
| "As-received" | 4.82 | $3.88 \pm 0.02 \times 10^{-7}$ | 4.0 ± 0.6 | 46.4 ± 2.1 | 49.6 ± 2.3 |
| $Ar^+$ Sputter | 4.71 | $1.95 \pm 0.01 \times 10^{-4}$ | 81.3 ± 5.1 | 18.7 ± 5.1 | 0 |
| **Pb** | | | | | |
| "As-received" | 4.43 | $2.90 \pm 0.02 \times 10^{-5}$ | 24.6 ± 1.5 | 35.2 ± 2.6 | 40.2 ± 3.4 |
| $Ar^+$ Sputter | 4.66 | $2.36 \pm 0.01 \times 10^{-4}$ | 100 | 0 | 0 |
| **Ti** | | | | | |
| "As-received" | 4.86 | 0 | 7.2 ± 0.6 | 39.2 ± 1.5 | 53.6 ± 1.5 |
| $Ar^+$ Sputter | 4.47 | $3.29 \pm 0.02 \times 10^{-4}$ | 60.7 ± 5.1 | 12.9 ± 3.7 | 14.9 ± 5.9 |
| **V** | | | | | |
| "As-received" | 5.51 | $1.39 \pm 0.01 \times 10^{-6}$ | 13.2 ± 0.7 | 47.3 ± 1.8 | 39.5 ± 2.0 |
| $Ar^+$ Sputter | 5.00 | $2.21 \pm 0.01 \times 10^{-5}$ | 61.7 ± 3.8 | 18.7 ± 3.7 | 3.3 ± 3.3 |
| Heated to 250°C | 5.32 | $1.01 \pm 0.01 \times 10^{-5}$ | 54.2 ± 1.5 | 24.4 ± 1.1 | 15.4 ± 1.9 |
| **Zr** | | | | | |
| "As-received" | 4.51 | $3.88 \pm 0.02 \times 10^{-6}$ | 7.6 ± 0.4 | 48.3 ± 1.6 | 44.1 ± 1.5 |
| $Ar^+$ Sputter | 4.26 | $2.89 \pm 0.02 \times 10^{-4}$ | 74.3 ± 3.9 | 12.5 ± 3.3 | 0 |

In this work, 1 $cm^2$ samples were cut from bulk polycrystalline metal sheets with "as rolled" surface finishes. The metals in this study were sourced from either Goodfellow or Advent Research Materials.

**Aluminium**

Aluminium is a very reactive metal and therefore the "as-received" surface is typically oxidised [91]. A quantification of the elemental composition, as calculated from the survey spectra (see Figure 4.1c)), shows that for Al "as-received", oxygen accounts for 46% of the sample surface, carbon 30% and aluminium metal 24%. The "as-received" sample was cut from 99.9+% purity aluminium sheet from Advent Research Materials. The chemical state of aluminium is derived from region scans. For the "as-received" surface (see figure 4.1a)) the major Al 2p peak is positioned at approximately 75.8 eV, which is in the range of aluminium oxide. Additionally a smaller peak occurring at 73 eV corresponds to metallic aluminium. The oxide component accounts for 92% and the metal for 8%.

Figure 4.1b) shows that upon $Ar^+$ sputtering, the binding energy for the Al 2p peak is shifted to 74.3 eV; this still falls in the range of aluminium oxide [92]. Variation in peak position in aluminium oxide is indicative of a change in the thickness of the oxide layer and can be used to estimate the thickness of the oxide film [93]; though not completely removed, the oxide may have reduced. Why does the oxide persist? Why did the metallic component of the Al 2p peak disappear? Upon sputtering, mixing may occur; this is a process by which a coating (or in this case an oxide/carbide layer) mixes with the substrate (or the bulk metal) [94]. This can resolve the observation of an overall reduction in oxygen content and the persistent oxide as suggested by the position of the Al 2p peak.

Figure 4.1d) shows the reduction in the intensity of the O 1s peak after a cycle of sputtering; this correlates with the observations from the Al 2p region spectra. The O 1s peaks occur at higher binding energies (between 533-534 eV) indicative of the formation of a metal hydroxide. Additionally Figure 4.1e) shows a reduction in intensity of the C 1s peak by a factor of a half. A shift in peak position from 285.7 to 284.3 eV is observed, which corresponds to the chemical states C-O-C and C-C respectively. The reduction in oxygen and carbon correlates with some improvement in QE (factor of 2.3). The WF increases by approximately 0.9 eV after sputtering.

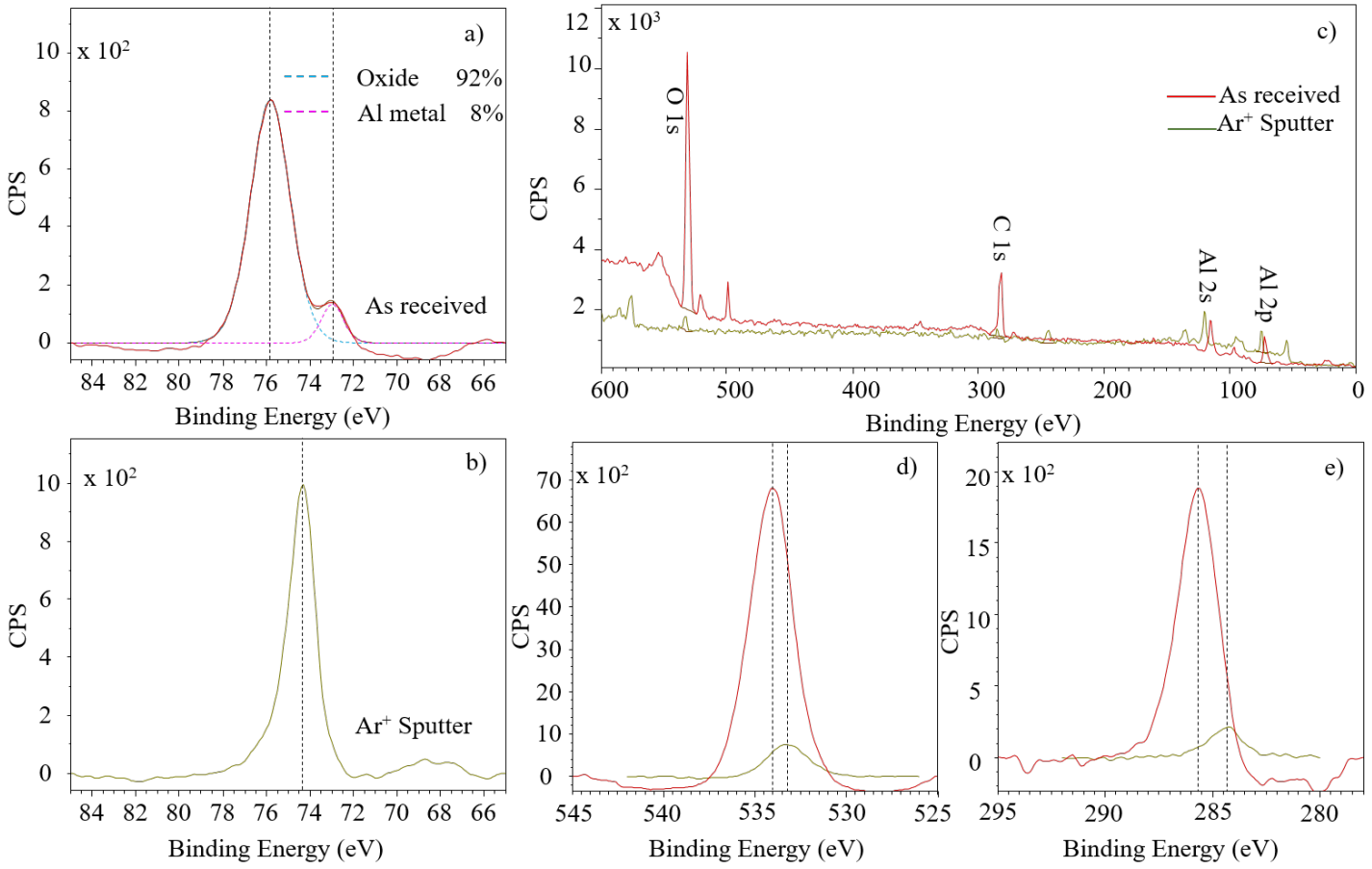


FIGURE 4.1: XPS spectra for bulk polycrystalline aluminium "as-received" and $Ar^+$ sputtered. High resolution Al 2p region scan for a) "as-received surface" and b) $Ar^+$ sputtered surface. c) Overlay of survey scans for "as-received" and $Ar^+$ sputtered surface, d) O 1s region overlay and e) C 1s region overlay for "as-received" and $Ar^+$ sputtered surface.

**Copper**

A comparison of copper surfaces "as-received", after $Ar^+$ sputtering and after heating to 200°C is shown in Figure 4.2 and 4.3. The "as-received" surface is dominated by oxygen and adventitious carbon, with trace levels of copper as derived from the survey spectra. The "as-received" sample was cut from 99.95+% purity O.F.H.C copper sheet from Goodfellow. The survey spectra for $Ar^+$ sputtered and heated surfaces show a reduction in the background level, a reduction of oxygen and carbon to trace level, and the emergence of copper. There is a slight emergence of O 1s after heating the sample which could be due to the migration of contaminants. O 1s and C 1s region scans (Figure 4.2 b) and c)) show the total reduction of O 1s and C 1s for sputtered and heated surfaces.

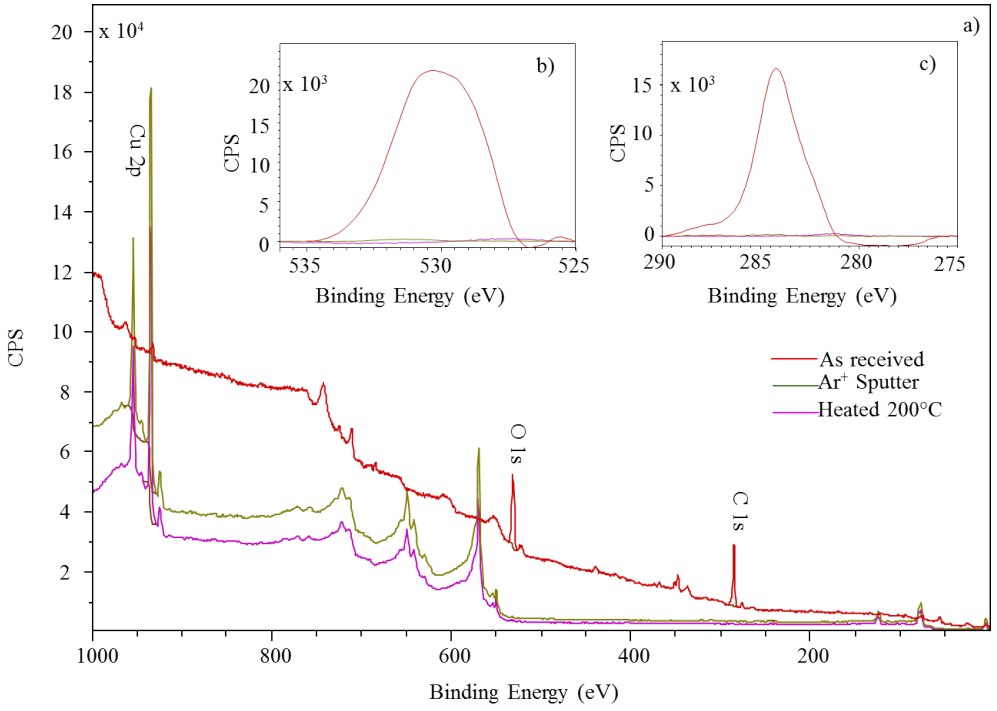


FIGURE 4.2: XPS spectra for bulk polycrystalline copper "as-received" and $Ar^+$ sputtered. a) Overlay of survey scans for Cu "as-received", $Ar^+$ sputtered and heated to 200°C b) Overlay of O 1s region scans and c) C 1s region scans

Figure 4.3 for Cu 2p region scans show changes in the chemical state for each of these processes. "As-received", the chemical state of copper is CuO. It is very easy to distinguish this particular oxide from the region scan because of the characteristic shake-up lines; they occur at approximately 9 eV higher binding energies to the main Cu 2p peaks for CuO [92]. Additionally the breadth of the Cu 2p peaks is wider in the case of CuO. Both of these features are observed in Figure 4.3 a). Upon sputtering, the satellites are reduced to trace level, and the Cu 2p peaks reduce in breadth. Cu 2p

region scans for Cu metal and $Cu_2O$ are indistinguishable, and therefore from Figure 4.3b) alone, it cannot be said with certainty the chemical state of the Cu [64]. However, the O 1s region shown in Figure 4.2b) shows the oxygen reduces to trace levels, which would suggest that it is Cu metal that dominates the surface after this process. There is a factor of two increase in QE after sputtering, and very little change in the measured WF. After heating the Cu sample to 200°C the elemental quantification from the survey spectra suggests that trace levels of oxygen appear. The appearance of oxygen on the sample surface may be attributed to the sharp rise of residual oxygen in the chamber upon heating. If the rate of heating was high, then outgassing of CO, $CO_2$ and even $H_2O$ may have occurred. The region scan (see Figure 4.3c)) shows little to no change in the Cu 2p binding energy suggesting that no chemical change has occurred with respect to the copper.

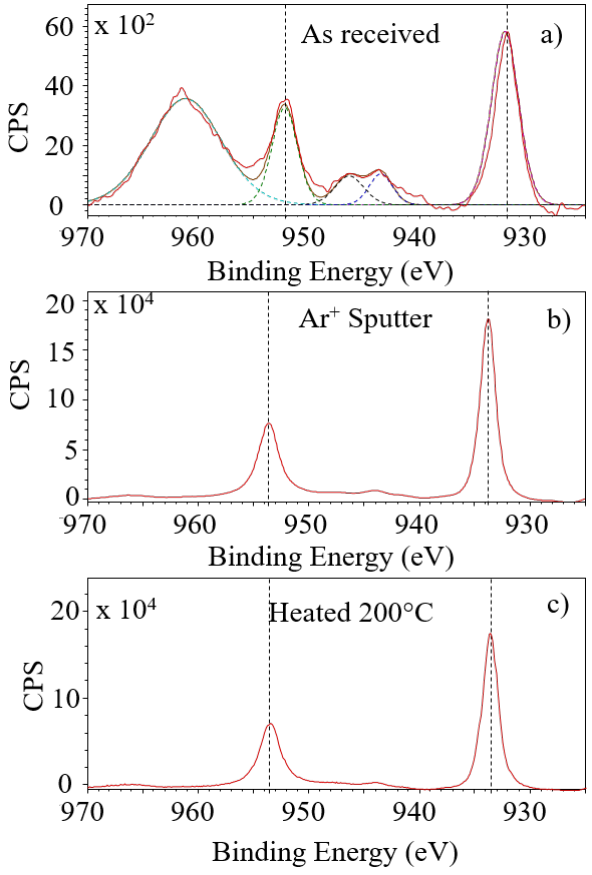


FIGURE 4.3: Core level Cu 2p region spectra with peak fittings a)"as-received, b) $Ar^+$ sputtered and c) heated to 200°C.

**Lead**

The lead sample was cut from 99.95+% purity lead sheet from Advent Research Materials. The survey spectra for the lead sample (see Figure 4.4b)), shows the reduction of oxygen and carbon contaminants after $Ar^+$ sputtering. The higher resolution region scan (Figure 4.4a)) indicates that there are two chemical states of lead present "as received": $Pb_3O_4$ (as fitted by the blue curves) and Pb metal (fitted in pink). The position of Pb 4f peaks associated with $Pb_3O_4$ occur at approximately 1.5 eV higher binding energy than Pb metal [92]. Sputtering eliminates the lead oxide component and the Pb metal component becomes dominant; this correlates with an increase in the QE value by three orders of magnitude (see Table 4.1). The O 1s peak "as-received" is split in two components: metal oxide and metal carbonate, 58.48% and 41.52% respectively. This is reduced to trace level upon sputtering. The measured WF for Pb increases from 4.43 eV "as received" to 4.66 after $Ar^+$ sputtering. Both measured values are higher than the literature quoted values for a clean lead surface (4.25 eV) [35].

**Magnesium**

The magnesium sample was cut from 99.9% purity magnesium sheet from Advent Research Materials. Magnesium is a very reactive metal [95], known to have a tenacious oxide, and therefore one would expect to see a significant amount of contamination on the "as-received" surface [96]. Contaminants are observed in the "as-received" survey spectra (Figure 4.5b)), the elemental quantification for which is presented in Table 4.1. The survey spectrum suggests that magnesium accounts for only 12% of the surface. From the Mg 2p region scan (Figure 4.5a)), a low intensity Mg 2p peak at approximately 50.2 eV is observed, which falls between the range of Mg metal and oxide. To better identify the chemical state of the magnesium, we can consider the position of the principal Mg KLL peak; this occurs at 306.2 eV, corresponding to magnesium oxide (see Figure 4.5 b)), which is approximately 5.2 eV higher than the expected position for Mg metal [93]. For the sputtered surface, the carbon is reduced to trace level, and the oxygen is significantly reduced. The Mg 2p region scan (see Figure 4.5) indicates that there are two chemical states of Mg after sputtering: Mg metal at 48.9 eV and MgO at 51.8 eV. The principal Mg KLL peak is shifted to a lower binding energy of 299.7 eV which corresponds to Mg metal; this is in good agreement with the conclusions drawn from the Mg 2p region- that the dominant chemical state is Mg metal, with partial remaining oxide. The increase in the Mg metal correlates with the highest increase in QE (more than 2 order of magnitude). Despite partial oxidation, the QE achieved by $Ar^+$ sputtering this Mg sample is more than two orders of magnitude higher than that of copper. The WF measurement for the Mg sample was appromimately 3.4 eV; this is only 0.26 eV lower than the literature value [35]. Surprisingly, the measured WF does not significantly change despite significant changes to elemental and chemical composition.

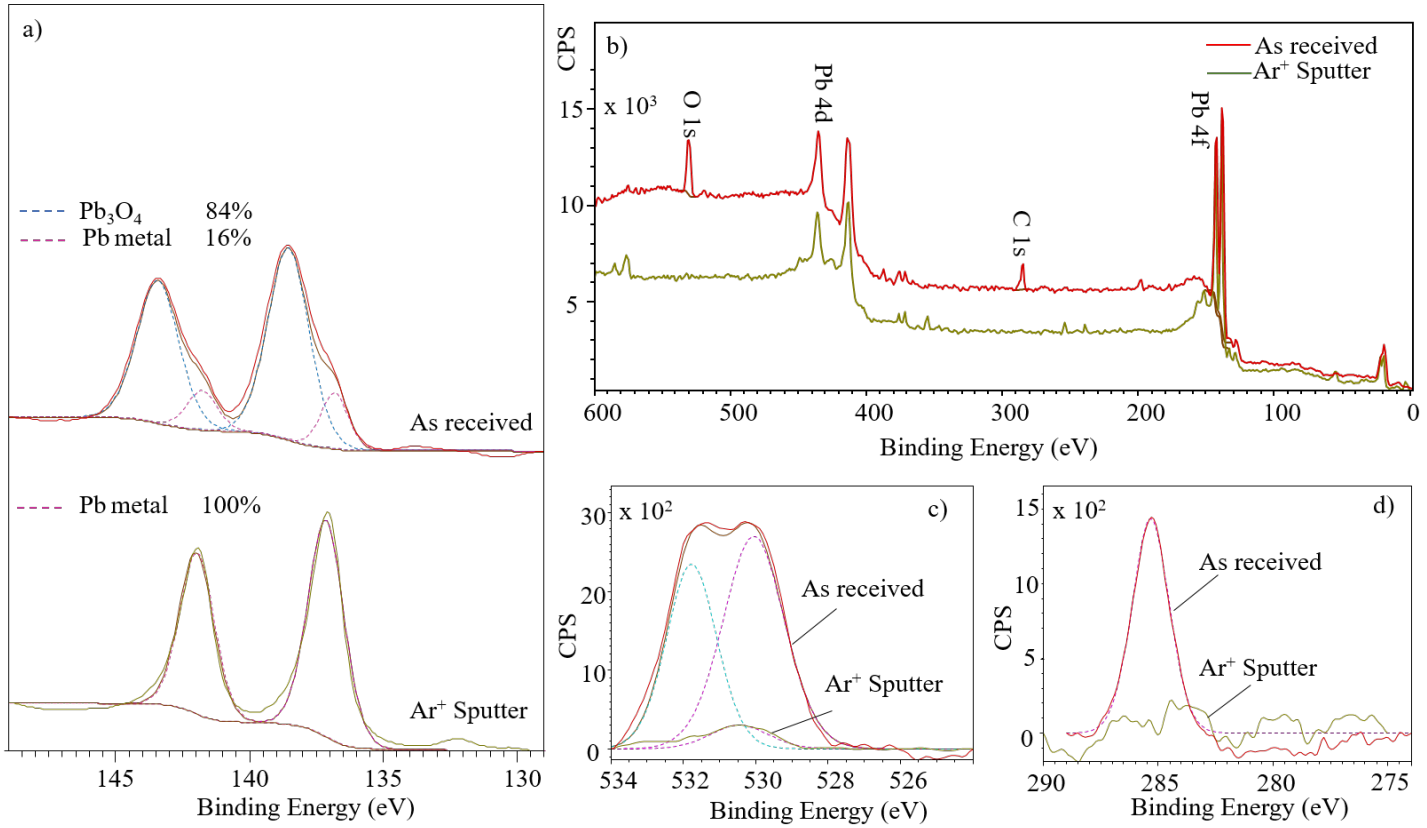


FIGURE 4.4: XPS spectra for bulk polycrystalline lead "as-received" and $Ar^+$ sputtered. a) Pb $4f_{5/2-7/2}$ region spectrum with fittings (top) "as received" and (bottom) after $Ar^+$ Sputtering. b) Overlay of Pb survey spectra with labelled peaks "as received" and after $Ar^+$ Sputtering. Overlay of c) O 1s region spectra and d) C 1s region spectra"as received" and after $Ar^+$ Sputtering for Pb sample.

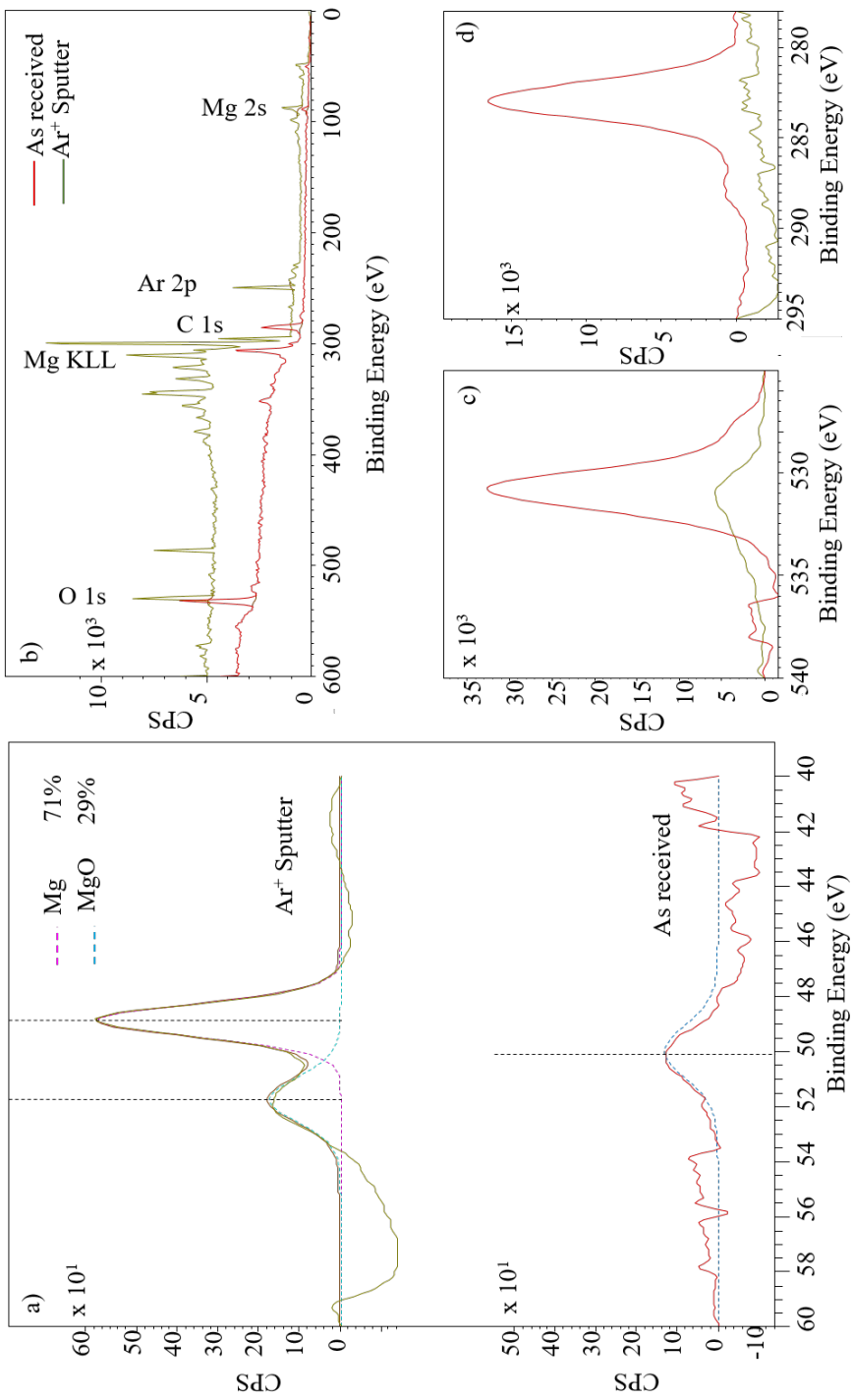


FIGURE 4.5: XPS spectra for bulk polycrystalline magnesium "as-received" and $Ar^+$ sputtered. a) Mg 2p region spectra with fittings: (top) after $Ar^+$ Sputtering and (bottom) "as received". b) Overlay of Mg survey spectra with labelled peaks "as received" and after $Ar^+$ Sputtering. Overlay of c) O 1s region spectra and d) C 1s region spectra"as received" and after $Ar^+$ Sputtering for Mg sample.

**Molybdenum**

The molybdenum sample was cut from 99.9% purity molybdenum sheet from Goodfellow. The "as-received" molybdenum surface seems to have a rather thick carbonaceous layer and a significant oxide which buries the molybdenum (see Table 4.1). The region scan for Mo 3d reveals that the "as-received" surface exists in two chemical states: $MoO_2$ and $MoO_3$, with the former dominating at 82% and the latter at 18%. $Ar^+$ sputtering typically reduces the oxides to a mixture of lower oxidation states and some metal components [93]. In this case, the $MoO_3$ component is reduced and the Mo 3d peaks are shifted to a binding energy that lies between Mo metal and $MoO_2$; this suggests a mixture of $MoO_2$ and perhaps a sub-oxide. Further cycles of sputtering may have been required to rid the surface of the carbon contamination and further reduce the oxide. The literature WF value of molybdenum is approx 4.6 eV (0.5 eV less than Cu) [35], however higher values were measured: 5.07 and 5.18 eV "as-received" and sputtered respectively. With respect to the QE, the initial "as-received" measurements were very poor. Partial removal of the carbonaceous layer and reduction of the oxide improved the QE by over an order of magnitude from $1.5 \times 10^{-7}$ to $2.5 \times 10^{-6}$. This is still almost an order of magnitude lower than for a clean Cu surface.

**Niobium**

The "as-received" sample was cut from 99.9 % purity niobium sheet from Advent Research Materials. Under ambient conditions, the most stable state of niobium is $Nb_2O_5$ [97]. This chemical state is observed in the "as-received" region scan (see Figure 4.7a)). The Nb 3d peaks are shifted by approximately 5.5 eV to a higher binding energy, compared with the expected position for Nb metal, and this is indicative of $Nb_2O_5$ [97]. Sputtering the niobium surface reduces the stable oxide into a mixture of sub oxides; predominantly a mix of NbO and $NbO_2$. Sputtering produces a reduction in the carbon signal, and also a shift in the C 1s peak to a lower binding energy; this corresponds to a change in chemical state from C-O-C (peak at 286 eV) to C-C (peak at 284.8 eV). The QE increases by over two orders of magnitude following this cleaning, finally yielding $1.9 \times 10^{-4}$, which is an order of magnitude higher than for Cu. With respect to the WF, the measured value drops from 4.82 to 4.71 eV after sputtering. These values are significantly larger than the literature value for Nb metal which is 4.3 eV [35]; this higher WF value may be accounted for by the persisting oxide.

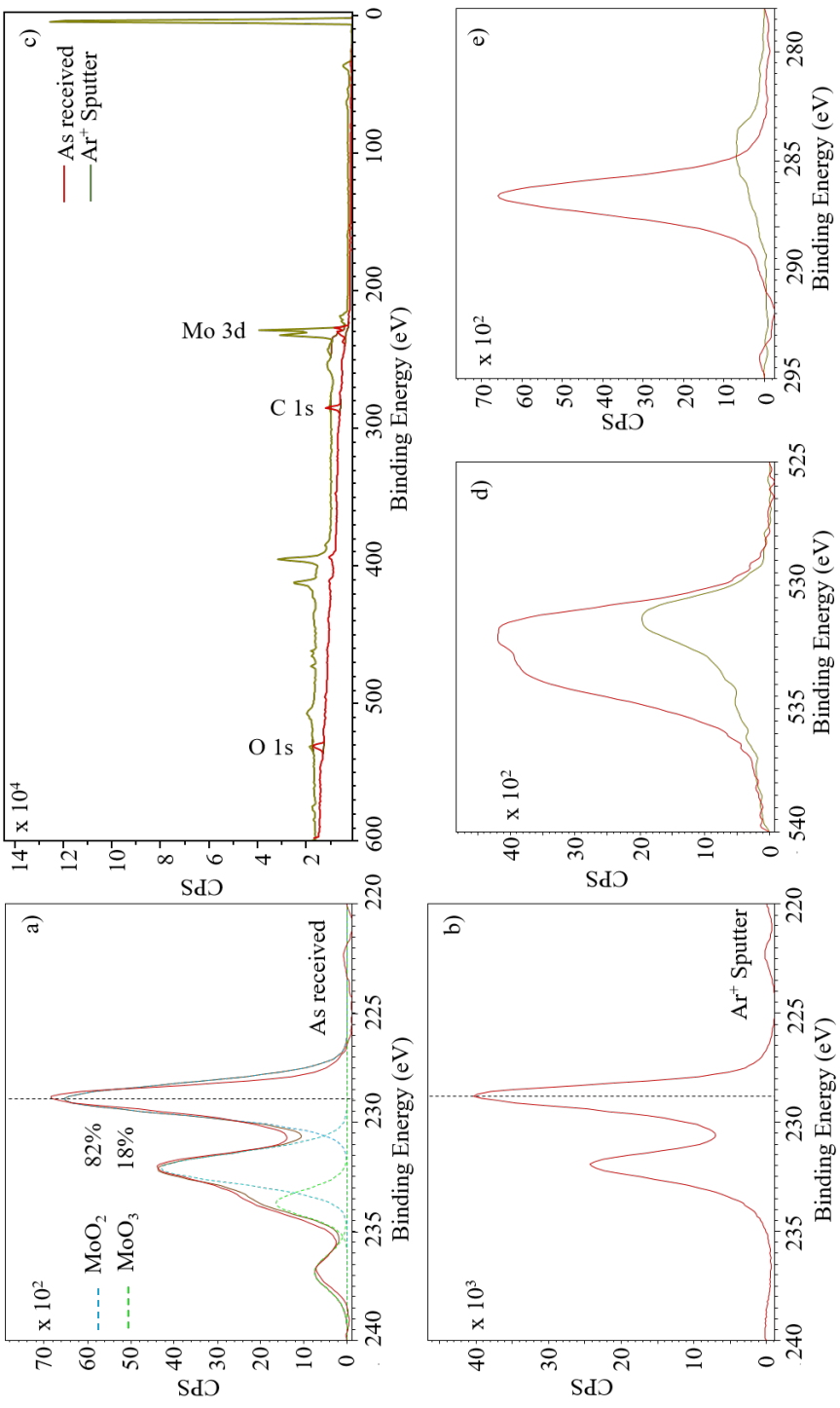


FIGURE 4.6: XPS spectra for bulk polycrystalline molybdenum "as-received" and $Ar^+$ sputtered. a) Mo $3d_{5/2-7/2}$ region spectra with fittings: (top) "as received" and (bottom) after $Ar^+$ sputtering. b) Overlay of Mo survey spectra with labelled peaks "as received" and after $Ar^+$ Sputtering. Overlay of c) O 1s region spectra and d) C 1s region spectra "as received" and after $Ar^+$ Sputtering for Mo sample.

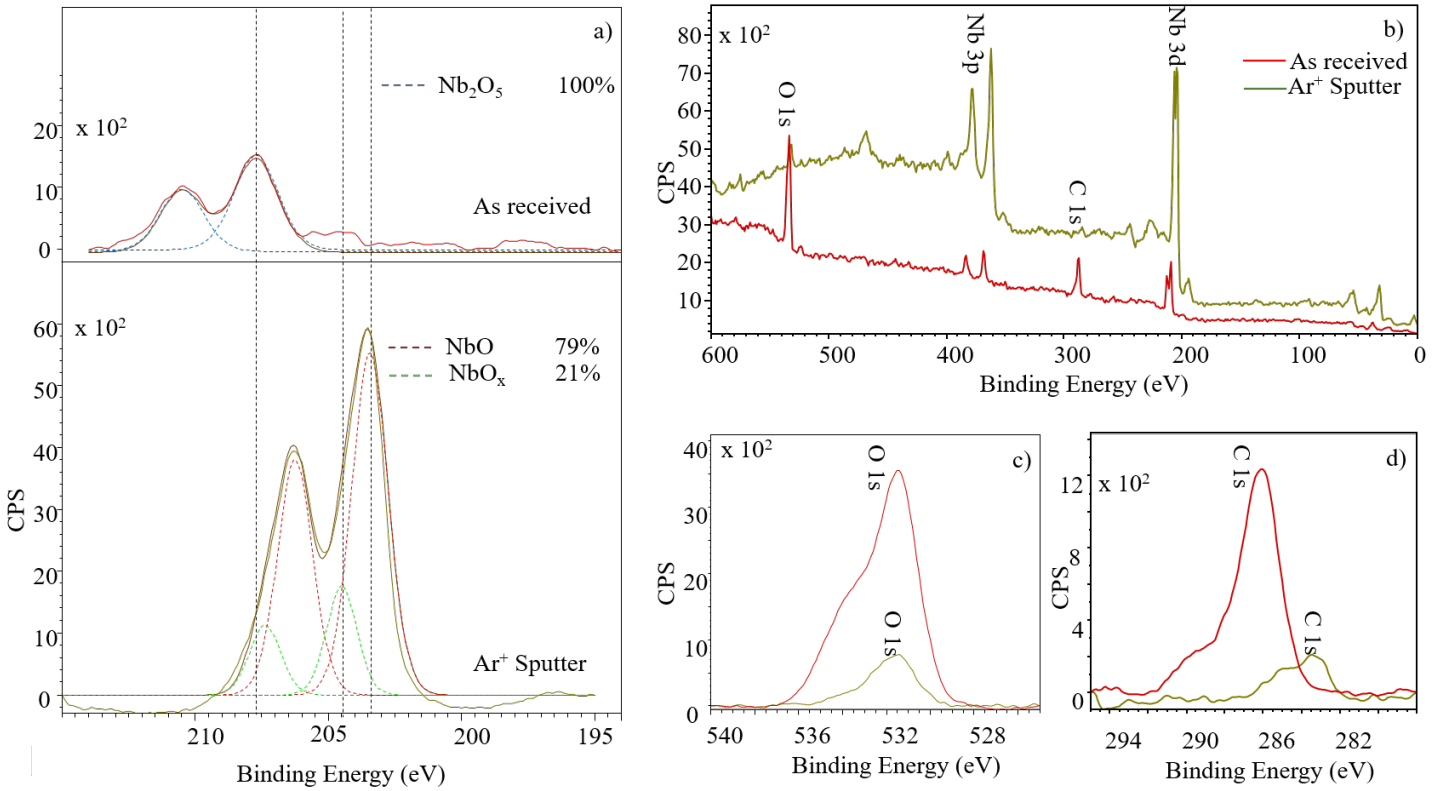


FIGURE 4.7: XPS spectra for bulk polycrystalline niobium "as-received" and $Ar^+$ sputtered. a) Nb $3d_{3/2-5/2}$ region spectra with fittings: (top) "as received" and (bottom) after $Ar^+$ sputtering. b) Overlay of Nb survey spectra with labelled peaks "as received" and after $Ar^+$ Sputtering. Overlay of c) O 1s region spectra and d) C 1s region spectra"as received" and after $Ar^+$ sputtering for Nb sample.

**Silver**

The "as-received" sample was cut from 99.97% purity silver sheet from Advent Research Materials. Silver is a noble metal and therefore does not oxidise under typical ambient conditions. It is therefore not surprising that a single cycle of $Ar^+$ sputtering was sufficient to reduce surface contaminants to trace levels (see Figure 4.8). The intensity of the Ag 3d peaks increases significantly upon sputtering and a shift of approximately 0.2 eV to a higher binding energy is observed. The Ag 3d peaks are further shifted up by 0.5 eV after heat treatment. These shifts are difficult to explain in terms of changes to the chemical states; there are no chemical states for silver that exist at these higher binding energies. It is possible therefore that the shifts are due to unwanted charging effects. Upon heating, the O 1s and C 1s region scans show slight increases in the oxygen and carbon content. As with the copper sample, it is possible that the sample heating induced outgassing of CO, $CO_2$ etc. from the chamber which in turn adsorbed onto the sample surface.

With respect to the WF, there is very little change in the measured value between the "as-received", $Ar^+$ sputtered and heated silver sample. The measured values are approximately 0.7 eV higher than the literature values for clean silver [35]. The QE value increase first by a factor of 5 after sputtering, and further increase by a factor of 2 after heating.

**Titanium**

The titanium sample was cut from 99.6+% purity titanium sheet from Advent Resesarch Materials. The WF value for titanium as quoted in the literature is approximately 4.33 eV [35]. The measured WF for the "as-received" and $Ar^+$ sputtered titanium is 4.86 eV and 4.47 eV respectively. There is potentially some correlation between reduction of surface contaminants and reduction of measured WF in this case. No photocurrent was measured for the "as-received" titanium sample, hence the 0 value for QE. However, upon sputtering the measured photocurrent gave a QE of $3.3 \times 10^{-4}$; this is over an order of magnitude greater than for copper. The XPS data shows that the "as-received" surface is made up of two components: $TiO_2$ and a sub oxide somewhere between Ti metal and TiO (see Figure 4.9 a)). The main Ti 2p peaks (fitted in blue) are shifted by approximately 5 eV to a higher binding energy than Ti metal; this corresponds to $TiO_2$ [98]. The smaller Ti 2p peaks (fitted in green) occur at 0.5 eV higher binding energy than Ti metal which falls in the middle of the range for Ti metal and TiO. After sputtering, the region scan shows that the $TiO_2$ is reduced to TiO predominantly (83%) and also Ti(111) (17%).

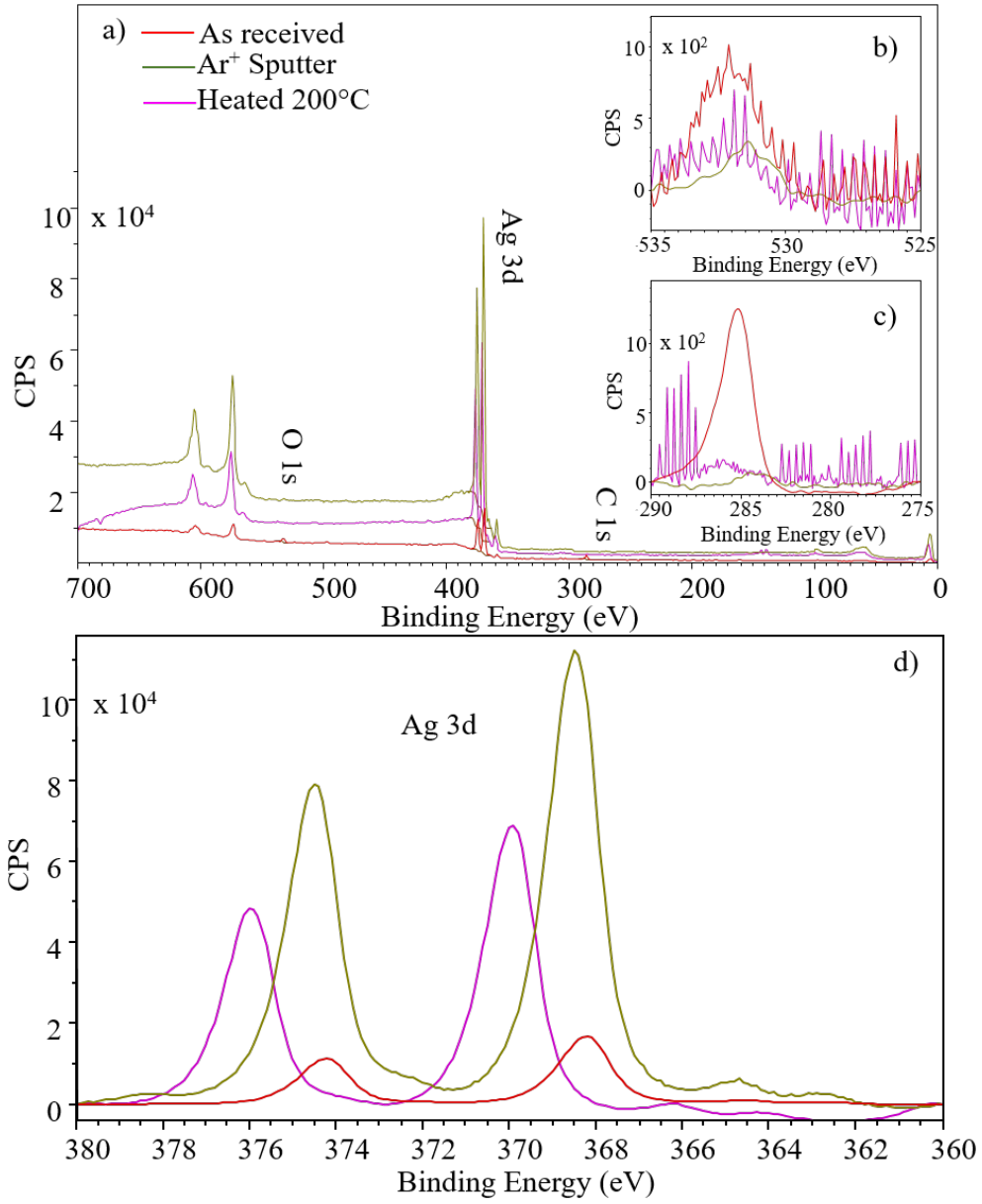


FIGURE 4.8: XPS spectra for bulk polycrystalline silver "as-received", $Ar^+$ sputtered and heated to 200°C. a) Overlay of Ag survey spectra with labelled peaks "as received", after $Ar^+$ Sputtering and heated to 200°C. Overlay of b) O 1s region spectra and c) C 1s region spectra"as received" and after $Ar^+$ sputtering, d) Overlay of Ag $3d_{3/2-5/2}$ region spectra "as received" (red), after $Ar^+$ sputtering (green) and heated to 200°C (pink).

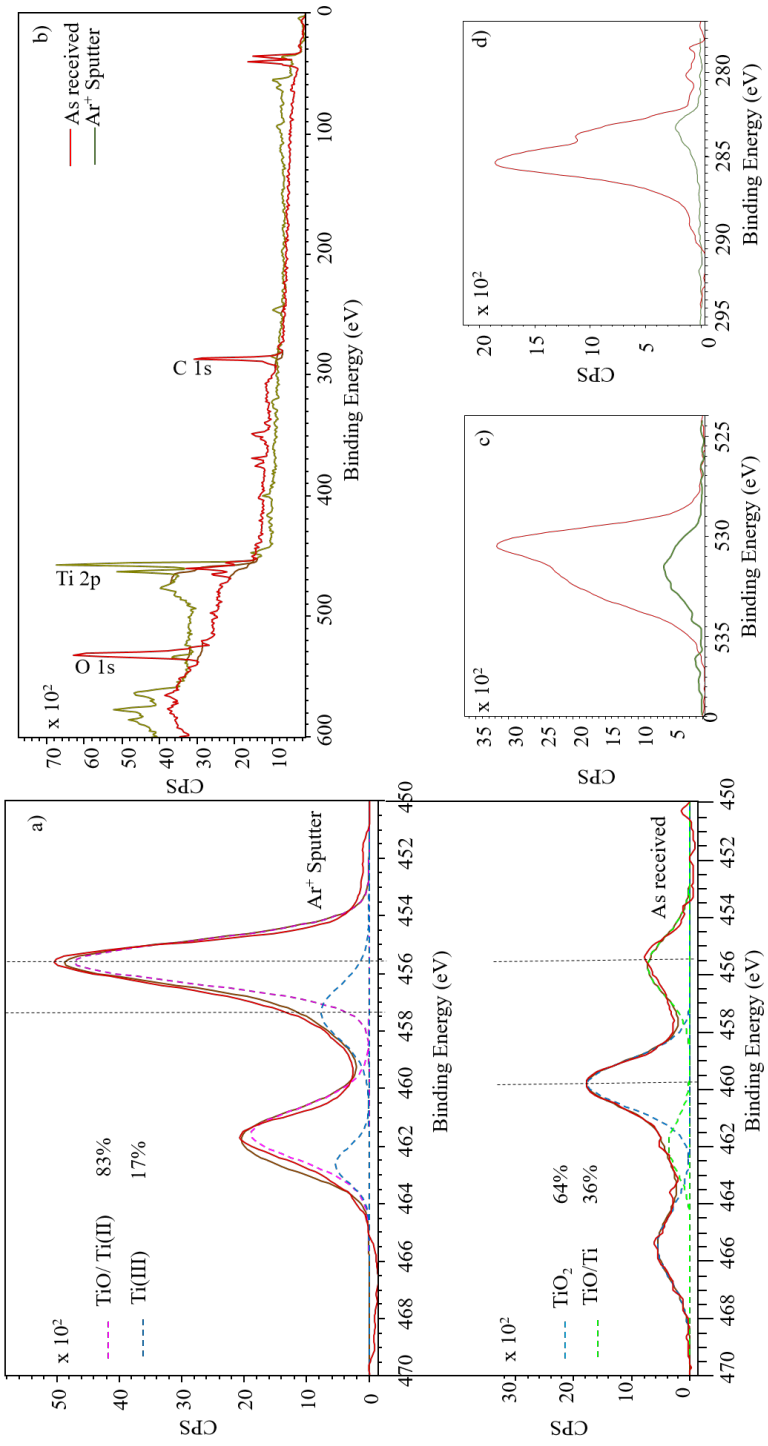


FIGURE 4.9: XPS spectra for bulk polycrystalline titanium "as-received" and $Ar^+$ sputtered. a) Ti $2p_{1/2-3/2}$ region spectra with fittings: (top) after $Ar^+$ sputtering and (bottom) "as received". b) Overlay of Ti survey spectra with labelled peaks "as received" and after $Ar^+$ Sputtering. Overlay of c) O 1s region spectra and d) C 1s region spectra"as received" and after $Ar^+$ sputtering for Ti sample.

**Vanadium**

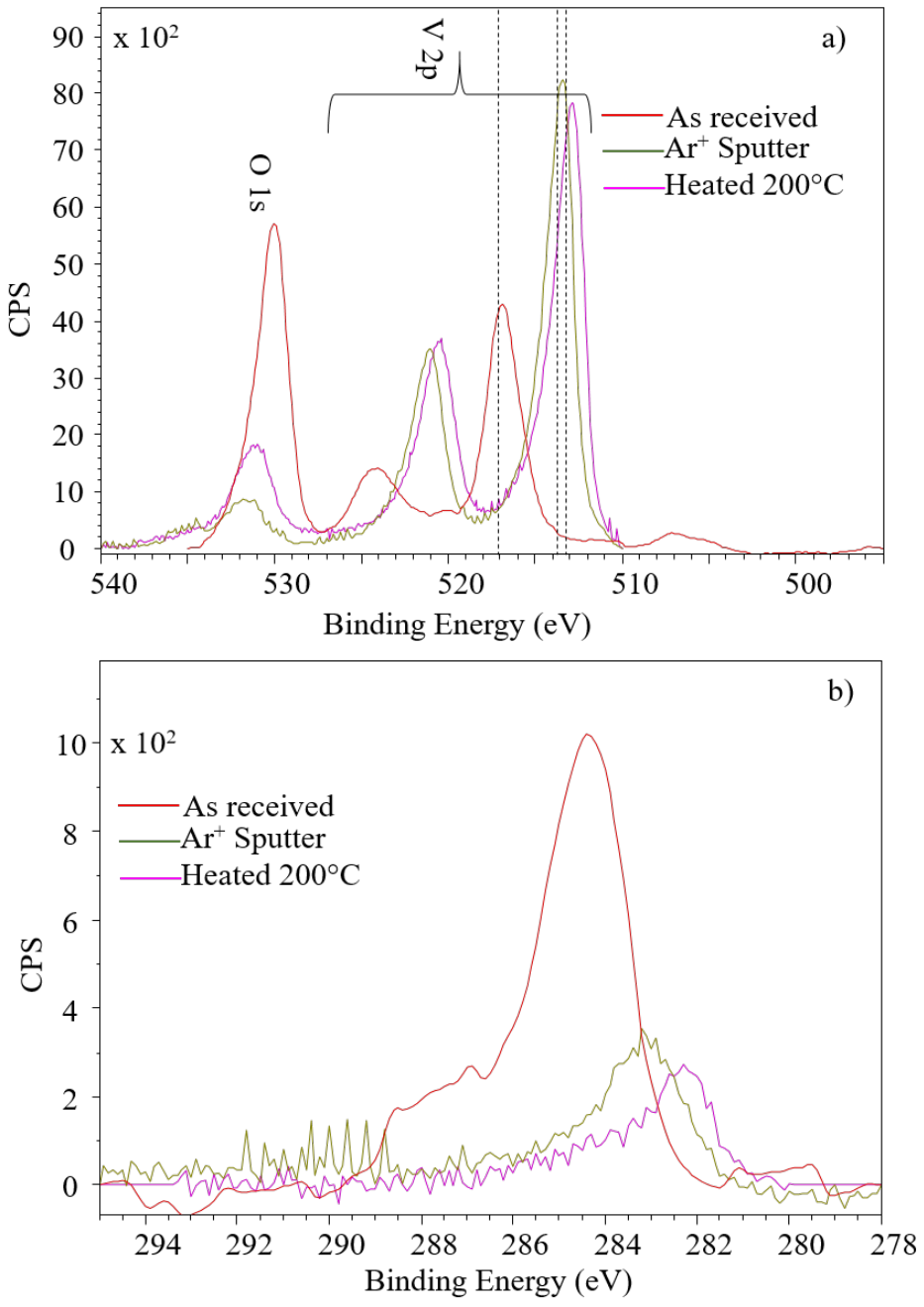


FIGURE 4.10: XPS spectra for bulk polycrystalline vanadium "as-received", $Ar^+$ sputtered and heated to 200°C. a) Overlay of V $2p_{1/2-3/2}$ and O 1s region spectra and b) Overlay of C 1s region spectra.

The "as-received" sample was cut from 99.8 % purity vanadium sheet from Goodfellow. The binding energy of the V $2p_{3/2}$ "as-received", after $Ar^+$ sputtering and after heating to 200°C is 516.8 eV, 513.5 eV and 512.9 eV respectively (see Figure 4.10a).

These shifts to lower binding energies are indicative of the reduction of the surface oxidation of the vanadium sample. "As-received", the position of the V 2p peaks is somewhere in the middle between the expected binding energies for $VO_2$ and $V_2O_5$ [98]. After $Ar^+$ sputtering the sample, the shift in the position of the V 2p peaks correspond to VO. Heating to 200°C results in a further shift to a lower binding energy; however the V 2p peak positions are somewhere in the middle between V metal and VO. The total amount of oxygen detected reduces from 47% "as-received", to 19% after sputtering. However, upon heating the sample, there is an increase up to 24% (see Figure 4.10a) and Table 4.1). A similar phenomenon is observed for the carbon detected on the surface (see Figure 4.10b). The further reduction of the vanadium oxide after heating (as derived from analysis of the V 2p region spectra) and the simultaneous increase in total amount of O 1s and C 1s detected (as shown in the O 1s and C 1s region scans) may be attributed to the outgassing of the chamber with heating. For each of the heated samples (copper, silver and vanadium), trace levels of oxygen or carbon appear on the sample surfaces after heating. Another possible explanation is that the contaminants migrated across the surface from the sample holder.

With respect to QE and WF, there is certainly a correlation between the quantity of surface contaminants and both QE and WF. "As-received", the QE is the least when the surface is dominated by oxides and carbides. Upon sputtering, when the surface is rid of carbonaceous layers and the oxide is reduced, the QE increase by an order of magnitude. Heating the surface produces an increase in oxygen and carbon on the surface, the effect of which is to reduce the QE by half. The WF for clean vanadium according to the literature is 4.3 eV [35]. The "as-received" surface was measured at 5.5 eV: 1.2 eV higher than the expected value for a clean surface, which this was not. As the surface became cleaner after sputter treatment, the WF reduced by 0.5 eV. With the appearance of oxygen and carbon on the surface upon heating, the WF again increases. The cleaner the surface, the lower the WF in the case of this vanadium sample. This is at least in agreement with the theory.

**Zirconium**

Zirconium is a reactive metal and readily forms $ZrO_2$ at ambient conditions [93]. This is observed in the XPS spectrum for the sample "as-received" (see Figure 4.11a)) and correlates with a relatively low QE value. The Zr $3d_{5/2}$ peak is shifted from a binding energy of 182.6 eV "as-received", down to approximately 179.6 eV after argon ion sputtering. The shift to a lower binding energy corresponds to a sub-oxide of zirconium [92]; this yields a QE almost two orders of magnitude greater than "as-received". The QE obtained for the sputtered zirconium is $2.9 \times 10^{-4}$ which is an order of magnitude greater than for copper. As with vanadium, the measured WF is observed to decrease in correlation with the reduction of surface contaminants; again in agreement with theory.

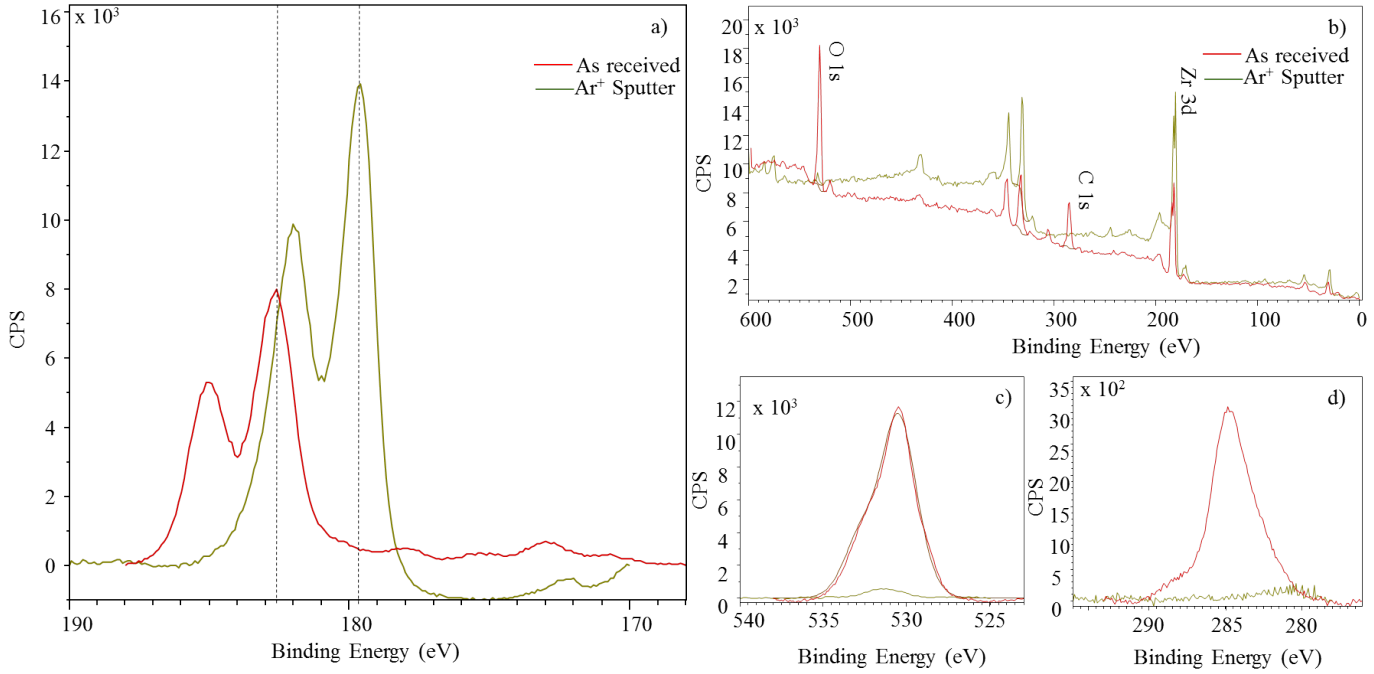


FIGURE 4.11: XPS spectra for bulk polycrystalline zirconium "as-received" and $Ar^+$ sputtered. a) Zr $3d_{3/2-5/2}$ region spectrum "as-received" (red) and $Ar^+$ sputtered (green). b) Overlay of Zr survey spectra with labelled peaks "as-received" and $Ar^+$ sputtered. Overlay of c) O 1s region spectra, and d) C 1s region spectra "as-received" and $Ar^+$ sputtered.

### 4.1.2 Discussion

The aim of this study was to characterise a range of clean metals for consideration as photocathode candidate materials. Despite multiple cycles of $Ar^+$ sputtering, it was not possible to produce a "clean" surface in all ten cases. For silver, copper and lead, only one cycle of sputtering was required to reduce the surface contaminants to trace level. The ease with which the desired surface was achieved is of course an advantage with respect to the preparation of photocathode materials. In the case of other metals such as aluminium and magnesium, the oxide is particularly tenacious and therefore sputtering certainly reduced the oxide but not entirely. Though a clean surface was not always achieved, a correlation between the reduction of surface contaminants and an increase in QE was observed. The highest QE was measured with the sputtered magnesium sample- over two orders of magnitude greater than sputtered copper. Additionally the greatest increase in the QE between the "as-received" and the sputtered surface was observed for the magnesium sample. Can this increase in QE be attributed to the removal of the carbonaceous layer alone? Or is it the reduction of the oxide component and the subsequent increase in the metal component? Of course, magnesium has the lowest WF of the selected metals in this study and therefore a greater proportion of the excited electrons will have sufficient energy to escape the potential barrier than for those metals with higher WF. The next highest QE values came from titanium, zirconium, lead and niobium; all four metals gave a QE that was an order of magnitude higher than copper. These five metals: magnesium, titanium, zirconium, lead, niobium along with copper, for reference, will be subject to further investigation based on their superior electron yield.

There appears to be no trend with respect to changes in the measured WF "as-received" and after sputtering. WF is a measure that is sensitive to surface contaminants, and so a varying value is to be expected during the preparation processes. There is a double layer of charge at the surface of a metal due to the fact that the surface atoms are unbalanced; matter on one side and not on the other [62]. Therefore, any contamination on the surface will modify this double layer and hence the apparent WF. Oxygen and carbon contaminants will be expected to modify the double layer in such a way as to increase the WF. Based on this reasoning, a decrease in WF after sputtering is expected for all samples; for there is a reduction in surface contaminants in each case. However, this may be too idealised a model; it is possible that the oxide/carbide layers "as-received" are so thick that the dipole effect is not significant with respect to WF measurements or phtoemission (photoemission may only be occuring within the contaminant layer). During $Ar^+$ sputtering, the removal of surface layers is not the only physical process occurring. The effect of $Ar^+$ sputtering may also alter the surface morphology of the sample and hence alter the WF [66] as highlighted in Chapter 2. As discussed above, the QE is expected to increase with decreasing WF. Figure 4.12 shows the measured QE against the literature value WF for the ten metals investigated. And Figure 4.13

shows the measured QE plotted against the measured WF for sputtered surfaces. In both cases the expected trend is certainly observed.

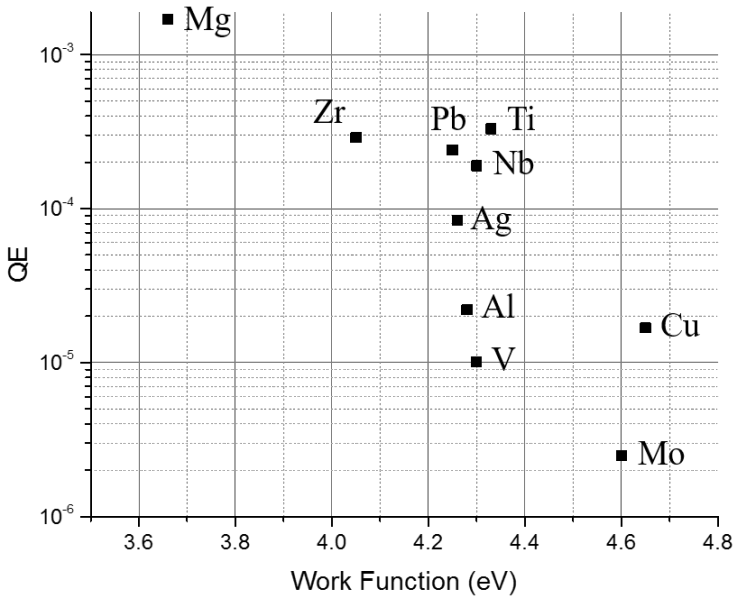


FIGURE 4.12: QE variation for $Ar^+$ sputtered Mg, Nb, Pb, Ti and Zr as a function of literature value WF .

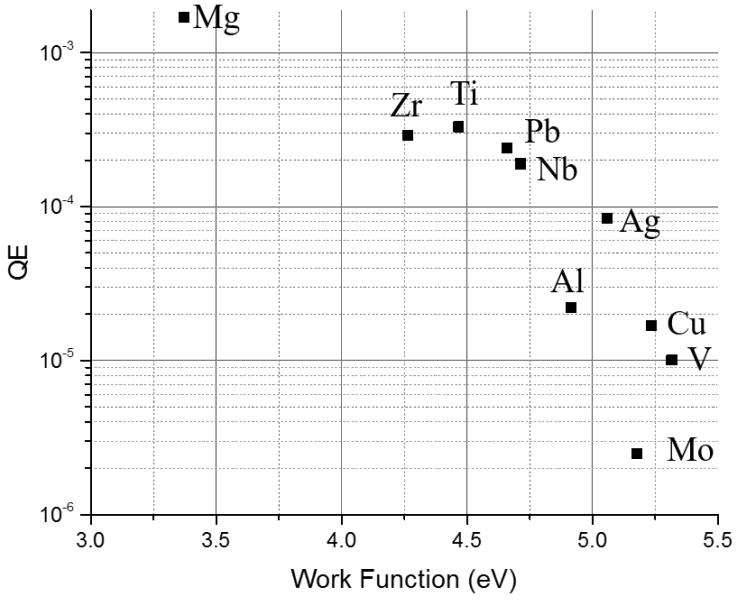


FIGURE 4.13: QE variation for $Ar^+$ sputtered Mg, Nb, Pb, Ti and Zr as a function of measured WF values.

## 4.2 Plasma treatment of bulk metals in ESCALAB

$Ar^+$ sputtering, whilst an effective method for removing surface layers from a metal sample, can have a potentially detrimental effect with respect to the surface morphology. An increase in surface roughness can lead to an increase in intrinsic emittance of the photocathode [69]. Therefore, a surface preparation procedure that does not influence the surface morphology, but still enhances the electron yield is required for real photocathodes used in an accelerator system.

*Ex-situ* oxygen plasma treatment followed by *in-situ* heat treatment is the procedure developed for the preparation of the copper photocathode used in VELA [99]. During *ex-situ* plasma treatment of the copper photocathode, oxygen ions from the plasma react with contaminants on the copper surface, forming volatile reaction products that are subsequently pumped away [99]. For example, oxidised hydrocarbons will react and become CO, $CO_2$, and $H_2O$. Once the surface contaminants are removed, copper oxide is formed through the reaction of oxygen ions with the now hydrocarbon-free copper surface. The plasma treated copper photocathode is subsequently heated in vacuum (*in-situ*), the result of which is to reduce the surface oxide, thus leaving a Cu metal surface finish. The advantages of this procedure are twofold: a) plasma treatment is a chemical process and therefore does not influence the morphology of the photocathode surface [99] and b) the oxide layer produced upon plasma treatment acts as a protective barrier thereby enabling transport of the photocathode in atmosphere prior to installation, without risk of further contamination [99]. In this study the effects of this procedure are investigated for magnesium, niobium, lead, titanium and zirconium (these metals exhibited QE values greater than copper after $Ar^+$ sputtering) and copper for reference. Additionally the substitution for Ar plasma in place of O plasma is investigated for these six metals. The experimental process for these experiments is described below. Both sample and sample holder were placed inside the plasma cleaner for 20 minutes at full power (200 W). The sample and holder were then loaded into the ESCALAB load lock, transferred through the preparation chamber and then into the analysis chamber where XPS, QE and WF measurements were taken. The samples were then transported back into the preparation chamber for heat treatment after which the surface characterisation measurements were repeated.

Prior to taking these measurements, the transition between UV LED and UV LASER was made. For the QE measurements presented in this section, the photocurrent was measured at a fixed laser power of 9.32 mW with the samples biased at -18 V.

For these sets of measurements there has been some misalignment with respect to the sample position and the XPS analyser aperture. The XPS data below would suggest that a portion of the sample holder (made of stainless steel) has also been included in the data collected. Therefore we cannot quantify the elemental composition; however, a qualitative analysis of the metal regions has been used to identify the chemical state of the elements and how they change with plasma treatment and heat treatment.

### 4.2.1 Results

TABLE 4.2: A summary of WF and QE measurements for O plasma / Ar plasma treated and heat treatment for a selection of metals.

| | WF (eV) | QE |
|---|---|---|
| **Cu** | | |
| O plasma | 5.65 | 0 |
| Heated to 250°C 1/2 hr | 5.72 | $1.47 \pm 0.08 \times 10^{-6}$ |
| Ar plasma | 5.40 | $3.3 \pm 0.2 \times 10^{-9}$ |
| Heated to 250°C 1/2 hr | 4.71 | $9.0 \pm 0.5 \times 10^{-7}$ |
| Heated to 250°C 24 hr | 4.66 | $1.26 \pm 0.07 \times 10^{-6}$ |
| **Mg** | | |
| O plasma | 4.40 | $6.1 \pm 0.3 \times 10^{-9}$ |
| Heated to 200°C 1/2 hr | 3.87 | $3.8 \pm 0.2 \times 10^{-7}$ |
| Heated to 200°C 24 hr | 3.63 | $1.11 \pm 0.06 \times 10^{-6}$ |
| Ar plasma | 4.02 | 0 |
| Heated to 200°C 1/2 hr | 4.73 | $1.10 \pm 0.06 \times 10^{-7}$ |
| **Nb** | | |
| O plasma | 5.71 | $8.3 \pm 0.5 \times 10^{-9}$ |
| Heated to 300°C 1/2 hr | 4.51 | $2.1 \pm 0.1 \times 10^{-6}$ |
| Ar plasma | 5.26 | $5.5 \pm 0.3 \times 10^{-10}$ |
| Heated to 300°C | 4.30 | $9.3 \pm 0.5 \times 10^{-7}$ |
| **Pb** | | |
| O plasma | 5.62 | $5.5 \pm 0.3 \times 10^{-9}$ |
| Heated to 200°C 1/2 hr | 4.47 | $2.6 \pm 0.2 \times 10^{-7}$ |
| Ar plasma | 4.91 | $2.0 \pm 0.1 \times 10^{-8}$ |
| Heated to 200°C 1/2 hr | 4.72 | $3.3 \pm 0.2 \times 10^{-7}$ |
| **Ti** | | |
| O plasma | 5.77 | 0 |
| Heated to 250°C 1/2 hr | 4.50 | $1.00 \pm 0.06 \times 10^{-6}$ |
| Heated to 300°C 24 hr | 4.27 | $1.8 \pm 0.1 \times 10^{-6}$ |
| Ar plasma | 5.48 | $5.5 \pm 0.3 \times 10^{-9}$ |
| Heated to 250°C 1/2 hr | 5.04 | $5.8 \pm 0.3 \times 10^{-8}$ |
| **Zr** | | |
| O plasma | 4.94 | $6.1 \pm 0.3 \times 10^{-9}$ |
| Heated to 250°C 1/2 hr | 4.26 | $1.10 \pm 0.06 \times 10^{-6}$ |
| Heated to 300°C 24 hr | 4.80 | $2.2 \pm 0.1 \times 10^{-6}$ |
| Ar plasma | 5.15 | $1.54 \pm 0.09 \times 10^{-8}$ |
| Heated to 250°C 1/2 hr | 5.02 | $1.22 \pm 0.07 \times 10^{-7}$ |

A summary of the QE (using UV LASER) , WF (using Kelvin Probe) and qualitative XPS measurements is presented in Table 4.2.

**Copper**

The survey spectra for the O plasma treated copper surface is shown in Figure 4.14 a): ambient temperature (red) and heated to 250°C (green). The O plasma treated spectrum shows trace levels of carbon; this is significantly less than the "as-received" copper surface (see Figure 4.2). The reduction of hydrocarbon contaminants as a result of the plasma treatment is evidenced by the trace levels of carbon seen in Figure 4.14 a). For both spectra, trace elements of silver, iron and calcium are observed, highlighting the issue afore mentioned; that the misalignment in the sample position with respect to the analyser aperture has resulted in photoelectron spectra collected from both sample and sample holder. Therefore, relevant information with respect to how O/Ar plasma followed by heat treatment influences the surface chemistry can only be gleaned from the metal sample region scans. From the O 1s and C 1s regions in these experiments, it is impossible to differentiate between the oxide associated with the metal sample of interest and the oxide associated with the sample holder metals. The Cu 2p region scans are shown in Figure 4.14 b) and c). The chemical state of the copper is CuO after O plasma treatment; the characteristic shake-up lines that occur at approximately 9 eV higher binding energies than the main Cu 2p peaks are observed in Figure 4.14 b) indicative of CuO. Upon heating, these shake up lines significantly reduce, but do not disappear entirely, suggesting a reduction in CuO. The breadth of the Cu 2p peaks reduce, and the intensity of the peaks increase. Shoulders to the right of both Cu 2p peaks may be indicative of a CuO component. In the case of copper, the region spectra for Cu metal and $Cu_2O$ are identical. Without further information from the O 1s region or the Cu LMM region it is difficult to be certain of the chemical state. Therefore, the effect of heating an O plasma treated copper sample could be a) to produce a predominantly metallic Cu surface with trace elements of CuO or b) predominantly $Cu_2O$ with trace elements of CuO. Either way, the effect of heating has been to reduce the oxide either partly or entirely. With respect to the QE and WF values measured, O plasma treatment produced a surface from which no photocurrent was measured, giving a non-value for QE. Heating the sample and therefore reducing the oxide yielded a QE value of $1.5 \times 10^{-6}$. The WF measurement for this sample was at least 1 eV higher than the literature values for clean Cu metal [35], and did not vary much upon heating.

In the case of Ar plasma treatment followed by heating to 250°C for half an hour, the region scans show comparatively much smaller shake up lines, and not much change in the position of the Cu 2p peaks (see Figure 4.15 b)). There is some change in the intensity of the peaks, but it is not consistent; the $2p_{3/2}$ peak increase in intensity upon heating, whereas the $2p_{1/2}$ peak decreases. Further heating at 250°C for 24 hours, again increases the intensity of the Cu $2p_{3/2}$ peak, indicating an increase in copper detected on the surface.

The Ar plasma treated copper sample gave a QE of $3.3 \times 10^{-9}$. After heating to 250°C for half an hour, the QE improves by two orders of magnitude to $9.0 \times 10^{-7}$. Further heating at 250°C for 24 hours further increased the QE to $1.3 \times 10^{-6}$. Although the XPS data collected shows very little change with respect to the surface composition after heating the Ar plasma treated copper sample, the significant (almost three order of magnitude) improvement in the QE would suggest that a change has occurred. The inability to analyse the O 1s region and the lack of a high resolution Cu LMM scan halts any progress with respect to understanding the bigger picture. Interestingly, the QE for Ar plasma followed by heating is comparable to O plasma followed by heating for the copper samples.

**Magnesium**

Figure 4.16 a) shows the survey spectra for Mg O plasma treated (red), heated to 200°C for half an hour and heated to 200°C for 24 hours (pink). In the case of the Mg 2p region spectra (see Figure 4.16 b)), it is challenging to fit the peaks accurately due to a number of additional peaks from chromium and iron (sample holder materials) which interfere with the peak of interest (Mg 2p). However an attempt at peak fitting has been made. The Mg 2p region spectrum after O plasma treatment is fitted with two peaks indicative of two different chemical states. The more dominant of the fitted peaks corresponds to MgO (70%), and the other to Mg metal (30%). Heating the Mg sample to 200°C for half an hour produces some significant changes to the Mg 2p spectrum. There are perhaps two peaks that could be associated with Mg metal and an oxide occurring at 50.1 eV and 52.6 eV. Additionally, a peak with binding energy 54.5 eV emerges which could be assigned to Fe 3p; this may suggest that with heating either iron species from the sample holder migrated towards the Mg sample, or that with heating the oxide layer covering the sample holder reduces revealing more of the iron beneath. After heating to 200°C for a longer duration, the XPS region scan would suggest that the chemical state of the magnesium is the same as straight after O plasma treatment, but with a greater intensity.

In the case of the Ar plasma treated magnesium sample, the Mg 2p region scan (see Figure 4.17 b)) shows that the chemical state is MgO. Heating to 200°C produces a mixture of MgO (70%) and Mg metal (30%). No photocurrent was measured in the case of the Ar plasma treated surface, yielding a QE of 0. However, heating to 200°C gave a QE of $1.1 \times 10^{-7}$; this is comparable to the heated O plasma Mg sample after half an hour at 200°C.

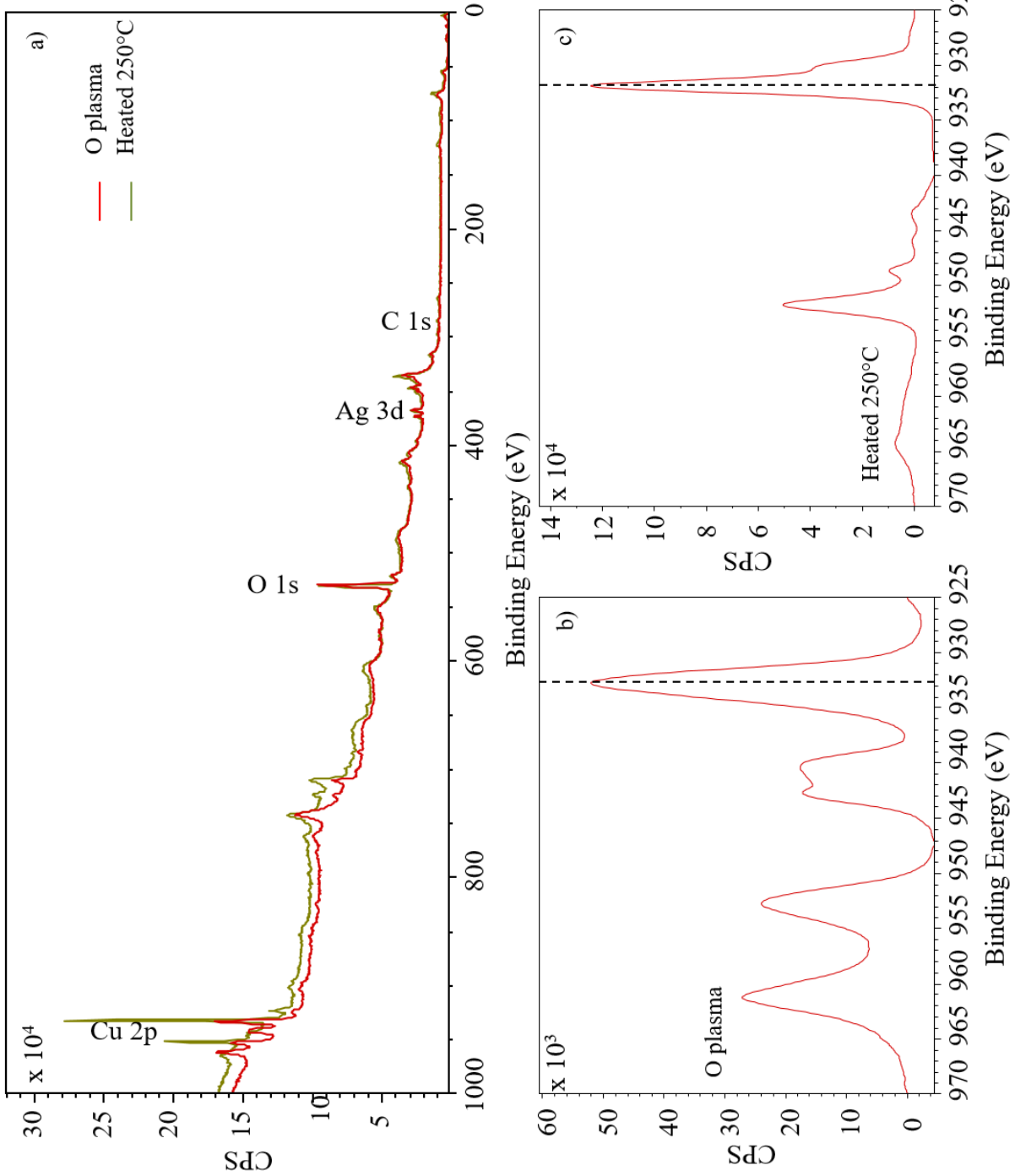


FIGURE 4.14: XPS spectra for bulk polycrystalline copper after O plasma treatment and heating to 250°C for half an hour. a) Overlay of survey scans for O plasma treated and heated to 250°C copper surfaces. Cu 2p region scans for b) O plasma treated surface and c) heated to 250°C.

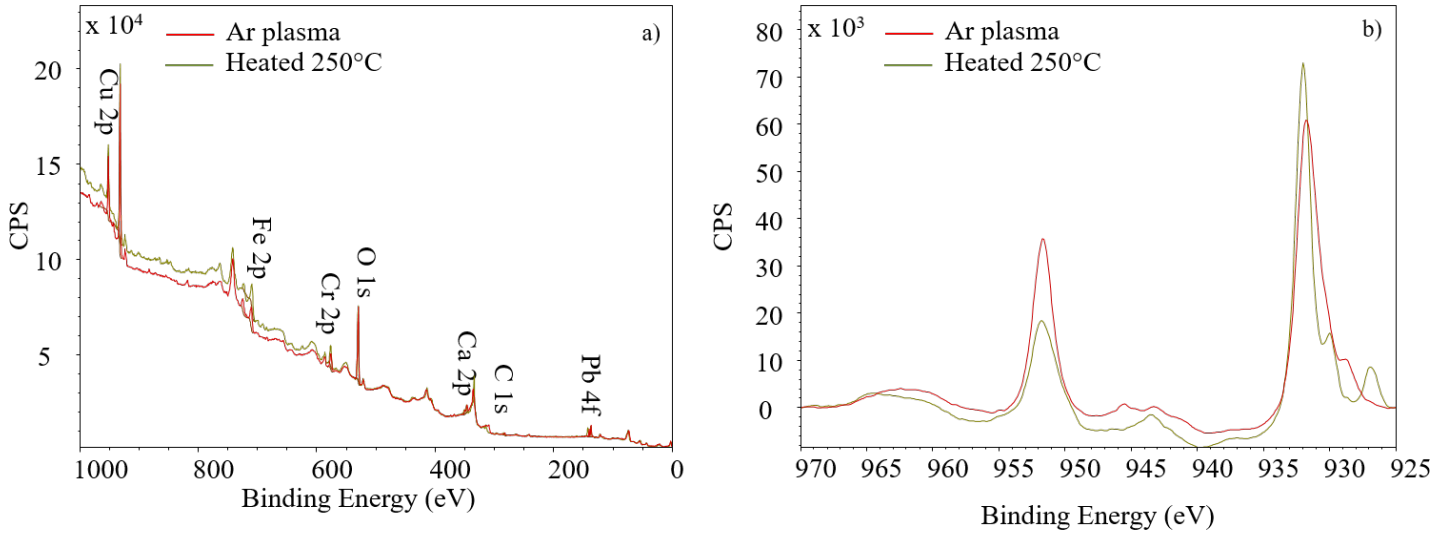


FIGURE 4.15: XPS spectra for bulk polycrystalline copper after Ar plasma treatment and heating to 250°C for half an hour. Overlay of a) survey scans and b) Cu 2p region scans for Ar plasma treated and heated to 250°C copper surfaces.

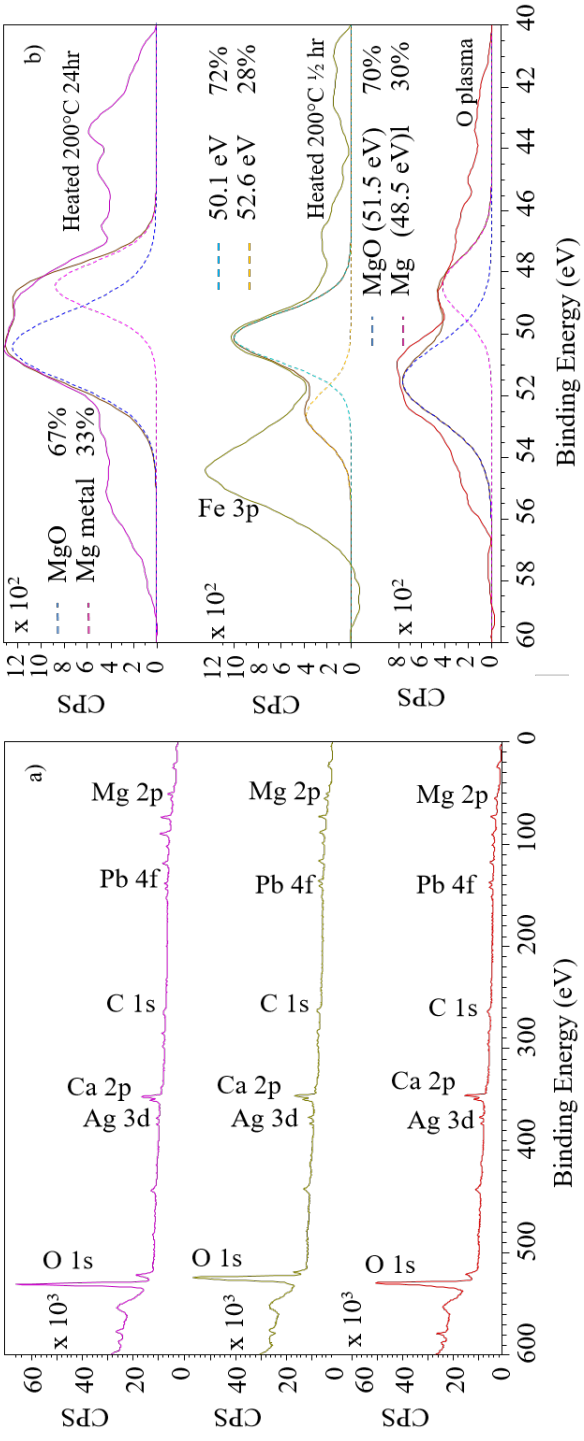


FIGURE 4.16: XPS spectra for bulk polycrystalline magnesium O plasma treated, heated to 200°C for half an hour and heated to 200°C for 24 hours. a) Overlay of survey spectra, and b) stacked Mg 2p region spectra.

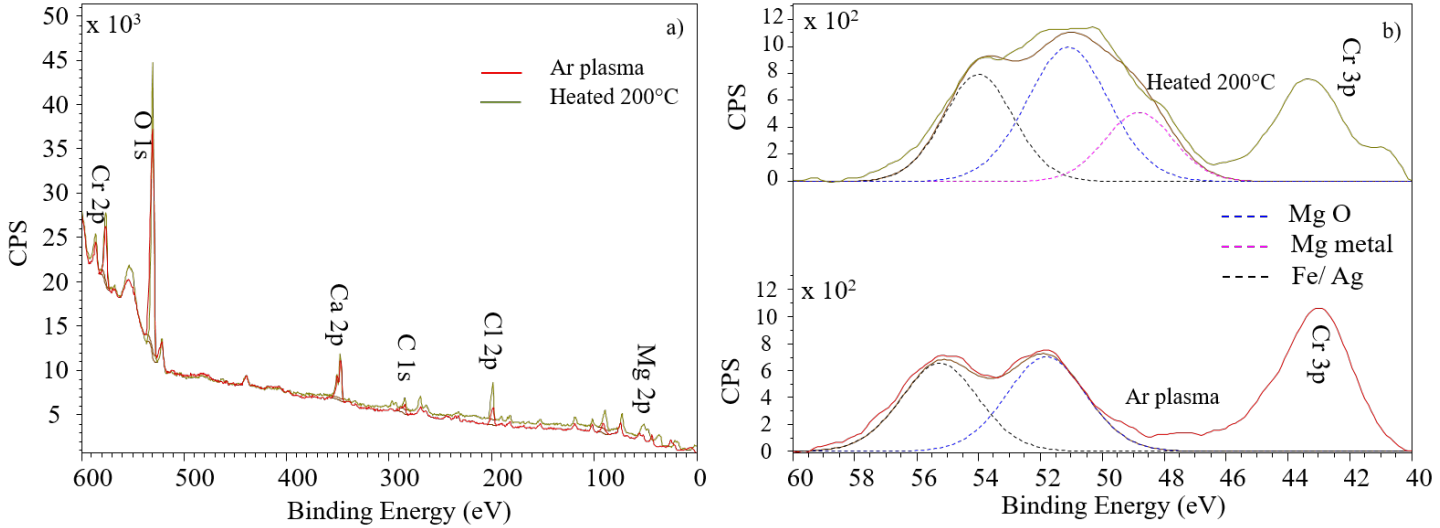


FIGURE 4.17: XPS spectra for bulk polycrystalline magnesium Ar plasma treated and heated to 200°C for half an hour. a) Overlay of survey spectra, and b) stacked Mg 2p region spectra.

**Niobium**

The effect of O plasma is certainly to reduce hydrocarbon contamination; carbon is detected only at trace level in the survey spectrum for the O plasma treated niobium surface (see Figure 4.18 a). The O plasma treated Nb 3d region scan (see Figure 4.18 b)) shows that the Nb 3d peaks have shifted by +4 eV to a higher binding energy compared to Nb metal, corresponding to $NbO_2$. Interestingly this is not the stable oxide formed at atmosphere ($Nb_2O_5$). Upon heating to 300°C, the Nb 3d peaks shift to a lower binding energy suggesting a reduction of the oxide. Figure 4.18 c) shows that the spectrum for the heated niobium surface can be fitted with two sets of peaks corresponding to two chemical states: NbO and Nb metal at 56% and 44% respectively. As with all of the samples investigated, the O plasma treated niobium sample produced a very low QE. However, upon heat treatment, the QE increases by more than two orders of magnitude. There is a correlation between reduction of oxide and increase in QE as found with the $Ar^+$ sputter experiments. With respect to the WF , the O plasma treated niobium has a much larger WF compared with the literature value. The effect of heating appears to reduce the WF to a value closer to the expected value for clean Nb metal. In this case there is a correlation between decreasing WF and reduction of oxide.

The effect of Ar plasma appears to be very similar to O plasma (see Figure 4.19). The Nb 3d region scan after Ar plasma treatment shows that the Nb 3d peak positions are shifted to a higher binding energy corresponding to $NbO_2$ chemical state, as was the case after O plasma treatment. However, the effect of heating produces some divergence between O plasma and Ar plasma treated Nb surfaces. Upon heating the Ar plasma treated Nb sample, the region scan shows that the ratio of Nb metal to NbO is significantly higher than for the O plasma treated Nb sample. There is a three order of magnitude improvement in the QE after heating the Ar plasma treated sample to 300°C. In comparison with the O plasma treated Nb sample, this is marginally lower, but not significantly. The WF for the Ar plasma treated sample is again higher than the literature value, but not as high as the O plasma treated measurement. And upon heating it further reduces to 4.3 eV; a value that is in agreement with the literature [35].

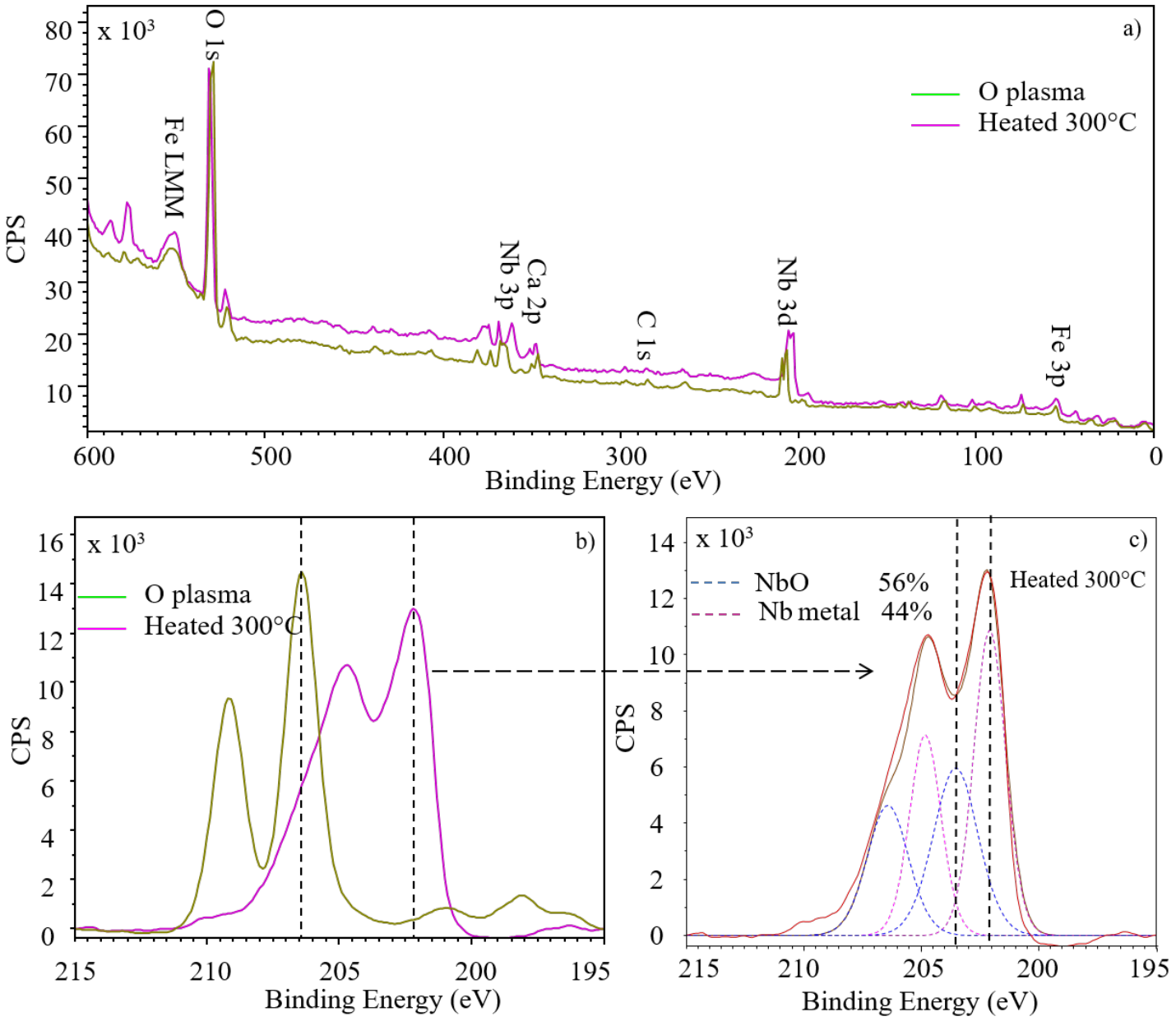


FIGURE 4.18: XPS spectra for bulk polycrystalline niobium O plasma treated and heated to 300°C for half an hour. a) Overlay of survey spectra, b) overlay of Nb 3d region spectra, and c) Nb 3d region spectra after heating to 300°C for half an hour with peak fittings.

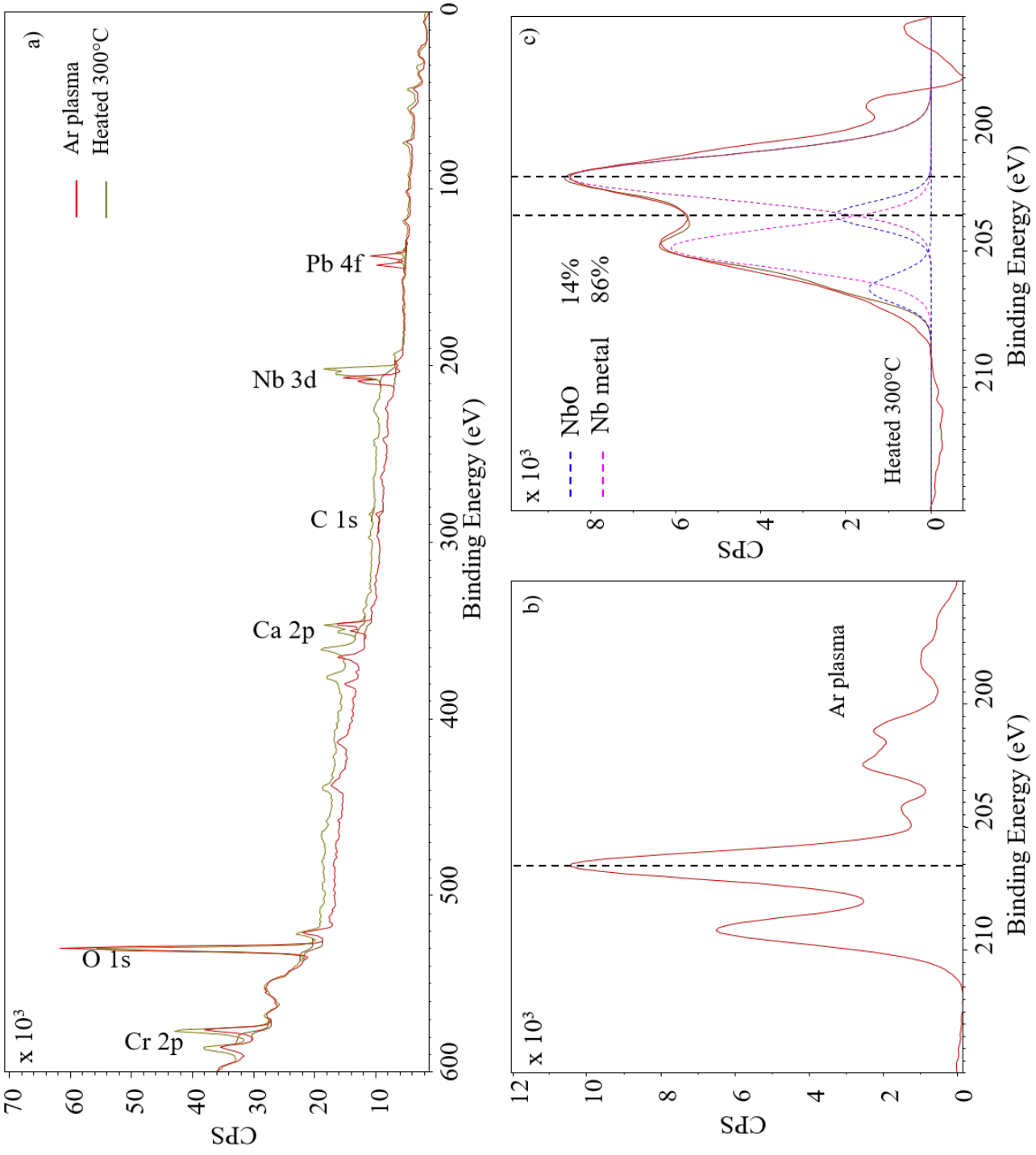


FIGURE 4.19: XPS spectra for bulk polycrystalline niobium Ar plasma treated and heated to 300°C for half an hour. a) Overlay of survey spectra, b) Nb 3d region spectra after Ar plasma treatment and c) Nb 3d region spectra after heating to 300°C for half an hour with peak fittings.

**Lead**

Figure 4.20 b) shows the Pb 4f region scan. After O plasma treatment the Pb $4f_{7/2}$ peak occurs at a binding energy of 137 eV; this corresponds to Pb metal. This is not consistent with the results for the other metals; typically the surface is oxidised as a result of the interaction of the oxygen ions with the lead surface layer. Indeed, after heating the sample, the Pb $4f_{7/2}$ peak shifts by approximately 0.9 eV to a higher binding energy of 137.9 eV indicative of $PbO_2$. The increase in oxide upon heating is rather unusual, and is not in keeping with the results for other metals. The QE for the O plasma treated lead sample was very low, $5.5 \times 10^{-9}$. This improves upon heating by almost two orders of magnitude, to $2.6 \times 10^{-7}$. The WF measurements for the O plasma treated lead is measured to be much higher than clean lead, according to the literature value [35]. The measured WF decreases however upon heat treatment; this is mostly consistent with the other metals. In the case of the Ar plasma treated lead sample, the Pb region scan is fitted with two sets of peaks corresponding to Pb metal (19%) and $PbO_2$ (81%). Unlike the as-received surface which was dominated by $Pb_3O_4$, the Ar plasma treated surface is dominated by a sub-oxide, $PbO_2$. Upon heating, the Pb region spectrum is fitted to show three sets of Pb 4f peaks corresponding to three chemical states. The metal component increases from 19% to 44% after heating. However, alongside that there is an emergence of $Pb_3O_4$ occurring at higher binding energies.

The QE for the Ar plasma treated lead is comparable to the QE calculated for the O plasma treated Pb, before and after heating. The WF for the Ar plasma treated lead is closer to the literature value, and upon heating reduces further bringing it closer still to the value expected for a clean lead surface.

**Titanium**

Figure 4.22 presents the XPS data for the titanium sample after O plasma treatment, post heat treatment to 250°C and further heat treatment to 300°C. The Ti 2p region spectrum shows that the O plasma treated surface is characterised by an intermediate oxide between Ti(III) and Ti(IV); the Ti 2p peaks occur at a binding energy approximately 4 eV higher than the position associated with titanium metal (see Figure 4.22 a). Upon heating first to 250°C, the Ti 2p peaks gain a shoulder. The spectrum is fitted with three sets of Ti 2p peaks suggesting three different chemical states. This fit suggests that upon heating to 250°C there is a break down in the oxide to three distinguishable oxidation states: Ti(IV), Ti(III) and TI(II). Further heating to 300°C produces a shift in the position of the Ti 2p peaks to a lower binding energy, and only one chemical state is observed: Ti(0). The effect of heating the O plasma treated titanium to 250°C was to improve the photocurrent from non-measurable to yielding a QE of $1.0 \times 10^{-6}$. Further heating to a higher temperature improved the QE further by almost a factor of two. As has been the case with the other metals, the O plasma treated metal surfaces always yield a WF value significantly greater than the literature values. This can be

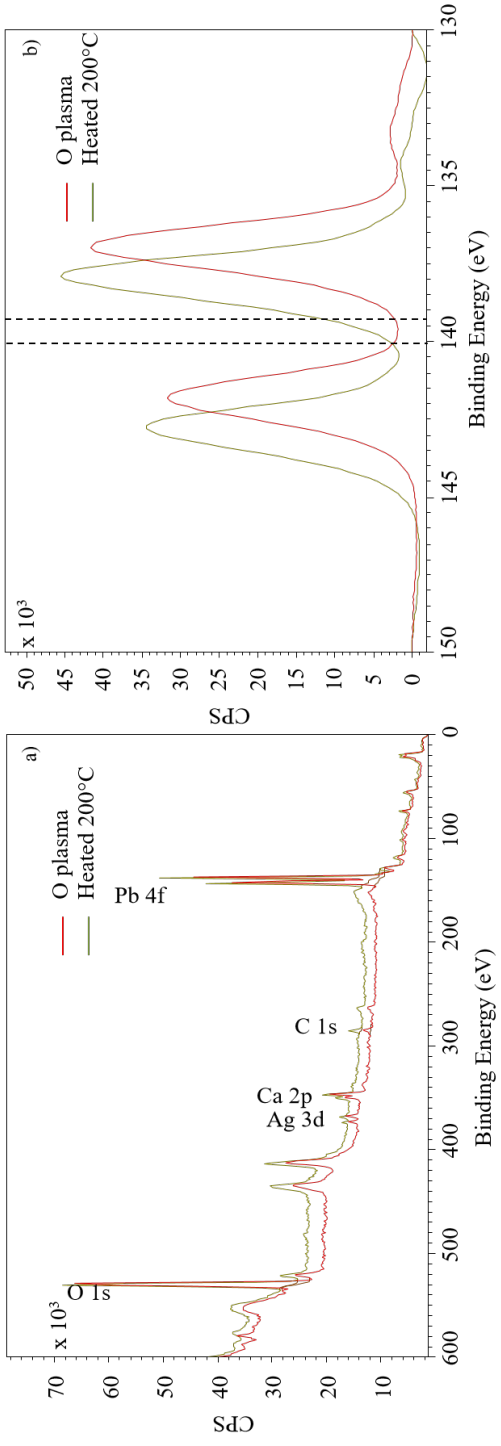


FIGURE 4.20: XPS spectra for bulk polycrystalline lead O plasma treated and heated to 200°C for half an hour. a) Overlay of survey spectra, and b) overlay of Pb 4f region spectra.

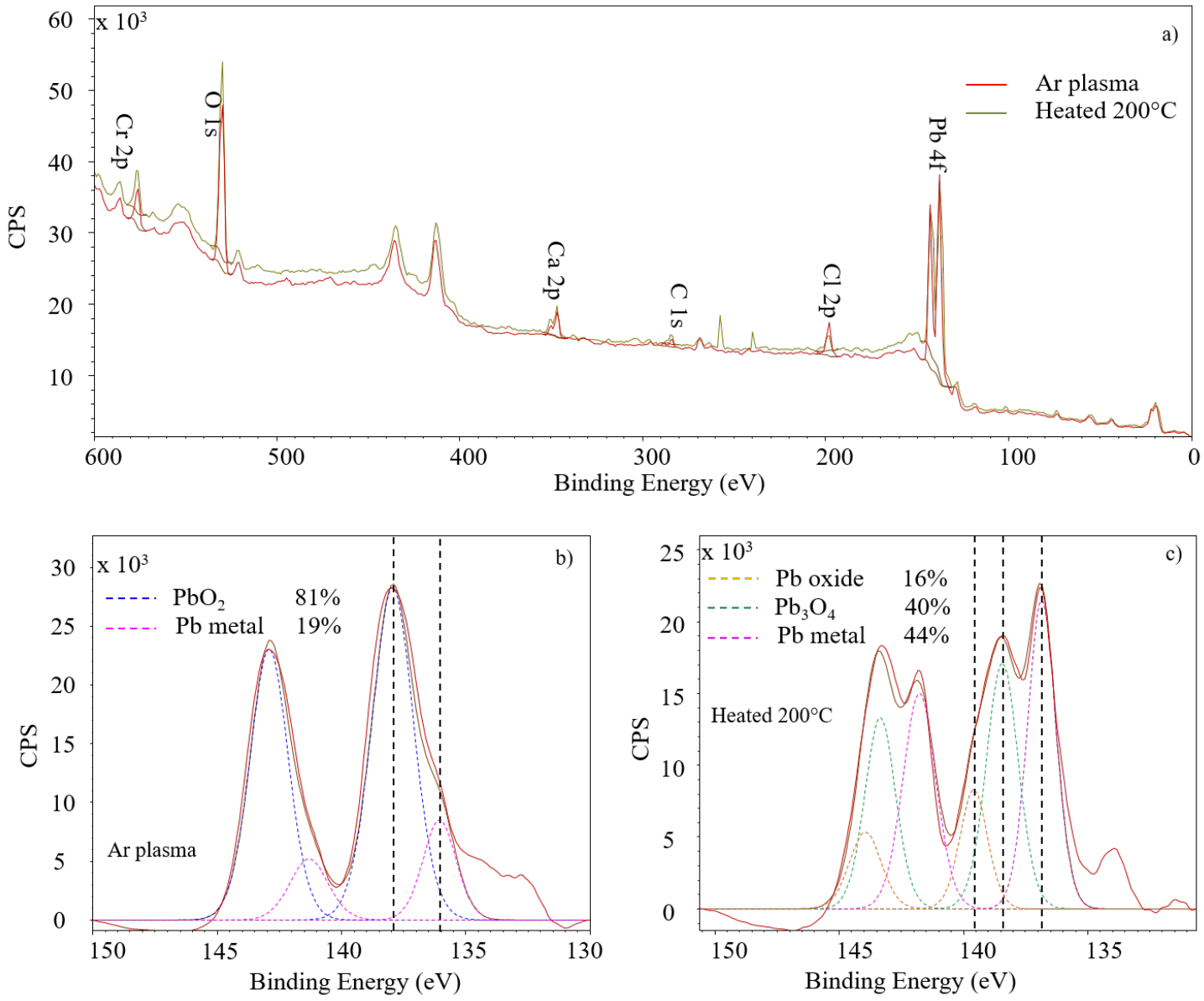


FIGURE 4.21: XPS spectra for bulk polycrystalline lead Ar plasma treated and heated to 200°C for half an hour. a) Overlay of survey spectra, b) Pb 4f region spectrum after Ar plasma treatment with peak fittings and c) Pb 4f region spectrum after heating to 200°C with peak fittings.

accounted for by the oxide layer. Upon heating, the WF decreases, in correlation with the reduction of the oxide.

In the case of the Ar plasma treated titanium sample, the Ti 2p region scan shows the spectrum is fitted with two sets of peaks corresponding to Ti(0) and an oxide between Ti(III)-and TI(IV) at 32% and 68% respectively. This titanium sample was only heated to 250°C, and as with the O plasma treated titanium, upon heating, the effect of this is to produce a mixture of chemical states (see Figure 4.23 c). The dominant chemicals states are between Ti(II)-Ti(III)-Ti(IV). There is also a small percentage of Ti(O). The effect of heating the Ar plasma treated sample was to improve the QE by an order of magnitude from $5.5 \times 10^{-9}$ to $5.8 \times 10^{-8}$. However this is not comparable with the results for O plasma treated titanium. The differences in the QE can be attributed to the variation in the surface chemistry. The WF reduces upon heating, from 5.48 eV to 5.04 eV; this is not as low as the measurement for the O plasma treated titanium sample after heating. In the case of titanium, it would seem that simply reducing the oxide to improve the QE is not enough, otherwise we would see a comparable improvement in the Ar plasma treated sample as the O plasma treated sample.

**Zirconium**

The effect of O plasma treatment on the zirconium sample appears to be to produce a surface layer of $ZrO_2$. This is evidenced in Figure 4.24 b); the Zr $3d_{5/2}$ and Zr $3d_{3/2}$ peaks are shifted up to 182.716 eV and 185.107 eV characteristic of $ZrO_2$. The shift in the position of the Zr 3d peaks to lower binding energies indicate that heating to 250°C reduces the oxide to a mixture of Zr metal and sub-oxides (see Figure 4.24 c)). Further heating to 300°C increases the metal component and reduces the sub-oxides to trace level. With respect to the QE, the O plasma treated surface yields a poor QE of $6.1 \times 10^{-9}$. The QE improves by almost three orders of magnitude with heating, once again showing a correlation between reduction of oxide and improvement in QE. The WF for O plasma treated zirconium is measured to be 4.94 eV. This reduces upon heating to 250°C by approximately 0.7 eV. Further heating actually increases the WF unexpectedly.

Figure 4.25 shows the XPS spectra for an Ar plasma treated zirconium sample. Ar plasma treating zirconium produces a mixture of a sub-oxide and Zr metal at 75% and 25% respectively as shown in Figure 4.25 b). Upon heating, although the metal component increases, $ZrO_2$ emerges. The QE for the heated Ar plasma treated Zr sample is over an order of magnitude less than for the heated O plasma treated zirconium. Additionally the WF measurement is higher for the for the Ar plasma treated zirconium. The differences in the QE and WF may be attributed to the lingering $ZrO_2$ on the surface of the heated Ar plasma treated zirconium as shown in Figure 4.25 c).

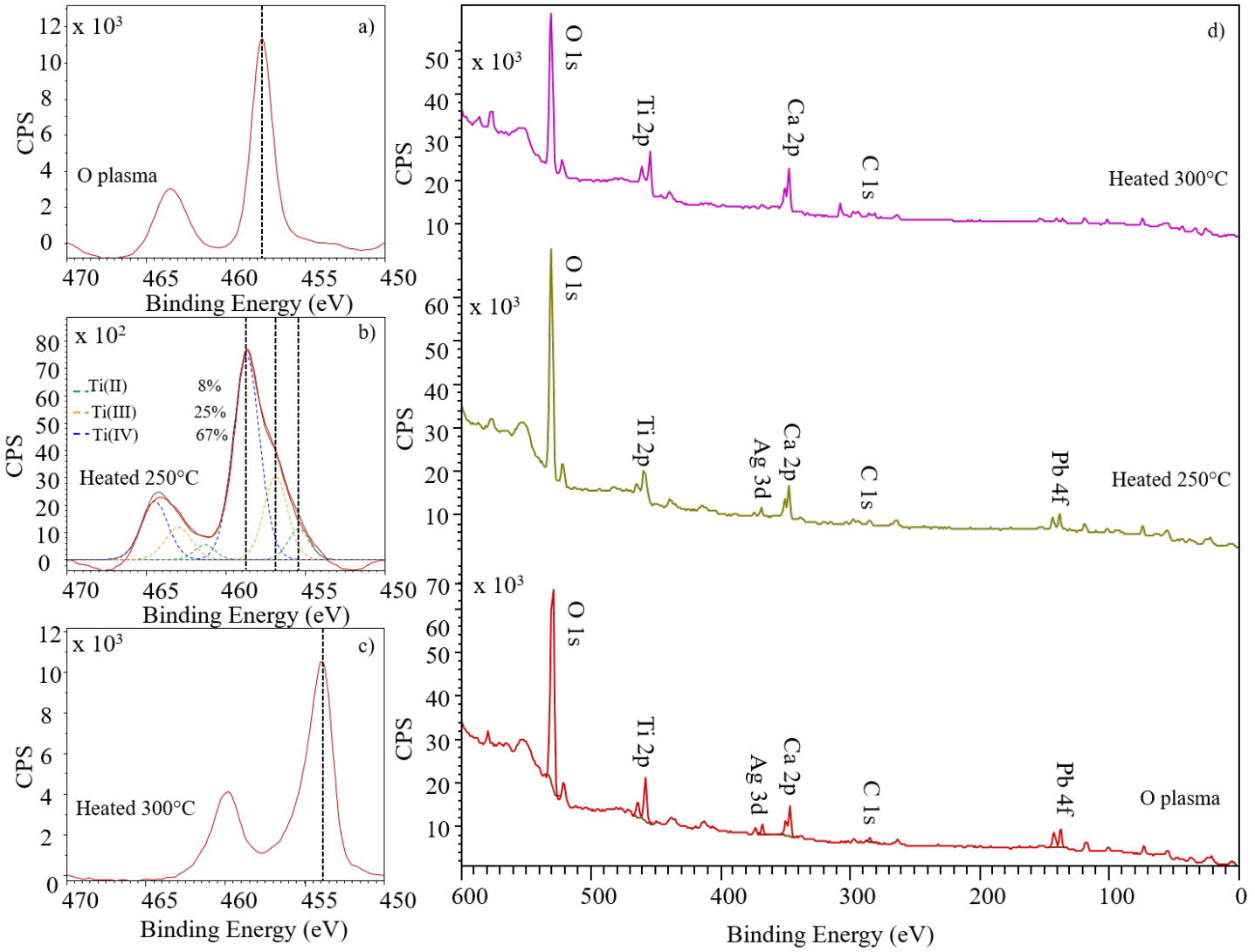


FIGURE 4.22: XPS spectra for bulk polycrystalline titanium O plasma treated, heated to 250°C for half an hour and heated to 300°C for 24 hours. a) Ti 2p region spectrum after O plasma treatment, b) Ti 2p region spectrum after heating to 250°C with peak fittings, c) Ti 2p region spectrum after heating to 300°C and d) stacked survey spectra.

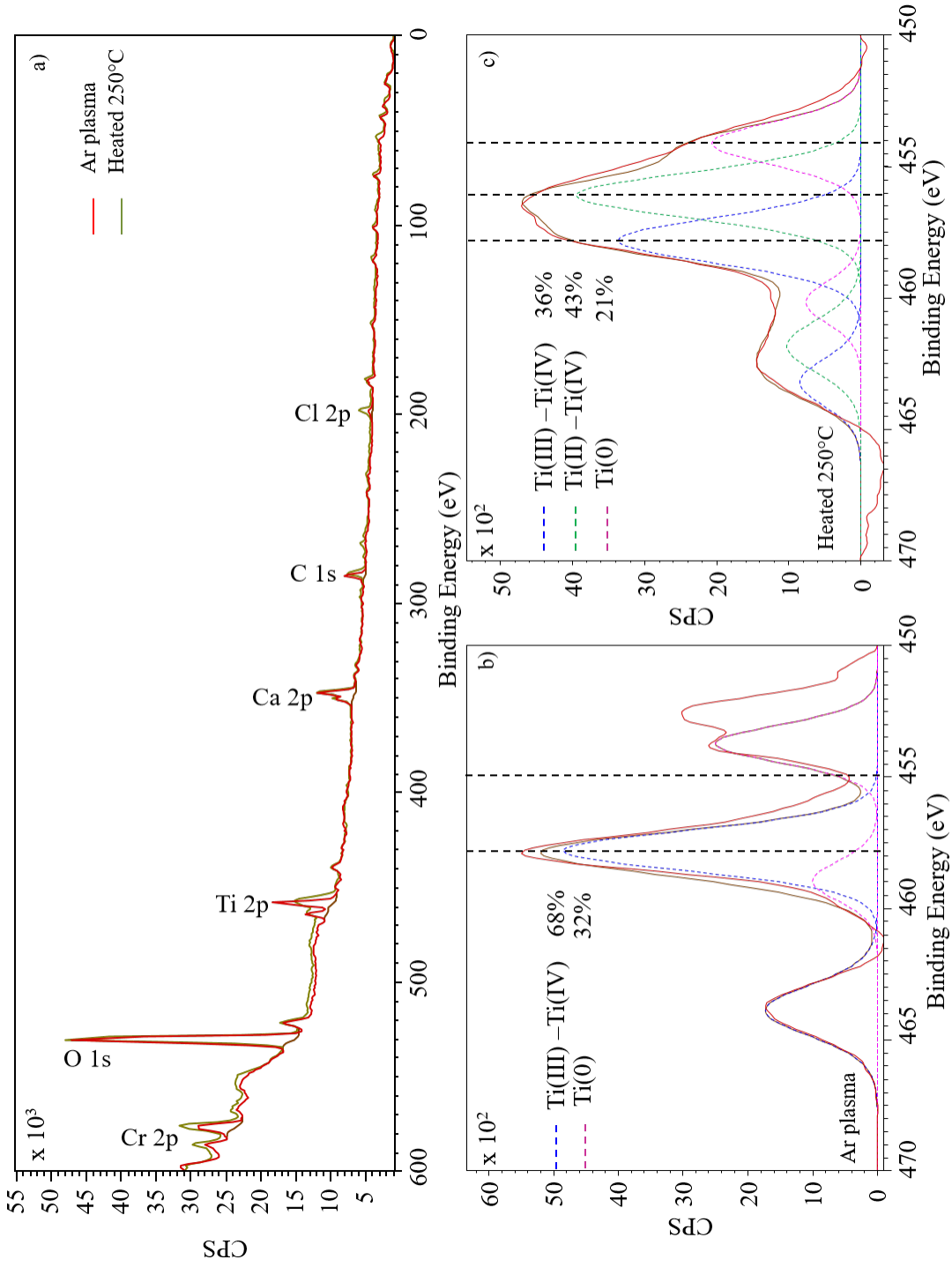


FIGURE 4.23: XPS spectra for bulk polycrystalline titanium Ar plasma treated and heated to 250°C for half an hour. a) Overlay of survey spectra, b) Ti 2p region spectrum after Ar plasma treatment with peak fittings and c) Ti 2p region spectrum after heating to 250°C with peak fittings.

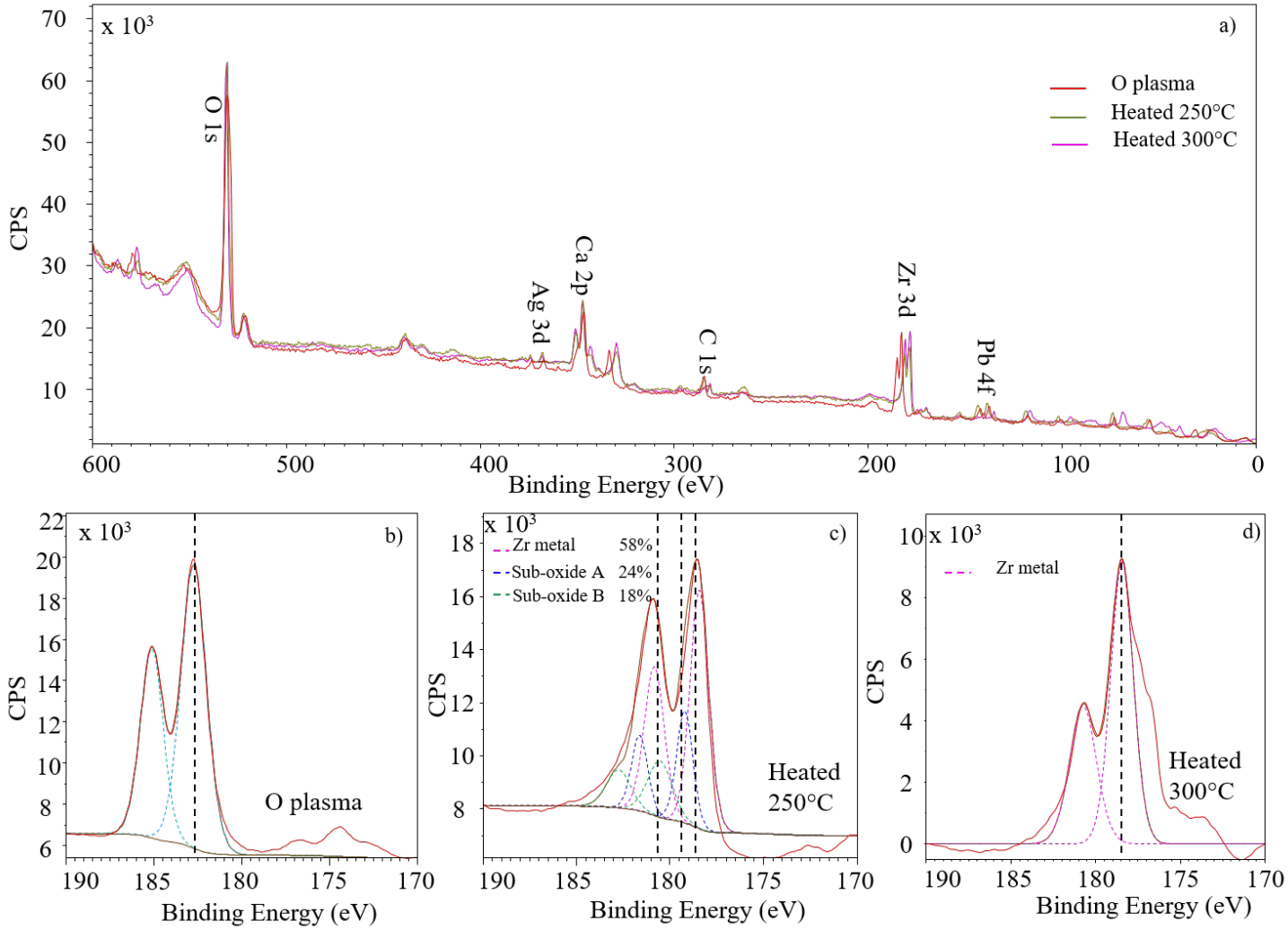


FIGURE 4.24: XPS spectra for bulk polycrystalline zirconium O plasma treated, heated to 250°C for half an and heated to 300°C for 24 hours. a) Overlay of survey spectra, b) Zr 3d region spectrum after O plasma treatment, c) Zr 3d region spectrum after heating to 250°C with peak fittings and c) Zr 3d region spectrum after heating to 300°C .

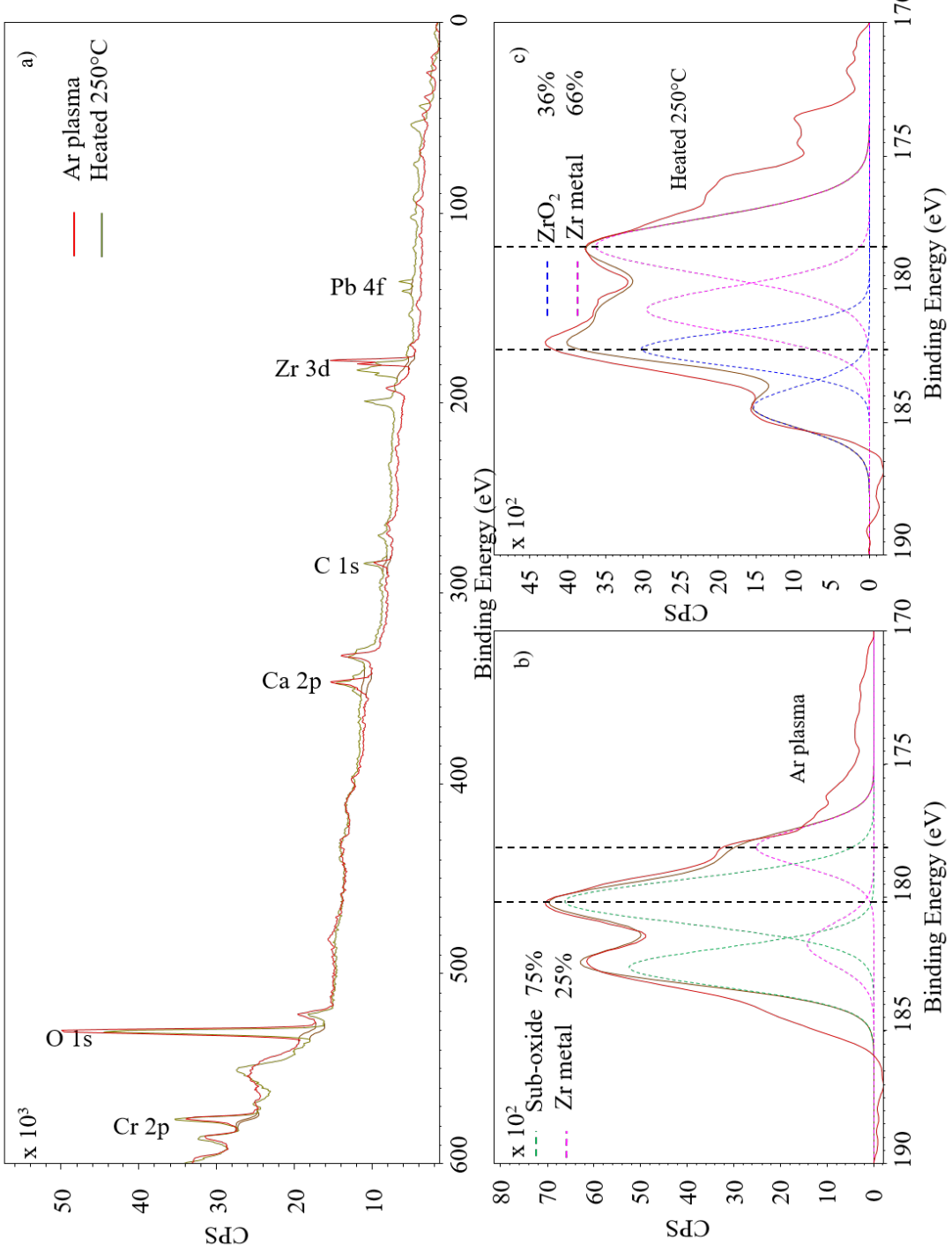


FIGURE 4.25: XPS spectra for bulk polycrystalline zirconium Ar plasma treated and heated to 250°C for half an hour. a) Overlay of survey spectra, b) Zr 3d region spectrum after Ar plasma treatment with peak fittings and c) Zr 3d region spectrum after heating to 250°C with peak fittings.

### 4.2.2 Discussion of the effects of plasma cleaning

The QE for the plasma treated metals are very low ranging between 0-$10^{-6}$. It is interesting to note that despite the removal of hydrocarbon contaminants, the surface continues to yield little to no photocurrent. Generally, heating the plasma treated samples produced an improvement in the QE; this correlates with a reduction in the oxide. In the case of copper, niobium and lead, the QE achieved after heating both the Ar plasma and O plasma treated samples is comparable. However, for magnesium, titanium and zirconium, the O plasma treated samples gave a QE at least an order of magnitude greater than the Ar plasma treated samples. With respect to WF measurements, there is some divergence in the results for O plasma and Ar plasma treated samples. In all cases except for zirconium, the measured WF is greater for the O plasma treated sample compared with the Ar plasma treated sample. Compared with the WF measurements "as-received", the O/Ar plasma treated metals yielded higher values in each case. These higher WF values correlate with low QE as expected. XPS survey spectra and C 1s regions show that the effect of the plasma treatments is indeed to reduce the carbon to trace level. This is true for each metal investigated. From analysis of the metal region scans, the data shows that the O plasma treatment of metals produces a surface metal oxide which upon heating is reduced. A similar effect takes place for the Ar plasma treated samples. For the most part however, the oxide layer appears to be less thick in the case of the Ar plasma treated samples. This is because for most of the metals, the effect of heating produces a greater percentage of metal in the case of the Ar plasma treated samples. However, as previously mentioned, the exact effects of plasma treatment cannot be known from this study alone due to misalignment of the sample.

## 4.3 Medium Energy Ion Scattering of plasma treated bulk copper

As discussed in the previous section, the procedure of *ex-situ* oxygen plasma treatment followed by *in-situ* heat treatment has been developed for the preparation of copper photocathodes utilised in VELA. It has been reported that this preparation procedure allows for a QE of $10^{-5}$ to be achieved [99]. XPS analysis shows oxygen plasma treatment produces a thin oxide layer which upon annealing is reduced. There is little understanding of how the cleaning procedure leads to the required surface properties for electron emission. In this section a detailed study of the effects of plasma treatment on copper surfaces is described.

### 4.3.1 Results and discussion

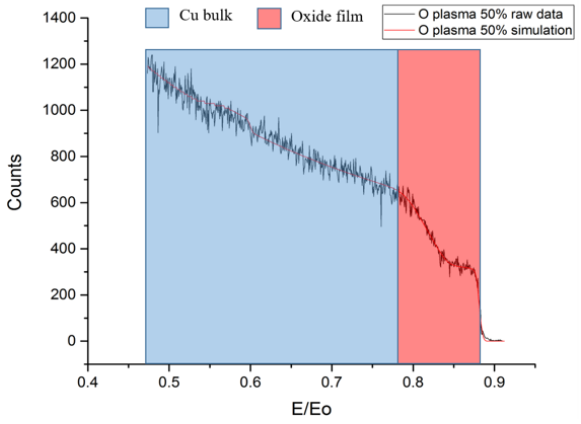


FIGURE 4.26: Energy spectrum of 100 keV $He^+$ backscattered from O plasma (50% power) treated copper surface.

The four layer model used to fit the energy spectra is shown in Figure 4.26 along side the energy spectrum from an O plasma (50% power) treated copper surface. The fitting procedure is outlined in Chapter 3. The region highlighted in pink on the energy spectrum corresponds to the oxide film (Layers 1, 2 and 3) and the region highlighted in blue corresponds to the copper bulk. The effect of different surface treatments, such as oxygen plasma cleaning, is to alter the surface chemistry and composition; these changes are most notable in the surface regions (pink) of the energy spectra. This is evident in the spectra shown in Figure 4.27. In this plot, the energy spectra from an "as received", O plasma treated (50% plasma power) and $Ar^+$ sputtered copper surface are overlaid and compared. The energy spectrum obtained for the $Ar^+$ sputtered copper surface (green) is characteristic of pure copper; it is evident from Figure 4.27 that the simulation for pure copper is in good agreement with the raw data. If we compare the energy spectrum of the $Ar^+$ sputtered copper with that of the oxygen plasma treated copper, one observes that the main difference lies in the surface regions (between $E/E_0$ = 0.8 and 0.88). This spectrum has been fitted using a simulation of an oxidised copper surface. A quantification of the thickness and composition of the oxygen plasma treated copper sample is shown in Table 4.3. The units for the thickness is calculated in atoms per unit area (Atoms/$cm^2$). Dividing by the atoms per unit volume (Atoms/$cm^3$) provides a more useful unit of length. As a rough approximation $10 \times 10^{15}$Atoms/$cm^2$ is equivalent to approximately 100 nm.

Interestingly, the ratio of copper to oxygen in layers 1 and 2 corresponds to $CuO_2$. Though this is certainly not a common oxide of copper, it is not unheard of for $CuO_2$ to form in certain specific conditions [100]. The simulation for CuO presented in figure 4.29 shows that this fit is not appropriate for this spectrum. Deeper into the oxide layer (layer 3) the copper content increases and the oxygen is reduced; the ratio of copper to

oxygen becomes closer to 2:1. This is indicative of $Cu_2O$. Between layers 3 and 4, the oxygen content gradually reduces until only pure copper is present.

In the case of the energy spectra for as received Cu, once again the principal difference occurs at the surface. The surface region has been simulated with a layer of hydrocarbons and organic contaminants (see Table 4.3). Below this contamination the energy spectra is fitted with an inter-facial layer of $Cu_2O$. The data clearly demonstrates that the effect of O plasma treatment is to remove the hydrocarbon contamination; this is in agreement with the conclusions drawn from XPS studies.

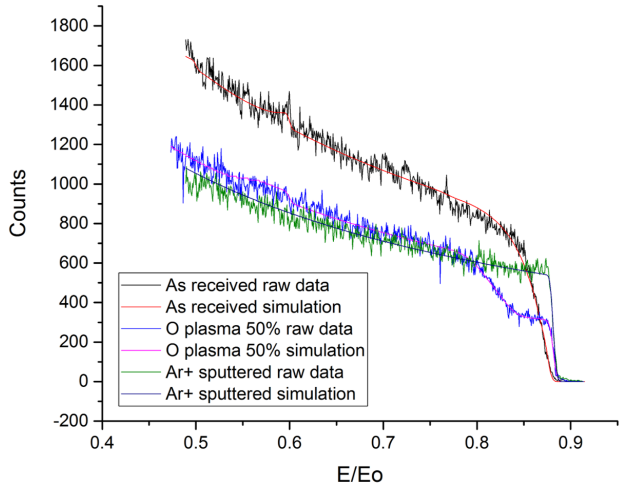


FIGURE 4.27: A comparison of the energy spectra of 100 keV $He^+$ ions backscattered from copper surfaces "as received", O plasma (50% power) treated and $Ar^+$ sputtered with associated simulated data fits. Energy spectra from O plasma (50% power) treated copper fitted with a) a simulation corresponding to $CuO_2$ surface layers.

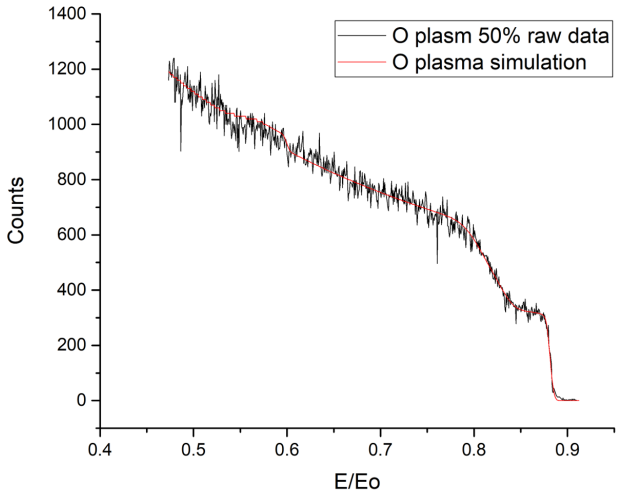


FIGURE 4.28: Energy spectra from O plasma (50% power) treated copper fitted with a simulation corresponding to $CuO_2$ surface layers.

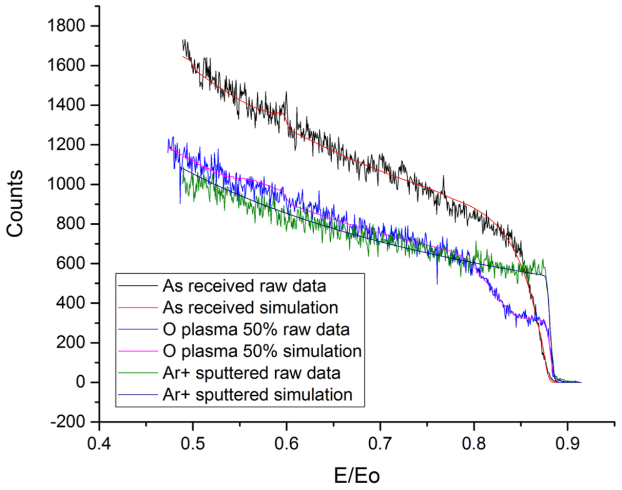


FIGURE 4.29: Energy spectra from O plasma (50% power) treated copper fitted with a simulation corresponding to CuO surface layers.

TABLE 4.3: Quantitative data for fractional composition and thickness of Cu layers as-received, O plasma treated (50%) and $Ar^+$ sputtered.

| | Depth ($10^{15}$ At/cm$^2$) | Cu | O | C |
|---|---|---|---|---|
| **As-received** | | | | |
| Layer 1 | 42.21 | 0 | 0.54 | 0.46 |
| Layer 2 | 8.23 | 0.71 | 0.29 | 0 |
| Layer 3 | 1200 | 1 | 0 | 0 |
| **50% O plasma** | | | | |
| Layer 1 | 10 | 0.38 | 0.62 | |
| Layer 2 | 70.49 | 0.39 | 0.61 | |
| Layer 3 | 32.52 | 0.68 | 0.32 | |
| Layer 4 | 1200 | 1 | 0 | |
| **$Ar^+$ Sputtered** | | | | |
| Layer 1 | 10 | 1.0 | 0 | |
| Layer 2 | 1000 | 1.0 | 0 | |

The two parameters which can be varied for the plasma treatment are the power level and the treatment time. The results from these studies are presented in the sections below.

**Effects of variable plasma power on copper surface layers**

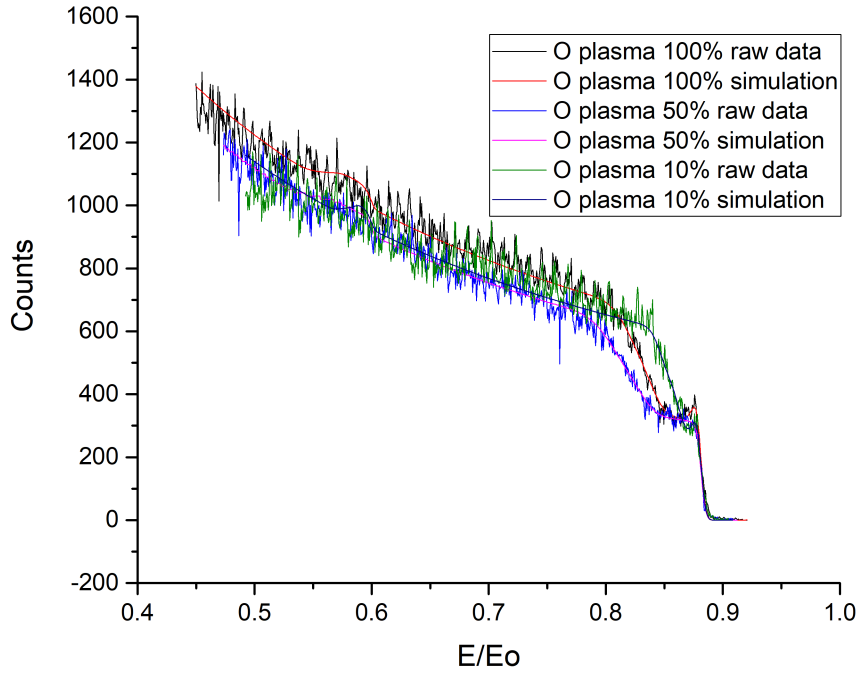


FIGURE 4.30: Energy spectra of 100 keV $He^+$ backscattered from O plasma (100%, 50%, 10% power) treated copper surfaces and associated simulations.

The effects of varying plasma power on the composition depth profile of copper samples was investigated by applying power levels between 10 and 100 % to five copper samples. Each sample was plasma treated for a fixed time duration of 20 minutes. The energy spectrum from each surface was collected and analysed after plasma treatment and after *in-situ* heating to 300°C.

A comparison of the energy spectra for copper samples with variable O plasma power exposure (100, 50 and 10%) is presented in Figure 4.30. From inspecting the spectra alone, it is evident that varying plasma power is most impacting on the surface regions. To assess this in finer detail a quantification of the composition and thickness of the surface layers obtained from the simulations for plasma treated and post heated copper is shown in Table 4.4.

TABLE 4.4: Quantitative data for fractional composition and thickness of copper surface layers as a function of O plasma power after O plasma treatment and post heating to 300°C.

| | O plasma treated | | | Heated to 300°C | | |
|---|---|---|---|---|---|---|
| | Depth ($10^{15}$ At/cm$^2$) | Cu | O | Depth ($10^{15}$ At/cm$^2$) | Cu | O |
| **100% Power** | | | | | | |
| Layer 1 | 10 | 0.48 | 0.52 | 10 | 0.43 | 0.57 |
| Layer 2 | 55.57 | 0.36 | 0.64 | 54.77 | 0.41 | 0.59 |
| Layer 3 | 26.56 | 0.68 | 0.32 | 36.48 | 0.64 | 0.36 |
| **75% Power** | | | | | | |
| Layer 1 | 10 | 0.39 | 0.61 | 10 | 0.52 | 0.48 |
| Layer 2 | 55.43 | 0.36 | 0.64 | 42.39 | 0.42 | 0.58 |
| Layer 3 | 34.38 | 0.70 | 0.30 | 45.85 | 0.73 | 0.27 |
| **50% Power** | | | | | | |
| Layer 1 | 10 | 0.38 | 0.62 | 10 | 0.47 | 0.53 |
| Layer 2 | 70.49 | 0.39 | 0.61 | 72.78 | 0.53 | 0.47 |
| Layer 3 | 32.52 | 0.68 | 0.32 | 25.88 | 0.75 | 0.25 |
| **25% Power** | | | | | | |
| Layer 1 | 10 | 0.35 | 0.65 | 10 | 0.39 | 0.61 |
| Layer 2 | 37.2 | 0.32 | 0.68 | 26.52 | 0.36 | 0.64 |
| Layer 3 | 22.93 | 0.71 | 0.29 | 27.79 | 0.60 | 0.40 |
| **10% Power** | | | | | | |
| Layer 1 | 10 | 0.44 | 0.56 | 10 | 0.68 | 0.32 |
| Layer 2 | 19.41 | 0.31 | 0.69 | 33.61 | 0.56 | 0.44 |
| Layer 3 | 20.15 | 0.61 | 0.39 | 15.12 | 0.78 | 0.22 |

The relationship between the plasma power applied to the Cu sample and the thickness of the resulting oxide is evaluated in the plots shown in Figure 4.31. In Figure 4.31 (a) the total thickness of the oxide layer (layer 1 + 2 + 3) is plotted against the plasma power used to treat the samples. For plasma powers up to 50%, the oxide layer increases as a function of plasma power. However, subsequent data points corresponding to 75% and 100% plasma power show a reduction in the thickness of the oxide layer. This is contrary to our expectations. By varying the plasma power, the voltage supplied to the electrode can be altered to either increase or decrease the ionising potential of the oxygen gas; this in turn will impact the rate at which oxygen ions will react with the sample surface and therefore should determine the thickness of the oxide layer formation. This inconsistency in the effect of increasing plasma power on the thickness of the resulting oxide layer suggests that there is a plasma density inhomogeneity at higher power settings.

It is interesting to note that post heating to 300°C produced insignificant changes in the

overall thickness of the oxide layer. Consider the effects of plasma power on the thickness of layers 2 and 3 separately. The correlation between plasma power and the thickness of layer 2 again shows a peak in thickness at 50% oxygen plasma power, after which a reduction in thickness is observed (see Figure 4.31 (b). In the case of the interface layer (layer 3) the thickness increases more gradually with increasing plasma power, peaking at 75% and then reducing at 100%. It is not surprising that the interfacial layer should not suffer significant change with variable plasma power, as the increasing plasma power is more likely to alter the surface layers (layer 1 and 2).

The effects of changing plasma power on the fractional composition of copper and oxygen is presented in Figures 4.32. In Layer 1 (see Figure 4.32 (a) and d)), the copper content is between 35% and 50%, and the oxygen content is between 50% and 65%; this corresponds to the stoichiometry for $CuO_2$ and CuO respectively. In the case of layer 2, (see Figure 4.32 (b) and (e)) the content of copper and oxygen are typically 35% and 65% respectively; this is indicative of the stoichiometry for $CuO_2$. The content of copper and oxygen at layer 3 is close to 66% and 33% respectively, close to the ideal stoichiometry for $Cu_2O$. Varying the plasma power has some effect on the fractional composition, however it is difficult to identify a clear trend. Upon heating the samples to 300°C however, some patterns begin to emerge. For example, after plasma treatment at 10% power, the stoichiometry within layer 1 was initially closer to CuO, whereas upon heating, the composition becomes closer to $Cu_2O$. A similar change is observed in layers 2 and 3. The overall reduction in the oxide, and increase in copper content is most significant for the 10% plasma power treated copper sample. This is perhaps to be expected, as the oxide formed at 10% plasma power is not very thick, and therefore the reduction in the oxide brought about by heating to 300°C is more apparent than in the case for thicker oxides.

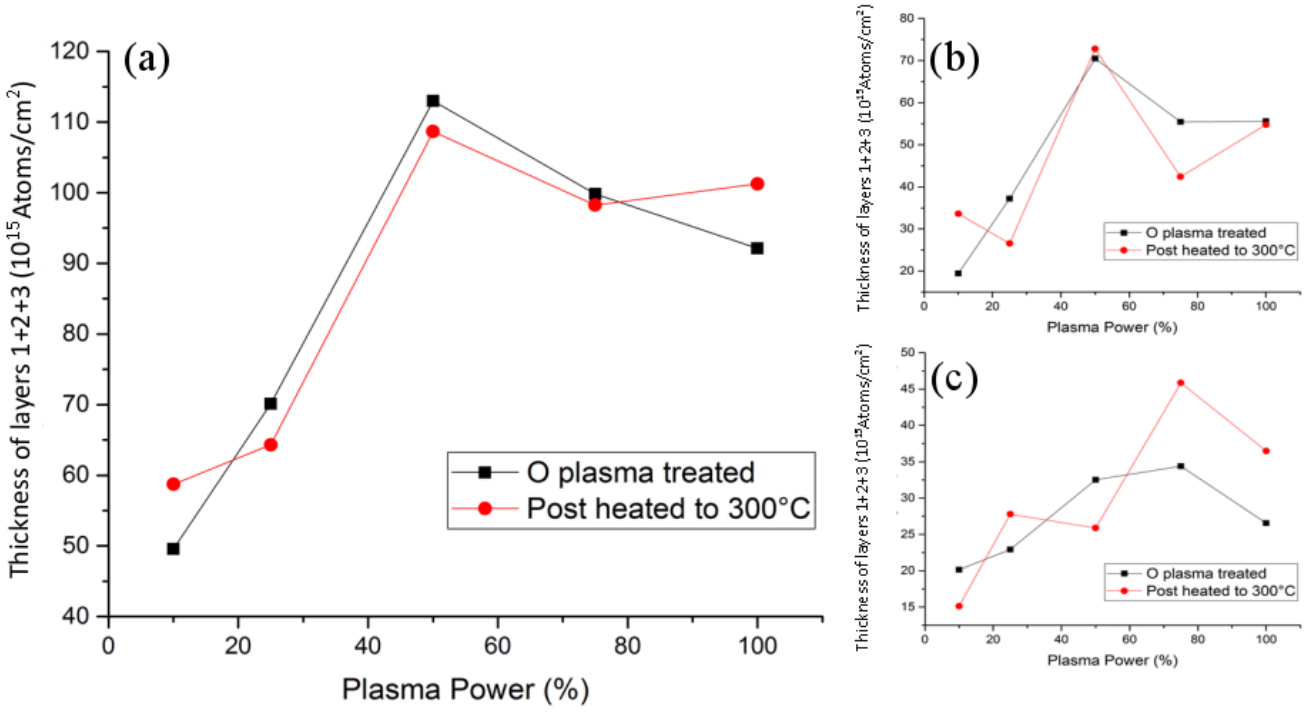


FIGURE 4.31: a) Thickness of layers 1 + 2 + 3 b) layer 2 and c) layer 3, as a function of the plasma power applied to the copper samples at room temperature and after heating to 300°C.

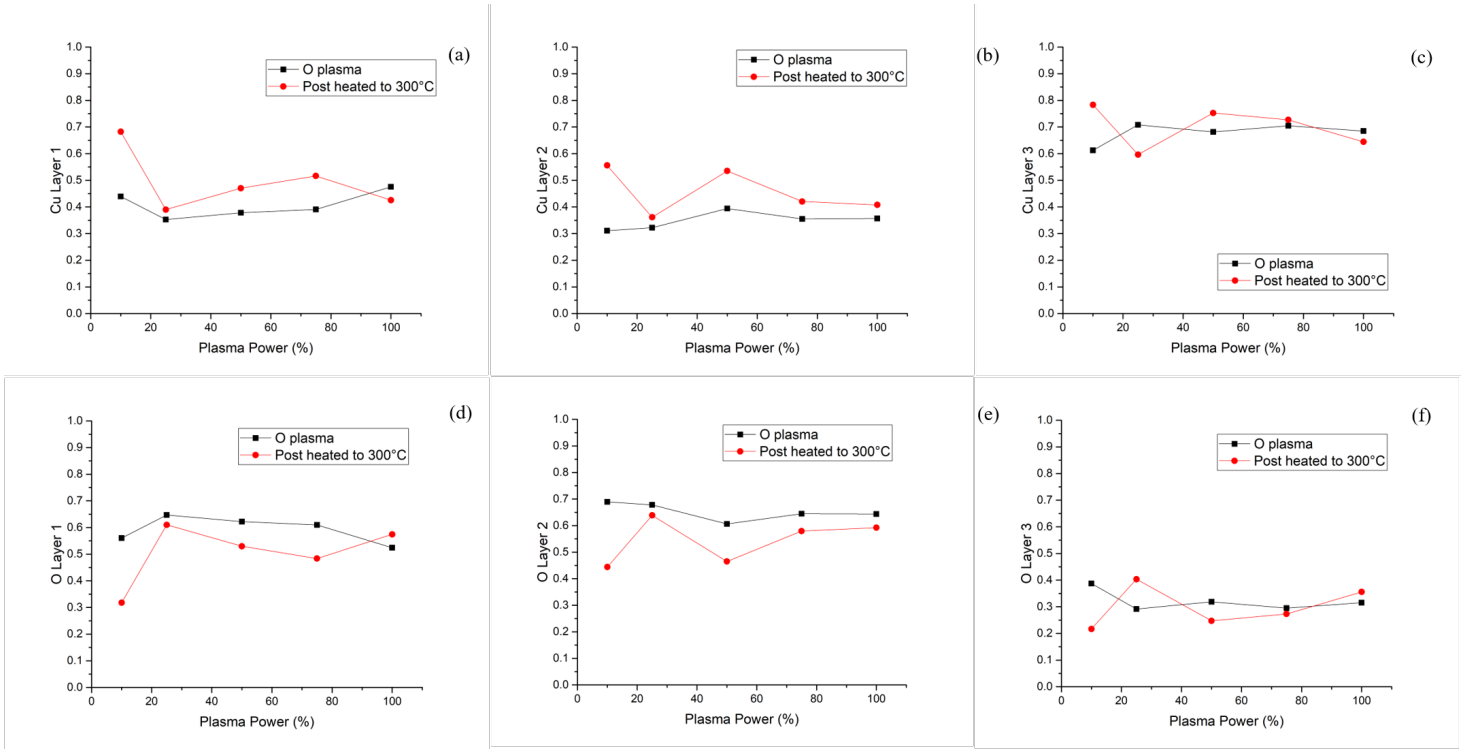


FIGURE 4.32: Fractional composition of a) copper content in layer 1 b) layer 2 c) layer 3 and oxygen content in d) layer 1 e) layer 2 and f) layer 3 as a function of plasma power.

**Effects of variable plasma treatment time on copper surface layers**

The effect of plasma treatment time was investigated by treating copper samples for 10, 20 and 40 minutes at 50% plasma power. The quantification of composition and depth after O plasma treatment and after heating are presented in Table 4.5.

TABLE 4.5: Quantitative data for fractional composition and thickness of copper surface layers as a function of O plasma treatment time before and after heat treatment.

| | O plasma treated | | | Heated to 300°C | | |
|---|---|---|---|---|---|---|
| | Depth ($10^{15}$ At/cm$^2$) | Cu | O | Depth ($10^{15}$ At/cm$^2$) | Cu | O |
| **10 minutes** | | | | | | |
| Layer 1 | 10 | 0.37 | 0.63 | 10 | 0.36 | 0.64 |
| Layer 2 | 32.60 | 0.35 | 0.65 | 31.41 | 0.34 | 0.66 |
| Layer 3 | 24.44 | 0.64 | 0.36 | 27.75 | 0.64 | 0.36 |
| **20 minutes** | | | | | | |
| Layer 1 | 10 | 0.38 | 0.62 | 10 | 0.47 | 0.53 |
| Layer 2 | 70.49 | 0.39 | 0.61 | 72.78 | 0.53 | 0.47 |
| Layer 3 | 32.52 | 0.68 | 0.32 | 25.88 | 0.75 | 0.25 |
| **40 minutes** | | | | | | |
| Layer 1 | 10 | 0.48 | 0.52 | 10 | 0.52 | 0.48 |
| Layer 2 | 82.15 | 0.46 | 0.54 | 71.59 | 0.47 | 0.53 |
| Layer 3 | 42.33 | 0.75 | 0.25 | 39.18 | 0.72 | 0.28 |

The effect of treatment time on the thickness of the overall oxide is presented in Figure 4.33 (a). Additionally, the thickness of the oxide layer 2 and the interfacial layer 3 is presented as a function of treatment time in Figures 4.33 (b) and 4.33 (c) respectively. For each layer, the thickness increases with increasing treatment time. The rate of increase appears to be greater between 10 minutes and 20 minutes for Layer 2 (bulk of oxide) compared with further treatment up to 40 minutes. A possible explanation for this is that a saturation point is reached at some point after 20 minutes of exposure to oxygen plasma, after which the rate at which the film is grown onto the copper surface is reduced and may finally plateau. As with the study on variable plasma power, the effect of heating on the thickness of the oxide layers would seem insignificant.

Figure 4.34 shows the fractional composition of copper and oxygen as a function of O plasma treatment time.

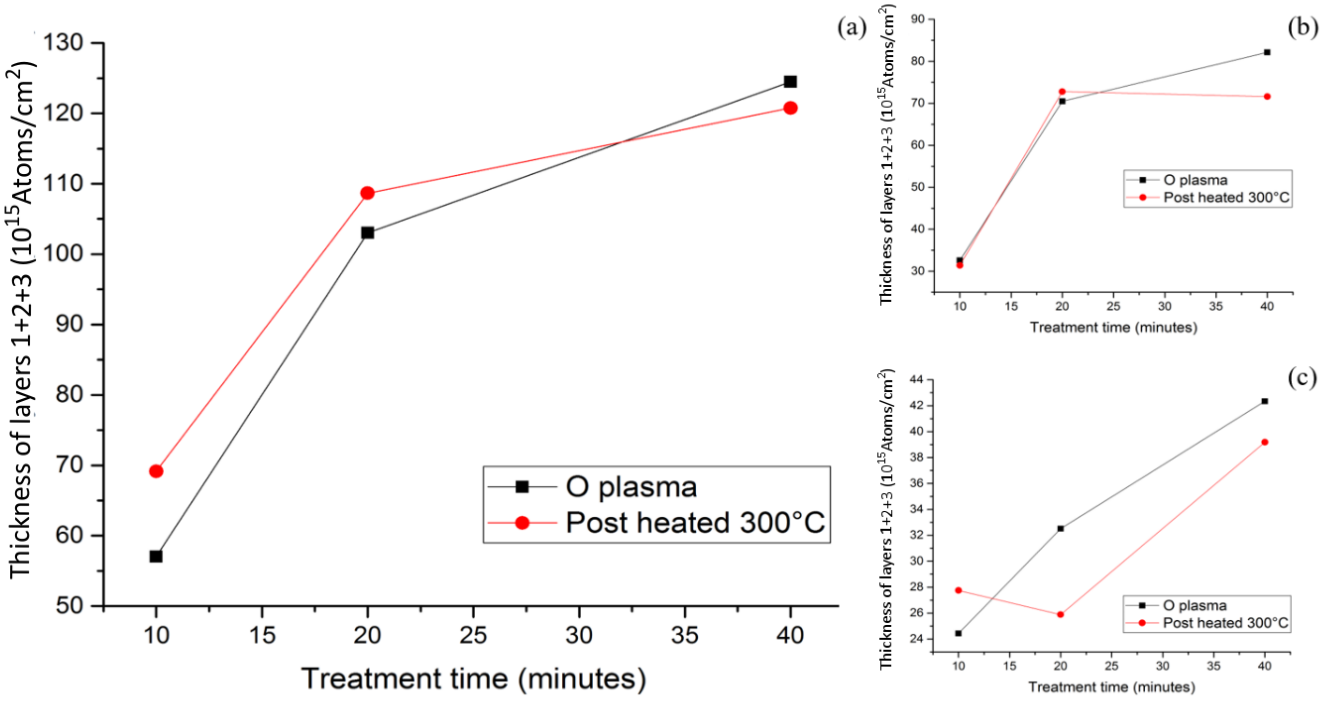


FIGURE 4.33: a) Thickness of layers 1 + 2 + 3 b) layer 2 and c) layer 3, as a function of the plasma treatment time applied to the copper samples at room temperature and after heating to 300°C.

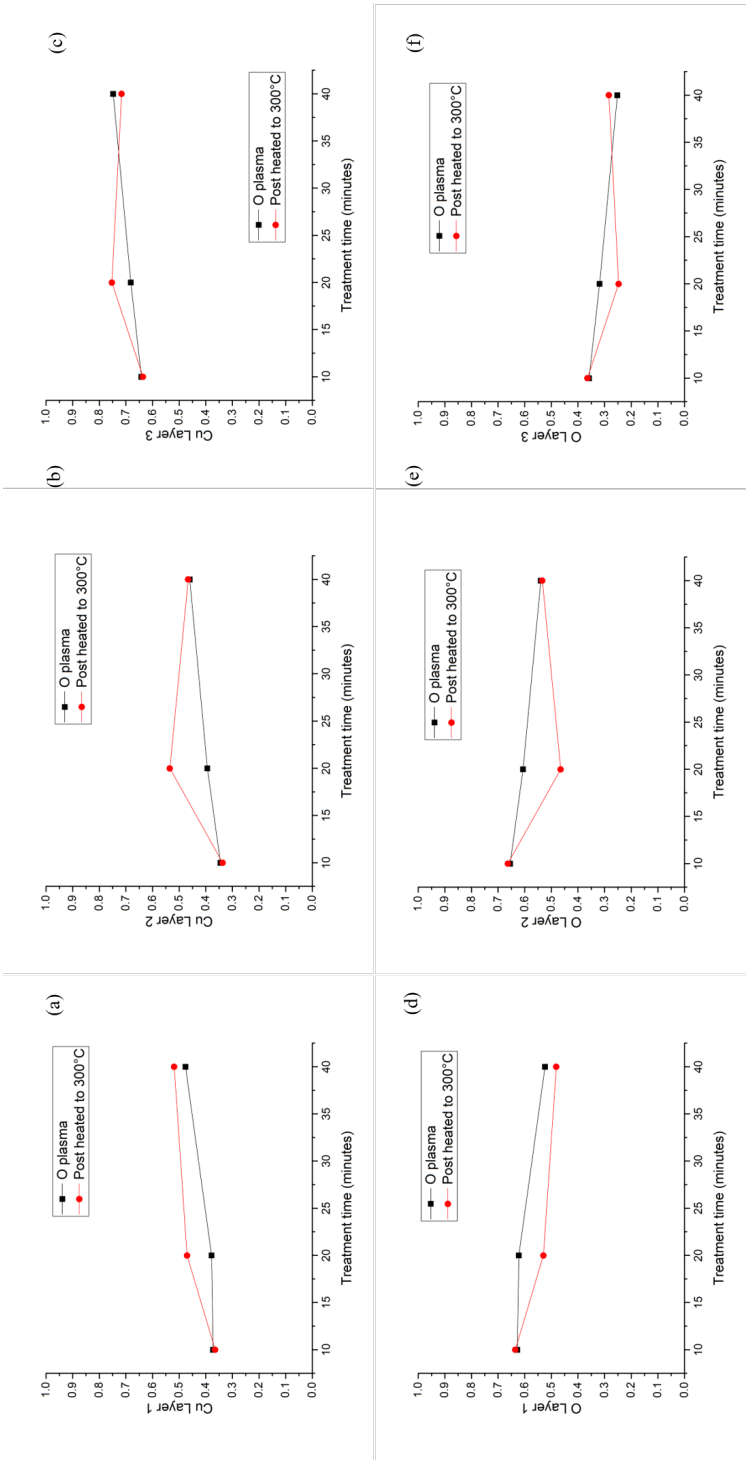


FIGURE 4.34: Fractional composition of a) copper content in layer 1 b) layer 2 c) layer 3 and oxygen content in d) layer 1 e) layer 2 and f) layer 3 as a function of plasma treatment time.

**Effects of heating O plasma treated copper samples**

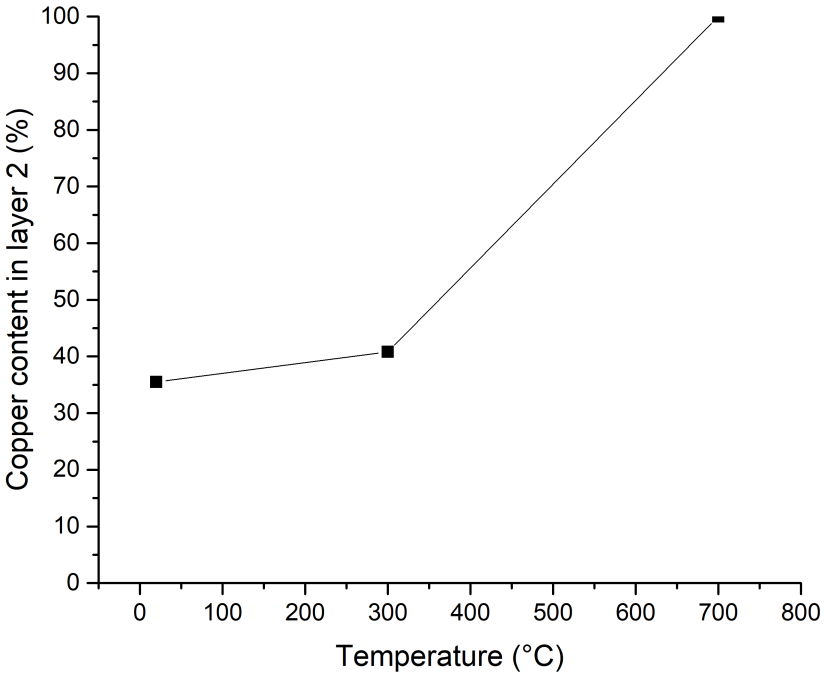


FIGURE 4.35: Fractional composition of copper in layer 2 as a function of temperature.

In Figure 4.35 the percent of copper in layer 2 as a function of temperature is presented for O plasma treated copper samples. Though only three data points are recorded, it is clear that there is a positive relationship between increasing temperature and increasing copper content. The exact nature of this correlation is not clear from this data alone. The lowest temperature at which the surface oxide reduces completely is still unknown, but it suffices to say that heating to approximately 300°C alone is insufficient to shift the oxide formed after O plasma treatment (at 100% power).

## 4.4 Plasma treatment of Cu and Mo in Multiprobe

Further investigations on the effect of plasma treatment were required due to issues with the previous investigation in ESCALAB i.e. XPS data was collected for sample and sample holder. Therefore, it was necessary to repeat some of the measurements in order to be clear of the effects of different surface preparation procedures.

In the interest of time and efficiency, only a couple of metals were selected for these experiments. Copper and molybdenum were chosen as they are materials that are of interest in the process of commissioning CLARA. The first beam was to be achieved with just the photocathode plug, which is made of molybdenum.

In the future, photocathode materials (copper and alternatives to copper) will be deposited onto the molybdenum plug and used to generate electron beam. But in the mean time, for the first run, it was important to know if sufficient electron beam could be extracted from the molybdenum plug. Therefore a study to investigate what sort of QE to expect from a molybdenum photocathode, and how best to prepare the surface to obtain maximum achievable QE was carried out, so as to inform the CLARA commissioning group in the preparation of the molybdenum plug.

In the sections below, the results for copper and molybdenum samples are presented. QE measurements were taken using the UV Laser 2 set-up on the Multiprobe system. Photocurrent, XPS and UPS measurements were taken after each process: after plasma treatment, after sequentially heating to 250°C, 450°C and 550°C.

Overall, the QE measurements in section 4.2 were lower than anticipated, and therefore an investigation into the photocurrent measurements and laser power measurements was conducted. By varying the laser power and the sample bias, the photocurrent and QE values could be evaluated.

For each set of measurements, the photocurrent was measured at fixed laser powers of 3.75 mW, 8.87 mW and 12.67 mW (10%, 50% and 100%) and variable bias (0-108 V in incremental steps of 9 V). Additionally, photocurrent measurements were taken at fixed bias of 72 V and variable laser power.

### 4.4.1 Plasma treatment comparison

Firstly an experiment comparing the effects of O, Ar and O + Ar plasma treatment followed by heating to 250°C on copper samples was conducted. The results are summarised in Figure 4.36. XPS data presented in the table in Figure 4.36 shows the elemental composition for each preparation procedure as derived from XPS survey spectra, as well as the chemical state of the copper as deduced from the Cu LMM region scan. These results indicate that Ar plasma treatment followed by heating produced the cleanest surface. Photocurrent measurements for variable power and variable bias for each preparation procedure are shown in 4.36 a) and 4.36 b) respectively. These plots clearly demonstrate that higher photocurrent was extracted from the Ar plasma treated sample. As a result of this experiment, Ar plasma treatment followed by heating has

been agreed upon as the preferred method for preparation of the copper/molybdenum photocathode plug for CLARA commissioning. A full characterisation and determination of the optimal heating treatment required is discussed in the sections below.

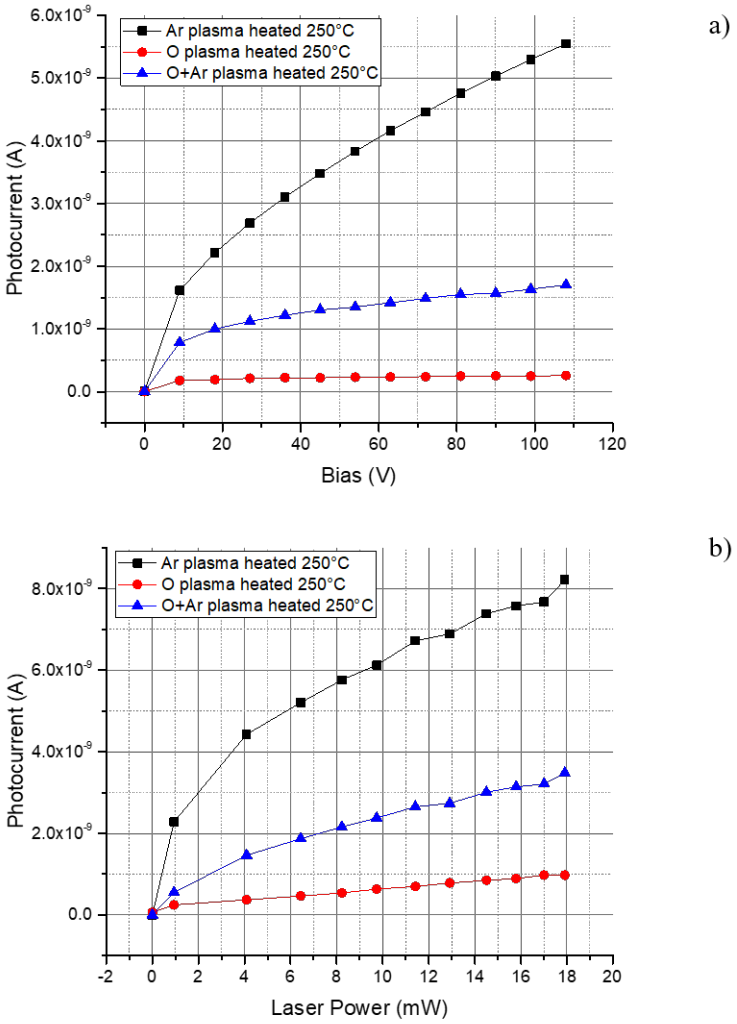


| | **O 1s (%)** | **Cu 2p (%)** | **Chemical State (Cu LMM)** |
|---|---|---|---|
| Ar plasma, heated 250°C | 12.3±1.3 | 87.7±1.3 | Cu Metal |
| O plasma, heated 250°C | 50.0±1.6 | 50.0±1.6 | $Cu_2O$ |
| O + Ar plasma, heated 250°C | 25.8±2.9 | 74.2±2.9 | Cu Metal |

FIGURE 4.36: a) Photocurrent as a function of sample bias and b) photocurrent as a function of laser power for copper Ar plasma treated and heated to 250°C (black), O plasma treated and heated to 250°C (red) and O + Ar plasma treated and heated to 250°C (blue). Table representing the elemental quantification of each copper sample after Ar/O/O+Ar treatment followed by heating.

### 4.4.2 Molybdenum

XPS, QE, and UPS measurements were taken for the Ar plasma treated molybdenum sample after Ar plasma treatment, after heating to 250°C, 450°C, and 550°C (each for half an hour).

In Figure 4.37 the photocurrent as a function of bias is plotted for a) 3.75 mW b) 8.87 mW and c) 12.67 mW laser power. Comparing the three plots, it is evident that the photocurrent extracted increases with increasing laser power as expected. In each case, the measurements show maximum photocurrent is achieved after the Ar plasma treated molybdenum is heated to 450°C for half an hour. A comparison of the photocurrent measurements vs. bias for 10%, 50% and 100% laser power after heating to 450°C for half an hour is shown along side the corresponding QE vs bias in Figure 4.38. Figure 4.38 b) shows that the maximum QE achievable occurs at 108 V and is in the range of $3.0 \times 10^{-6}$ to $5.5 \times 10^{-6}$. Figure 4.39 a) shows the photocurrent extracted as a function of variable laser power. In these plots, the photocurrent and therefore QE for heating to 450°C and 550°C are comparable.

With respect to the investigation over the unexpectedly low QE measurements, these plots are very revealing. Figure 4.37 shows the photocurrent measurements as a function of variable bias. As the bias across the sample is increased, one would expect that the photocurrent would plateau as saturation is reached, i.e. when the maximum photocurrent is extracted for a given laser power. However, the results presented do not reflect this. Instead, the photocurrent continues to increase up to the highest bias available. If the electron emission is increasing continuously with increasing bias, then it is possible that not all the photocurrent is being measured as drain current. Furthermore, the plots for QE as a function of variable laser power are not in agreement with the theory. The ratio of extracted photocurrent to laser power should be constant; the QE should not vary with variable laser power, for a given wavelength. Yet in Figure 4.39), the QE is shown to decrease with increasing laser power. These measurements would suggest that the QE values obtained cannot be taken as absolute values, but relative. Similar trends are observed for the copper sample investigated.

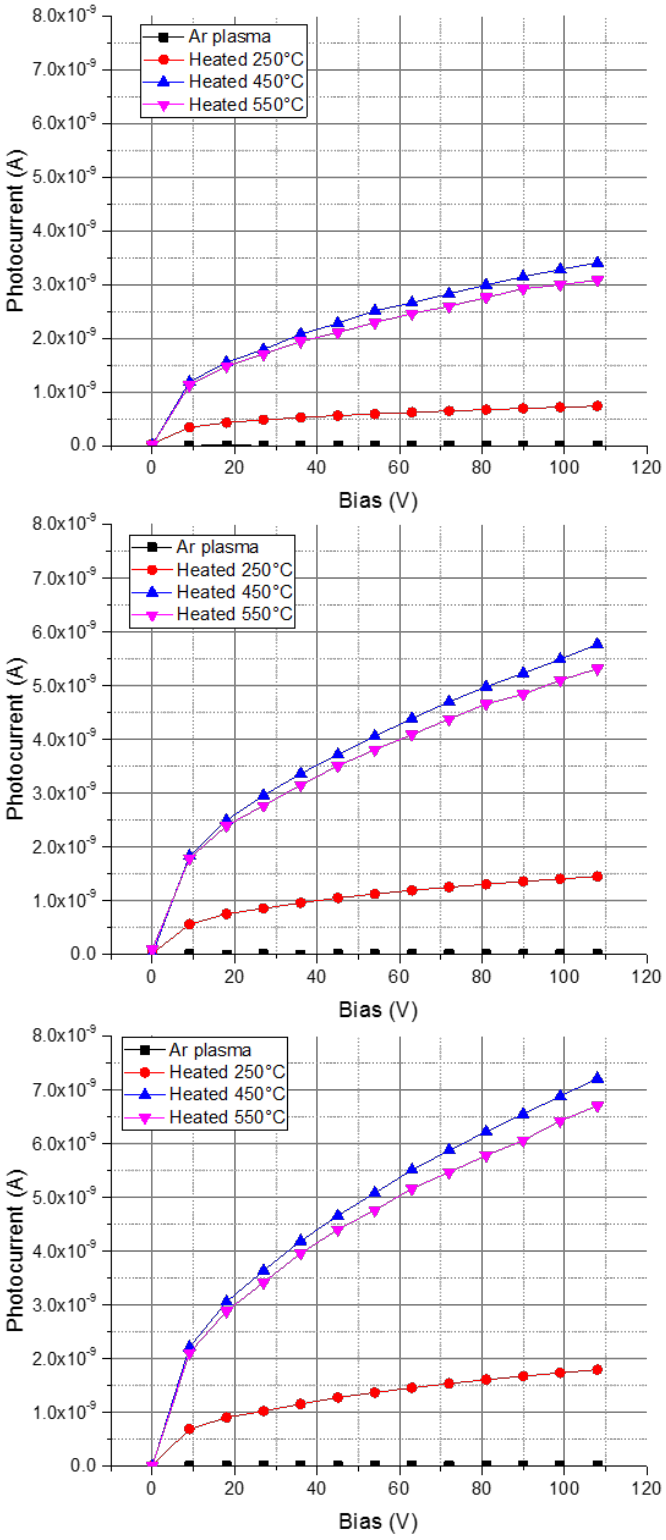


FIGURE 4.37: Photocurrent measurements for Ar plasma treated molybdenum sample as a function of variable bias for laser power set to (top) 3.75 mW (10% laser power), (middle) 8.87 mW (50% laser power) and (bottom) 12.67 mW (100% laser power).

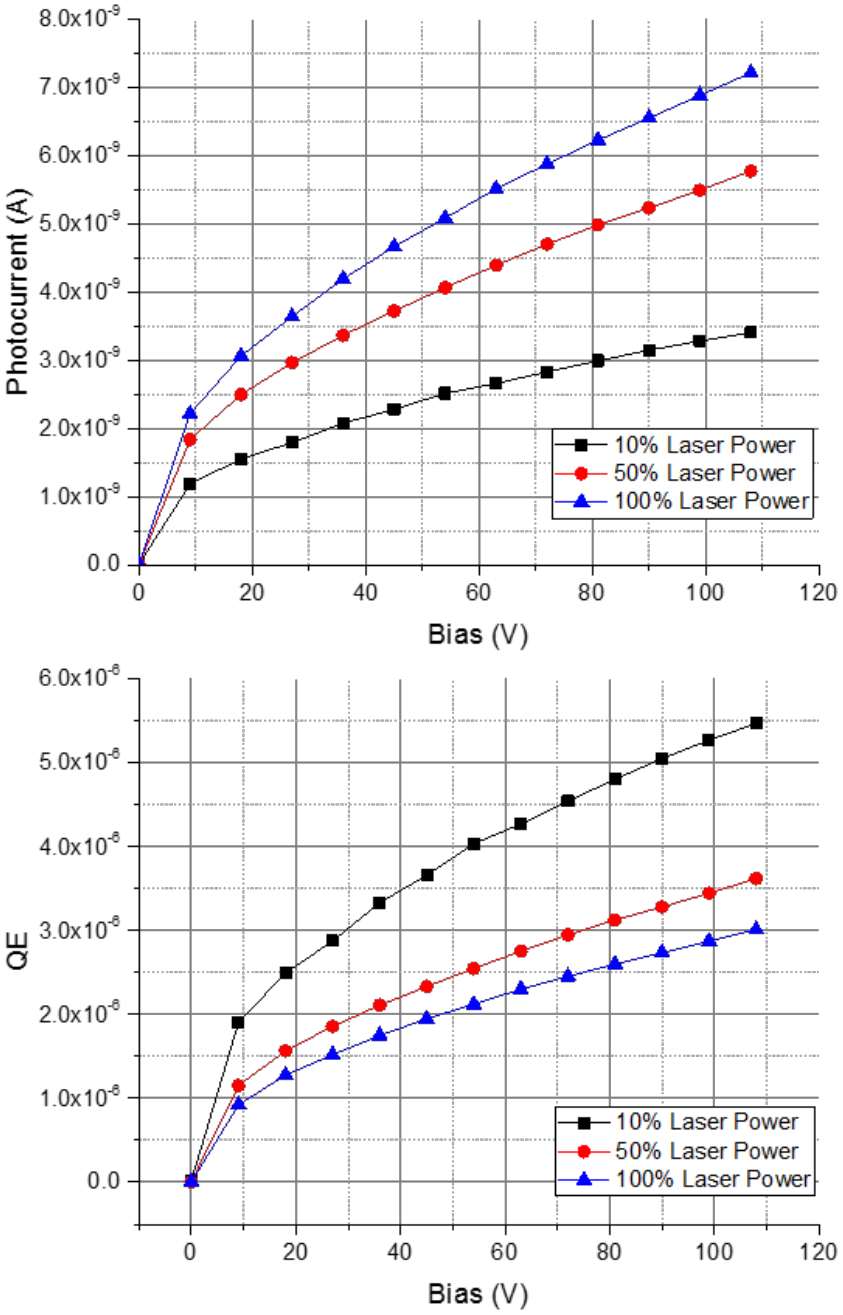


FIGURE 4.38: Photocurrent (top) and QE (bottom) measurements for Ar plasma treated molybdenum heated to 450°C sample as a function of variable bias for laser power set to (black) 3.75 mW (10% laser power), (red) 8.87 mW (50% laser power) and (blue) 12.67 mW (100% laser power).

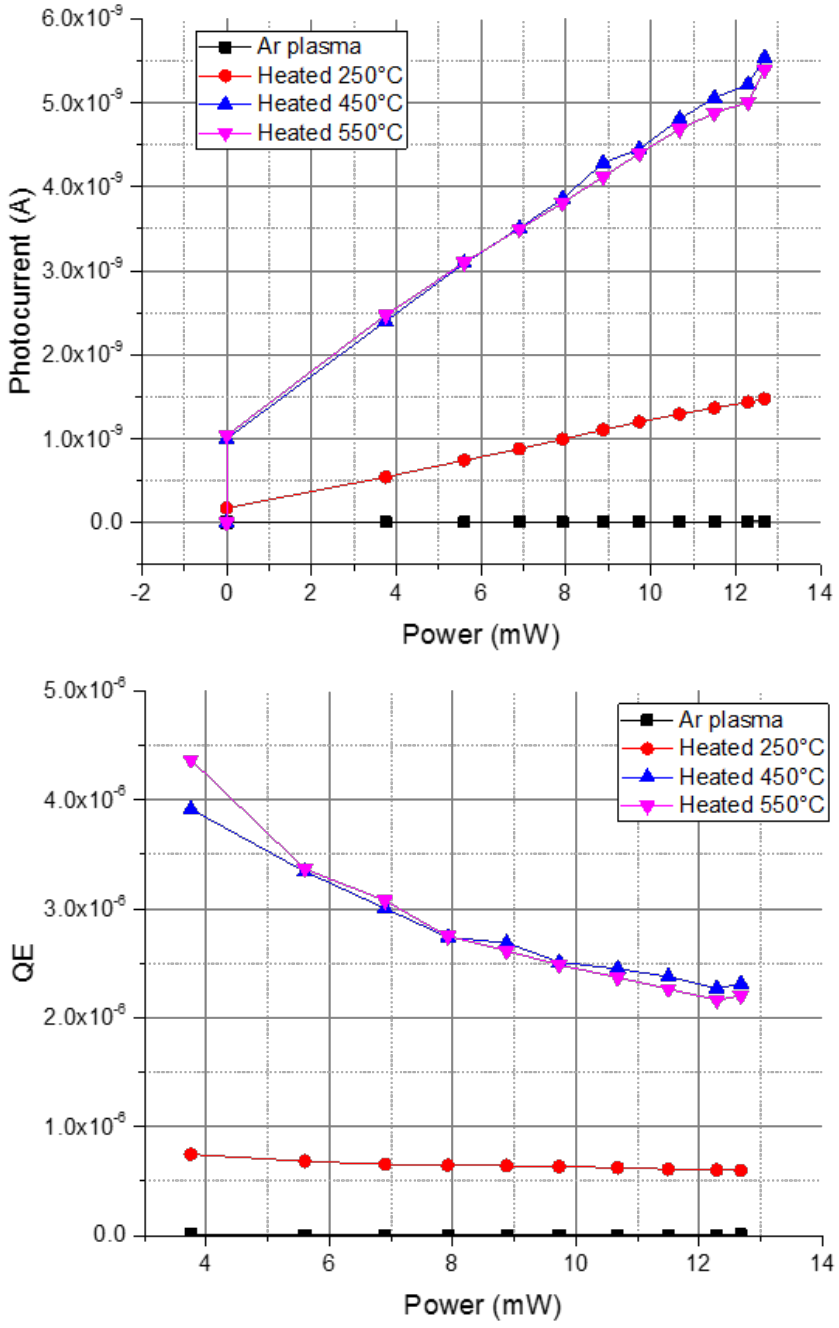


FIGURE 4.39: Photocurrent (top) and QE (bottom) measurements for Ar plasma treated molybdenum sample as a function of variable laser power at a fixed sample bias of 72 V.

The XPS data for Ar plasma treated molybdenum, quantified from the survey spectra in Figure 4.40, is summarised in Table 4.6.

TABLE 4.6: Summary of quantitative XPS data from Mo survey spectra.

| Ar plasma treated Mo | Mo 3d (%) | O 1s (%) | C 1s (%) | Na (%) |
|---|---|---|---|---|
| Ar plasma | 31.7 ± 0.8 | 66.5 ± 0.9 | 0 | 1.8 ± 0.5 |
| Heated 250°C | 37.8 ± 1.6 | 51.8 ± 2.1 | 7.7 ± 3.3 | 2.7 ± 0.5 |
| Heated 450°C | 46.0 ± 2.0 | 41.0 ± 2.0 | 10.6 ± 3.3 | 2.4 ± 0.7 |
| Heated 550°C | 57.9 ± 3.0 | 34.1 ± 2.1 | 8.0 ± 4.3 | 0 |

From this data it is evident that the effect of Ar plasma treatment was to remove hydrocarbon contamination; this is consistent with the results from previous studies (see section 4.2). The elemental composition of the surface is approximately 67% oxygen and 32% molybdenum. Additionally trace elements of sodium were found in each scan except the last, when the sample is heated to 550°C. Upon heating the molybdenum sample, there is a general decrease in the oxygen content (see Figure 4.40 c)), an increase in the molybdenum (see Figure 4.40 b)) and an emergence of carbon (see Figure 4.40 d)). An explanation for the emergence of carbon is that sub-surface contaminants are known to migrate to the surface upon heating. Figure 4.40b) clearly shows that not only is there an increase in intensity of the Mo 3d peaks upon heating, but there is also clearly a change in position and shape of the peaks. The components of each Mo region spectra are fitted in Figure 4.41 indicating the chemical states of the molybdenum after each process. A quantification of the results from these spectra are presented in Table 4.7.

TABLE 4.7: Summary of quantitative XPS data from Mo 3d region spectra.

| Ar plasma treated Mo | Mo metal (%) | MoO2 (%) | MoO3 (%) |
|---|---|---|---|
| Ar plasma | 37 | 0 | 63 |
| Heated 250°C | 46 | 43 | 11 |
| Heated 450°C | 67 | 33 | 0 |
| Heated 550°C | 86 | 14 | 0 |

The Ar plasma treated Mo 3d spectrum is fitted with two sets of Mo 3d peaks; the $3d_{5/2}$ peaks in each case occurs at 232.85 eV and 228.18 eV corresponding to $MoO_3$ (63%) and Mo metal (37%) respectively. First heating to 250°C produces three different chemical states: Mo metal (46%), $MoO_2$ (43%) and $MoO_3$ (11%). The Mo $3d_{5/2}$ peak corresponding to $MoO_2$ is positioned at 229.7 eV. The $MoO_3$, which dominated after Ar plasma treatment, is mostly reduced down to $MoO_2$ after heating to 250°C. Additionally, the metal component increases by approximately 10%. Further heating to 450°C produces an overall reduction in the binding energy of the Mo 3d peaks. The $MoO_3$ is reduced down to trace level, and now the surface is characterised by Mo metal (67%) and and $MoO_2$ (33%) only. Finally heating to 550°C for half an hour reduces the $MoO_2$ component down to trace level and Mo metal dominates the surface.

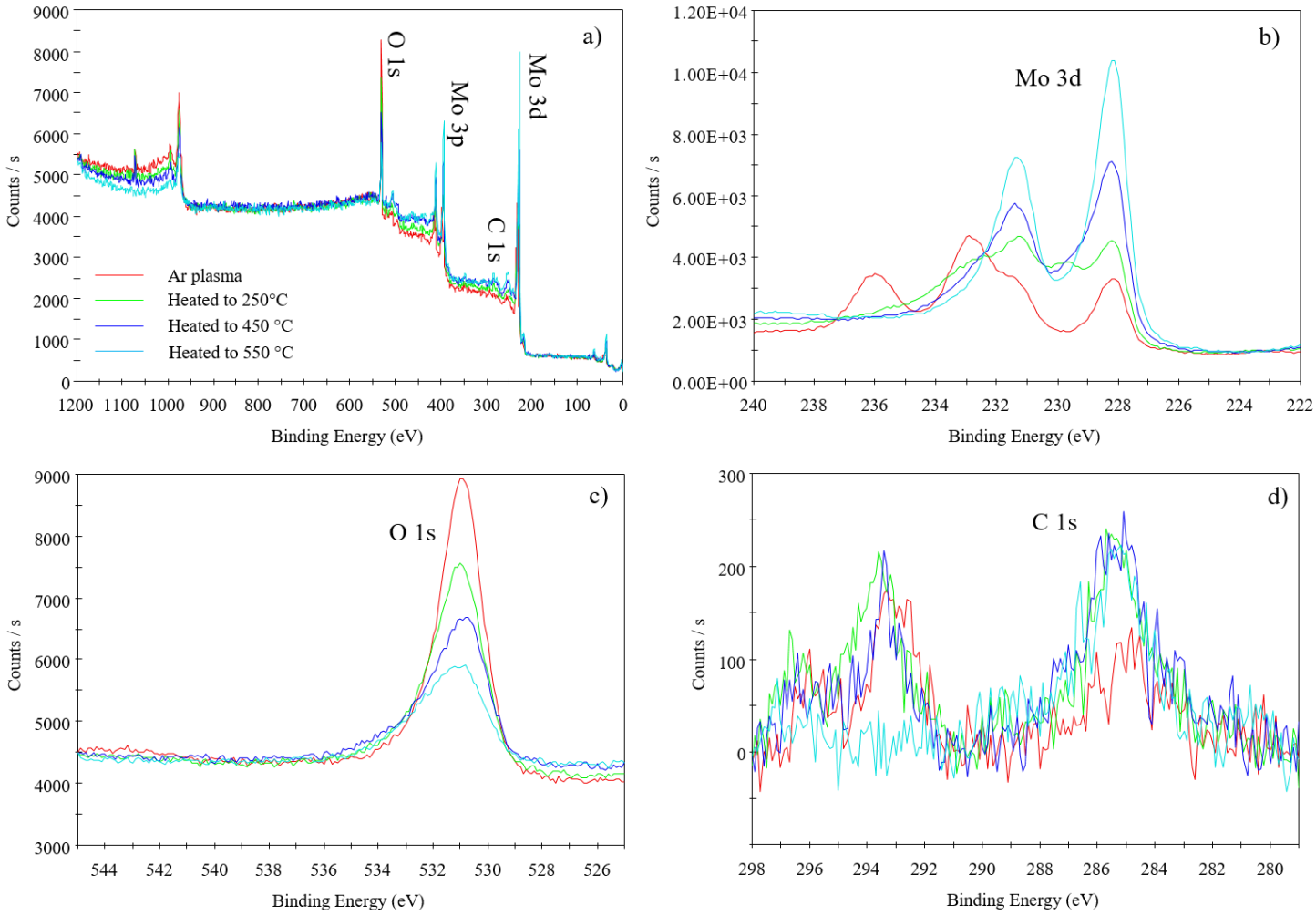


FIGURE 4.40: XPS spectra for bulk polycrystalline molybdenum Ar plasma treated, heated to 250°C, 450°C and 550°C. a) Overlay of survey spectra, b) overlay of Mo 3d region spectra, c) overlay of O 1s region spectra and d) overlay of C 1s region spectra.

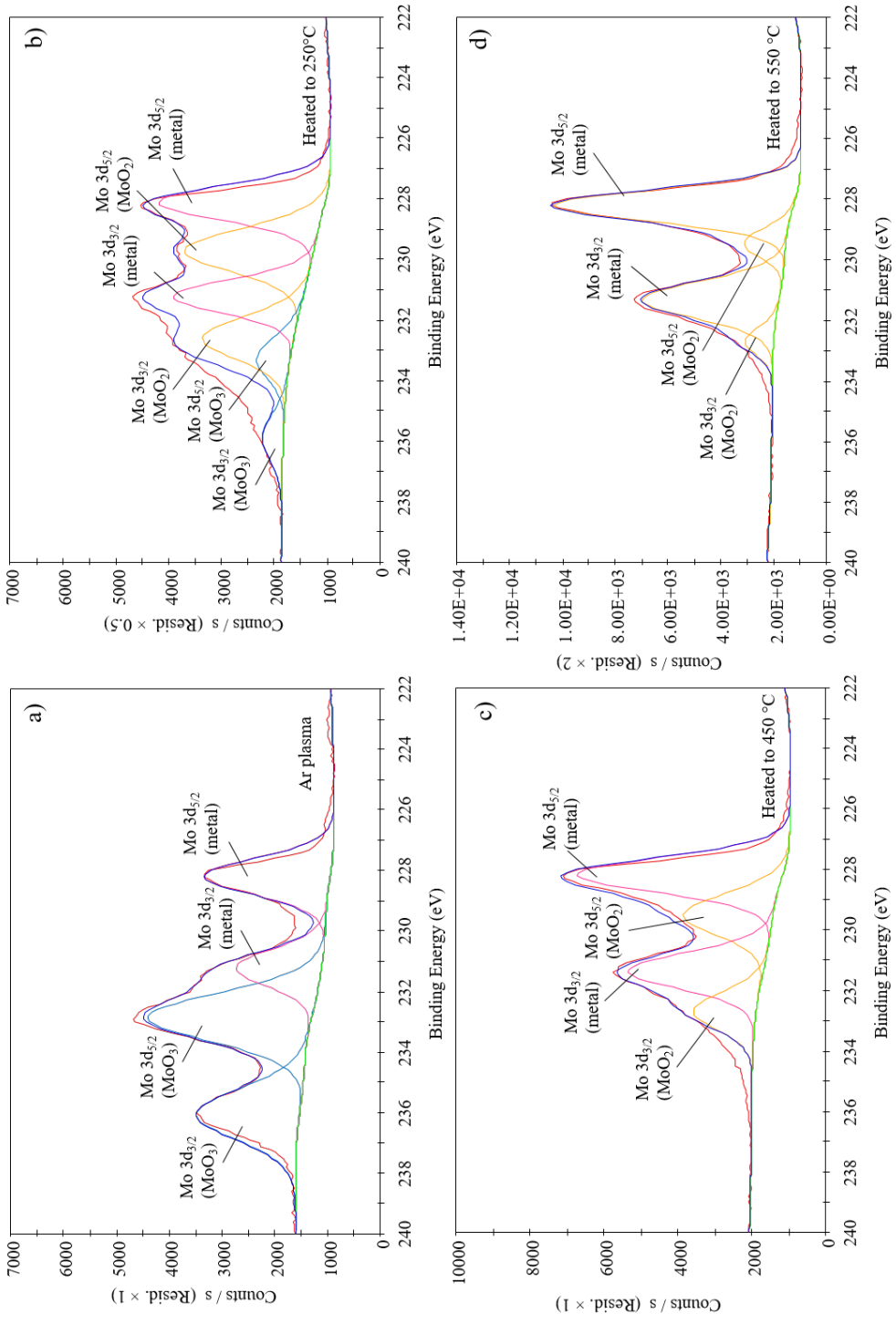


FIGURE 4.41: Mo 3d region spectra for bulk polycrystalline molybdenum a) Ar plasma treated, b) heated to 250°C, c) 450°C and d) 550°C.

UPS measurements were taken after each process too: a long survey scan followed by high resolution region scans of the Fermi edge and secondary electron cut-off at -9 V bias. The bias is necessary to shift the spectrum away from the analyser secondary electron edge. An overlay of the survey spectra is presented in Figure 4.42. This shows how the width of the photoemission spectra (from Fermi edge to secondary electron cut-off) varies with each process. The positions of the secondary electron cut-off is more clearly presented in Figure 4.44. The secondary electron cut-off value is taken at half the maxima of the secondary electron peak. This value occurs at a kinetic energy of 13.9 eV for the Ar plasma treated molybdenum sample. Upon first heating to 250°C, this value is shifted by approximately 1 eV down to 13.0 eV. This is further shifted down to 12.6 eV after heating to 450°C. However after heating to 550°C there is a slight increase up to 12.8 eV. Figure 4.45 shows the region spectra for the Fermi edges. Except in the case of the 4.45 c) when the sample is heated to 550°C, there is no discernible Fermi edge. This is because the Fermi edge can only be observed in the photoemission spectra if the metal is clean, i.e. free of oxide. If we were to assume that the position of the Fermi edge remains constant throughout, then upon heating, the width of the spectra generally increases; this would result in a decreasing WF. The values for the WF determined in this way are presented in Figure 4.43. The standard errors are the highest contributing error for the WF measurements. Scans of the secondary edge and fermi edge were repeated five times; the error was calculated to be approximately 6%.

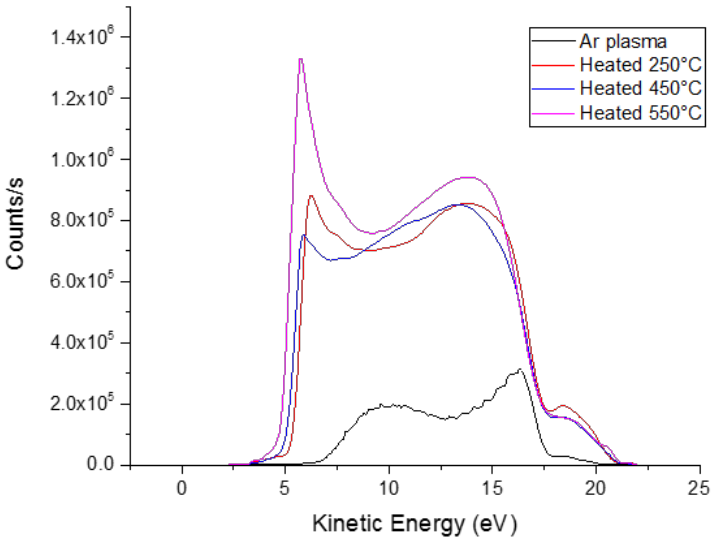


FIGURE 4.42: UPS survey spectra overlay for molybdenum Ar plasma treated, heated to 250°C, 450°C and 550°C.

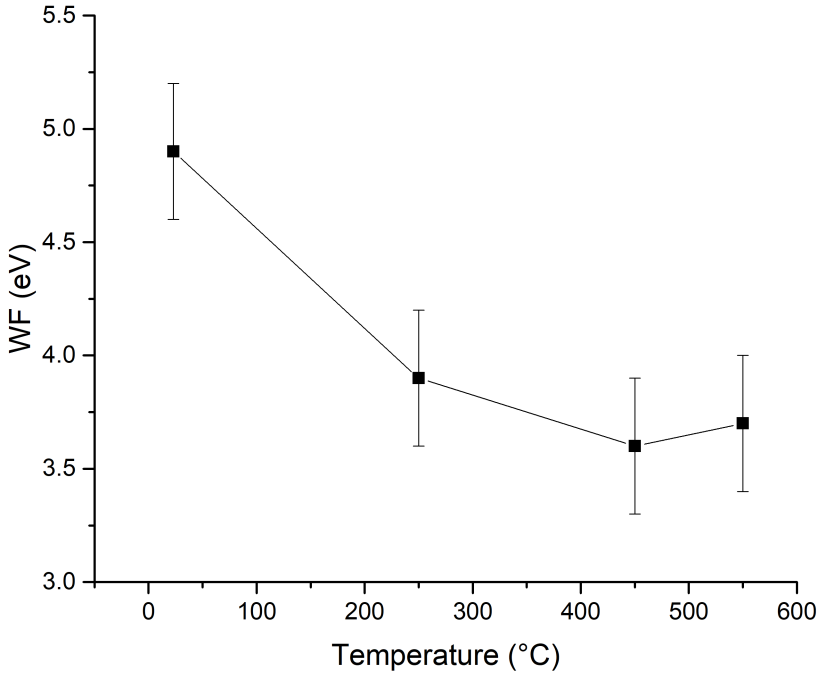


FIGURE 4.43: WF measurements for Ar plasma treated Mo as a function of temperature.

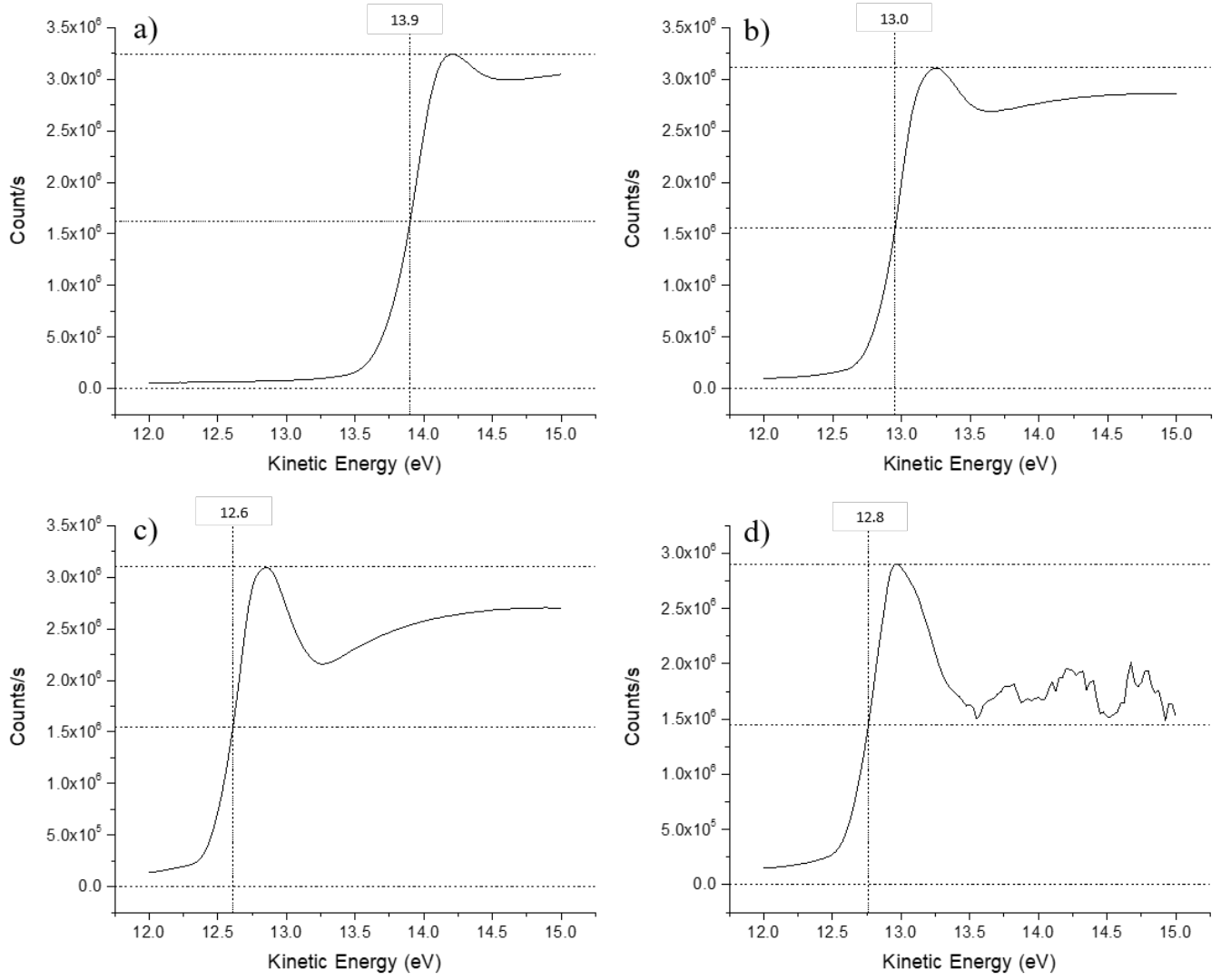


FIGURE 4.44: UPS secondary electron cut-off region spectra for bulk Mo a) Ar plasma treated, b) heated to 250°C, c) heated to 450°C and d) heated to 550°C.

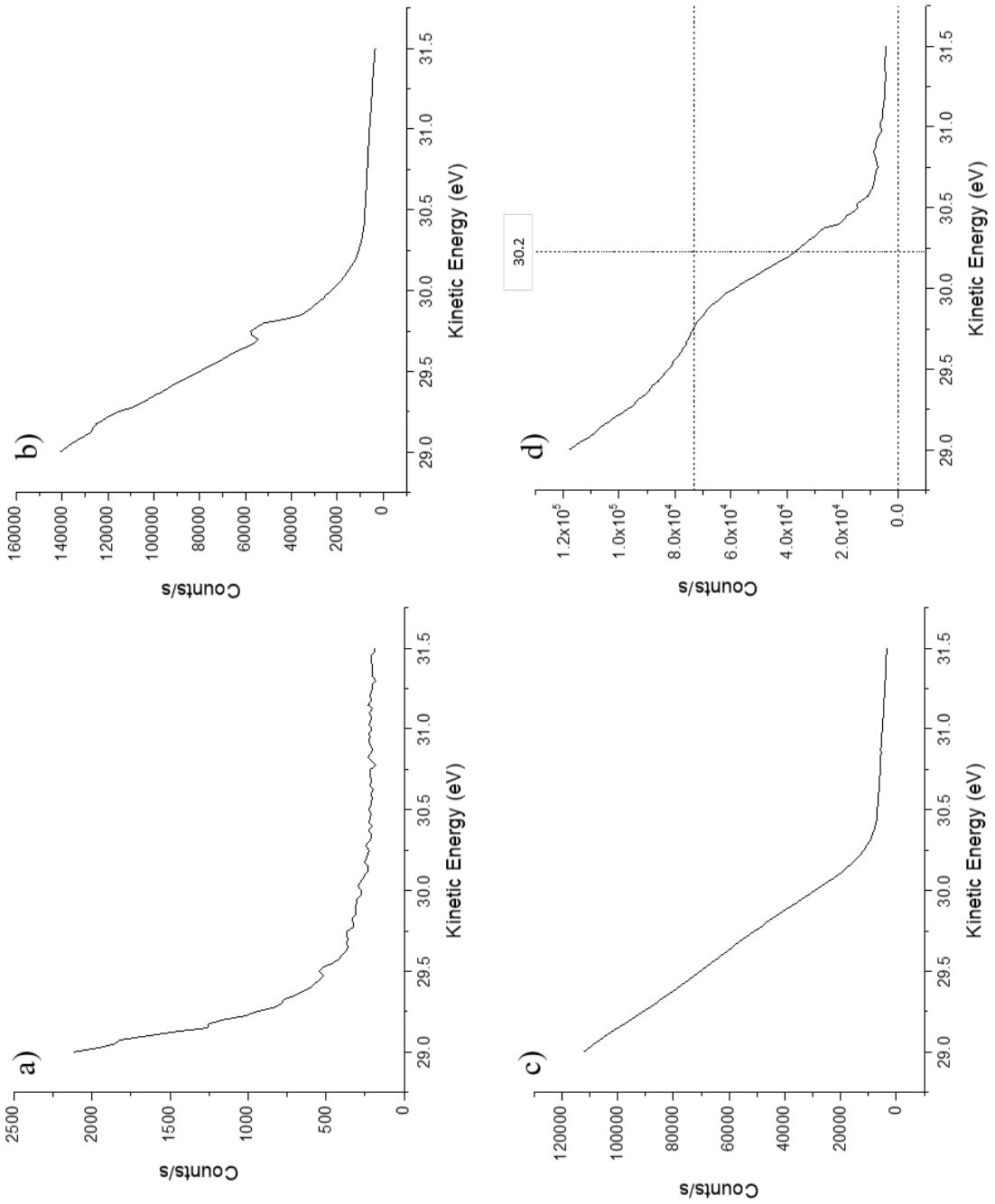


FIGURE 4.45: UPS Fermi edge region spectra for bulk Mo a) Ar plasma treated, b) heated to 250°C, c) heated to 450°C and d) heated to 550°C.

### 4.4.3 Copper

As with the molybdenum sample, XPS and QE measurements were taken for the Ar plasma treated copper sample after Ar plasma treatment, after heating to 250°C and 450°C (each for half an hour). Due to difficulties with equipment, UPS measurements were not obtained.

Figure 4.47 shows the change in photocurrent with variable bias for a) 10% laser power, b) 50% laser power and c) 100% laser power.

The greatest photocurrent is extracted at maximum bias (108 V), maximum laser power and after heating to 450°C for half an hour. Figure 4.48 shows a comparison of the photocurrent measurements and the corresponding QE as a function of bias after heating to 450°C for the different laser powers. This shows that the maximum QE ranges between $4.4 \times 10^{-6}$ and $6.9 \times 10^{-6}$ for argon plasma treated copper heated to 450°C. Figure 4.49 shows photocurrent and QE as a function of variable laser power, again demonstrating that the highest QE is achieved by heating the Ar plasma treated copper sample to 450°C.
The XPS data for Ar plasma treated copper, quantified from the survey spectra in Figure 4.50, is summarised in Table 4.8.

An overlay of the survey spectra, Cu 2p region, O 1s region and C 1s regions for Ar plasma treated copper, heated to 250°C and heated to 450°C is presented in Figure 4.50. From Figure 4.50 a), there is very little significant and observable changes in each of the three spectra, except for a decrease in the intensity of the O 1s peak after heat treatment. Indeed, even the Cu 2p region scans (see Figure 4.50c) ) remain largely unchanged between each procedure. The Cu 2p region scan indicates that the chemical state of the copper surface is either Cu metal or $Cu_2O$ in all cases. Referring to the Cu LMM regions will clarify which chemical state. The O 1s regions show a significant reduction upon heating to 250°C, and a further reduction after heating to 450°C. The C 1s regions suggest trace levels of carbon are detected after Ar plasma treatment and after heating to 250°C. However, after heating to 450°C, there is a resurgence of carbon, perhaps due to migration of contaminants to the surface from the bulk. Figure 4.51 shows the Cu LMM region scans. From these scans it is evident that although the Cu 2p region scans each look the same after Ar plasma treatment and subsequent heating, the Cu LMM region show that there is indeed some change to the surface chemistry. To characterise the chemical state from the Cu LMM region scans, S. Poulston's work on surface oxidation and reduction of copper [64] is used as a reference (see Figure 4.46). The Cu LMM region scan after Ar plasma treatment might suggest an intermediate state between Cu metal and $Cu_2O$. Although the main peak corresponding to Cu metal occurring at 918.5 eV is observed, there is an additional shoulder occurring at 916.5 eV indicative of $Cu_2O$. Upon heating, this additional shoulder diminishes and the scans begin to resemble that of Cu metal.

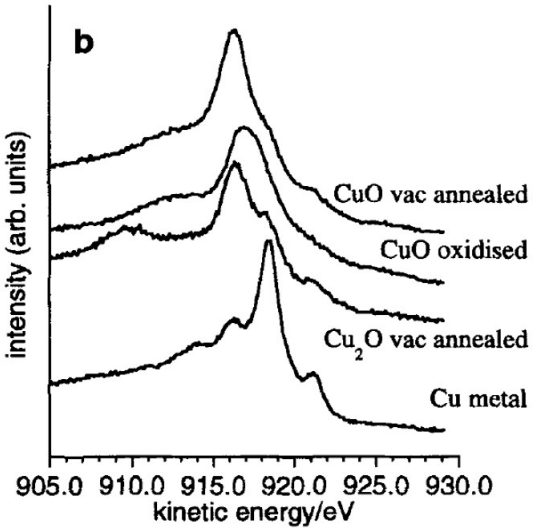


FIGURE 4.46: XPS spectra for Cu LMM region spectra for various chemical states of copper as sourced from [64].

Figure 4.52 shows the O 1s region scans for Ar plasma treated copper, and how the position and intensity change with heat treatment. In Figure 4.52 b), c) and d) the O 1s peaks are fitted to show the different components. A quantification of the relative chemical states is presented in Table 4.9. The Ar plasma treated O 1s peak is fitted with a mixture of three chemical states: C-O, metal oxide and C=O, with C-O making up half of the total. Upon heating to 250°C, the intensity of the O 1s peak reduces by a half, and the C=O component disappears. The C-O component now makes up 87% of the total O 1s peak, and the metal oxide component reduces from 30% to 13%. Further heating to 450°C reduces the metal oxide component entirely, and the chemical states of the oxygen is now wholly associated with C-O.

TABLE 4.8: Summary of quantitative XPS data from Cu survey spectra.

| Ar plasma treated Cu | Cu 2p (%) | O 1s (%) | C 1s (%) |
|---|---|---|---|
| Ar plasma | 72.3 ± 1.2 | 27.7 ± 1.2 | 0 |
| Heated 250°C | 87.7 ± 1.3 | 12.3 ± 1.3 | 0 |
| Heated 450°C | 71.2 ± 2.6 | 16.1 ± 1.2 | 12.7 ± 3.0 |

TABLE 4.9: Quantitative data from O 1s peak fitting for Cu sample.

| | Metal Oxide (%) | C-O | C=O |
|---|---|---|---|
| Ar plasma treated | 30 | 51 | 19 |
| Heated 250°C | 13 | 87 | 0 |
| Heated 450°C | 0 | 100 | 0 |

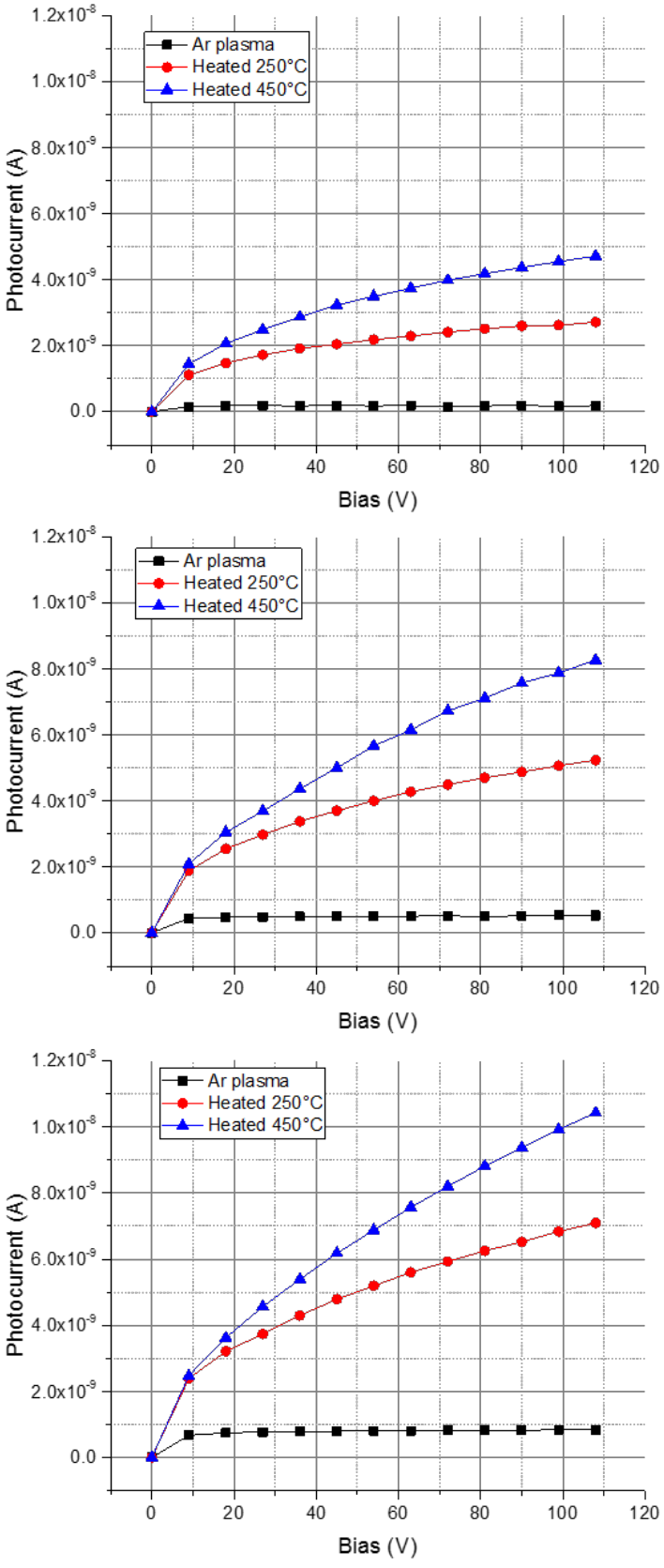


FIGURE 4.47: Photocurrent measurements for Ar plasma treated copper sample as a function of variable bias for laser power set to (top) 3.75 mW (10% laser power), (middle) 8.87 mW (50% laser power) and (bottom) 12.67 mW (100% laser power).

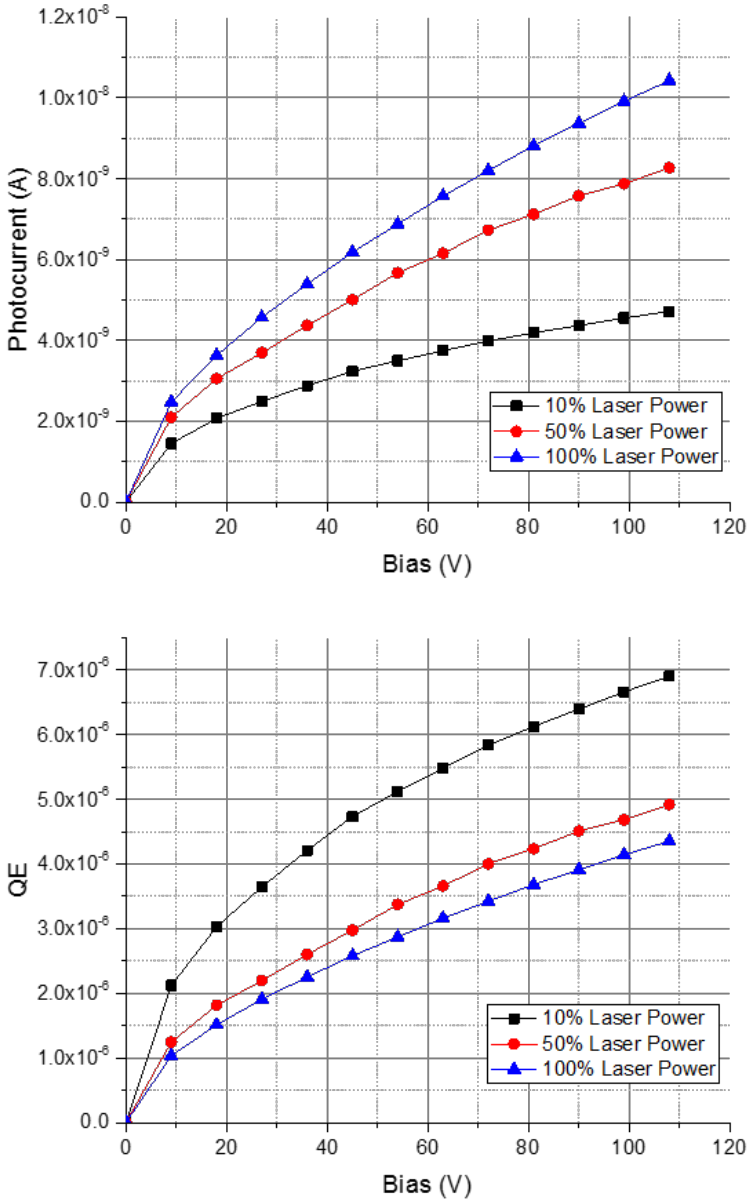


FIGURE 4.48: Photocurrent (top) and QE (bottom) measurements for Ar plasma treated copper heated to 450°C sample as a function of variable bias for laser power set to (black) 3.75 mW (10% laser power), (red) 8.87 mW (50% laser power) and (blue) 12.67 mW (100% laser power).

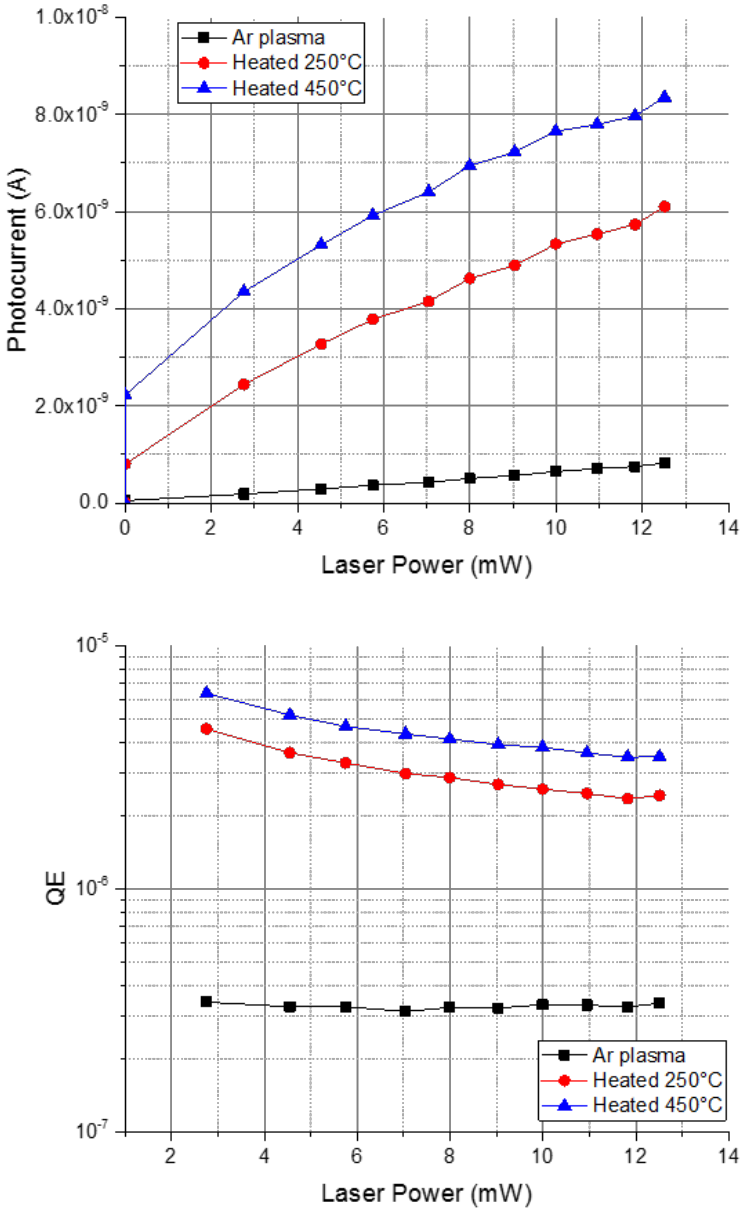


FIGURE 4.49: Photocurrent (top) and QE (bottom) measurements for Ar plasma treated copper sample as a function of variable laser power at a fixed sample bias of 72 V.

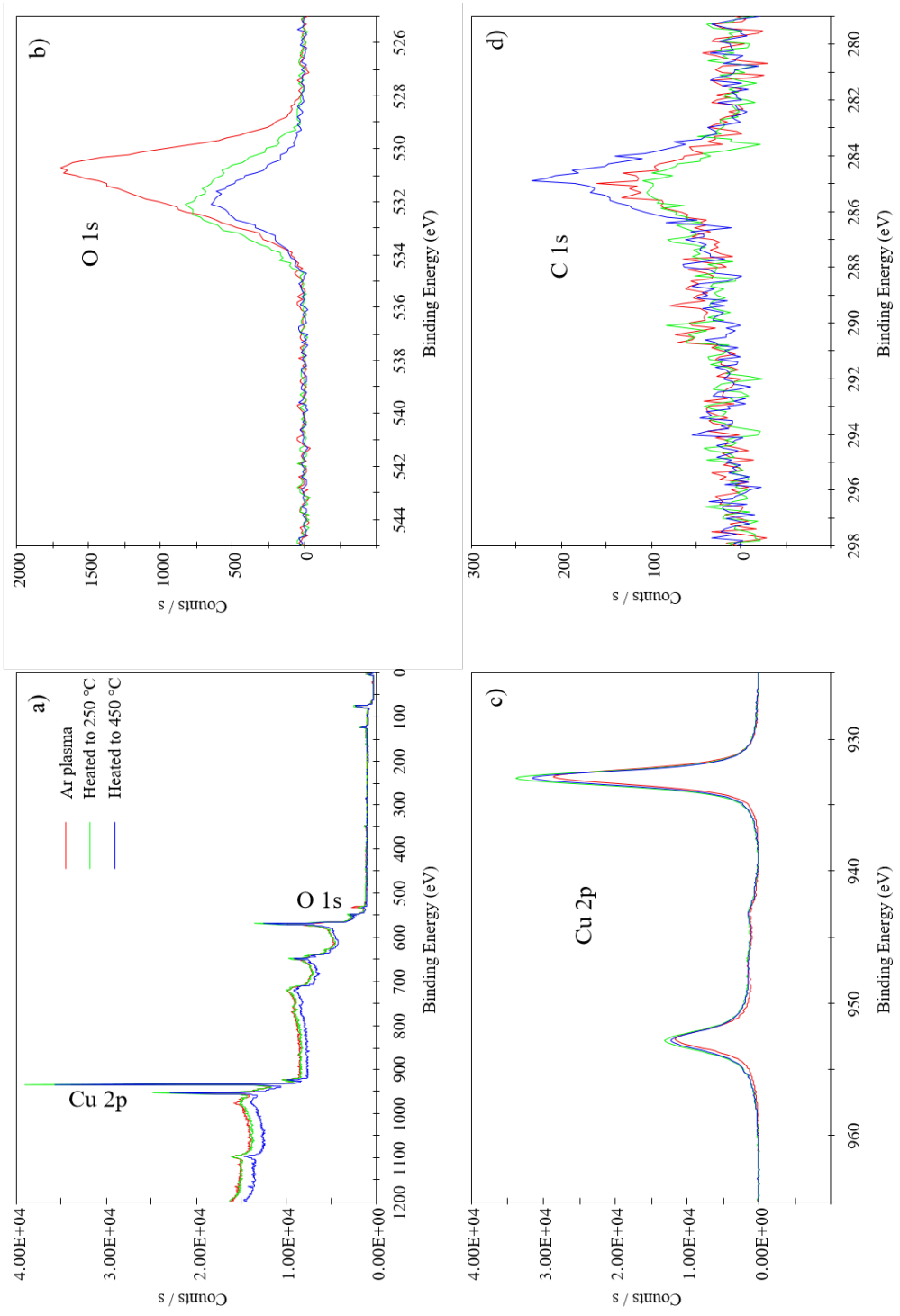


FIGURE 4.50: XPS spectra for bulk polycrystalline copper Ar plasma treated, heated to 250°C and 450°C. a) Overlay of survey spectra, b) overlay of O 1s region spectra, c) overlay of Cu 2p region spectra and d) overlay of C 1s region spectra.

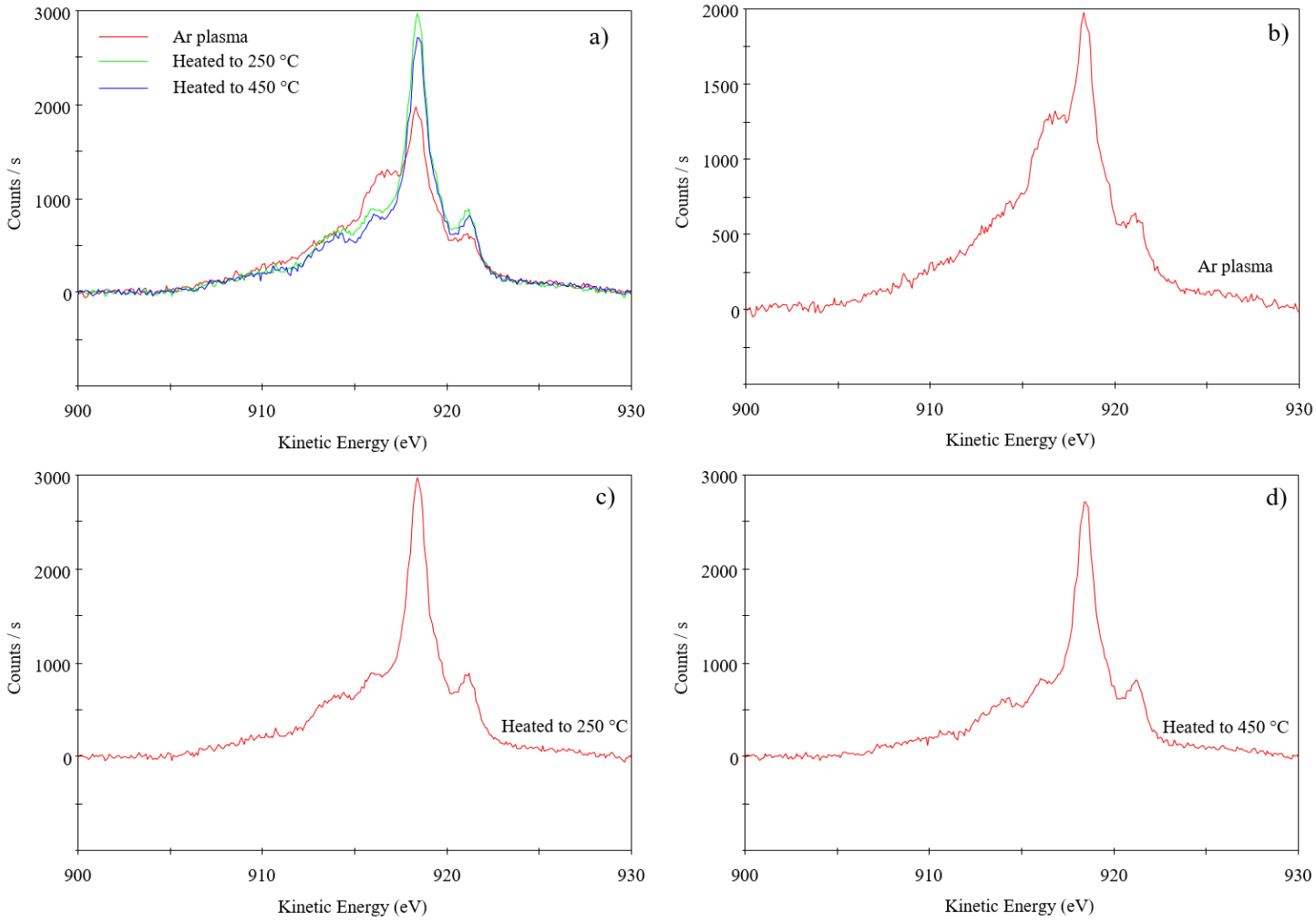


FIGURE 4.51: XPS Cu Auger spectra for bulk polycrystalline copper. a) Overlay of Cu LMM region for copper Ar plasma treated, heated to 250°C and 450°C. Cu LMM region spectrum b)Ar plasma treated, c) heated to 250°C and d) heated to 450°C.

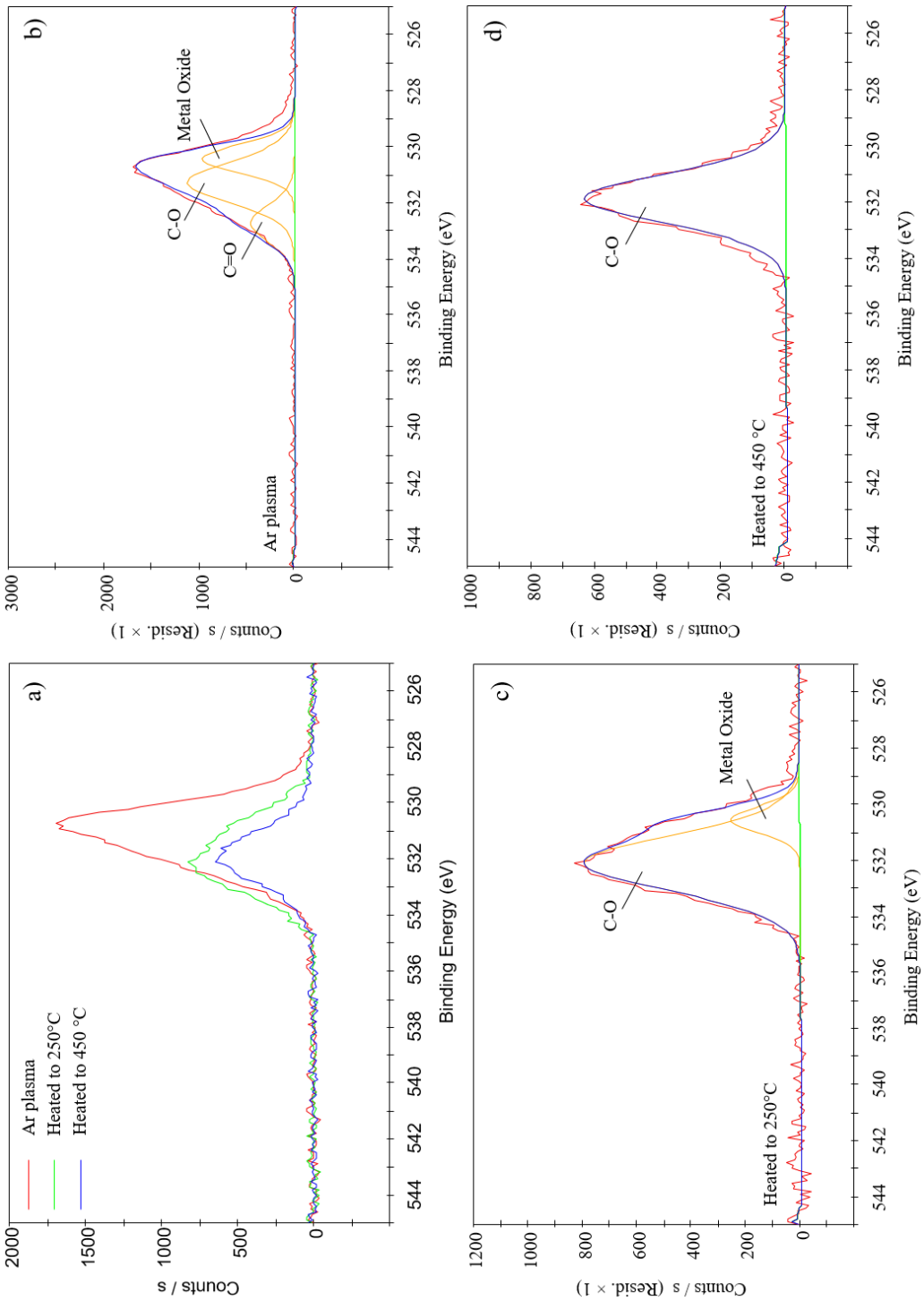


FIGURE 4.52: XPS O 1s region spectra for bulk polycrystalline copper. a) Overlay of O 1s region for copper Ar plasma treated, heated to 250°C and 450°C. Fitted O 1s region spectrum b) Ar plasma treated, c) heated to 250°C and d) heated to 450°C.

### 4.4.4 Discussion

For both Ar plasma treated copper and molybdenum, maximum photocurrent is extracted after heating to 450°C. This is now established as the optimum preparation procedure (*ex-situ* Ar plasma treatment followed by *in-situ* heating to 450°C for 1 hour) for bulk metals, and has been implemented in the preparation of the molybdenum plug installed into CLARA electron gun in order to generate first beam. The QE for copper was fractionally greater than for molybdenum according to the measurements, however,it must be noted that the photocurrent may not have been fully extracted and therefore QE measurements are relative and not absolute.

With respect to XPS measurements, the results confirm that Ar plasma treatment removes surface hydrocarbon contamination, and heating increases the metal component for copper and molybdenum. There is undoubtedly a correlation between the reduction of the metal oxide and increasing QE.

UPS measurements for the molybdenum sample yielded WF values that were lower than anticipated after heat treatment. However, the general trend seemed to be a reduction of the WF with heating. This correlates with an increase in molybdenum metallic component and an increase in QE.

In this work, attempts have been made to understand and rectify issues with photocurrent measurements. A possible explanation for the inconsistent QE was space charge effects. With the introduction of a UV LASER, the charge emitted over the area illuminated became greater compared with the UV LED. It was possible therefore, that this image charge (see Chapter 2, Equation 2.28) has some retarding effect on the photoemission. In order to investigate this, the laser spot size was increased by defocusing the laser beam; however the changes were negligible, and the QE was certainly not constant over variable laser power. In the future, there are plans to re-configure the QE measurement circuit so that rather than measuring the drain current from the photocathode, the photocurrent is measured at an anode some distance away from the photocathode. This method should ensure that all photocurrent is measured. With the current set-up, due to additional electrical connections for the heater stage and thermocouple, despite efforts to isolate these connections from each other, it is possible that there was some leakage or some adverse effects that influenced the sensitive QE measurements.

## 4.5 Conclusions

In this chapter, several surface preparation procedures for bulk metals have been investigated, and a range of surface characterisation techniques have been employed to achieve this. One of the first conclusions drawn in the preparation of bulk metals is that it is essential to treat the metals prior to use as a photocathode; the “as-received” surfaces yield poor photocurrent and therefore low QE. XPS measurements show a correlation

between surface contaminants and photoemission, suggesting that surface oxides and hydrocarbons reduce the photo-emissivity of the metals investigated. Though each metal investigated improved in QE after $Ar^+$ sputtering, only a selection exhibited QE values greater than copper. Additionally, measurements with the Kelvin Probe show a correlation between increasing WF values and decreasing QE. Therefore those metals with lower WF are favourable as photocathode materials. Consequently only those metals with WF equal to or lower than copper, and QE greater than copper were investigated further, them being: magnesium, niobium, titanium, zirconium, and copper (for reference). Though $Ar^+$ sputtering is an effective surface preparation technique, it may not be appropriate for photocathode preparation as studies have shown that the increase in surface roughness after $Ar^+$ sputtering can lead to an increase in the transverse energy component of the photoelectrons. Both O and Ar plasma treatment followed by heat treatment were investigated as an alternative.

In order to investigate the effects of O plasma treatment, MEIS was carried out to characterise the stoichiometry of the oxide layer. Several conclusions were drawn with respect to the procedure of O plasma treatment followed by heat treatment. In agreement with XPS studies, the MEIS spectra confirmed that the effect of O/Ar plasma treatment is to remove hydrocarbon surface contaminants from "as-received" copper surfaces. The studies suggested that the oxide layer of the O plasma treated copper surface is composed of $CuO_2$. The thickness of the $CuO_2$ layer varied between 300-700 nm depending on the variable plasma power. The effect of heating the O plasma treated copper to 300°C did not influence the thickness of the oxide layer, but changes in the fractional composition were observed. The surface layer stoichiometry changed from $CuO_2$ to $Cu_2O$ suggesting a reduction in the oxide. This reduction is in agreement with the XPS measurements. Only annealing to higher temperatures (approximately 700°C) resulted in the complete reduction of the oxide in the surface layers. In practice, *in-situ* heating of the photocathode in the gun would be limited due to the mechanisms of the cathode holder, and so heating to such high temperatures is not viable.

On the other hand, XPS studies reveal that Ar plasma treatment does not create so thick an oxide layer that heating (to 450°C)) cannot reduce. Heating O plasma treated copper to the same temperature does not result in as high a QE compared with Ar plasma treated copper. Therefore Ar plasma treatment followed by heating is the preferred preparation technique for metal photocathodes.

# Chapter 5

# Thin Film Growth on Cu, Mo and Si Substrates

Ultimately the application for this research is to produce and prepare metallic thin films deposited onto a molybdenum plug which will then be inserted into the high repetition rate gun that will eventually drive CLARA. Therefore, a critical part of the research program is to investigate the production and preparation of metallic thin films. The technique used to create thin films is PVD. Investigations of several metals deposited on silicon, molybdenum and copper substrates is presented in this chapter. The elemental composition and purity of the films, QE, WF and surface morphology of the films have been studied.

## 5.1 Cu and Nb thin films grown on Si substrates

The results from this work are published in the IPAC '15 conference proceedings [101]. Magnetron sputtering has been used to deposit polycrystalline copper and niobium thin films on silicon(100) substrates; this was a preliminary experiment, and so for operational photocathodes an appropriate substrate material will be chosen. The silicon substrates were cleaned and degreased in ultrasonic baths of acetone, IPA, methanol and then finally washed in deionised water. Niobium and copper were sputtered onto the silicon substrates; krypton sputter gas was used at a pressure of 3 mbar and the magnetron was operated at 600 W DC power. The thickness of the films can be assumed to be of the order of 1 $\mu$m. Though not measured directly, previous studies using the same growth parameters employed here yield similar results. As was the procedure for the polycrystalline photocathodes, the thin films were carefully inserted into a sample holder and cleaned in an ultrasonic bath of acetone for 10 minutes prior to installation in the ESCALAB system where the surfaces of the films were characterised. These measurements were taken prior to the installation of UV LASER 1 in the ESCALAB system, and so measurements were taken using the UV LED. Additionally, WF measurements were taken using the KP technique. In the case of the copper thin film, after characterisation "as-received", the sample was heated with the aim to reduce the surface oxide.

The copper thin film was not sputtered with $Ar^+$ for fear of removing the film entirely, but was heated to 250°C for 30 minutes. A summary of the quantified XPS data, WF and QE measurements for the copper thin film is presented in Tables 5.1 5.2.

TABLE 5.1: A summary of WF and QE "as-received" and after heating to 250°C for 30 minutes for copper thin film on a silicon substrate

| | WF (eV) | QE |
|---|---|---|
| **Cu on Si** | | |
| "As-received" | 5.14 | $1.47 \pm 0.01 \times 10^{-6}$ |
| Heated to 250°C | 4.68 | $1.14 \pm 0.01 \times 10^{-4}$ |

TABLE 5.2: A summary of quantified XPS data "as-received" and after heating to 250°C for 30 minutes for copper thin film on a silicon substrate

| | Cu 2p (%) | O 1s (%) | C 1s (%) | N 1s (%) | Si 2p (%) |
|---|---|---|---|---|---|
| **Cu on Si** | | | | | |
| "As-received" | 8.3 ± 0.3 | 22.2 ± 0.8 | 64.1 ± 1.1 | 5.4 ± 0.9 | |
| Heated to 250°C | 13.2 ± 0.6 | 14.7 ± 0.9 | 44.8 ± 1.9 | 2.8 ± 0.9 | 24.5 ± 2.4 |

Firstly consider the "as-received" copper film surface. The quantified XPS data obtained from the survey scans (see Figure 5.1a)) show that the surface is dominated by carbon contamination (approximately 64%). Additionally there is a significant amount of oxygen detected on the surface, and trace levels of copper and nitrogen. After deposition, the films had to be exposed to atmosphere before transferring into the ESCALAB system for analysis. Thus adventitious carbon layers would undoubtedly have formed on the surface during this period. Additionally exposure to atmosphere would also have oxidised the surface of the copper film. A similar elemental composition is observed for the "as-received" bulk polycrystalline copper (see Chapter 4). A closer look at the Cu 2p region scans show additional to the Cu 2p peaks, small satellite peaks occurring at approximately 9 eV higher binding energies to the main Cu 2p peaks; this is characteristic of CuO. Upon heating the film, the survey spectrum shows a slight increase in the copper content and a significant reduction of carbon and oxygen. Additionally there is an emergence of silicon on the surface. Evidently the effect of heating has exposed the silicon substrate beneath the film. The region scan for Cu 2p shows an increase in the intensity of the Cu 2p peaks, and perhaps a slight reduction of the satellites associated with CuO. Without a region scan of the Cu LMM peaks, it is not possible to distinguish between Cu metal and $Cu_2O$. However, the O 1s region scan shows a reduction in the intensity of the O 1s peak and a shift in the binding energy. This corresponds to a

change in chemical state from a mixture of C=O and C-O to metal oxide, as well as a reduction of oxygen.

The WF of the "as-received" copper film was measured to be approximately 5.1 eV which is approximately 0.45 eV higher than the literature quoted values for clean copper [35] [102]. This result is somewhat comparable to the measured WF value for the bulk polycrystalline copper sample, which was approximately 5.35 eV. After heat treatment, the measured WF reduced to approximately 4.68 eV. As discussed previously, an oxidised surface will serve to increase the WF and so the measured value for an "as-received" copper thin film is within the range of expectation. The WF measured after heat treatment is comparable with the literature value for a clean copper surface. This may suggest that the chemical state of the heated copper film is indeed Cu metal, and that the remaining oxygen may be associated with the silicon substrate.

The QE for both bulk and thin film copper "as-received" is comparable: $10^{-6}$ . Upon heating, the QE of the copper film increases by almost two orders of magnitude; this seems to correlate with a decrease in WF and decrease in surface contaminants. This value is an order of magnitude higher than the QE obtained from clean bulk polycrystalline copper.

For the niobium thin film, after characterisation "as-received", the sample was also heated to 250°C for 30 minutes. This did not produce a significant improvement in the QE or a QE that was comparable to the $Ar^+$ sputtered bulk polycrystalline niobium sample. The sample was then further heated to 300°C for 30 minutes and then finally $Ar^+$ Sputtered for 10 minutes. A summary of the quantified XPS data, WF and QE measurements for the niobium thin film is presented in Table 5.3.

Table 5.3: A summary of WF, QE and quantified XPS data for niobium thin film on a silicon substrate "as-received", after heating to 250°C for thirty minutes, heating to 300°C for thirty minutes and $Ar^+$ Sputtering for 10 minutes.

| | WF (eV) | QE | Nb 3d (%) | O 1s (%) | C 1s (%) |
|---|---|---|---|---|---|
| **Nb on Si** | | | | | |
| "As-received" | 4.35 | $7.75 \pm 0.04 \times 10^{-7}$ | 11.6 ± 0.8 | 63.1 ± 2.4 | 25.3 ± 2.8 |
| Heated to 250°C | 4.89 | $2.45 \pm 0.01 \times 10^{-5}$ | 34.2 ± 2.2 | 61.5 ± 3.6 | 4.3 ± 5.2 |
| Heated to 300°C | 5.14 | $5.66 \pm 0.03 \times 10^{-6}$ | 28.2 ± 1.6 | 55.8 ± 2.7 | 16.0 ± 3.8 |
| $Ar^+$ Sputter | 4.77 | $2.64 \pm 0.02 \times 10^{-4}$ | 90.4 ± 3.8 | 9.6 ± 3.8 | 0 |

The elemental composition of the niobium film as quantified from the survey spectra (see Figure 5.2a)) is shown in Table 5.3. "As-received" the surface of the film is highly oxidised with O 1s making up approximately 63% of the surface. Adventitious carbon is also observed on the surface (25%) and niobium accounts for only 11% of the surface composition. Upon heating first to 250°C, the metal component increases by a factor of three, and the carbon content reduces to a quarter of the original amount. However,

the oxide does not significantly reduce. After further heating to 300°C there is a re-emergence and increase in the surface carbon. This is either due to degassing of the chamber during heating or migration of carbon from below the sample surface. After a cycle of $Ar^+$ sputtering (10 minute cycles at 5 keV and $50\mu A$), the oxygen and carbon reduce to trace levels and the Nb component becomes dominant. An overlay of the Nb 3d region scans "as-received", after heating to 250°C, to 300°C and after sputtering is shown in Figure 5.2 b). As well as changes with respect to the intensity of the Nb 3d peaks there are clearly changes in the binding energy of the peaks which suggests changes in the chemical states. These plots have been fitted to identify the chemical states after each process in Figure 5.3. "As-received", Figure 5.3 a) shows two sets of Nb 3d peaks. The dominant set, accounting for 82%, have binding energies corresponding to $Nb_2O_5$. Smaller Nb 3d peaks at lower binding energies corresponding to Nb metal accounting for 18% are also observed. This region scan would suggest that the surface of the thin film "as-received" is mixed with respect to its chemical state. Upon heating to 250°C, the oxide reduces into another mix of chemical states; the main Nb 3d peaks have binding energies associated with NbO, and the second set of peaks have binding energies between that of $NbO_2$ and NbO. Further heating to 300°C results in a surface entirely characterised by NbO. The effect of sputtering is to further reduce the chemical state to Nb/NbO.

The WF measurements for the niobium thin film alter at every stage of the preparation. "As-received" the WF is measured to be 4.35 eV, which is in good agreement with the literature values for a clean niobium surface. However, this measurement is lower than the expected value for an oxidised niobium surface. Heating the sample increases the WF both at 250°C and at 300°C. It is possible that changes to the surface morphology contributes to this increase. As described in Chapter 2, sharp micro-structures in rough surfaces have been shown to have a lower WF than smoother surfaces [66]. Thus a possible explanation for the increase in the WF is that heating the samples may have resulted in a reduction of the surface roughness, bringing about an increase in the WF. Finally sputtering the film reduces the WF by approximately 0.3 eV. This may correlate with a reduction of surface contaminants or an increase in surface roughness.

The QE measurements on the other hand seem to correlate with the amount of surface contaminants. For example, the lowest QE is measured for the "as-received" surface; the large quantity of oxygen and carbon contamination may explain this. Heating the sample increases the QE by a factor of thirty. This correlates with an increase in the Nb metal component and a significant decrease in the carbon content. Further heating reduces the QE by an order of magnitude. This correlates with a reduction in the Nb metal component and a re-emergence of surface carbon. The effect of sputtering is to produce a QE of the order of $10^{-4}$. This value is comparable with the measurement obtained for the $Ar^+$ sputtered bulk polycrystalline niobium sample.

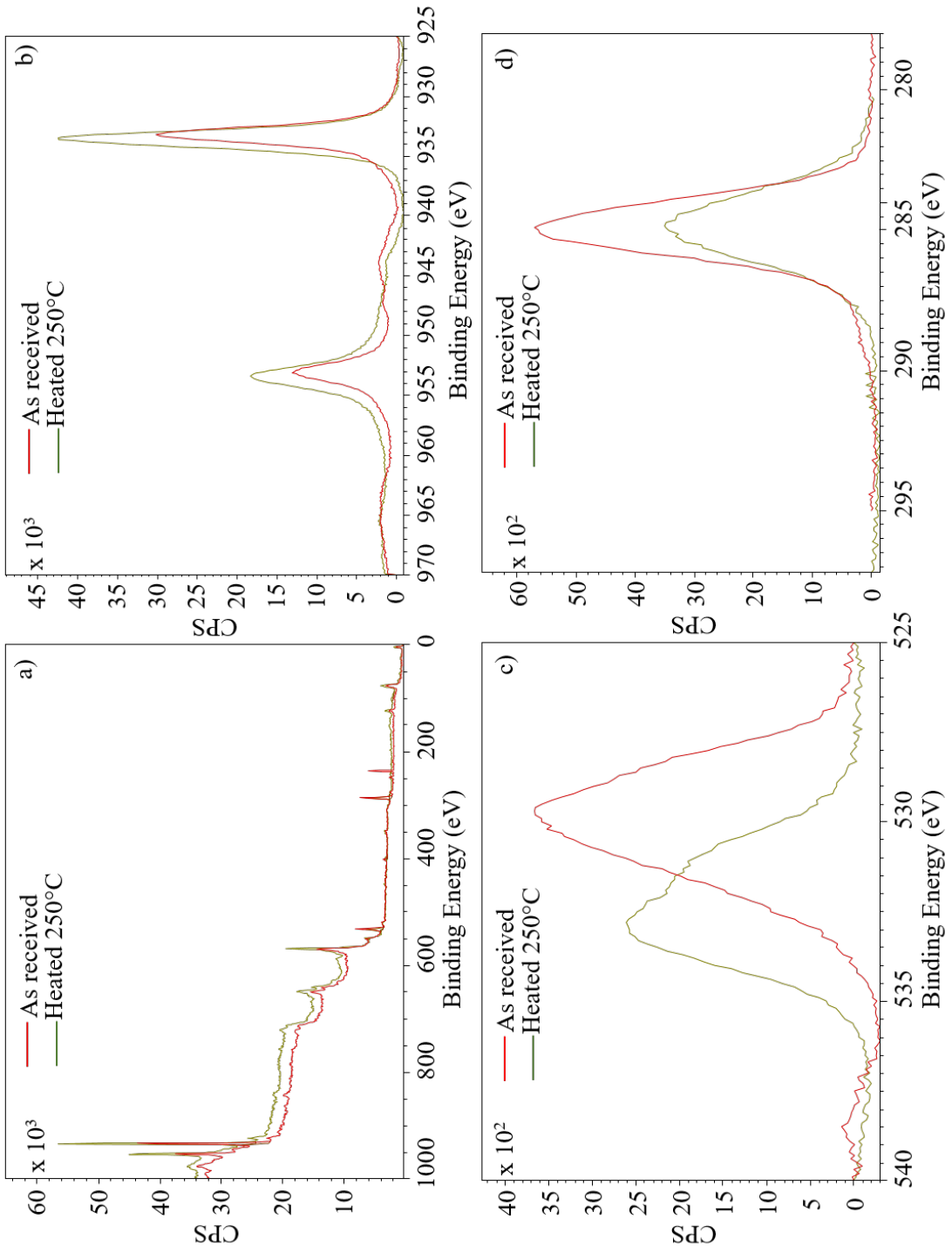


FIGURE 5.1: XPS spectra for copper thin film on a silicon substrate "as-received" and heated to 250°C for 30 minutes. a) Overlay of survey spectra, b) overlay of Cu 2p region spectra, c) overlay of O 1s region spectra and d) overlay of C 1s region spectra.

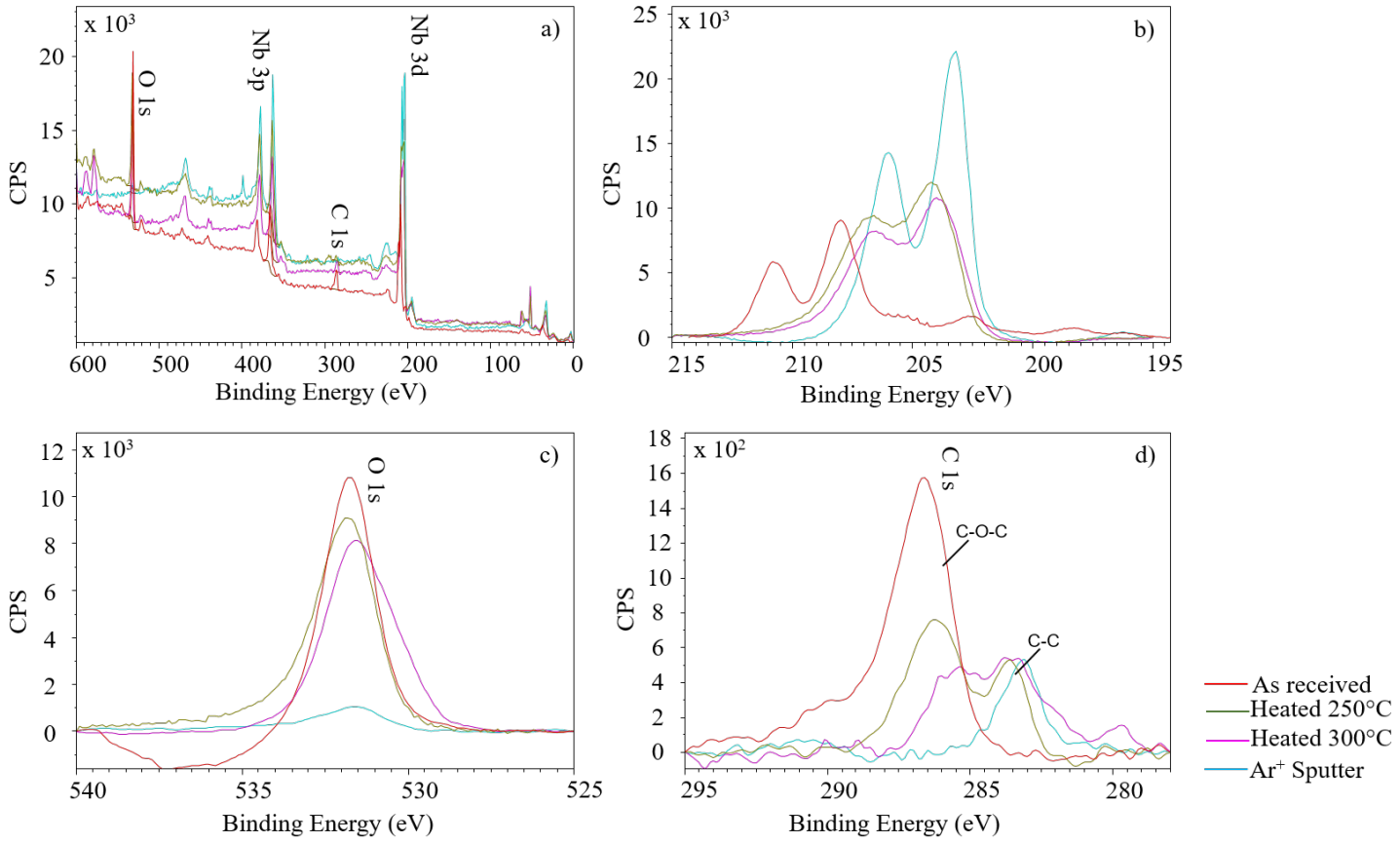


FIGURE 5.2: XPS spectra for niobium thin film on a silicon substrate "as-received", heated to 250°C for 30 minutes, heated to 300°C for 30 minutes and $Ar^+$ sputtered for 10 minutes. a) Overlay of survey spectra, b) overlay of Nb 3d region spectra, c) overlay of O 1s region spectra and d) overlay of C 1s region spectra.

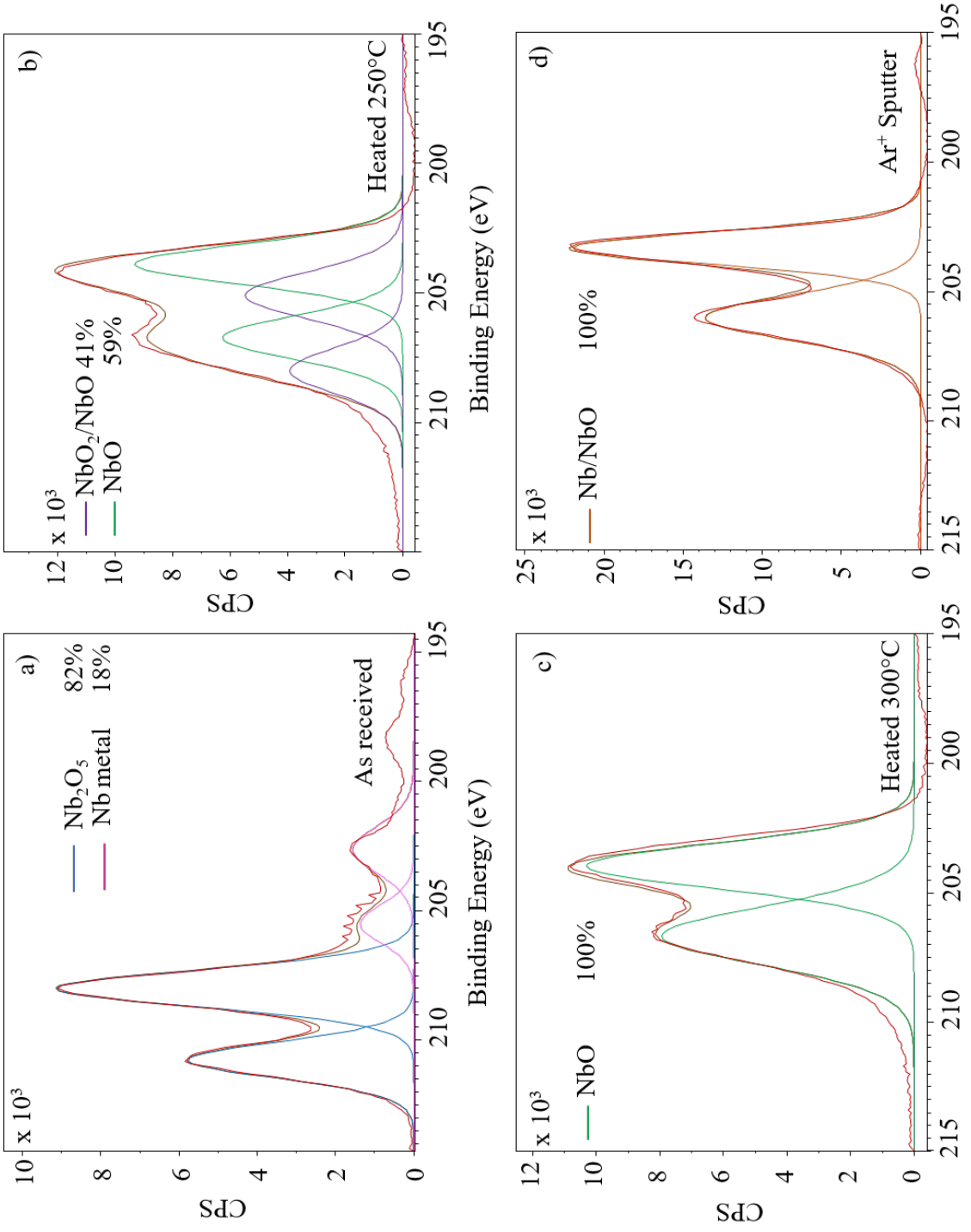


FIGURE 5.3: XPS spectra for Nb 3d region a) "as-received", b) after heating to 250°C for 30 minutes, c) after heating to 300°C for 30 minutes and d) after $Ar^+$ sputtering for 10 minutes.

## 5.2 Cu, Pb and Zr thin films grown on Cu, Mo and Si substrates

A second attempt to grow metallic thin films on different substrates was made almost a year after the afore mentioned work in section 5.1. In this work the preparation and characterisation of copper, lead and zirconium thin film photocathodes is described. The results from this work are published in the IPAC '16 conference proceedings [103].
The samples grown onto copper and molybdenum substrates were analysed and tested as photocathodes in the Multiprobe system. Molybdenum is the choice substrate material for the CLARA photocathode and copper has been selected as the baseline photocathode material. The films deposited onto silicon substrates were used to characterise the morphology of the film.

The deposition procedure for these films are very similar to the procedure outlined in section 5.1. Copper, lead and zirconium thin films were produced by DC magnetron sputtering onto copper, molybdenum and silicon substrates. The substrates were cleaned and degreased in ultrasonic baths of acetone and then washed in deionised water. Krypton sputter gas was used at approximately $5 \times 10^{-2}$ mbar at ambient temperature for each deposition, using a pulsed DC power supply. The parameters are listed below in Table 5.4. As a precautionary measure, lead was deposited at a lower power due to its lower melting temperature.

TABLE 5.4: Parameters for deposition of copper, lead and zirconium films by DC magnetron sputtering.

| Metal | DC Power (W) | Pressure (mbar) | Time (hrs) |
|---|---|---|---|
| **Copper** | 300 | $5.4 \times 10^{-2}$ | 1 |
| **Lead** | 100 | $4.3 \times 10^{-2}$ | 3 |
| **Zirconium** | 300 | $8.5 \times 10^{-2}$ | 1 |

Each thin film was subsequently taken out of the chamber and stored at atmosphere for a short period of time prior to loading into the Multiprobe system for analysis. UV LASER 2 was used for QE measurements in the Multiprobe system. Additionally UPS technique was used to determine the WF of the thin films. As discussed in Chapter 4, the error associated with the UPS WF calculations are quite high (approxiately 6%). The samples were characterised in the Multiprobe analysis chamber under UHV conditions and ambient temperature.

Table 5.5 summarises the quantitative results from the analysis of the films deposited on both copper and molybdenum substrates "as-received" and after half an hour of $Ar^+$ sputtering.

TABLE 5.5: A summary of WF, QE and quantified XPS data for copper, lead and zirconium films "as-received" and after $Ar^+$ Sputtering for 30 minutes.

| | WF (eV) | QE | Metal (%) | O 1s (%) | C 1s (%) |
|---|---|---|---|---|---|
| **Cu on Cu** | | | | | |
| "As-received" | 4.7 | $4.08 \pm 0.02 \times 10^{-7}$ | 39.6 ± 1.3 | 60.4 ± 1.3 | 0 |
| $Ar^+$ Sputter | 4.5 | $9.85 \pm 0.06 \times 10^{-7}$ | 93.3 ± 2.1 | 6.7 ± 2.1 | 0 |
| **Cu on Mo** | | | | | |
| "As-received" | 4.6 | $2.03 \pm 0.01 \times 10^{-6}$ | 36.4 ± 2.4 | 48.5 ± 3.1 | 15.1 ± 4.8 |
| $Ar^+$ Sputter | 4.4 | $2.75 \pm 0.02 \times 10^{-6}$ | 100 | 0 | 0 |
| **Pb on Cu** | | | | | |
| "As-received" | 3.8 | $2.55 \pm 0.01 \times 10^{-6}$ | 69.7 ± 4.0 | 30.3 ± 4.0 | 0 |
| $Ar^+$ Sputter | 4.1 | $4.10 \pm 0.02 \times 10^{-6}$ | 100 | 0 | 0 |
| **Pb on Mo** | | | | | |
| "As-received" | 3.6 | $1.88 \pm 0.01 \times 10^{-6}$ | 47.5 ± 2.6 | 52.5 ± 2.6 | 0 |
| $Ar^+$ Sputter | 4.1 | $4.35 \pm 0.02 \times 10^{-6}$ | 100 | 0 | 0 |
| **Zr on Cu** | | | | | |
| "As-received" | 3.8 | $9.35 \pm 0.05 \times 10^{-7}$ | 26.8 ± 1.3 | 73.2 ± 1.3 | 0 |
| $Ar^+$ Sputter | 3.7 | $2.15 \pm 0.01 \times 10^{-6}$ | 89.4 ± 6.8 | 10.6 ± 6.8 | 0 |
| **Zr on Mo** | | | | | |
| "As-received" | 3.7 | $7.29 \pm 0.04 \times 10^{-7}$ | 24.6 ± 1.5 | 75.4 ± 1.5 | 0 |
| $Ar^+$ Sputter | 3.6 | $2.31 \pm 0.01 \times 10^{-6}$ | 87.6 ± 6.7 | 12.4 ± 6.7 | 0 |

### 5.2.1 Copper films

XPS quantitative data for copper films deposited on copper and molybdenum substrates is shown in Table 5.5. "As-received" the Cu on Cu film surface comprises of copper (40 %) and oxygen (60 %). However in the case of the Cu on Mo film, 15% of the surface is comprised of carbon; this inconsistency can be explained by the difference in atmospheric exposure times. Though both films were deposited at the same time, the Cu on Cu film was the first to be characterised in the Multiprobe system and so it will have spent a significantly shorter time at atmosphere than the Cu on Mo sample.

For the Cu on Cu film, the chemical state of the copper "as-received" is determined by analysis of the Cu 2p region scan and the Cu LMM region scan as shown in Figure 5.6 a) and b). The Cu 2p region scan suggests the presence of CuO by the distinctive satellite peaks occurring at binding energies of 942 eV and 962 eV. More information is obtained from the Cu LMM region scan which shows both features of Cu metal and CuO. There are two peak maxima occurring at 918.2 eV and 916.8 eV corresponding to Cu metal and CuO respectively.

For the Cu on Mo film "as-received", unlike the Cu on Cu scan, there are no significant satellite peaks in the Cu 2p region scan (see Figure 5.9 a)) to suggest that there

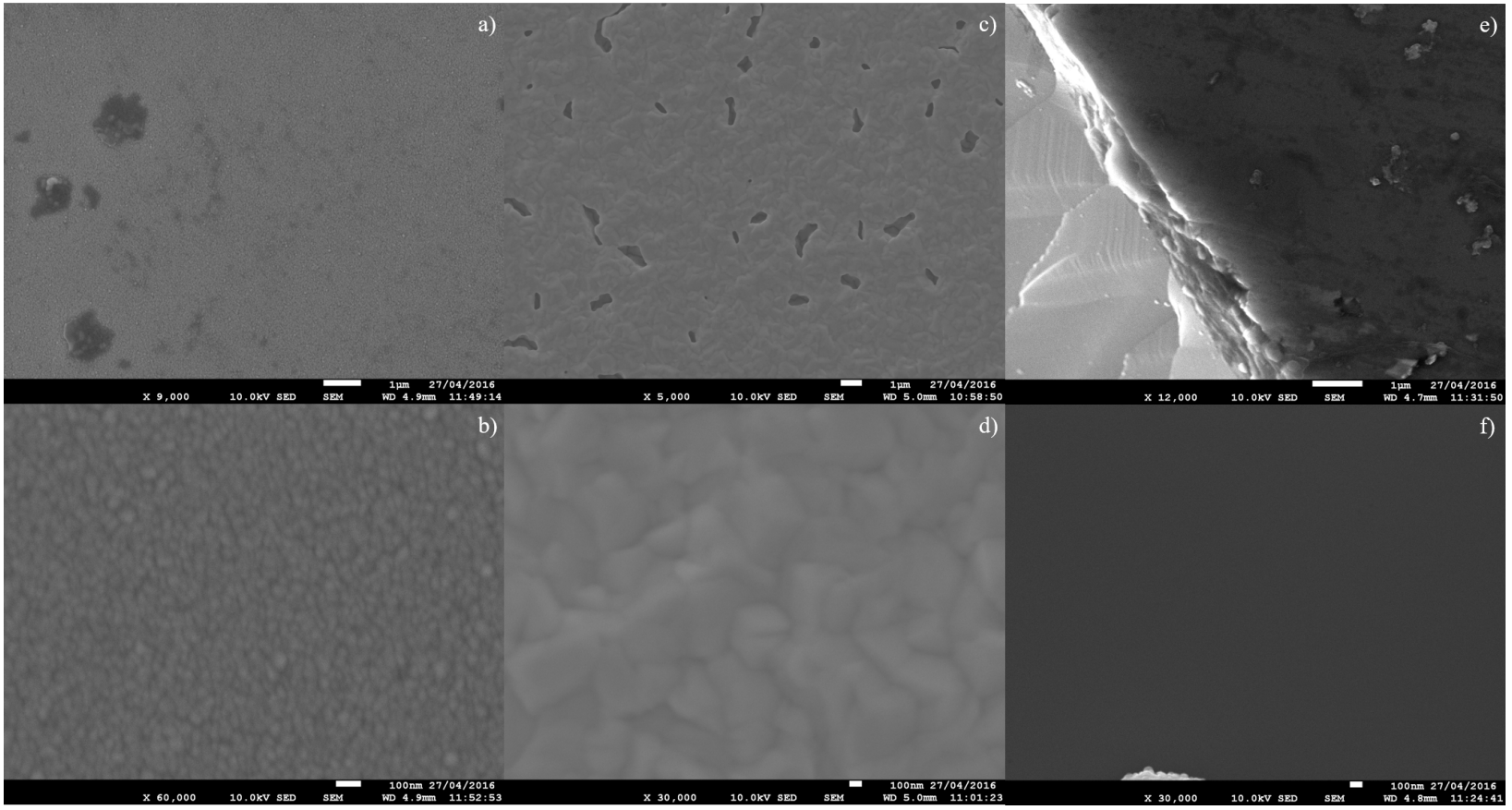


FIGURE 5.4: SEM images for films grown on Si substrates. a) Copper 1 um resolution, b) Copper 100 nm resolution, c) Lead 1 um resolution, d) Lead 100 nm resolution, e) Zirconium 1 um resolution, f) Zirconium 100 nm resolution.

is any CuO on the surface. The Cu LMM region scan shown in Figure 5.9 b) suggests a mixture of two chemical states. There are peaks occurring at 918.3 eV and approximately 921 eV corresponding to Cu metal. Additionally there is a peak at 916.6 eV; this is midway between the oxidation state for CuO and $Cu_2O$.

The effect of sputtering the copper films is to reduce the surface oxygen and carbon to trace level (see Table 5.5). This is evidenced in Figures 5.5 and 5.8 for Cu on Cu and Cu on Mo respectively. Additionally, the Cu LMM region scans in Figure 5.6 d) and 5.9 d) both correspond to Cu metal.

The WF measurements for the sputtered films quoted in Table 5.5 were estimated from the UPS scans shown in Figures 5.11 and 5.12. As has been the case with all UPS measurements in this work, the Fermi edge is not clearly defined for contaminated surfaces in UPS spectra. However, for a given spectrometer, the Fermi edge is always in the same place; therefore the Fermi edge measured from the sputtered surface should be the same for the as-received surface. It is with this assumption that estimates for the WF "as-received" have been made.

From the high-resolution region scans of the secondary electron cut-off for both the Cu on Cu and Cu on Mo films (see Figures 5.11 a) and b) and Figures 5.12 a) and b) respectively) it is evident that the position of the secondary electron cut-off shifts to a lower binding energy after sputtering; this leads to an overall increase in the width of the spectra and therefore a reduction in the WF. The WF measurements for $Ar^+$ sputtered copper films is comparable: 4.5 eV and 4.4 eV respectively. These values are approximately 0.2 eV lower than the literature quoted values for clean copper [35]. With respect to the QE values, for both copper films the QE improves with sputtering in correlation with reduction of surface contaminants, as anticipated. However, the QE for the Cu on Mo film has a QE value that is of almost a factor of three greater than the QE of the Cu on Cu film.

In Figure 5.4 a) and b), SEM images for the copper film on a silicon substrate shows the film to have a dense columnar structure, and a grain size of approximately 50 nm.

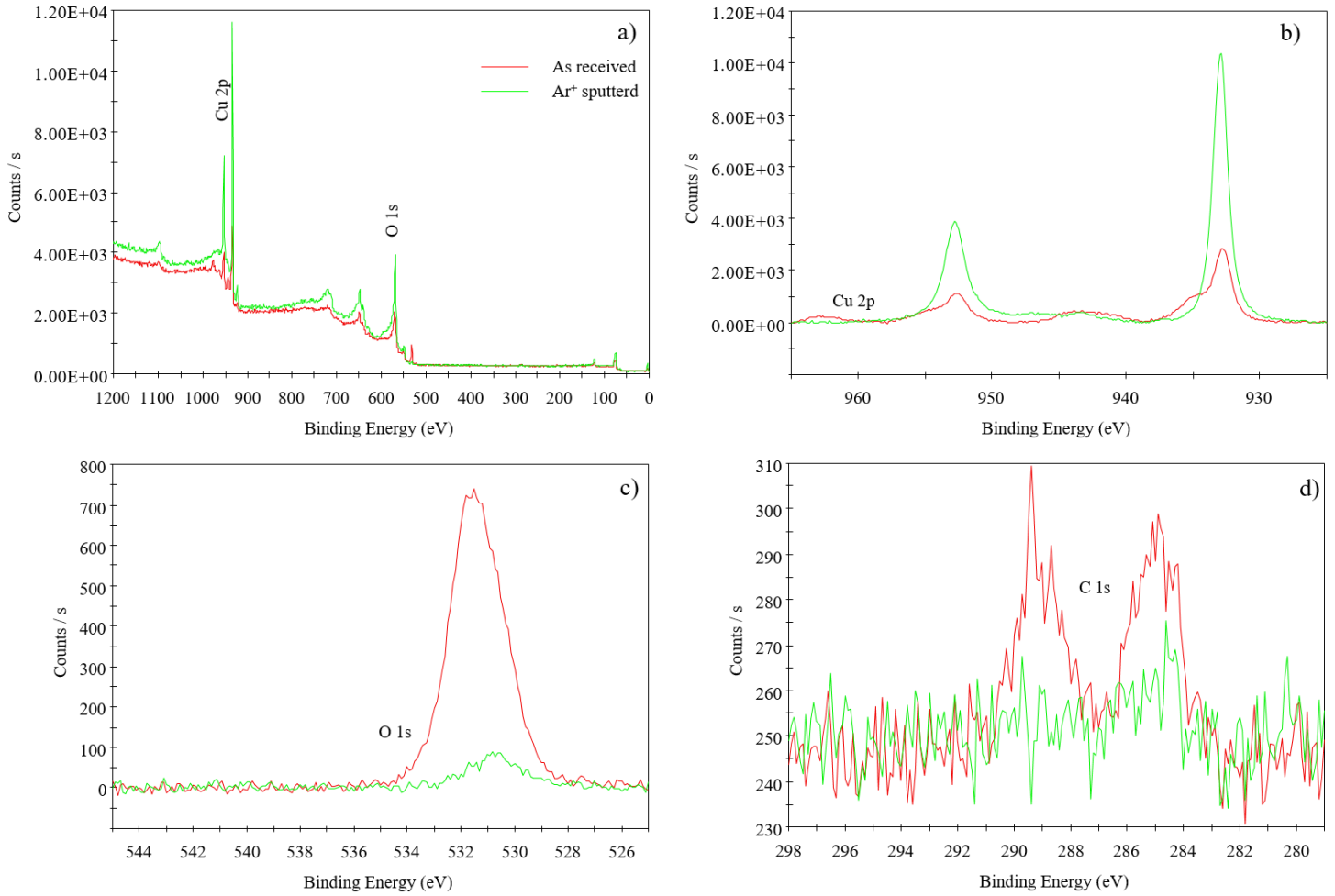


FIGURE 5.5: XPS spectra for copper thin film on a copper substrate "as-received" and after 30 minutes of $Ar^+$ sputtering. a) Overlay of survey spectra, b) overlay of Cu 2p region spectra, c) overlay of O 1s region spectra and d) overlay of C 1s region spectra.

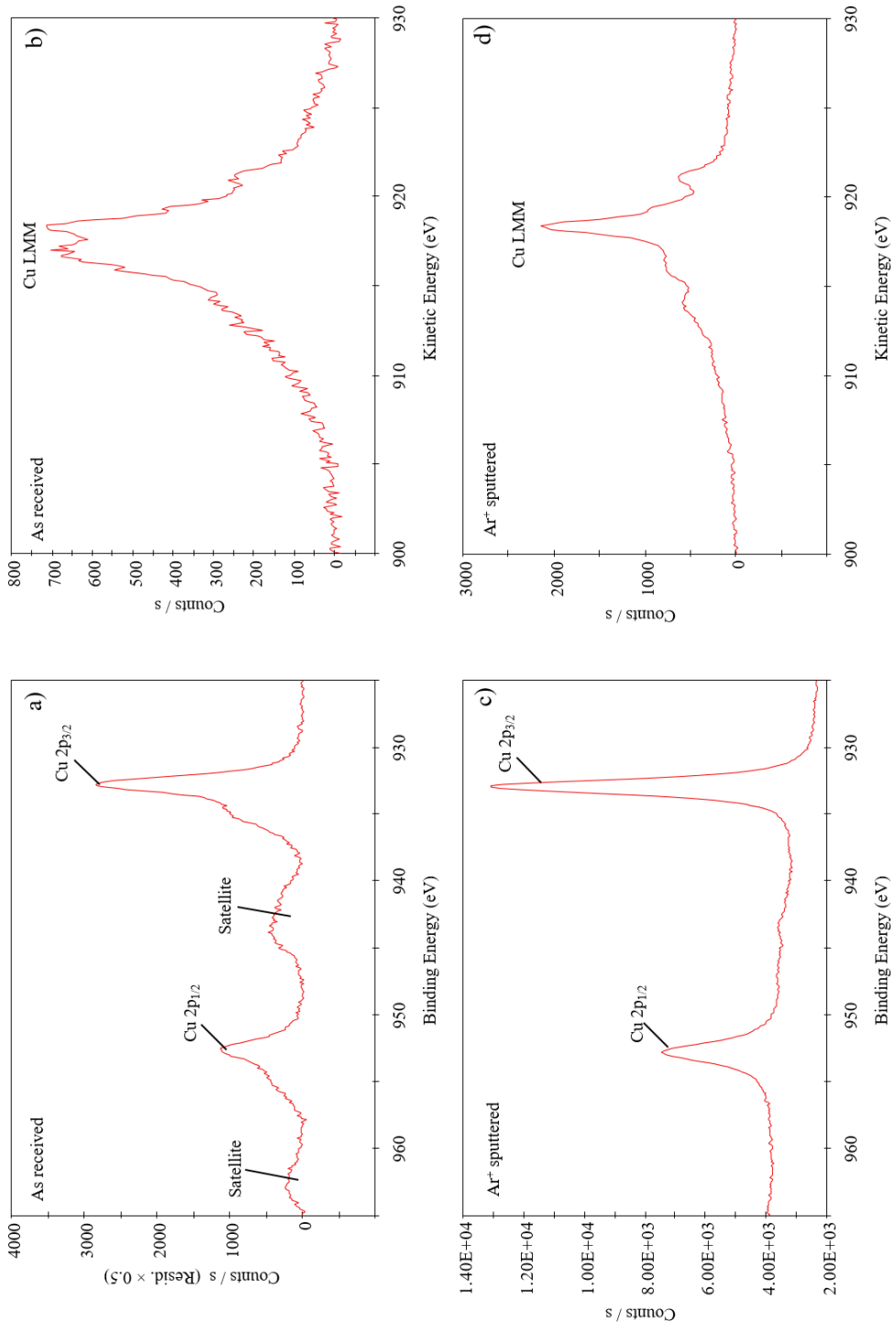


FIGURE 5.6: XPS spectra for Cu on Cu. a) Cu 2p region "as-received", b) Cu LMM region spectra "as-received", c) Cu 2p region $Ar^+$ sputtered for 30 minutes and d) Cu LMM region spectra $Ar^+$ sputtered for 30 minutes.

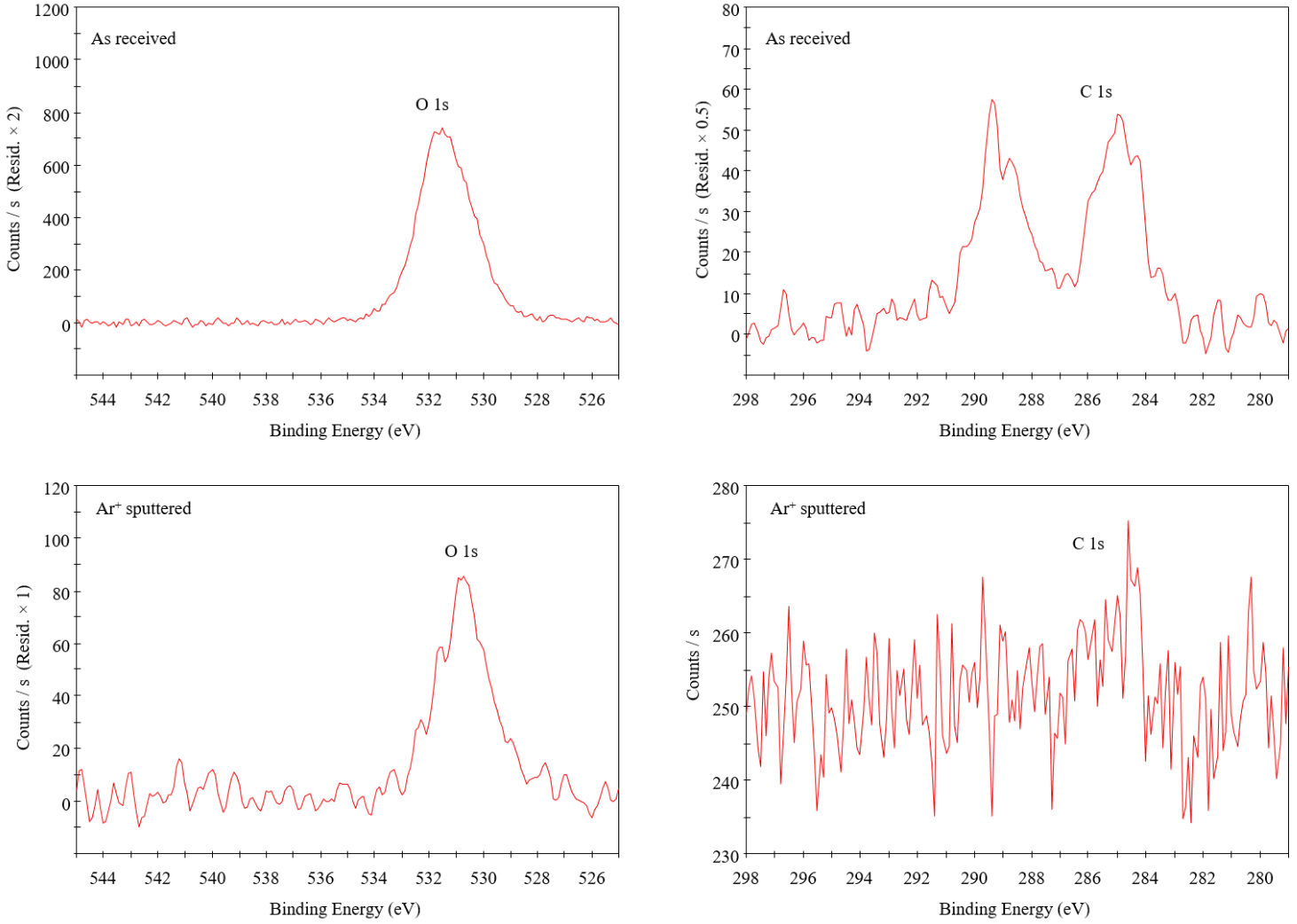


FIGURE 5.7: XPS spectra for Cu on Cu. a) O 1s region "as-received", b) C 1s region spectra "as-received", c) O 1s region $Ar^+$ sputtered for 30 minutes and d) C 1s region spectra $Ar^+$ sputtered for 30 minutes.

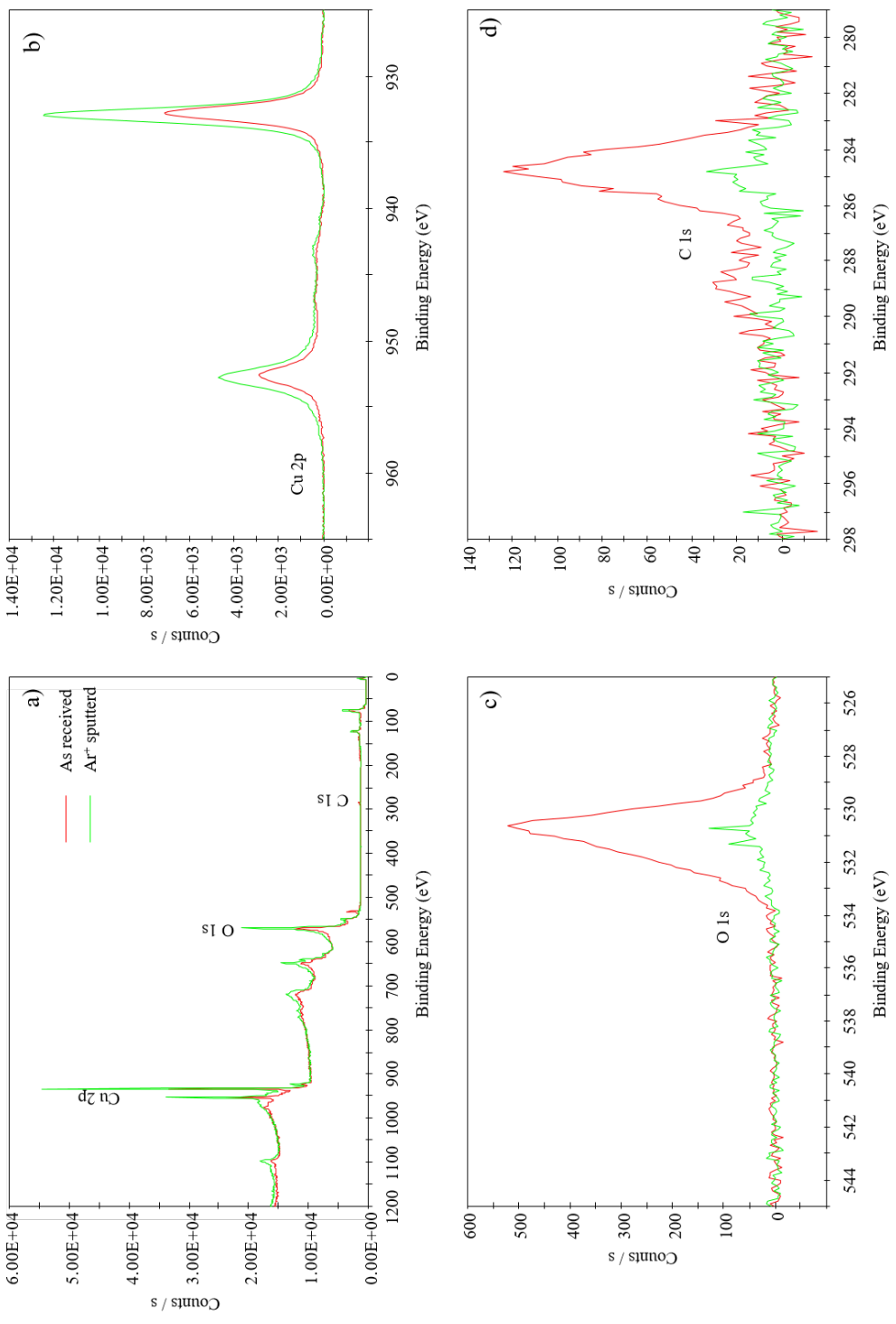


FIGURE 5.8: XPS spectra for copper thin film on a molybdenum substrate "as-received" and after 30 minutes of $Ar^+$ sputtering. a) Overlay of survey spectra, b) overlay of Cu 2p region spectra, c) overlay of O 1s region spectra and d) overlay of C 1s region spectra.

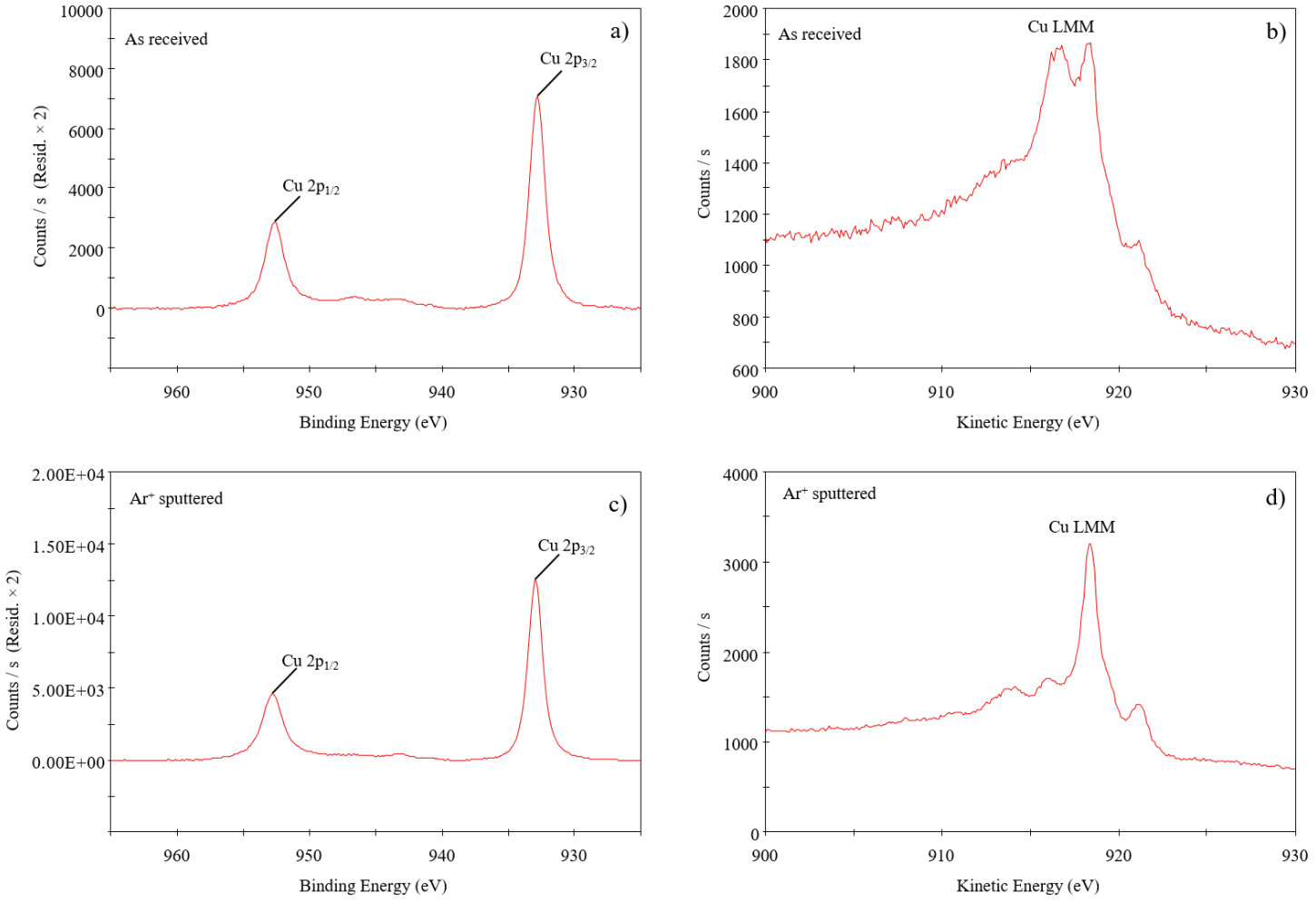


FIGURE 5.9: XPS spectra for Cu on Mo. a) Cu 2p region "as-received", b) Cu LMM region spectra "as-received", c) Cu 2p region $Ar^+$ sputtered for 30 minutes and d) Cu LMM region spectra $Ar^+$ sputtered for 30 minutes.

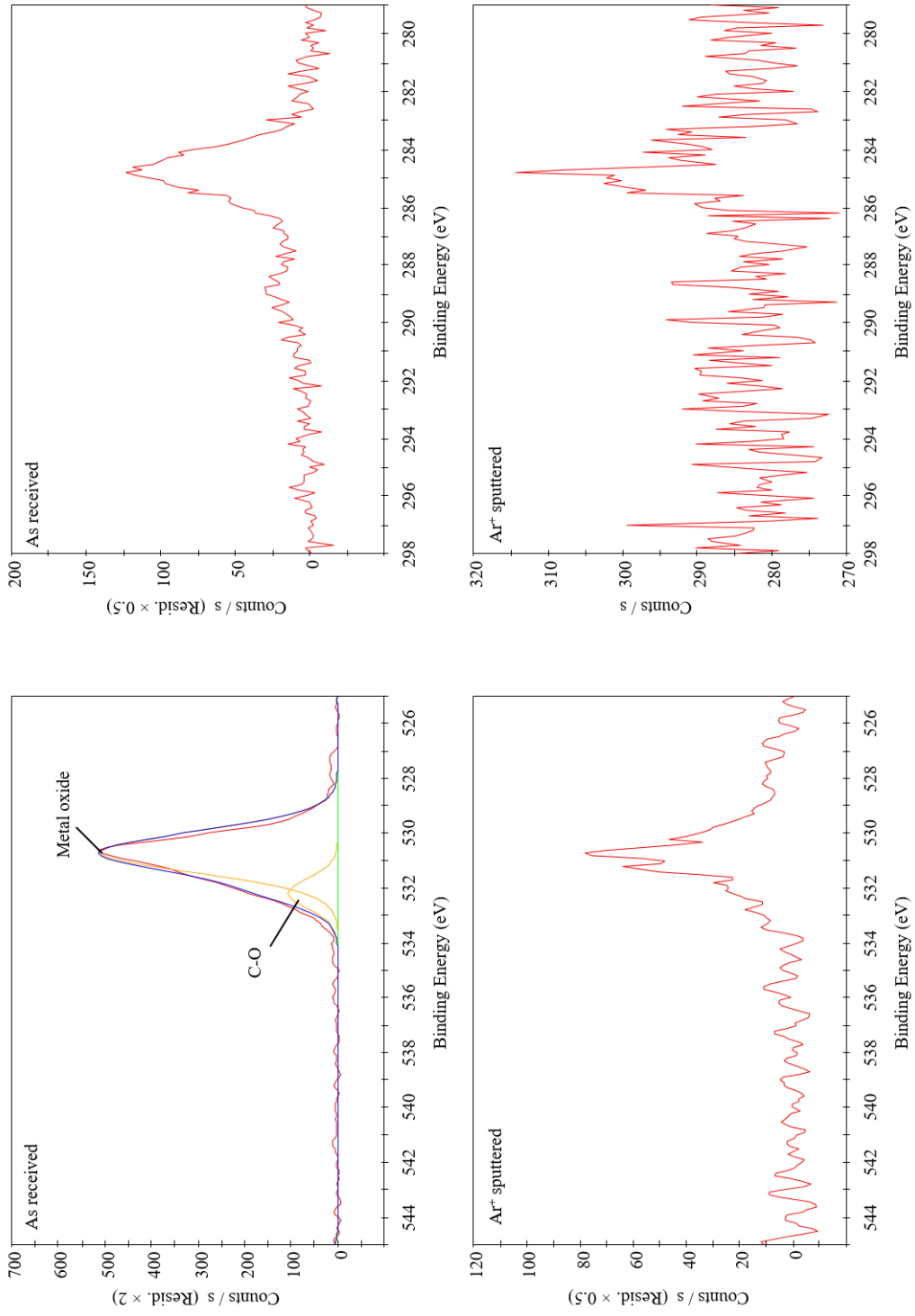


FIGURE 5.10: XPS spectra for Cu on Mo. a) O 1s region "as-received", b) C 1s region spectra "as-received", c) O 1s region $Ar^+$ sputtered for 30 minutes and d) C 1s region spectra $Ar^+$ sputtered for 30 minutes.

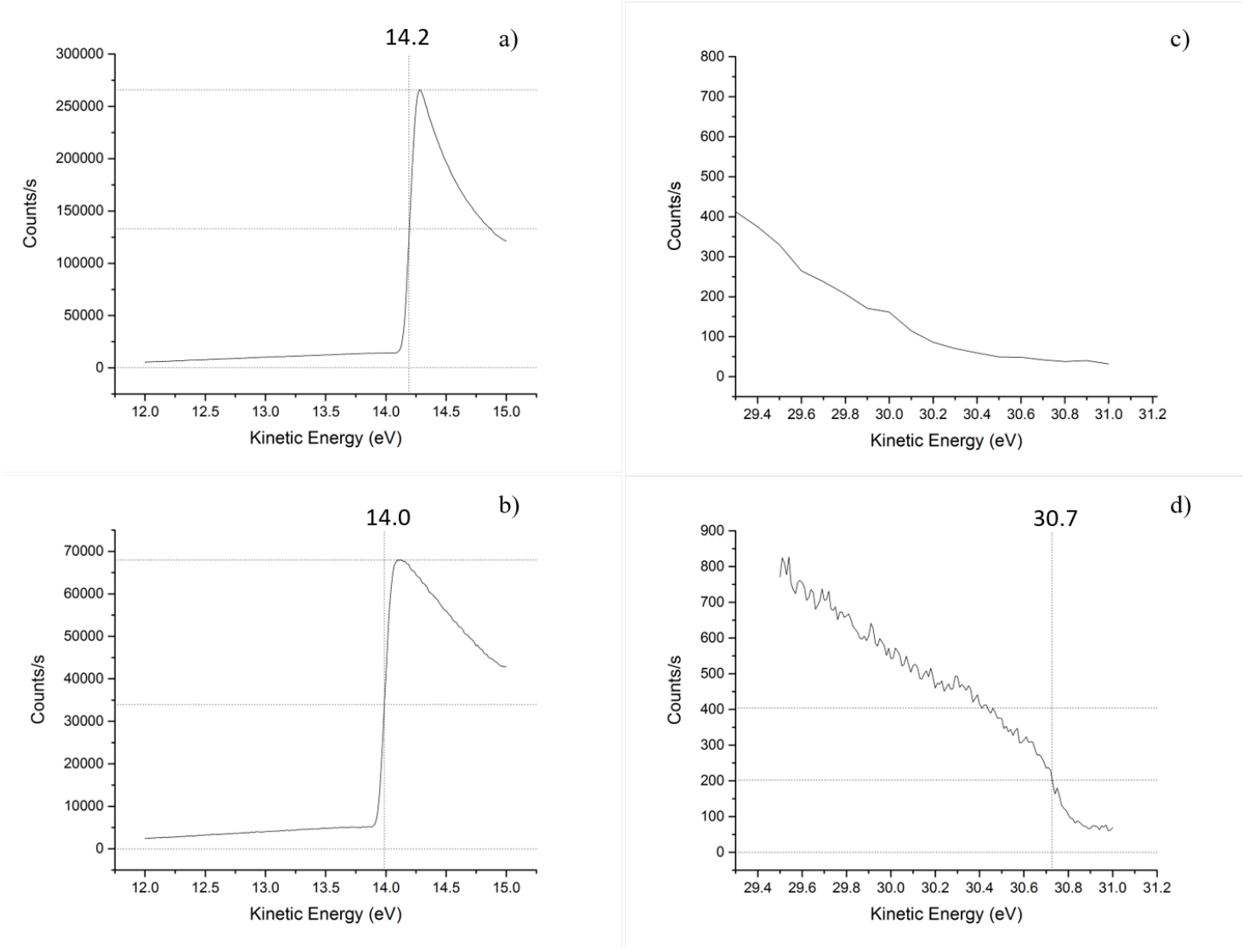


FIGURE 5.11: UPS spectra for Cu on Cu. a) Secondary electron cut-off region "as-received", b) after $Ar^+$ sputtering, c) Fermi edge region "as-received" and d) after $Ar^+$ sputtering.

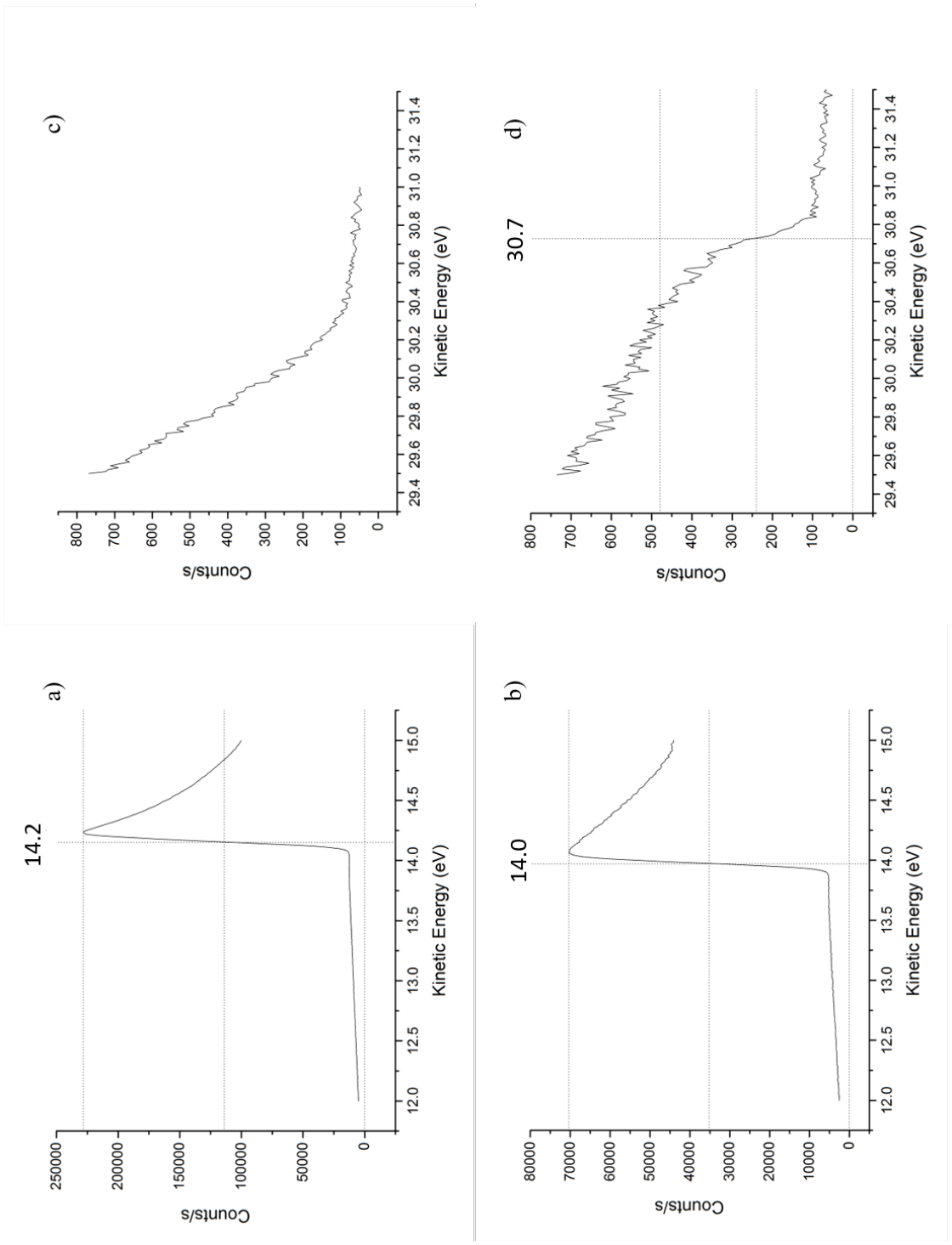


FIGURE 5.12: UPS spectra for Cu on Mo. a) Secondary electron cut-off region "as-received", b) after $Ar^+$ sputtering, c) Fermi edge region "as-received" and d) after $Ar^+$ sputtering.

### 5.2.2 Lead films

Results for the lead films are discussed in this section. A quantification of the elemental composition obtained from the survey spectra (see Figures 5.13 and 5.15) is presented in Table 5.5; the data show that both lead films "as-received" have oxygen contamination, but no carbon contamination. Upon sputtering, the oxygen is reduced to undetectable levels and a metallic lead surface is exposed as shown in in Figures 5.13 and 5.15.

For the Pb on Cu film, the Pb 4f region scans show a significant shift in the binding energy, an increase in the intensity and change in shape of the Pb 4f peaks after sputtering (see Figure 5.13 b)). The increase in intensity of the Pb 4f peaks indicate an increase in the quantity of lead on the surface. The Pb 4f peaks "as-received" are resolved into two sets of peaks as shown in Figure 5.14 a). The two Pb $4f_7/2$ peaks occur at 137 eV and 138.2 eV which correspond to Pb metal (33%) and $PbO_2$ (67%) respectively. After $Ar^+$ sputtering, the peaks corresponding to $PbO_2$ reduce to only 16% and the Pb metal component increases to 84% (see Figure 5.14c)).

For the Pb on Mo films, the Pb 4f peaks "as-received" and after $Ar^+$ sputtering are overlaid in Figure 5.15 b). As with the Pb on Cu Pb 4f region scans, the shift in position of the Pb 4f peaks correspond to a reduction in the lead oxide. The fitted Pb 4f peaks shown in Figure 5.16 a) show that the dominant chemical state is $Pb_3O_4$ (94%) with some Pb metal (6%) "as-received". After sputtering the oxide component reduces to 16% and the Pb metal component increases to 84%.

WF values for $Ar^+$ sputtered lead films presented in Table 5.5 are obtained from UPS scans in Figures 5.17 and 5.18 Both sputtered films had a WF of approximately 4.1 eV; the literature values for the WF of lead is 4.25 eV. Interestingly, the deduced WF values "as-received" are lower than for the sputtered lead films; this is difficult to correlate with the changes in the surface chemistry.

With very similar elemental composition and WF, it is not surprising that the QE values for the lead films deposited on copper and molybdenum are comparable.

In Figure 5.4 c) and d), SEM images for the lead film on a silicon substrate shows the film to have a dense columnar structure like the copper film, but with a much larger grain size of approximately 0.7 $\mu$m.

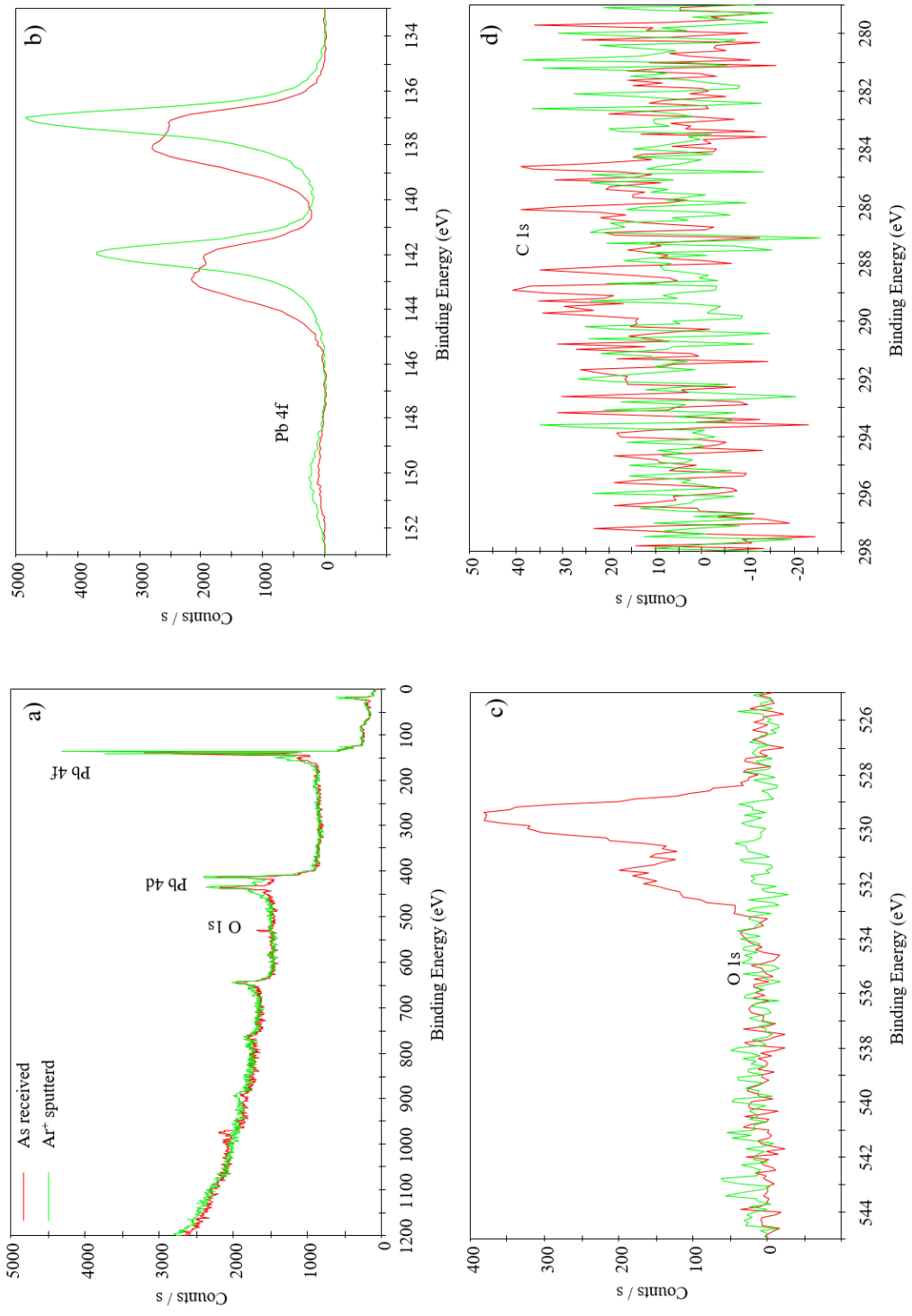


FIGURE 5.13: XPS spectra for lead thin film on a copper substrate "as-received" and after 30 minutes of $Ar^+$ sputtering. a) Overlay of survey spectra, b) overlay of Pb 4f region spectra, c) overlay of O 1s region spectra and d) overlay of C 1s region spectra.

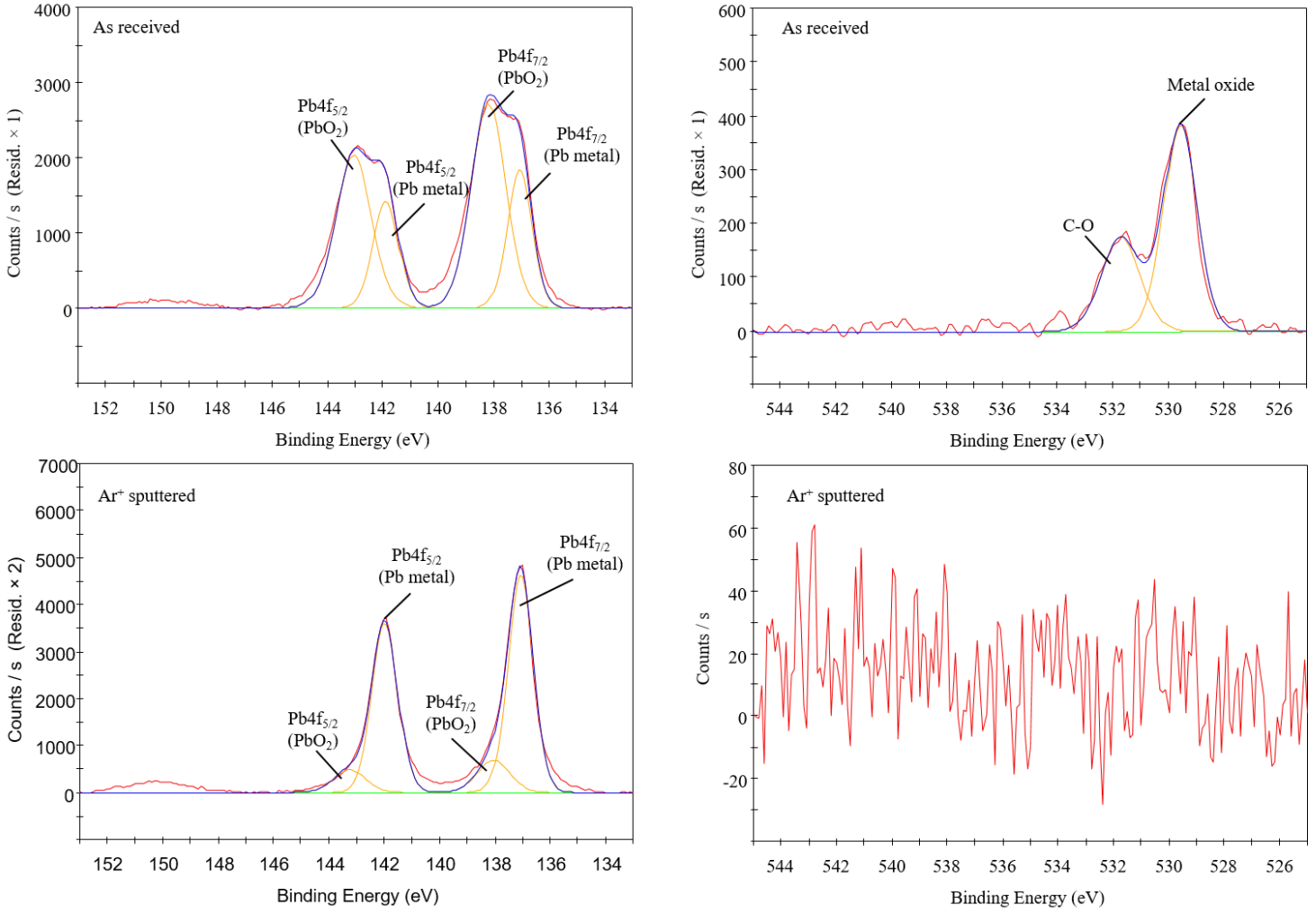


FIGURE 5.14: XPS spectra for Pb on Cu. a) Pb 4f region "as-received", b) O 1s region spectra "as-received", c) Pb 4f region $Ar^+$ sputtered for 30 minutes and d) O 1s region spectra $Ar^+$ sputtered for 30 minutes.

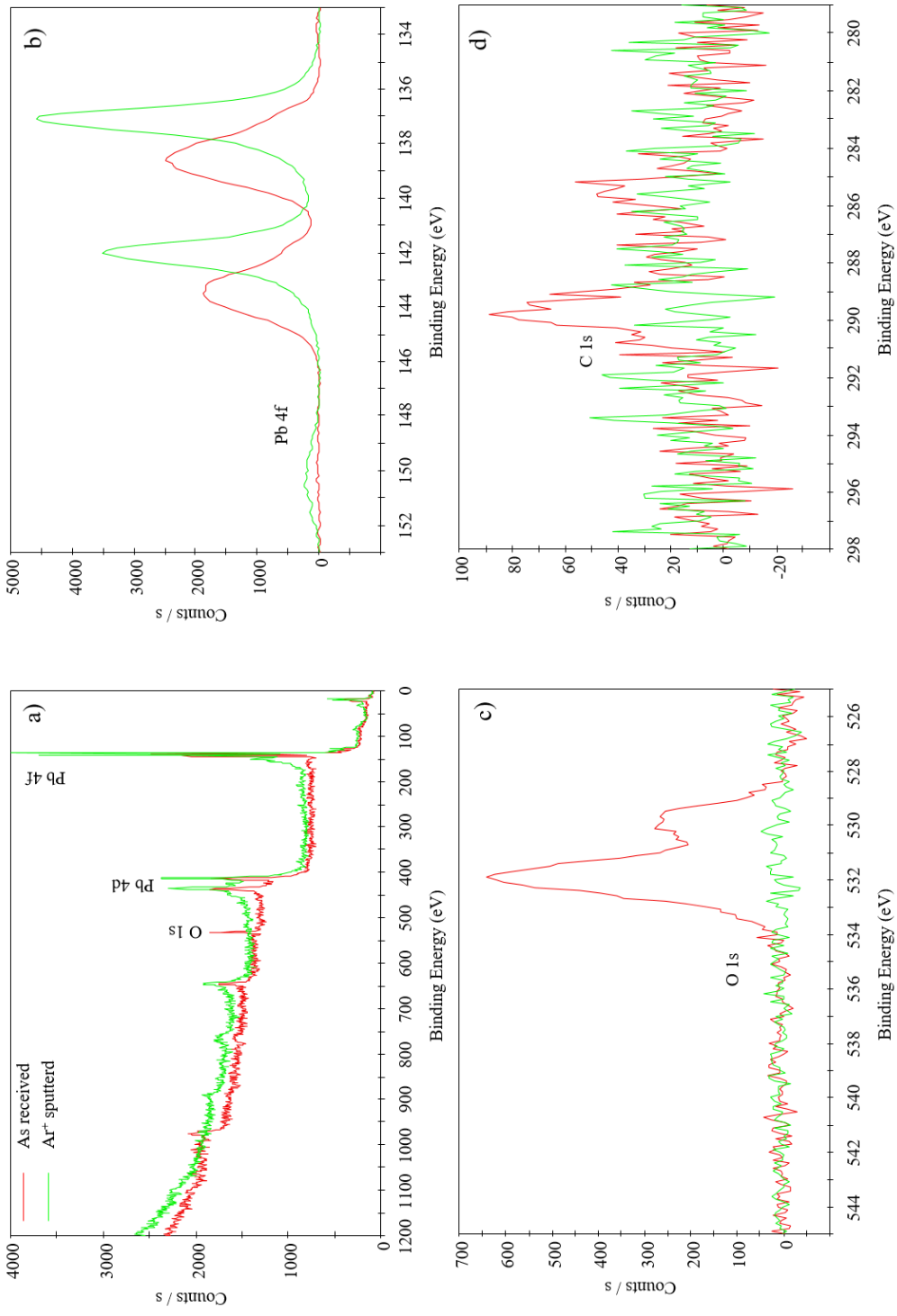


FIGURE 5.15: XPS spectra for lead thin film on a molybdenum substrate "as-received" and after 30 minutes of $Ar^+$ sputtering. a) Overlay of survey spectra, b) overlay of Pb 4f region spectra, c) overlay of O 1s region spectra and d) overlay of C 1s region spectra.

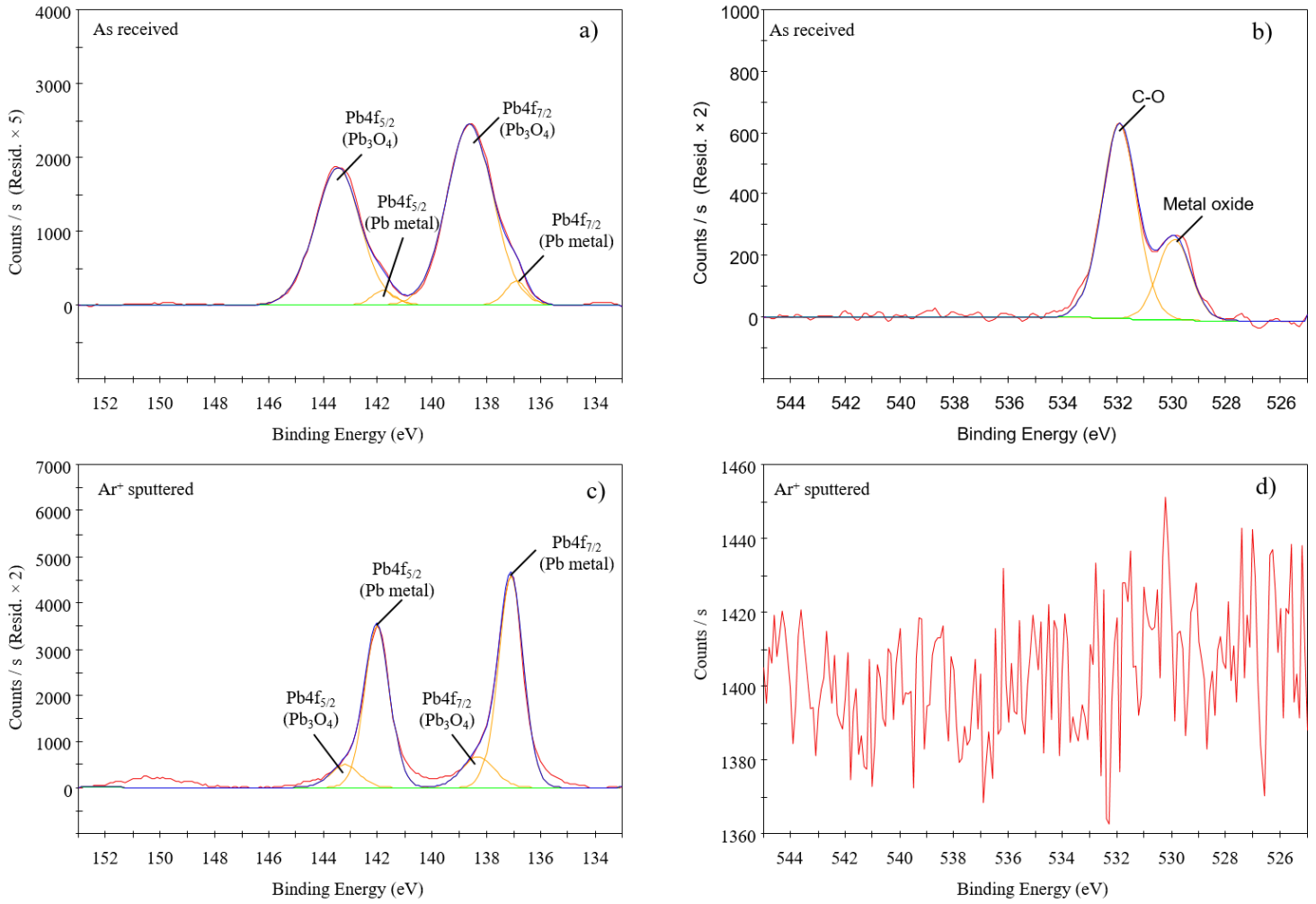


FIGURE 5.16: XPS spectra for Pb on Cu. a) Pb 4f region "as-received", b) O 1s region spectra "as-received", c) Pb 4f region $Ar^+$ sputtered for 30 minutes and d) O 1s region spectra $Ar^+$ sputtered for 30 minutes.

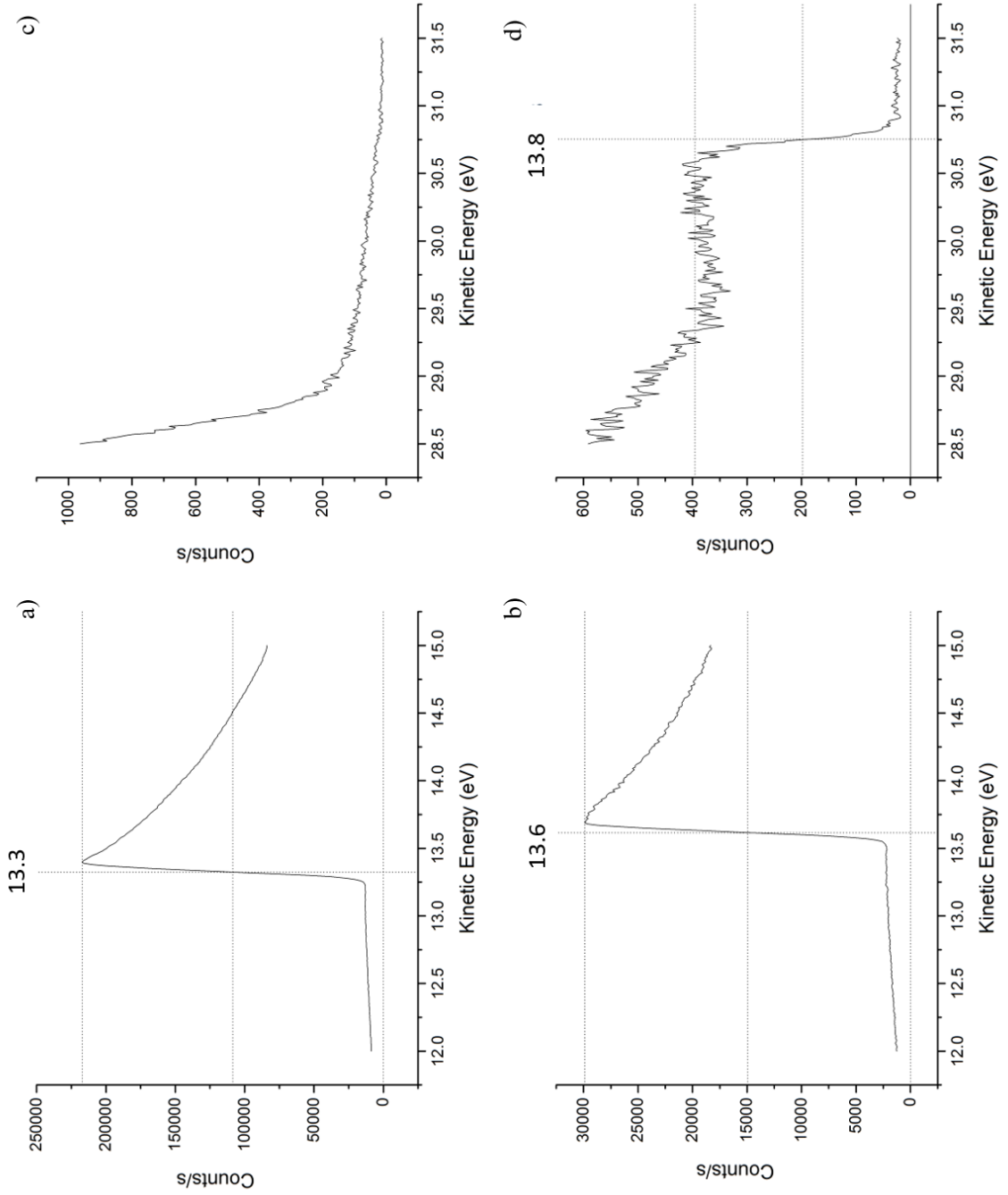


FIGURE 5.17: UPS spectra for Pb on Cu. a) Secondary electron cut-off region "as-received", b) after $Ar^+$ sputtering, c) Fermi edge region "as-received" and d) after $Ar^+$ sputtering.

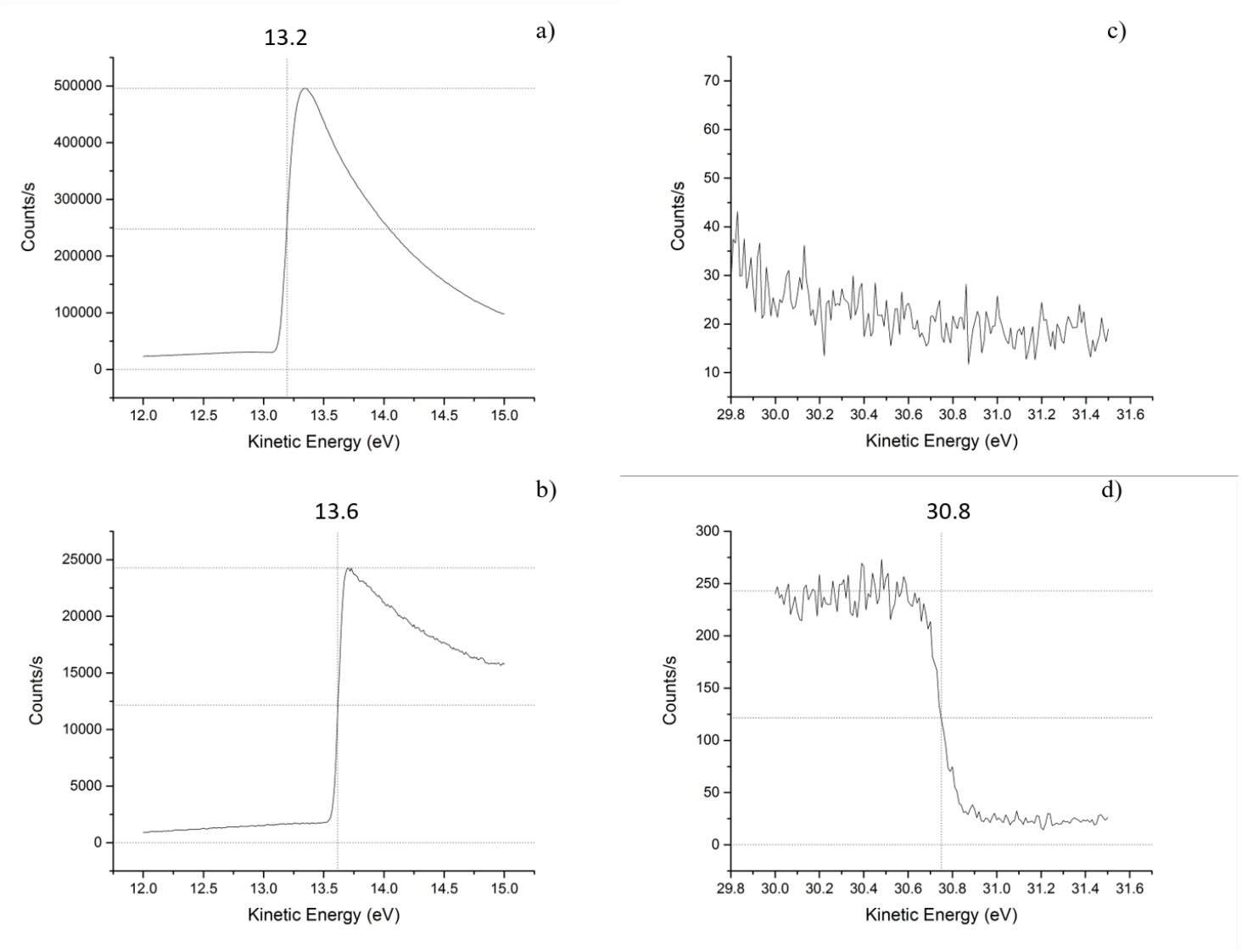


FIGURE 5.18: UPS spectra for Pb on Mo. a) Secondary electron cut-off region "as-received", b) after $Ar^+$ sputtering, c) Fermi edge region "as-received" and d) after $Ar^+$ sputtering.

### 5.2.3 Zirconium films

Overlays of survey spectra for zirconium films "as-received" and after $Ar^+$ sputtering are presented in Figures 5.19 a) and 5.21 a). From these survey spectra the elemental composition for the "as-received" surfaces are ascertained to be approximately 25-27% zirconium and 73-75% oxygen; upon sputtering only zirconium is detected from the spectra (see Table 5.5.) These spectra are quite noisy and therefore some trace elements may not have been detected. In the survey scans after sputtering, even though O 1s is not detected, trace levels are still observed from the region scans. The changes in the chemical state of zirconium can be determined through analysis of the Zr 3d peaks shown in Figures 5.20 and 5.22 for zirconium films deposited on copper and molybdenum respectively. For Zr on Cu, the chemical state "as-received" is predominantly $ZrO_2$ (93%) with some sub-oxide component (7%). The main Zr $3d_{5/2}$ peaks occurring at approximately 183 eV correspond to $ZrO_2$ and the smaller peak at approximately 179.5 eV corresponds to the sub-oxide. The $ZrO_2$ component significantly reduces upon sputtering as shown in Figure 5.20 c). In this plot, the spectrum is fitted with three sets of Zr 3d peaks corresponding to Zr metal (81%), a sub-oxide (14%) and $ZrO_2$ (5%). The remaining oxygen is also observed in the O 1s region scan in Figure 5.20 d).

In the case of the Zr on Mo sample, the Zr 3d region scan "as-received" (see Figure 5.22 a)) shows that the elemental composition is 93% $ZrO_2$and 7% Zr metal. As with the Zr on Cu film, $ZrO_2$ reduces with sputtering: the surface is now comprised of 74% Zr metal, 6% sub-oxide and 20% $ZrO_2$. The O 1s region scans "as-received" and after $Ar^+$ sputtering are shown in Figure 5.22 b) and d). The chemical state of the oxygen is a mixture of predominantly C-O and traces of C=O. There is little change in the ratio of these components before and after sputtering, but the overall intensity of the peaks decrease.

The WF values presented in Table 5.5 were obtained from the UPS plots shown in Figures 5.23 and 5.24. Both sputtered films yield similar WF values of approximately 3.2-3.7 eV. This is lower than the literature quoted values for zirconium by approximately 0.4 eV. The QE values for the zirconium films increase as the surface contaminants reduce with sputtering. Both films yield comparable QE values of $2.1 \times 10^{-6}$ and $2.3 \times 10^{-6}$ for the copper and molybdenum substrates respectively.

In Figure 5.4 e) and f), SEM images for the zirconium film on a silicon substrate are shown, however very little is seen from the image.

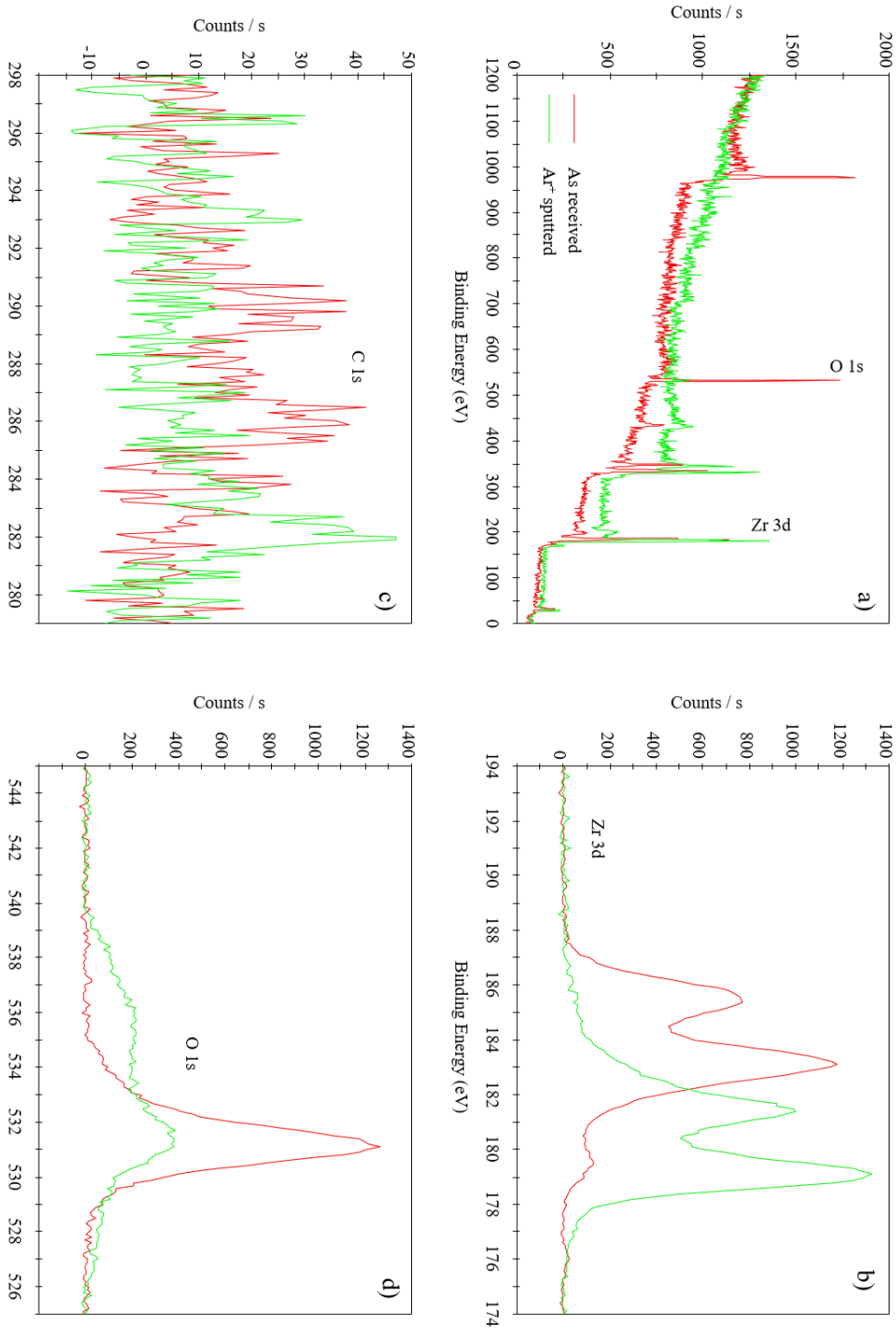


FIGURE 5.19: XPS spectra for zirconium thin film on a copper substrate "as-received" and after 30 minutes of $Ar^+$ sputtering. a) Overlay of survey spectra, b) overlay of Zr 3d region spectra, c) overlay of O 1s region spectra and d) overlay of C 1s region spectra.

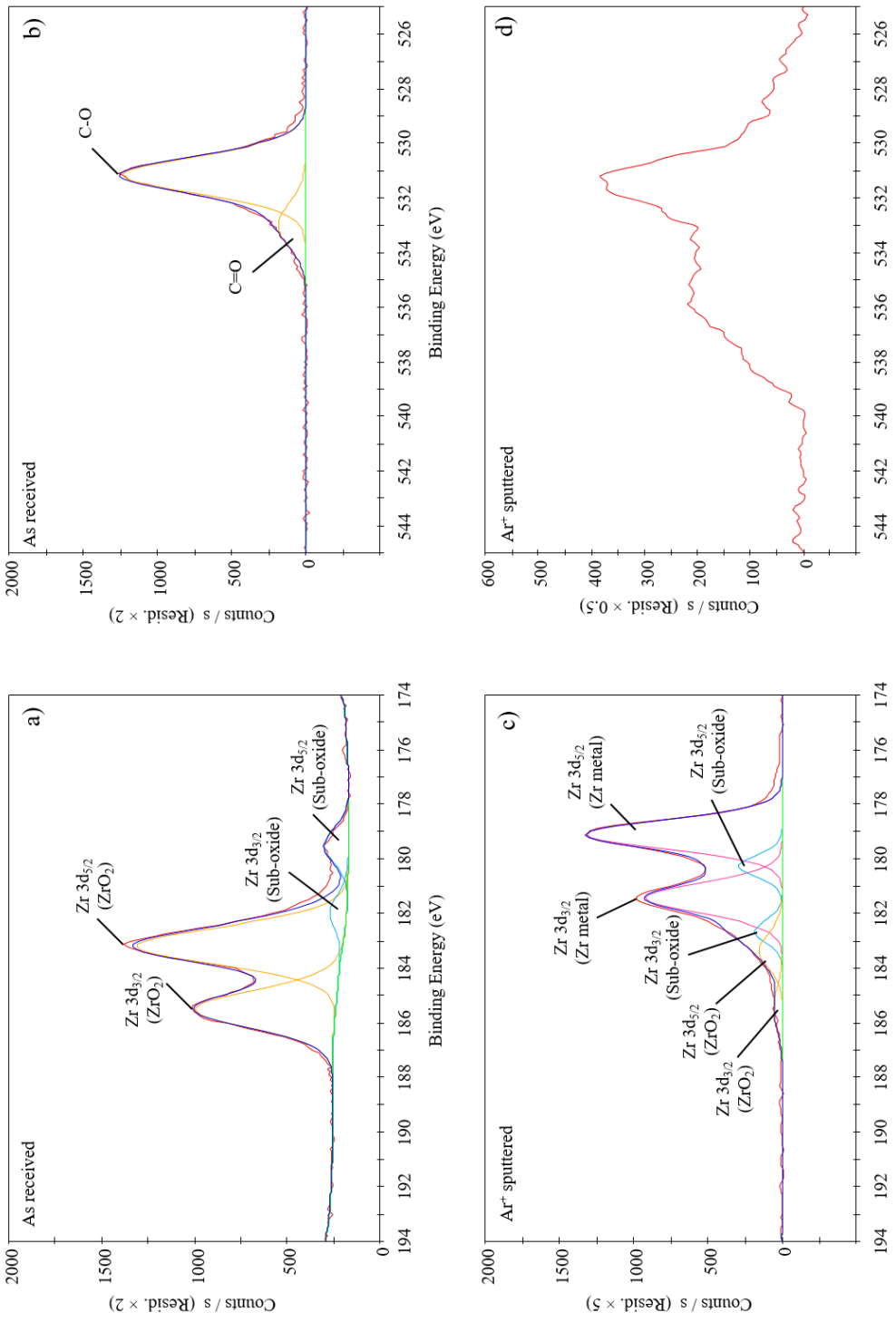


FIGURE 5.20: XPS spectra for Zr on Cu. a) Zr 3d region "as-received", b) O 1s region spectra "as-received", c) Zr 3d region $Ar^+$ sputtered for 30 minutes and d) O 1s region spectra $Ar^+$ sputtered for 30 minutes.

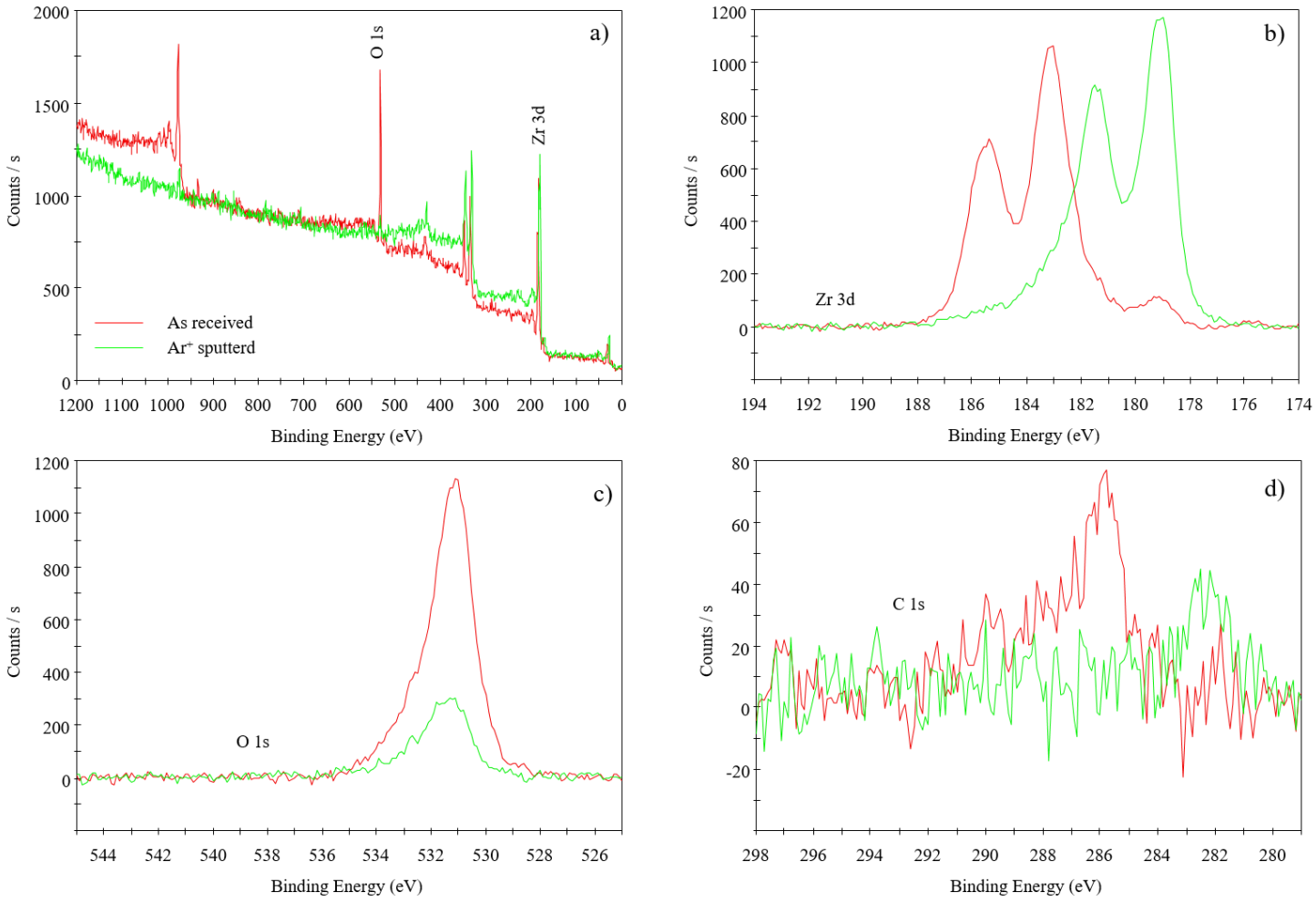


FIGURE 5.21: XPS spectra for zirconium thin film on a molybdenum substrate "as-received" and after 30 minutes of $Ar^+$ sputtering. a) Overlay of survey spectra, b) overlay of Zr 3d region spectra, c) overlay of O 1s region spectra and d) overlay of C 1s region spectra.

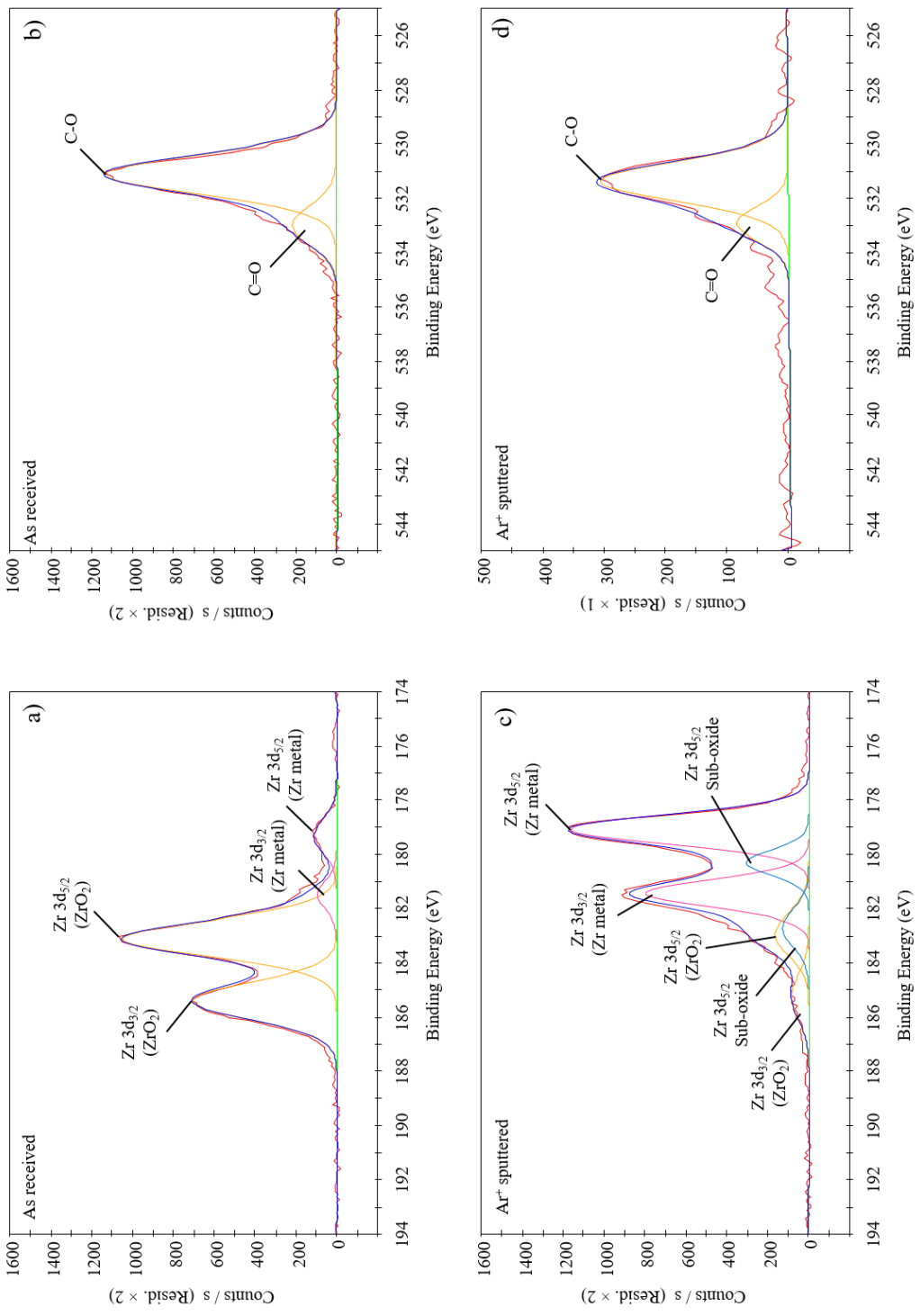


FIGURE 5.22: XPS spectra for Zr on Mo. a) Zr 3d region "as-received", b) O 1s region spectra "as-received", c) Zr 3d region $Ar^+$ sputtered for 30 minutes and d) O 1s region spectra $Ar^+$ sputtered for 30 minutes.

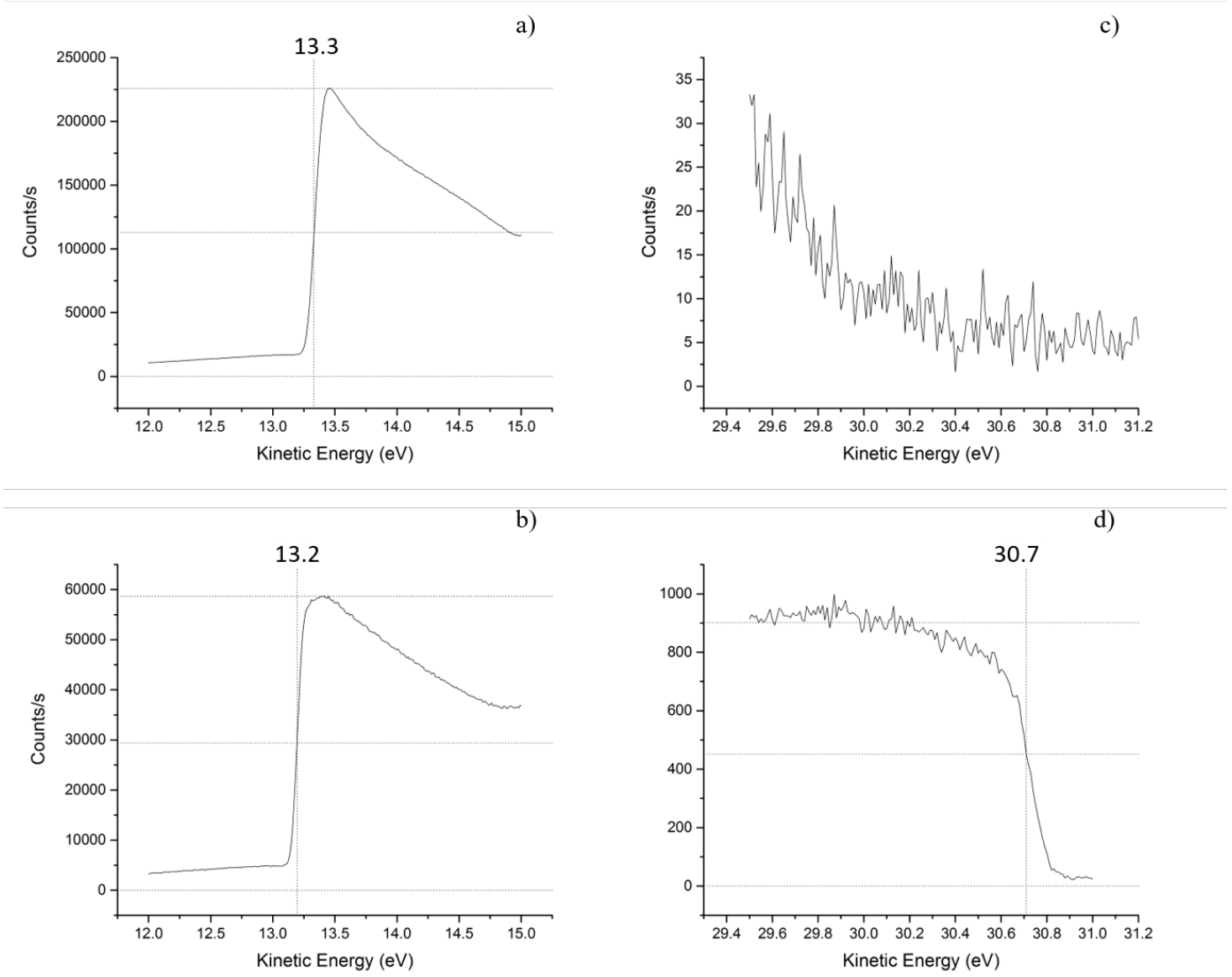


FIGURE 5.23: UPS spectra for Zr on Cu. a) Secondary electron cut-off region "as-received", b) after $Ar^+$ sputtering, c) Fermi edge region "as-received" and d) after $Ar^+$ sputtering.

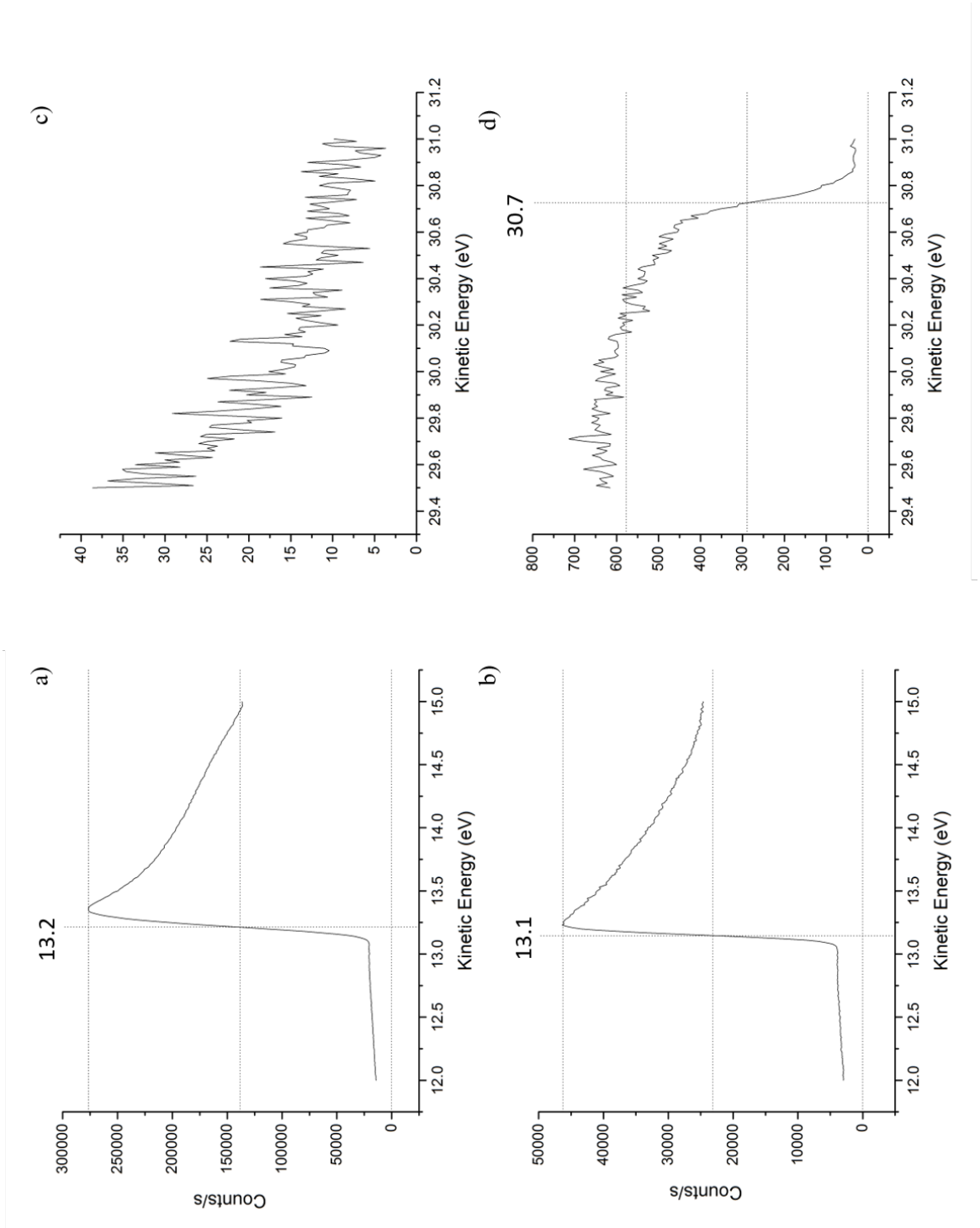


FIGURE 5.24: UPS spectra for Zr on Mo. a) Secondary electron cut-off region "as-received", b) after $Ar^+$ sputtering, c) Fermi edge region "as-received" and d) after $Ar^+$ sputtering.

## 5.3 Discussion and conclusions

The characterisation of niobium and copper thin films on silicon substrates brought up some interesting discussion points. In the case of the niobium film, the sputtered surface yielded similar surface properties to the sputtered bulk niobium. On the other hand, the copper film and bulk samples underwent different preparation procedures; the film was heated only, whereas the bulk copper was sputtered. This of course produced differences with respect to the surface composition, WF and QE, however some of these results were unexpected. The QE for the heated copper film ($1.1 \times 10^{-4}$) was an order of magnitude greater than for the sputtered copper bulk ($1.1 \times 10^{-5}$). This correlates with the Kelvin Probe measurements; the WF values measured for the sputtered copper bulk and heated copper film are 5.32 eV and 4.68 eV respectively. The significantly lower WF of the copper film may explain why it exhibits a greater QE than the bulk copper. But what is the reason for the difference? XPS data shows that despite the presence of oxygen, carbon and even some silicon substrate, the surface of the heated copper film exhibited greater photo-emissivity than the atomically clean sputtered bulk copper sample. This would suggest that the surface purity is not the only factor that contributes to a high QE. It is as yet unclear why the copper film produced so high a QE value compared with the bulk copper. A possible explanation is to do with the different effects of heating bulk copper and a copper film. In the case of bulk copper, heating reduces the surface oxide, dissolving into the bulk, and leaving a clean copper surface. Whereas in the case of the copper film on a silicon substrate, upon heating there is no bulk into which the oxide can dissolve. Thus it is possible that the effect of heating still may then produce a change in the chemical state (perhaps a change from CuO to $Cu_2O$) which may lead to an improved QE. Thus the effect of heating copper (or maybe even other metals) on the chemical composition, WF and QE may be substrate dependent.

The surface characterisation of films grown on different substrates show that the surface properties "as-received" and after sputtering are generally independent of the substrate material used. Indeed, the measurements for WF and chemical composition are comparable for films grown on copper and molybdenum substrates (see Table 5.5). Despite exposure to atmosphere between deposition and characterisation, clean sample surfaces were achieved without exposing the substrate material by employing $Ar^+$ bombardment. This shows that the conditions during deposition were favourable and that pure metallic films were produced; any contaminants detected will typically have formed during transport. Ultimately the photocathode material will be deposited and then transported to the gun in vacuum; therefore there may not be a requirement for removing surface contaminants from the photocathode. With respect to the WF measurements using UPS, although generally the measured values have been lower than the literature quoted values, the trend has been correct. The literature values of WF show that copper has the greatest WF, followed by lead and then zirconium; this order is observed in the measured values too (see Table 5.5).

# Chapter 6

# Effects of surface roughness on photoelectron energy distribution

In this section, first results from an experiment investigating the effects of surface roughness on the transverse energy spread of photoelectrons from copper and molybdenum photocathodes is presented. This work is a collaboration: transverse energy spread measurements have been conducted by Lee Jones and Thomas Beaver, and surface morphology measurements by myself. An IPAC conference proceedings paper of the results has been published [104].

In this study, three 6 mm diameter cathodes were investigated:

1. Cu.EF- bulk polycrystalline copper with an engineered finish
2. Cu.DT- bulk polycrystalline copper, diamond turned
3. Mo.EF- bulk polycrystalline molybdenum with an engineered finish

For the Cu.EF photocathode, the preparation procedure was the same as detailed in Chapter 4: ultra-sonic acetone bath followed by *ex-situ* Ar plasma treatment. After which the cathode was introduced into the UHV of the Multiprobe system where it was then heated to 450°C for 1 hour. As previous studies have demonstrated, this procedure leaves a clean cathode surface. Once again XPS was employed to confirm this. After surface characterisation, the Cu.EF cathode was transferred in vacuum via a vacuum suitcase into the Photocathode Preparation Facility (PPF) [105] where it was again heated to 450°C for half an hour before transverse energy spread measurements were made in the Transverse Energy Spread Spectrometer (TESS) chamber [105]. For the Cu.DT and Mo.EF, due to issues with the vacuum suitcase, the photocathodes were degreased in acetone and Ar plasma treated as per usual, and then loaded straight into PPF, bypassing surface characterisation in Multiprobe. However, previous experiments with bulk copper and molybdenum have shown that the cleaning procedure employed is sufficient to produce a clean surface. After measurements in TESS, each photocathode was taken out and stored for some time in atmosphere prior to surface roughness measurements.

## 6.1 Surface morphology measurements

Surface roughness measurements were taken using two techniques: *ex-situ* AFM and interferometric microscope (both of which are described in Chapter 3). For each photocathode, measurements were taken at 5 different positions around the cathode centre. For the AFM, the maximum scan area is 50 $\mu$m $\times$ 50 $\mu$m; and each individual scan was repeated twice. For the MicroXam, scans were taken using a 50$\times$ objective over 173 $\mu$m $\times$ 131 $\mu$m areas and each repeated 4 times at each position.

A selection of three out of the five scans showing the cathode surface profiles are presented in the figures below (Figures 6.3,6.4, 6.1, 6.2, 6.5).

SPIP software was then used to extract quantitative data from each scan; the averaged results are presented in Table 6.1.

Sz is the 10 point average height measurement; it is the average height of the five highest peaks plus the average height of the five lowest valleys [106]. Sq is the root mean square of the surface roughness [106].

TABLE 6.1: Sz and Sq measurements for Cu.DT, Cu.EF and Mo.EF using AFM and MicroXam.

| | AFM-Sz (nm) | AFM-Sq (nm) | MicroXam-Sz (nm) | MicroXam-Sq (nm) |
|---|---|---|---|---|
| Cu.EF | 1083.2 | 143.9 | 1080.0 | 147.2 |
| Cu.DT | 728.6 | 83.4 | 919.7 | 81.9 |
| Mo.EF | - | - | 1691.6 | 241.4 |

Results from AFM and MicroXam are comparable. The averaged results show that the Cu.DT photocathode is, as expected, smoother that the Cu.EF, and that the Mo.EF is significantly rougher than both copper photocathodes. Indeed the surface of the Mo.EF photocathode was too rough to image using the AFM, which has a maximum height range of 5 $\mu$m. Consider the surface profiles of Cu.DT and Cu.EF in Figures 6.1 - 6.4. The 2D scans and 3D profiles for Cu.DT may appear to be rougher than for Cu.EF. However, the Cu.EF scans show deeper engineering scratches which are accountable for the higher rms roughness values. For the Cu.EF photocathode in particular, the three different scans from the AFM and the interferometric microscope shown in Figures 6.3 and 6.4 show three quite different surfaces. The non-uniformity of this photocathode is of course not ideal as the rms roughness may not accurately describe the localised area from which electrons are emitted in practice.

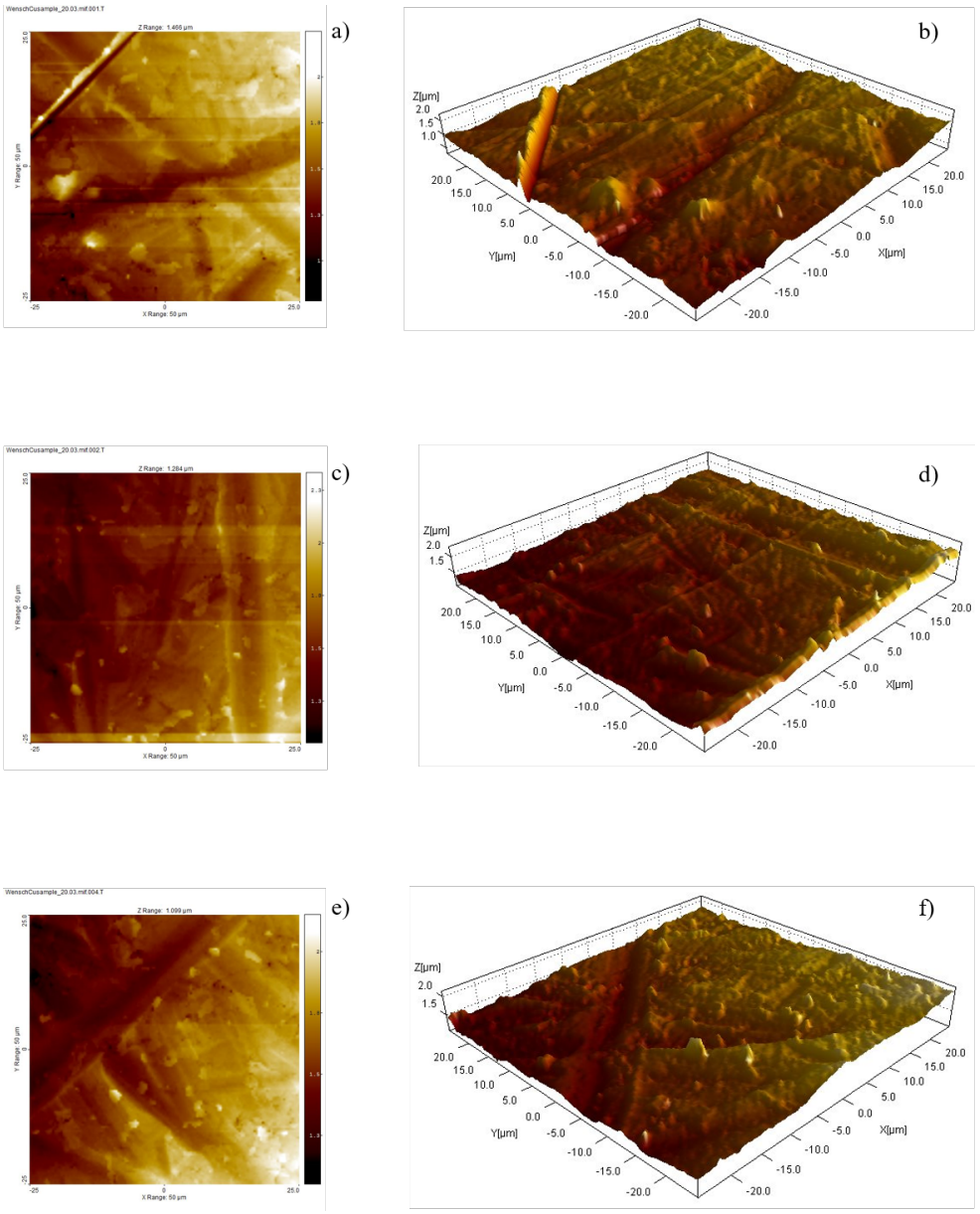


FIGURE 6.1: AFM scans for Cu.DT at three different locations presented in 2D and 3D.

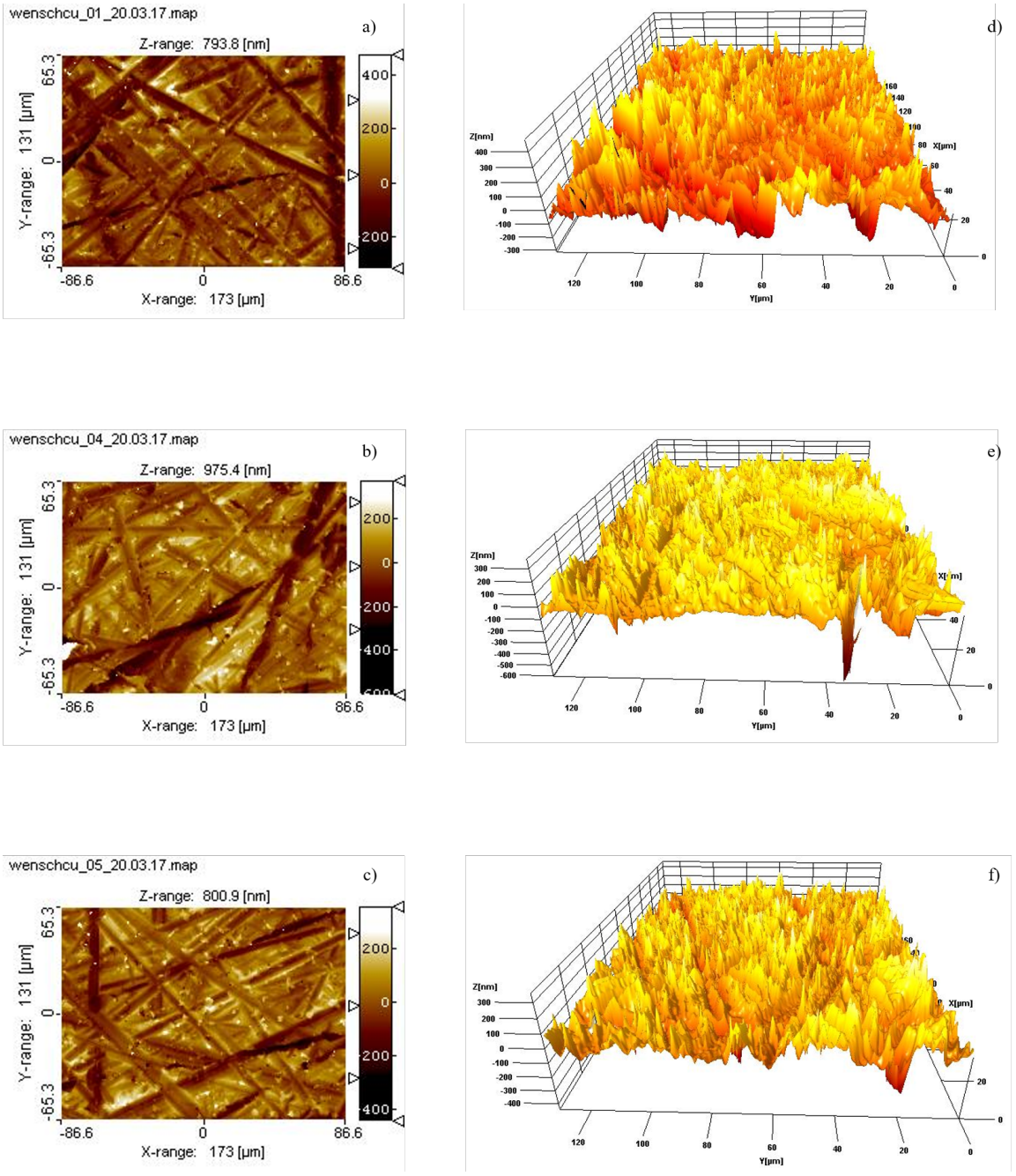


FIGURE 6.2: MicroXam scans for Cu.DT at three different locations presented in 2D and 3D.

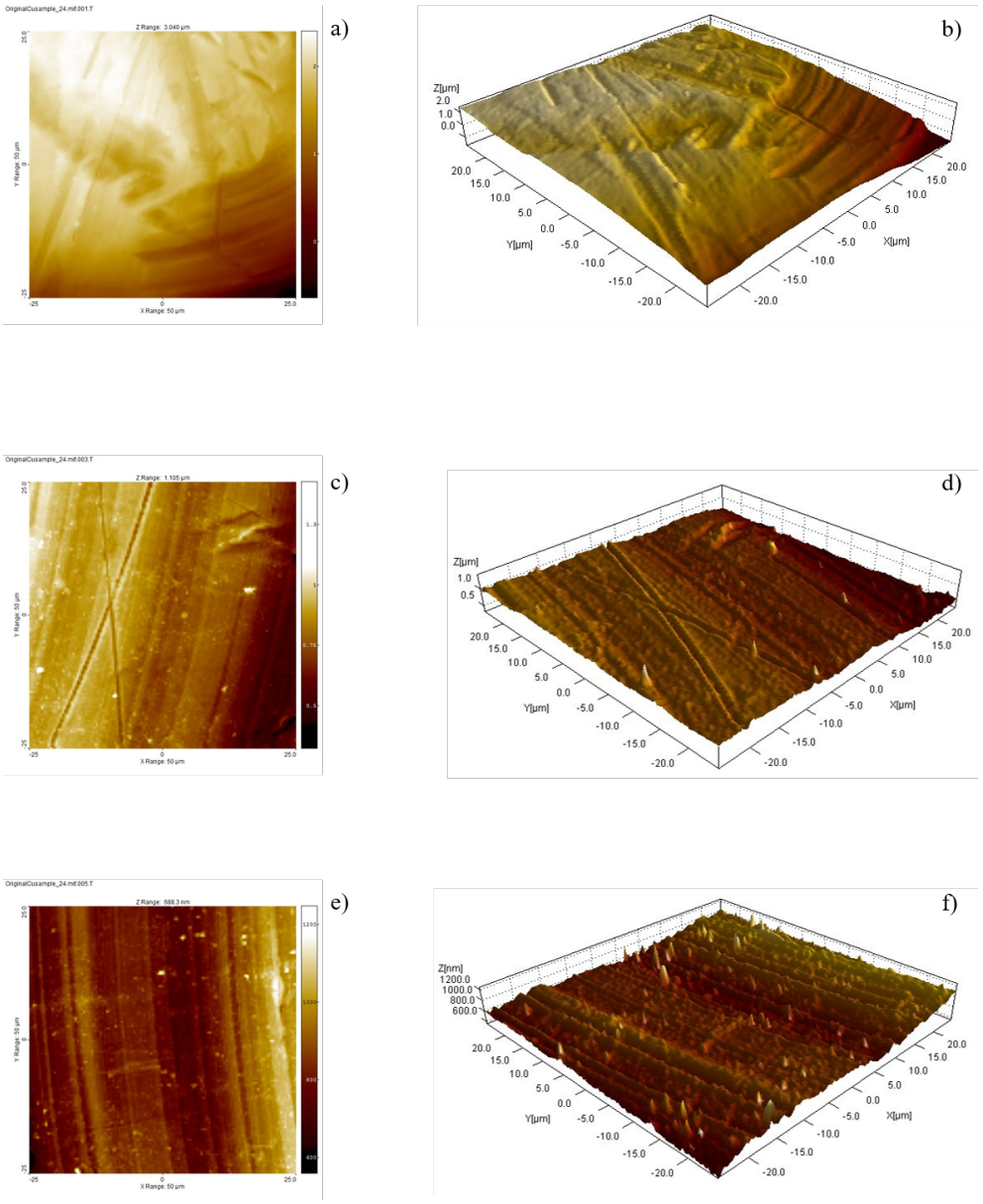


FIGURE 6.3: AFM scans for Cu.EF at three different locations presented in 2D and 3D.

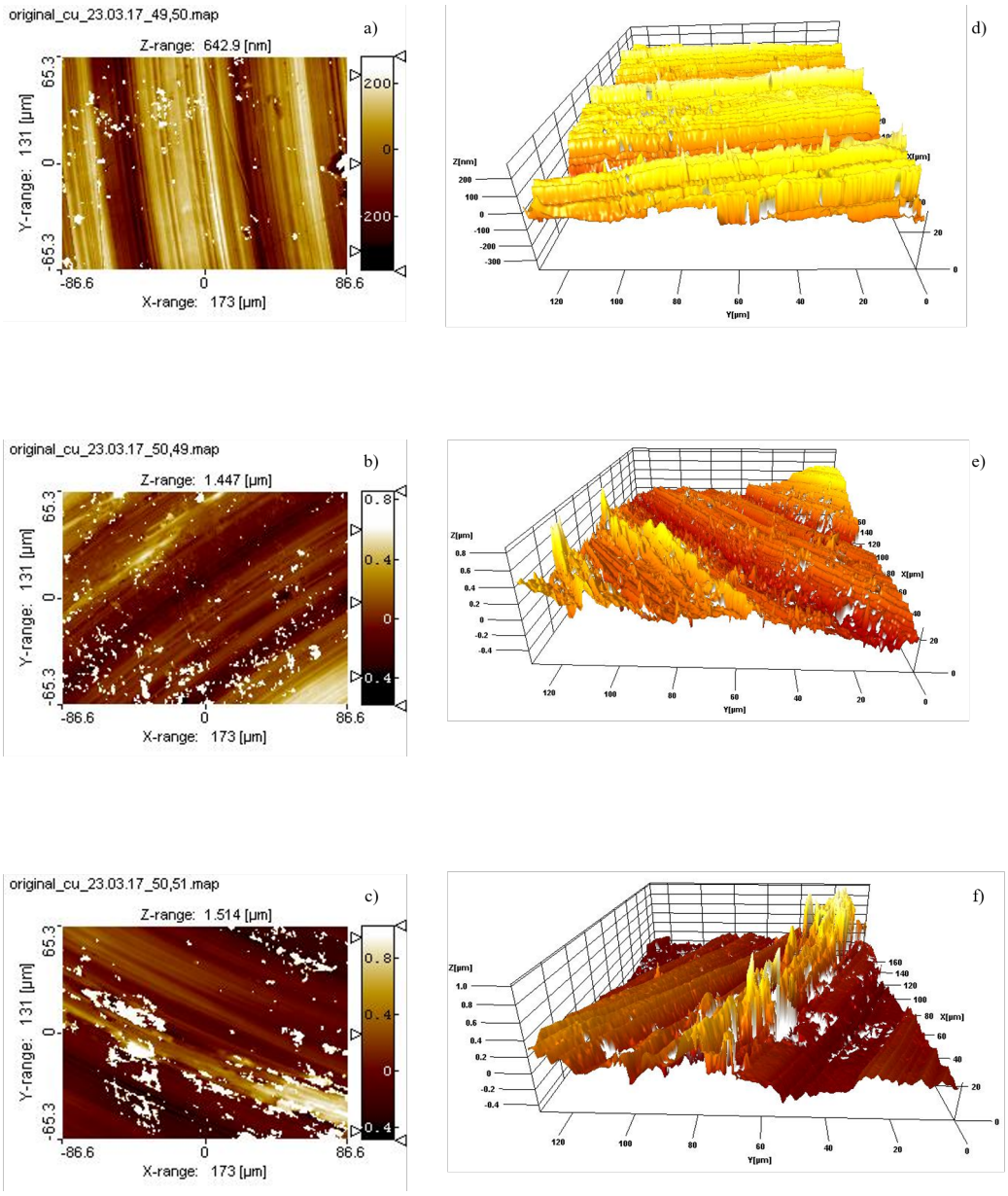


FIGURE 6.4: MicroXam scans for Cu.EF at three different locations presented in 2D and 3D.

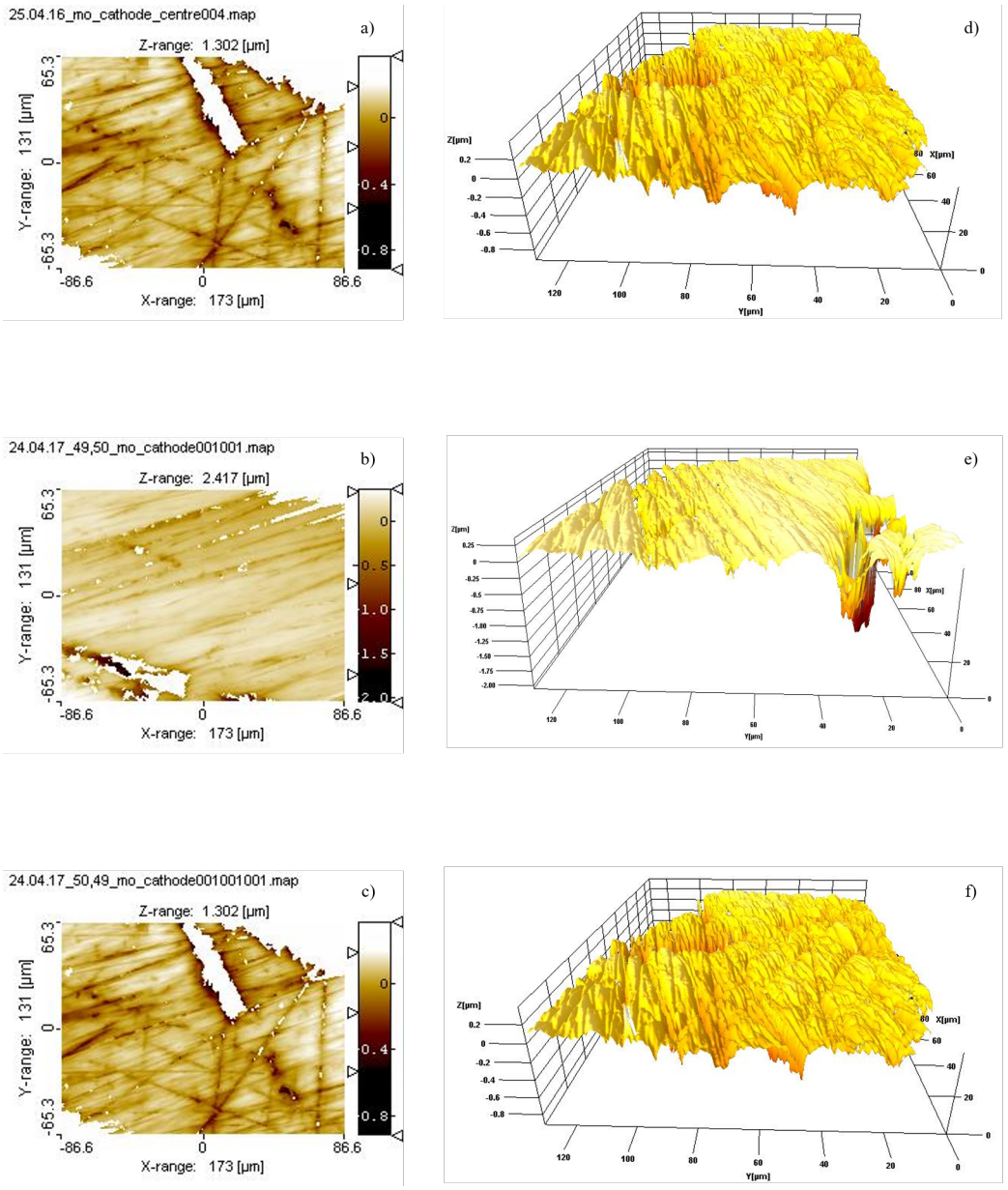


FIGURE 6.5: MicroXam scans for Mo EF at three different locations presented in 2D and 3D.

## 6.2 Surface Roughness Induced Emittance

The surface roughness induced emittance, $\epsilon_{ns}$, can be estimated by approximating a rough surface to a model with a periodic roughness as described by Equation 6.1 [107]:

$$z = a\cos\left(\frac{2\pi x}{b}\right) \tag{6.1}$$

where $a$ is equal to the amplitude of the surface and $b$ is equal to the period.

$\epsilon_{ns}$, as derived by D. Xiang *et al.*, would therefore be [107]:

$$\epsilon_{ns} = \sigma_x \sqrt{\frac{e\pi^2 a^2 E_{rf}}{2m_0 c^2 b}} \tag{6.2}$$

where $\sigma_x$ is the laser beam size and $E_{rf}$ is the applied electric field.

For a particular photoinjector, $\sigma_x$ and $E_{rf}$ remain fixed, and therefore Equation 6.2 can be simplified to Equation 6.3. In this case the typical parameters for CLARA photoinjector would be $\sigma_x = 1$ mm and $E_{rf} = 50$ MV/m . Thus $C = 2.19 \times 10^{-2}$.

$$\epsilon_{ns} = C\frac{a}{\sqrt{b}} \tag{6.3}$$

In order to ensure that the effect of the $\epsilon_{ns}$ is kept to a minimum, the photocathode surface must be prepared such that $a$ is small and $b$ is large. From Equation 6.3, it is evident that the the amplitude of the surface structure has a bigger effect on $\epsilon_{ns}$ than the periodicity. It is therefore critical that deep machine made ridges are smoothed.

Using this relation, the $\epsilon_{ns}$ from the copper photocathodes investigated in this section can be estimated. For these calculations, only Figures 6.4 a) and 6.1 a) will be used to calculate the $\epsilon_{ns}$ for Cu.EF and Cu.DT respectively. Firstly, $a$ and $b$ values must be extracted from the surface scans. The 10 point average height values, Sz, can be approximated to be twice the amplitude of the surface, $a$.

Trickier to obtain are the values for the period of fluctuation, $b$. Only the AFM and MicroXam scans for the Cu.EF photocathode show clear periodicity with respect to the surface by eye. However, by carrying out a Fast Fourier Transforms (FFT), values for dominant periods can be extracted to estimate $b$. A line profile of the scan was taken, approximately perpendicular to the direction of polishing marks, demonstrating the variation in height of the surface along the line profile (see Figure 6.6a) and d)). An FFT of this data was then performed in MATLAB from which a value of the period was determined.

The FFT for the Cu.EF line profile (see Figure 6.6 c)) shows that the peak in wavenumber is spread out and therefore, the corresponding period is also spread. The three peak values highlighted in the plot correspond to periodicities of 87.57 $\mu$m, 58.41 $\mu$m and 43.80 $\mu$m. Due to this spread, an average was taken for $\epsilon_{ns}$ calculations.

The FFT for the Cu.DT line profile shown in Figure 6.6 f) shows several peaks in wavenumber corresponding to several significant periodicities that can describe the surface morphology. Peak 1 corresponds to a periodicity of approximately 170 $\mu$m; this is comparable to the length of the scan and therefore it is an unlikely period. Adjacent to peak 1 there are three peaks labelled from 2-4, that have periods of 43.29 $\mu$m, 24.73 $\mu$m and 15.74 $\mu$m respectively. These values are more easily justified to describe the periodicity as evidenced in the line profile (Figure 6.6 d)). There are clearly at least three dominant periodicities, but for the task of estimating the $\epsilon_{ns}$, an average of the three is taken.

Values for $a$, $b$ and the calculated surface roughness induced emittance are presented in Table 6.2.

TABLE 6.2: Surface roughness induced emittance calculations.

| | Sz ($\mu$m) | a ($\mu$m) | b ($\mu$m) | $\epsilon_{ns}$ (mm.mrad) |
|---|---|---|---|---|
| Cu.EF | 0.62 | 0.31 | 63.26 | 0.86 |
| Cu.DT | 0.70 | 0.35 | 27.92 | 1.45 |

The calculations show that the surface roughness induced emittance for the Cu.DT surface would actually be 0.59 mm.mrad greater than for the Cu.EF surface. Although an average over five scans suggest that the surface roughness (Sq) is greater for Cu.EF, the individual scans selected for the calculation of $\epsilon_{ns}$, show greater $a$ values for Cu.DT than for Cu.EF, resulting in a larger $\epsilon_{ns}$ value for Cu.DT. Of course these are rough estimations; with the non-uniformity of the photocathode surfaces it is difficult to quantify the periodicity and the amplitude.

## 6.3 Transverse Energy Spread Measurements

Transverse energy spread measurements for Cu.DT, Cu.EF and Mo.EF samples were conducted in the TESS (transverse energy spread spectrometer) instrument. In this section a brief summary of the system and measurement process is described below, followed by results for copper and molybdenum samples.

**TESS system**

A full description of the TESS system can be found in the FEL '13 proceedings TESS commissioning paper [108]. A basic schematic of the transverse energy spread measurement set-up is shown in Figure 6.7. UV light generated from a white light source and monochromator is at grazing-incidence with a negatively biased photocathode [104]. Photoelectrons are accelerated towards the detector by an accelerating voltage acting between the photocathode and the detector. The detector serves as a retarding-field electron detector as well as an imaging system [108]. As demonstrated in Figure 6.7, the detector comprises three electrically isolated grids, a Hamamatsu 2-stage microchannel plate electron multiplier (MCP) and a phosphor screen positioned at the back of the detector. The detector grids and the MCP front plates are held at the same positive potential. By varying the bias on the source, the accelerating voltage can be altered thus controlling the time of flight, $\tau$, of the photelectrons over the distance between the photocathode and detector, $d$. As time of flight increases, the time for the transverse energy component to manifest also increases, leading to a greater transverse energy spread. The MCP back plate and the fluorescent phosphor screen are held at approximately +950 V and +3500 V respectively. The potential difference between the front and back of the MCP plates will determine the intensity of the photoemission footprint (see Figure 6.8).

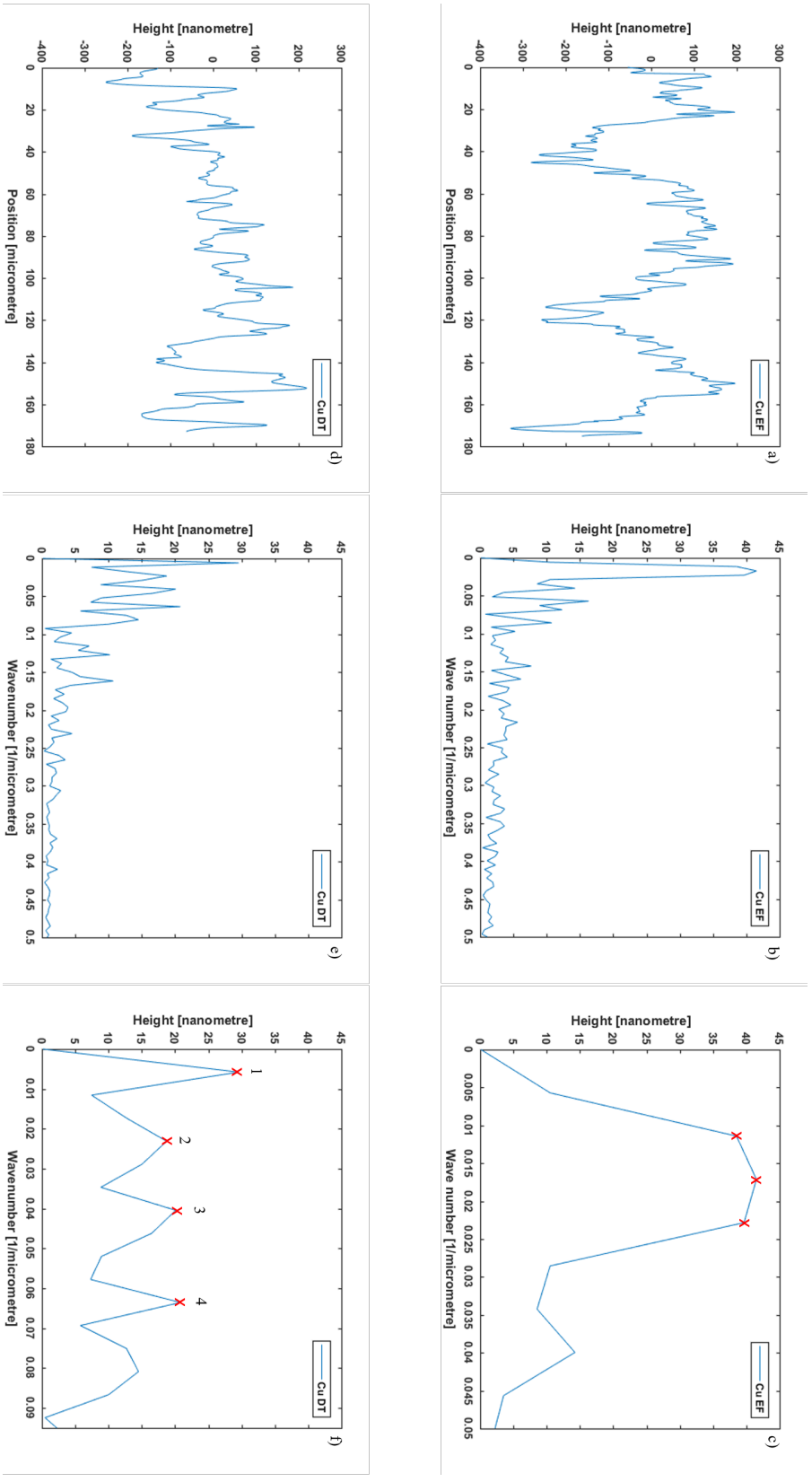


FIGURE 6.6: a) Line profile for Cu.EF MicroXam scan (see Figure 6.4 a)) and b) FFT of the line profile for Cu.EF. c) Line profile for Cu.DT MicroXam scan (see Figure 6.2 a)) and b) FFT of the line profile for Cu.DT.

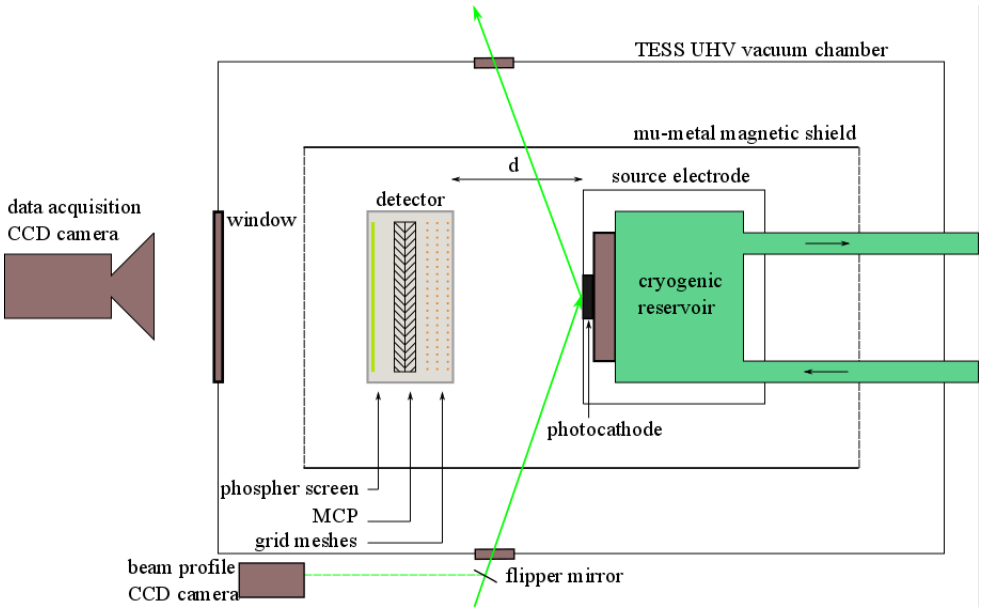


FIGURE 6.7: Schematic of TESS photocathode and detector set-up.

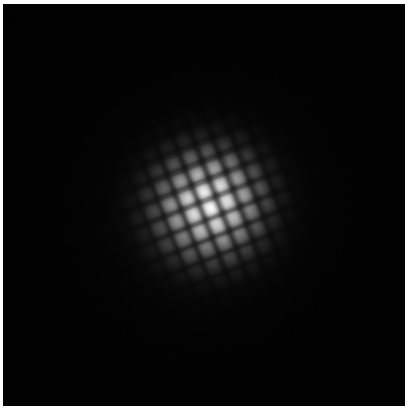

FIGURE 6.8: Example of electron emission footprint from TESS as imaged using a CCD camera.

Images such as the one shown in Figure 6.8 can be used to determine the transverse energy distribution of the photoemission footprint. Firstly, a histogram of the image is generated, summing each column in the data set [108]. The image centre is then determined and a radial distribution function, $I(r)$, is derived by analysis of the X- and Y- histograms. $I(r)$ represents the number of electrons incident on the phosphor screen as a function of radial displacement (where r=0 is the image centre); this is of course dependent on the transverse energy of the electron. A conversion of the radial distribution function, $I(r)$, to an energy distribution function, $N(\epsilon_{tr})$, is carried out resulting in a Transverse Energy Distribution Curve (TEDC).

**Results**

For each photocathode transverse energy measurements were recorded under incident laser light at wavelengths 266 nm, 271 nm, 276 nm, 281 nm and 286 nm.

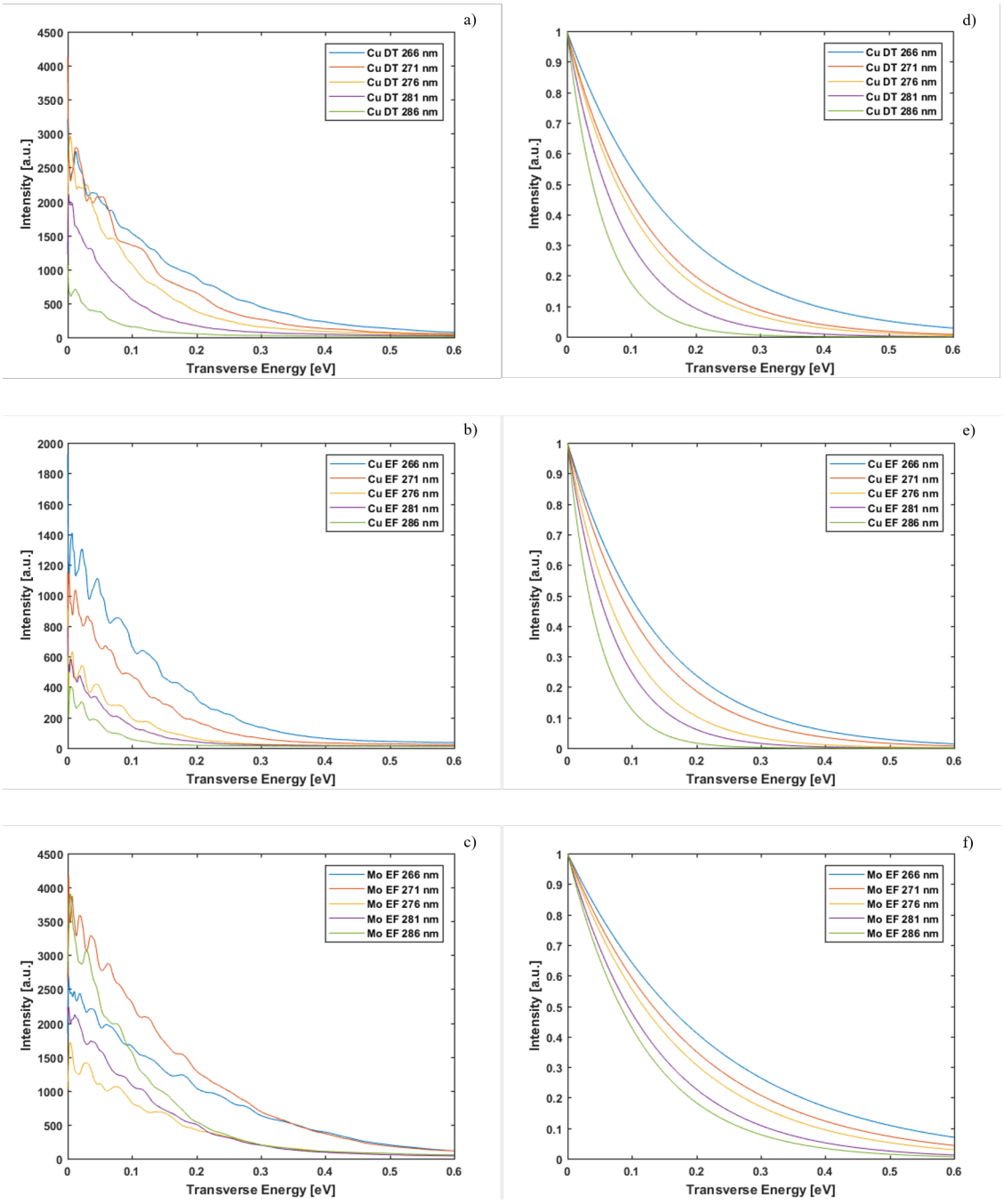


FIGURE 6.9: Cu.DT, Cu.EF and Mo.EF transverse energy distribution spectra a-c) raw data and d-f) fitted.

In Figure 6.9 the TEDCs for each photocathode at five different wavelengths is presented. The raw data spectra are shown in Figures 6.9 a-c). The raw data was fitted to exponential curves following the form:

$$y = a\exp(-bx) \tag{6.4}$$

where a is the peak intensity and b is $1/MTE$ at the $1/e$ level.

The fits were then normalised as shown in Figures 6.9 d-f). From the fitted spectra, Mean Transverse Energy (MTE) values were determined at the $1/e$ level (see Table 6.3.

Figure 6.10 compares the extracted MTE values as a function of wavelength for each photocathode.

TABLE 6.3: MTE at different wavelengths for Cu.DT, Cu.EF and Mo.EF

| $\lambda$ (nm) | MTE Cu.EF (eV) | MTE Cu.DT (eV) | MTE Mo.EF (eV) |
|---|---|---|---|
| 266 | 0.139 | 0.169 | 0.224 |
| 271 | 0.119 | 0.125 | 0.191 |
| 276 | 0.088 | 0.111 | 0.167 |
| 281 | 0.071 | 0.085 | 0.133 |
| 286 | 0.048 | 0.063 | 0.117 |

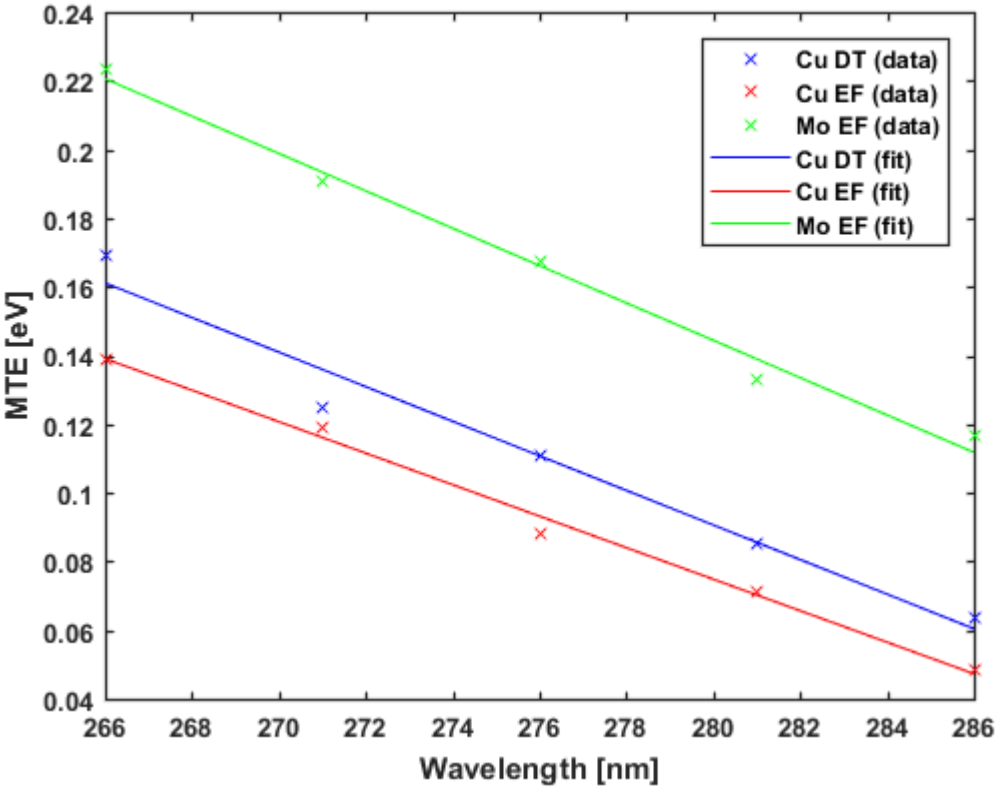


FIGURE 6.10: MTE as a function of wavelength for Cu.DT, Cu.EF and Mo.EF.

The data shows that increasing the wavelength of the incident light reduces the MTE of the photocathodes, but also reduces the intensity of the electrons emitted; this result is in agreement with Equation 2.26. The greater the excess energy, or kinetic energy of the emitted electrons, the higher the MTE will be and therefore the greater the intrinsic emittance.

As evidenced in Table 6.3 and Figure 6.10, the MTE values for the molybdenum photocathode is significantly larger compared with the copper photocathodes. The data show that for the Cu.DT photocathode the MTE is fractionally greater than the MTE for the Cu.EF sample. Discussion of these results with respect to the surface roughness measurements is presented in the section below.

## 6.4 Discussion and conclusions

TABLE 6.4: MTE and surface roughness measurements for Cu.DT, Cu.EF and Mo.EF

| | MicroXam-Sq (nm) | AFM-Sq (nm) | MTE at 266 nm (eV) |
|---|---|---|---|
| Cu.EF | 147.2 | 143.9 | 0.139 |
| Cu.DT | 81.9 | 83.4 | 0.169 |
| Mo.EF | 241.4 | - | 0.224 |

As discussed in Chapter 2, surface roughness contributes to intrinsic emittance growth. Therefore, the expectation would be that the rougher photocathode surfaces will exhibit a greater MTE. MTE values extracted from the transverse energy distribution curves show that the Mo.EF photocathode had the largest MTE. This can be attributed to the very high surface roughness of the molybdenum surface as measured from the MicroXam scans. Additionally, it is worth noting that the MTE is equivalent to the excess energy. The literature values of work function for molybdenum is approximately 0.5 eV lower than for copper, and so the excess energy for a given wavelength of incident light will be greater in the case of a molybdenum photocathode over a copper photocathode, resulting in a greater MTE.

However in the case of the copper photocathodes the results do not correlate well with the theory. The Cu.EF photocathode is rougher than the Cu.DT photocathode however it has a lower MTE.

A definitive reason for this is not yet apparent, but one such explanation may lie in the inhomogeneity of the photocathode surfaces. As demonstrated in the selected AFM and MicroXam images for the Cu.DT and Cu.EF photocathodes, between the different locations on the photocathode surface, the surface morphology varies. Therefore, the measured RMS surface roughness may not accurately characterise the surface morphology for the specific area illuminated by the laser light for TESS measurements. In the case of the Cu.EF photocathode, it is possible that the area of the surface illuminated by the UV beam (beam size approx 110 $\mu$m FWHM) may have been smoother than the

emitting surface of the Cu.DT photocathode. To conclude, a significant difference in the MTE for copper and molybdenum photocathodes is observed. This difference may be correlated with the different surface morphologies. However, more measurements of samples (with known and uniform surface roughness) are required to draw more substantial conclusions.

For future studies, it is critical that the photocathodes are prepared such that the surfaces are homogeneous; this way surface characterisation will be more relevant. A uniform surface will also improve approximations of photocathode surfaces to a model. This in turn will allow for more reliable estimations of the surface roughness induced emittance.

# Chapter 7

# Conclusions

## 7.1 Summary and conclusions

Metals are a reliable and robust choice of photocathode for applications requiring low to intermediate average currents. The major drawback to metal photocathodes is the low QE. By implementing alternative metals to the commonly used copper photocathode, and preparing the cathode surface to optimise the QE, the performance of metal cathodes can be improved upon. In this work an experimental exploration of the preparation and evaluation of metal photocathode properties has been conducted.

From a selection of vacuum compatible metals with work functions less than copper, several metals have been identified as potential photocathode materials. As shown in Chapter 4 section 4.1, magnesium, niobium, lead, titanium and zirconium all exhibited QE values that were greater than copper after $Ar^+$ sputtering. These materials have been further investigated in the course of this work.

As a result of this investigation a new preparation procedure for bulk metal cathodes has been developed, and has since been employed to prepare the copper cathode used in the first stage of CLARA commissioning: *ex-situ* Ar plasma treatment followed by *in-situ* heat treatment. Several surface preparation procedures for photocathodes have been explored in this work (see Chapter 4): $Ar^+$ sputtering, O/ Ar plasma treatment and heat treatment. The results have shown a strong correlation between QE and chemical composition, with surface contaminants generally reducing the emissivity of the cathode surfaces. More specifically, the particular chemical states of the metal with respect to the surface contaminants clearly influence the QE; as the metal component increases, so too does the QE. Though $Ar^+$ sputtering may be an efficient method for producing a clean surface and improving the electron yield, it can have detrimental effects with respect to surface morphology leading to intrinsic emittance growth. Plasma treatment followed by heating has been investigated as an alternative method to $Ar^+$ sputtering. In Chapter 4, sections 4.2-4.4, the effects of plasma treatments is explored. MEIS and XPS studies for heated O plasma treated copper samples, show that though the process reduces the surface hydrocarbon contaminants down to to trace level, it does not completely reduce the very thick oxide that forms on the surface, though it certainly changes the chemical

state. On the other hand Ar plasma treatment does not produce so thick an oxide that heating cannot reduce. This treatment does not appear to alter the surface morphology, it improves the QE of the "as-received" surface, and therefore it is a viable preparation procedure for metallic photocathodes.

In Chapter 5, thin film deposition of those materials with QE higher than copper has been conducted. The effect of different substrate materials on the films was explored; XPS, WF and QE measurements would suggest that the film properties "as-received" are independent of substrate material. Further experiments are necessary to determine the effects of different substrates on the transverse energy spread of photoemitted electrons.

In Chapter 6, first results exploring the effects of cathode surface morphology on the transverse energy spread and intrinsic emittance were presented for copper and molybdenum photocathodes. The results did not wholly agree with the trends predicted by the theory. Though the Mo.EF cathode with greater surface roughness did yield a greater MTE value compared with the smoother Cu.DT and Cu.EF cathodes, the smoother of the two copper cathodes, Cu.DT exhibited a larger MTE than Cu.EF. A major concern in this study was the non-uniformity of the cathode surfaces as characterised by AFM and MicroXam techniques. It is therefore possible that the roughness values may not accurately describe the surface illuminated by the UV beam for transverse energy measurements. Thus, as discussed in Chapter 6, a more systematic approach is required in which cathode surfaces are carefully prepared to a known level of roughness and homogeneity.

As discussed in Chapter 4, there have been some difficulties in resolving the discrepancy in the QE measurements; this is most likely due to issues with the method of extracting photocurrent. Consequently only relative values are reported in the latter part of this work. A re-design and simplification of the circuit in which the photocurrent is measured at an anode, rather than measuring the drain current may ensure that all photoelectrons are collected. Additionally the stage for photocurrent measurements must be isolated so that there is no risk of leakage- in the current design the stage is not only used for photocurrent measurements, but also as a heating stage. Another avenue for exploration for why the QE values were lower than anticipated would be to vary the angle of incidence of the laser light to reduce reflection at the cathode surface.

## 7.2 Recommendations for further work

A number of experiments could be conducted to further investigate the properties of metallic photocathodes, such as:

1. Investigation of substrate roughness on surface properties and photoemissive properties of deposited metallic films.

2. Explore the effects of varying film deposition parameters on the thickness, adhesion and grain sizes, as well as other surface properties (QE, intrinsic emittance, WF, chemical composition).

3. QE lifetime studies for metallic photocathodes.

4. Prepare and characterise homogeneous photocathode surfaces for low intrinsic emittance.

R&D in the intersection of surface science and accelerator technology holds the potential to better understand and optimise accelerators, present and future. The work presented in this thesis only begins to scratch the surface of ways in which surface characterisation techniques can be used to better understand metallic photocathode properties.

# List of Publications

1. R. Valizadeh, S. Mistry, K.J. Middleman, A.N. Hannah, B.L. Militsyn and T.C.Q. Noakes. *The preparation of atomically clean metal surfaces for use as photocathodes in normally conducting RF guns.* International Particle Accelerator Conference (IPAC14), Dresden, Germany, June 2014.JACOW, Geneva, Switzerland 2014. http://accelconf.web.cern.ch/AccelConf/IPAC2014/papers/mopri047.pdf

2. S. Mistry, M. Cropper, R. Valizadeh, K.J. Middleman, A.N. Hannah, B.L. Militsyn and T.C.Q. Noakes. *Preparation of polycrystalline and thin film metal photocathodes for normal conducting RF guns.* International Particle Accelerator Conference (IPAC15), Richmond, VA, USA, May 2015. JACOW, Geneva, Switzerland 2015. http://accelconf.web.cern.ch/AccelConf/IPAC2015/papers/tupje058.pdf

3. S. Mistry, M. Cropper, R. Valizadeh, L.B. Jones, K.J. Middleman, A.N. Hannah, B.L. Militsyn and T.C.Q. Noakes. *A Comparison of Surface Properties of Metallic Thin Film Photocathodes.* International Particle Accelerator Conference (IPAC'16), BEXCO, Busan Korea. JACOW, Geneva, Switzerland, 2016. http://inspirehep.net/record/1470596/files/thpmy017.pdf

4. L. Jones, T. Beaver, B. Militsyn, S. Mistry, T. Noakes, and R. Valizadeh. *Energy distribution and work function measurements for metal photocathodes with measured levels of surface roughness.* International Particle Accelerator Conference (IPAC'17), Copenhagen, Denmark, May 2017. JACOW, Geneva, Switzerland, 2017. http://accelconf.web.cern.ch/AccelConf/ipac2017/papers/tupab111.pdf

# Bibliography


[1] RJ Barlow, P Bailey, and JA van den Berg. The uk meis facility: a new future. JACOW, Geneva, Switzerland, 2012.

[2] Brian WJ McNeil and Neil R Thompson. X-ray free-electron lasers. *Nature photonics*, 4(12):814–821, 2010.

[3] DH Dowell, I Bazarov, B Dunham, K Harkay, C Hernandez-Garcia, R Legg, H Padmore, T Rao, J Smedley, and W Wan. Cathode R&D for future light sources. *Nuclear Instruments and Methods in Physics Research Section A: Accelerators, Spectrometers, Detectors and Associated Equipment*, 622(3):685–697, 2010.

[4] A Brachmann, F-J Decker, F Zhou, JL Turner, P Emma, RH Iverson, and P Stefan. LCLS RF gun copper cathode performance. In *Conf. Proc.*, volume 110904, pages 3202–3204, 2011.

[5] JA Clarke, D Angal-Kalinin, N Bliss, R Buckley, S Buckley, R Cash, P Corlett, L Cowie, G Cox, GP Diakun, et al. CLARA conceptual design report. *Journal of Instrumentation*, 9(05):T05001, 2014.

[6] R Scrivens. Electron and ion sources for particle accelerators. *CAS - CERN Accelerator School: Intermediate Course on Accelerator Physics, Zeuthen, Germany, 15 - 26 Sep 2003, pp.495-504*, 2006.

[7] Michael Borland. *A high-brightness thermionic microwave electron gun.* PhD thesis, to the Department of Applied Physics.Stanford University, 1991.

[8] Christian Travier. RF guns: Bright injectors for FEL. *Nuclear Instruments and Methods in Physics Research Section A: Accelerators, Spectrometers, Detectors and Associated Equipment*, 304(1-3):285–296, 1991.

[9] Joseph F Mulligan. Heinrich Hertz and Philipp Lenard: two distinguished physicists, two disparate men. *Physics in Perspective (PIP)*, 1(4):345–366, 1999.

[10] JE Clendenin. RF photoinjectors. In *Conf. Proc.*, volume 9608262, pages 298–302, 1996.

[11] D Dowell, S Lidia, and J Schmerge. Lecture 2: Electron emission and cathode emittance, USPAS course on high brightness electron injectors for 4th generation light sources, UC Santa Cruz, January 2008 Santa Rosa, CA.

[12] L Cultrera. Advances in photocathodes for accelerators. In *Proceedings of 5th International Particle Accelerator Conference (IPAC 2014)*, page MOZB02. JACoW Geneva, Switzerland, 2014.

[13] N Chanlek, JD Herbert, RM Jones, LB Jones, KJ Middleman, and BL Militsyn. The degradation of quantum efficiency in negative electron affinity GaAs photocathodes under gas exposure. *Journal of Physics D: Applied Physics*, 47(5):055110, 2014.

[14] Donald A Edwards and Michael J Syphers. *An introduction to the physics of high energy accelerators*. John Wiley & Sons, 2008.

[15] Fernando Sannibale. High brightness electron injectors for 4th generation light sources. *Free Electron Laser Conference - Shanghai, August 23, 2011.*

[16] F Stephan, CH Boulware, M Krasilnikov, J Bähr, G Asova, A Donat, U Gensch, HJ Grabosch, M Hänel, L Hakobyan, et al. Detailed characterization of electron sources yielding first demonstration of European X-ray free-electron laser beam quality. *Physical Review Special Topics-Accelerators and Beams*, 13(2):020704, 2010.

[17] Triveni Rao and David H Dowell. An engineering guide to photoinjectors. *arXiv preprint arXiv:1403.7539*, 2014.

[18] Ivan V Bazarov, Bruce M Dunham, Yulin Li, Xianghong Liu, Dimitre G Ouzounov, Charles K Sinclair, Fay Hannon, and Tsukasa Miyajima. Thermal emittance and response time measurements of negative electron affinity photocathodes. *Journal of Applied Physics*, 103(5):054901, 2008.

[19] JL McCarter, T Rao, J Smedley, J Grames, R Mammei, M Poelker, and R Suleiman. Performance study of K2CsSb photocathode inside a DC high voltage gun. *Proceedings of PAC11, New York, NY, USA*, 2011.

[20] K Aulenbacher, G Arz, R Barday, and V Tioukine. Photocathode life time research at mami. *Proceedings of the 16th International Spin Physics Symposium and Workshop on Polarized Electron Sources and Polarimeters. 10-16 October 2004 Trieste, Italy.*, 2005.

[21] K Batchelor, Ilan Ben-Zvi, Richard Clinton Fernow, J Fischer, AS Fisher, J Gallardo, G Ingold, HG Kirk, KP Leung, R Malone, et al. Performance of the Brookhaven photocathode RF gun. *Nuclear Instruments and Methods in Physics Research Section A: Accelerators, Spectrometers, Detectors and Associated Equipment*, 318(1-3):372–376, 1992.

[22] XiJie Wang, K Batchelor, I Ben-Zvi, D Lynch, J Sheehan, and M Woodle. Design and construction a full copper photocathode RF gun. In *Particle Accelerator Conference, 1993., Proceedings of the 1993*, pages 3000–3002. IEEE, 1993.

[23] P Murcek, K Moeller, R Xiang, H Buettig, M Freitag, J Teichert, P Kneisel, A Arnold, and P Michel. Modified 3.5-cell SC cavity made of large grain niobium for the FZD SRF photoinjector. Technical report, 2010.

[24] PR Bolton, JE Clendenin, DH Dowell, M Ferrario, AS Fisher, SM Gierman, RE Kirby, P Krejcik, CG Limborg, GA Mulhollan, et al. Photoinjector design for the LCLS. *Nuclear Instruments and Methods in Physics Research Section A: Accelerators, Spectrometers, Detectors and Associated Equipment*, 483(1):296–300, 2002.

[25] PA McIntosh, D Angal-Kalinin, N Bliss, R Buckley, S Buckley, JA Clarke, P Corlett, G Cox, GP Diakun, B Fell, et al. Implementation and commissioning of the new versatile electron linear accelerator (formerly EBTF) at Daresbury Laboratory for industrial accelerator system development. *THPWA036, these proceedings*, 2013.

[26] M Boscolo, M Ferrario, I Boscolo, F Castelli, and S Cialdi. Generation of short THz bunch trains in a RF photoinjector. *Nuclear Instruments and Methods in Physics Research Section A: Accelerators, Spectrometers, Detectors and Associated Equipment*, 577(3):409–416, 2007.

[27] Luigi Palumbo and James Rosenzweig. Technical design report for the SPARC advanced photo-injector. *Preprint INFNLNF*, pages 12–1, 2004.

[28] T Srinivasan-Rao, I Ben-Zvi, J Smedley, XJ Wang, MAWM Woodle, DT Palmer, and RH Miller. Performance of magnesium cathode in the S-band RF gun. In *Particle Accelerator Conference, 1997. Proceedings of the 1997*, volume 3, pages 2790–2792. IEEE, 1997.

[29] Terunobu Nakajyo, Jinfeng Yang, Fumio Sakai, and Yasushi Aoki. Quantum efficiencies of Mg photocathode under illumination with 3rd and 4th harmonics Nd: LiYF4 laser light in RF gun. *Japanese journal of applied physics*, 42(3R):1470, 2003.

[30] PJ Kelly and RD Arnell. Magnetron sputtering: a review of recent developments and applications. *Vacuum*, 56(3):159–172, 2000.

[31] J Smedley, T Rao, and J Sekutowicz. Lead photocathodes. *Physical Review Special Topics-Accelerators and Beams*, 11(1):013502, 2008.

[32] T Srinivasan-Rao, J Schill, I Ben Zvi, and M Woodle. Sputtered magnesium as a photocathode material for RF injectors. *Review of scientific instruments*, 69(6): 2292–2296, 1998.

[33] Giancarlo Gatti, Pawel Strzyzewski, Carlo Vicario, Carmen Ristoscu, Alessio Perrone, Angelamaria Fiori, Franco Tazzioli, Silvia Orlanducci, Jerzy Langner, Marek Sadowski, et al. Metal film photocathodes for high brightness electron injectors. Technical report, 2006.

[34] A Perrone, L Cultrera, A Pereira, M Rossi, S Cialdi, I Boscolo, F Tazzioli, C Vicario, and G Gatti. Ablated Mg films with a graphite cover as photocathodes. *Nuclear Instruments and Methods in Physics Research Section A: Accelerators, Spectrometers, Detectors and Associated Equipment*, 554(1):220–225, 2005.

[35] Herbert B Michaelson. The work function of the elements and its periodicity. *Journal of Applied Physics*, 48(11):4729–4733, 1977.

[36] T Srinivasan-Rao, J Fischer, and T Tsang. Photoemission from mg irradiated by short pulse ultraviolet and visible lasers. *Journal of applied physics*, 77(3): 1275–1279, 1995.

[37] L Cultrera, A Pereira, C Ristoscu, A Clozza, F Tazzioli, and C Vicario. Pulsed laser deposition of Mg thin films on Cu substrates for photocathode applications. *Applied Surface Science*, 248(1):397–401, 2005.

[38] R Xiang, P Lu, and H Vennekate. Highlights on metallic photocathodes used in SRF gun. *Proceedings of IPAC2016, Busan, Korea*, 2016.

[39] R Xiang, A Arnold, P Murcek, and J Teichert. Improvement of photoemission efficiency of magnesium photocathodes. *Proceedings of IPAC2017, Copenhagen, Denmark*, 2017.

[40] R Barday, A Burrill, A Jankowiak, T Kamps, J Knobloch, O Kugeler, A Matveenko, A Neumann, M Schmeißer, J Völker, et al. Characterization of a superconducting Pb photocathode in a superconducting RF photoinjector cavity. *Physical Review Special Topics-Accelerators and Beams*, 16(12):123402, 2013.

[41] F Gontad, A Lorusso, and A Perrone. Structure and morphology of laser-ablated Pb thin films. *Thin Solid Films*, 520(11):3892–3895, 2012.

[42] Francisco Gontad, Antonella Lorusso, Giancarlo Gatti, Massimo Ferrario, Laura Gioia Passione, Luana Persano, Nicola Lovergine, and Alessio Perrone. Characterisation of photocathodes based on Pb thin film deposited by UV pulsed laser ablation. *Journal of Materials Science & Technology*, 30(1):37–40, 2014.

[43] LN Hand and U Happek. Photoelectric quantum efficiency of niobium for $\lambda$= 193 nm and $\lambda$= 248 nm. *Nuclear Instruments and Methods in Physics Research Section A: Accelerators, Spectrometers, Detectors and Associated Equipment*, 372 (3):335–338, 1996.

[44] J Smedley, T Rao, and Q Zhao. Photoemission studies on niobium for superconducting photoinjectors. *Journal of applied physics*, 98(4):043111, 2005.

[45] Triveni Rao, I Ben-Zvi, Andrew Burrill, H Hahn, D Kayran, Y Zhao, Peter Kneisel, and M Cole. Photoemission studies on BNL/AES/JLAB all niobium, superconducting RF injector. In *Particle Accelerator Conference, 2005. PAC 2005. Proceedings of the*, pages 2556–2558. IEEE, 2005.

[46] L Cultrera, G Gatti, and A Lorusso. Photoemission studies on yttrium thin films. *Radiation Effects & Defects in Solids: Incorporating Plasma Science & Plasma Technology*, 165(6-10):609–617, 2010.

[47] Alessio Perrone, M DElia, F Gontad, M Di Giulio, G Maruccio, A Cola, NE Stankova, DG Kovacheva, and E Broitman. Non-conventional photocathodes based on Cu thin films deposited on Y substrate by sputtering. *Nuclear Instruments and Methods in Physics Research Section A: Accelerators, Spectrometers, Detectors and Associated Equipment*, 752:27–32, 2014.

[48] DH Dowell, FK King, RE Kirby, JF Schmerge, and JM Smedley. In situ cleaning of metal cathodes using a hydrogen ion beam. *Physical Review Special Topics-Accelerators and Beams*, 9(6):063502, 2006.

[49] Christoph Heßler, Eric Chevallay, Mikhail Martyanov, Valentin Fedosseev, Irene Martini, and Steffen Döbert. Recent results on the performance of Cs3Sb photocathodes in the PHIN RF -gun. Technical report, 2015.

[50] S Lederer, S Schreiber, P Michelato, L Monaco, C Pagani, D Sertore, and JH Han. Photocathode studies at FLASH. *Proc. EPAC 08, Genua, Italy, 23-27 Jun 2008*, 2008.

[51] SH Kong, J Kinross-Wright, DC Nguyen, and RL Sheffield. Photocathodes for free electron lasers. *Nuclear Instruments and Methods in Physics Research Section A: Accelerators, Spectrometers, Detectors and Associated Equipment*, 358(1-3):272–275, 1995.

[52] Carlos Hernandez-Garcia, T Siggins, S Benson, D Bullard, HF Dylla, K Jordan, C Murray, GR Neil, M Shinn, and R Walker. A high average current DC gaas photocathode gun for ERLs and FELs. In *Particle Accelerator Conference, 2005. PAC 2005. Proceedings of the*, pages 3117–3119. IEEE, 2005.

[53] Narong Chanlek. Quantum efficiency lifetime studies using the photocathode preparation experimental facility developed for the ALICE accelerator. 2012.

[54] E Chevallay, J Durand, S Hutchins, G Suberlucq, and M Wurgel. Photocathodes tested in the dc gun of the CERN photoemission laboratory. *Nuclear Instruments and Methods in Physics Research Section A: Accelerators, Spectrometers, Detectors and Associated Equipment*, 340(1):146–156, 1994.

[55] Jochen Teichert, JWJ Verschuur, Guy Suberlucq, and Xiang Rong. Report on photocathodes. Technical report, 2004.

[56] Daniele Sertore, Paolo Michelato, Laura Monaco, and Carlo Pagani. A study for the characterization of high QE photocathodes. In *Particle Accelerator Conference, 2007. PAC. IEEE*, pages 2760–2762. IEEE, 2007.

[57] SH Kong, DC Nguyen, RL Sheffield, and BA Sherwood. Fabrication and characterization of cesium telluride photocathodes: A promising electron source for the Los Alamos Advanced FEL. *Nuclear Instruments and Methods in Physics Research Section A: Accelerators, Spectrometers, Detectors and Associated Equipment*, 358 (1-3):276–279, 1995.

[58] David H Dowell. Advances in cathodes for high-current rf photoinjectors. In *Optoelectronics' 99-Integrated Optoelectronic Devices*, pages 14–21. International Society for Optics and Photonics, 1999.

[59] RA Loch. Cesium-telluride and magnesium for high quality photocathodes. *Masterdiploma thesis, University of Twente*, 2005.

[60] Harold Max Rosenberg. *The solid state*. Oxford University Press Oxford, 1988.

[61] Charles Kittel and Donald F Holcomb. Introduction to solid state physics. *American Journal of Physics*, 35(6):547–548, 1967.

[62] Martin Prutton. *Surface Physics*. Oxford University Press, London, 1975.

[63] Kwan Chi Kao. *Dielectric phenomena in solids*. Elsevier Academic Press, 2004.

[64] S Poulston, PM Parlett, P Stone, and M Bowker. Surface oxidation and reduction of CuO and Cu2O studied using XPS and XAES. *Surface and Interface Analysis*, 24(12):811–820, 1996.

[65] N Moody, DW Feldman, PG O'Shea, and KL Jensen. Fabrication and measurement of low workfunction cesiated dispenser photocathodes. In *Particle Accelerator Conference, 2005. PAC 2005. Proceedings of the*, pages 2953–2955. IEEE, 2005.

[66] Mingshan Xue, Wenfeng Wang, Fajun Wang, Junfei Ou, Changquan Li, and Wen Li. Understanding of the correlation between work function and surface morphology of metals and alloys. *Journal of Alloys and Compounds*, 577:1–5, 2013.

[67] CP Hauri, R Ganter, F Le Pimpec, A Trisorio, C Ruchert, and HH Braun. Intrinsic emittance reduction of an electron beam from metal photocathodes. *Physical review letters*, 104(23):234802, 2010.

[68] Shunya Matsuba, Yosuke Honda, Xiuguang Jin, Tsukasa Miyajima, Masahiro Yamamoto, Takashi Uchiyama, Makoto Kuwahara, and Yoshikazu Takeda. Mean transverse energy measurement of negative electron affinity GaAs-based photocathode. *Japanese Journal of Applied Physics*, 51(4R):046402, 2012.

[69] Zhe Zhang and Chuanxiang Tang. Analytical study on emittance growth caused by roughness of a metallic photocathode. *Physical Review Special Topics-Accelerators and Beams*, 18(5):053401, 2015.

[70] Siddharth Karkare and Ivan Bazarov. Effect of nanoscale surface roughness on transverse energy spread from GaAs photocathodes. *Applied Physics Letters*, 98 (9):094104, 2011.

[71] DJ Bradley, MB Allenson, and BR Holeman. The transverse energy of electrons emitted from GaAs photocathodes. *Journal of Physics D: Applied Physics*, 10(1): 111, 1977.

[72] D Brigg and MP Seah. Practical surface analysis: Auger and X-ray photoelectron spectroscopy, vol. 1, 1995.

[73] Lee Jones. *An investigation into the effect of a chiral adsorbate on surface magnetism using spin-resolved electron spectroscopy: tartaric acid on Ni {110}*. PhD thesis, University of Liverpool, 2006.

[74] Karl Jousten. Thermal outgassing. *CERN European organization for nuclear research-reports-CERN*, pages 111–126, 1999.

[75] Yoshio Umezawa and Charles N Reilley. Effect of argon ion bombardment on metal complexes and oxides studied by x-ray photoelectron spectroscopy. *Analytical Chemistry*, 50(9):1290–1295, 1978.

[76] John F Watts and John Wolstenholme. An introduction to surface analysis by XPS and AES. *An Introduction to Surface Analysis by XPS and AES, by John F. Watts, John Wolstenholme, pp. 224. ISBN 0-470-84713-1. Wiley-VCH, May 2003.*, page 224, 2003.

[77] N Fairley. Casaxps version 2.3. 14. *Casa Software Ltd*, 2005, 1999.

[78] Rudy Schlaf. Tutorial on work function. *Tampa: USF Surface Science Laboratory, Dept of Electrical Engineering at University of South Florida*, 2007.

[79] ID Baikie, S Mackenzie, PJZ Estrup, and JA Meyer. Noise and the kelvin method. *Review of scientific instruments*, 62(5):1326–1332, 1991.

[80] Rudy Schlaf. Tutorial on kelvin probe measurements. *Tampa: USF Surface Science Laboratory, Dept of Electrical Engineering at University of South Florida*, 2007.

[81] Peter Eaton and Paul West. *Atomic force microscopy*. Oxford University Press, 2010.

[82] The Future of DME SPM equipment scanning probe microscopy - an overview. `http://dme-spm.com/funktion.html`. Accessed: 2017-08-31.

[83] MicroXam surface mapping microscope. `http://www.ccmr.cornell.edu/wp-content/uploads/sites/2/2015/11/MicroXam-specs.pdf`. Accessed: 2017-08-31.

[84] Optical Profiler Basics optical profilers. `https://www.zygo.com/?/met/profilers/opticalprofilersabout.htm`. Accessed: 2017-08-31.

[85] F Ernst. Rutherford backscattering spectrometry. *EMSE-515-F05-08*, 2005.

[86] JB Craig. Practical surface analysis, volume 2ion and neutral spectroscopy: Edited by d. briggs and mp seah, wiley, chichester, 1992, xvi+ 738 pp.,£ 50.000. isbn 0-471-96498-0, 1997.

[87] Paul Bailey, TCQ Noakes, and DP Woodruff. A medium energy ion scattering study of the structure of Sb overlayers on Cu (111). *Surface Science*, 426(3): 358–372, 1999.

[88] Matej Mayer. Simnra user's guide. *Max-Planck-Institut für Plasmaphysik Garching*, 1997.

[89] MA Reading, JA Van den Berg, PC Zalm, DG Armour, Paul Bailey, TCQ Noakes, A Parisini, T Conard, and Stefan De Gendt. High resolution medium energy ion scattering analysis for the quantitative depth profiling of ultrathin high-k layers. *Journal of Vacuum Science & Technology B, Nanotechnology and Microelectronics: Materials, Processing, Measurement, and Phenomena*, 28(1):C1C65–C1C70, 2010.

[90] R Valizadeh, KJ Middleman, AN Hannah, BL Militsyn, TCQ Noakes, and S Mistry. The preparation of atomically clean metal surfaces for use as photocathodes in normally conducting RF guns. *Proc. IPAC*, 14.

[91] VF Henley. *Anodic Oxidation of Aluminium and Its Alloys: The Pergamon Materials Engineering Practice Series*. Elsevier, 2013.

[92] Jill Chastain, Roger C King, and JF Moulder. *Handbook of X-ray photoelectron spectroscopy: a reference book of standard spectra for identification and interpretation of XPS data*. Physical Electronics Eden Prairie, MN, 1995.

[93] Thermo Scientific xps reference table of elements. `www.xpssimplified.com/periodictable.php`. Accessed: 2017-08-10.

[94] Heiner Ryssel and Hans Glawischnig. *Ion Implantation: Equipment and Techniques: Proceedings of the Fourth International Conference Berchtesgaden, Fed. Rep. of Germany, September 13–17, 1982*, volume 11. Springer Science & Business Media, 2012.

[95] V Fournier, P Marcus, and I Olefjord. Oxidation of magnesium. *Surface and interface analysis*, 34(1):494–497, 2002.

[96] Catalin Fotea, James Callaway, and Morgan R Alexander. Characterisation of the surface chemistry of magnesium exposed to the ambient atmosphere. *Surface and interface analysis*, 38(10):1363–1371, 2006.

[97] M Delheusy, A Stierle, N Kasper, RP Kurta, A Vlad, H Dosch, C Antoine, Andrea Resta, Edvin Lundgren, and J Andersen. X-ray investigation of subsurface interstitial oxygen at Nb/oxide interfaces. *Applied Physics Letters*, 92(10):101911, 2008.

[98] Mark C Biesinger, Leo WM Lau, Andrea R Gerson, and Roger St C Smart. Resolving surface chemical states in XPS analysis of first row transition metals, oxides and hydroxides: Sc, Ti, V, Cu and Zn. *Applied Surface Science*, 257(3):887–898, 2010.

[99] R Valizadeh, AN Hannah, KJ Middleman, BL Militsyn, TCQ Noakes, MD Roper, and R Santer. Preparation of the polycrystalline copper photocathodes for VELA RF photocathode gun. In *International Particle Accelerator Conference*, pages 440–442, 2013.

[100] Y Pouillon and C Massobrio. A density functional study of CuO 2 molecules: structural stability, bonding and temperature effects. *Chemical Physics Letters*, 331(2):290–298, 2000.

[101] S Mistry, M Cropper, R Valizadeh, KJ Middleman, AN Hannah, BL Militsyn, and TCQ Noakes. Preparation of polycrystalline and thin film metal photocathodes for normal conducting RF guns.

[102] Josef Hölzl and Franz K Schulte. Work function of metals. In *Solid surface physics*, pages 1–150. Springer, 1979.

[103] Sonal Mistry, LB Jones, Reza Valizadeh, Adrian Hannah, Mike Cropper, Tim Noakes, BL Militsyn, and Keith Middleman. A comparison of surface properties of metallic thin film photocathodes. Technical report, 2016.

[104] Lee Jones, Thomas Beaver, Boris Militsyn, Sonal Mistry, Tim Noakes, and Reza Valizadeh. Energy distribution and work function measurements for metal photocathodes with measured levels of surface roughness. In *8th Int. Particle Accelerator Conf.(IPAC'17), Copenhagen, Denmark, 14â 19 May, 2017*, pages 1580–1583. JACOW, Geneva, Switzerland, 2017.

[105] BL Militsyn, I Burrows, RJ Cash, BD Fell, LB Jones, JW McKenzie, KJ Middleman, HE Scheibler, and AS Terekhov. First results from the iii-v photocathode preparation facility for the alice erl photoinjector. *Proceedings of IPAC'10*, 2010.

[106] SPIP Roughness spip classic roughness parameters for images. `https://spip.imagemet.com/WebHelp6/Default.htm#RoughnessParameters/Roughness_Parameters.htm`. Accessed: 2017-08-10.

[107] Dao Xiang, Wen-Hui Huang, Ying-Chao Du, Li-Xin Yan, Ren-Kai Li, Chuan-Xiang Tang, and Yu Zheng Lin. First principle measurements of thermal emittance for copper and magnesium. In *Particle Accelerator Conference, 2007. PAC. IEEE*, pages 1049–1051. IEEE, 2007.

[108] LB Jones, RJ Cash, BD Fell, KJ Middleman, TCQ Noakes, BL Militsyn, HE Scheibler, DV Gorshkov, and AS Terekhov. The commissioning of TESS: An experimental facility for measuring the electron energy distribution from photocathodes. *Proc. FEL2013, New York, USA*, 2013.